Studies of model systems for the low-temperature oxidation of CO by supported gold catalysts

A thesis submitted to The University of Manchester
for the degree of
PhD
in the Faculty of Engineering and Physical Sciences

2008

Simon Braun

School of Chemistry

Table of Contents

Chapter 2 Techniques

Chapter 3 Small volume cell for *in situ* measurements of flat samples

Chapter 4 Results

Word count: 71955

List of figures

Chapter 1 Introduction

Chapter 2 Techniques

Chapter 3 Small volume cell for *in situ* measurements of flat samples

Chapter 4 Results

Chapter 4.1 Growth of Au Nanoclusters on TiO_2(110) by Spin Coating

Chapter 4.2 *In situ* studies of oxidised gold under different environmental conditions

Chapter 4.3 Catalytic activity of gold powder of the CO oxidation

4.4 *In situ* XPS analysis of gold nanoparticles supported on TiO_2 powder

5 General Conclusions and further studies

List of Tables

Chapter 1 Introduction

Chapter 2 Techniques

Chapter 3 Small volume cell for *in situ* measurements of flat samples

Chapter 4 Results

Chapter 4.1 Growth of Au Nanoclusters on TiO_2(110) by Spin Coating

Chapter 4.2 *In situ* studies of oxidised gold under different environmental conditions

Chapter 4.3 Catalytic activity of gold powder of the CO oxidation

Chapter 4.4 *In situ* XPS analysis of gold nanoparticles supported on TiO_2 powder

Abstract

The preparation and reactivity of a range of model systems for the low temperature oxidation of CO by gold catalysts have been investigated with a view to assessing their feasibility for bridging the 'materials gap' between well-defined single crystalline models and practical supported catalysts. The studied systems included gold powder, electrochemically oxidized gold foil, gold nanoparticles prepared on TiO_2 single crystal surfaces by spin-coating and gold nanoparticles prepared on TiO_2 powder by deposition-precipitation. Particular attention was paid to the reduction of oxidised gold species, since these are the common precursors in the preparation of practical nanoparticular catalysts. Oxidised gold species may also be mechanistically relevant for the catalytic low-temperature CO oxidation.

A low volume reactor was designed for studies of flat gold model catalysts. It was tested with *in situ* X-ray absorption spectroscopy (XAS). The design of the reactor cell allows the use of further techniques including UV/Vis spectroscopy, X-ray differaction (XRD), Raman scattering and Infrared (IR) Spectroscopy. The reactor was also designed to permit reaction rate measurements with a mass spectrometer. In comparison to other reactors reported in the literature, this design is very cost efficient, not only in its construction but also due to its compatibility with a wide range of spectroscopic techniques.

In situ X-ray photoelectron spectroscopy (XPS) on gold particles supported on TiO_2 powder indicated that different atmosphere could change the morphology of the gold particles. This change is more prominent for smaller particles. The formation of graphite like spices under a CO atmosphere was observed as well.

X-ray photoelectron spectroscopy (XPS) and *in situ* Au L-edge XAS indicated that suitable gold nanoparticles could be prepared by spin coating of tetrachloroauric acid solutions onto rutile single crystals. Gold loadings as low as 0.1 and 0.03 monolayers could be achieved. The XAS data indicated the presence of low average Au-Au coordination numbers, suggesting the presence of very small nanoparticles. XA spectra taken under CO and O_2 atmosphere indicated that CO interacts with the gold particles.

In situ X-ray absorption near edge structure (XANES) C K-edge studies were carried out on electrochemically oxidised gold foils. When exposed to carbon monoxide at pressures up to 10^{-2} mbar the anodic oxide layers reduce rapidly. This process is accompanied by the formation of a carbonaceous layer at the surface. XPS studies revealed that the foils were superficially not fully reduced. Au L_{III}-edge spectra showed that the reduction of the samples proceeds also in oxygen at elevated temperatures, with an ultrathin oxidic layer remaining near the surface, similar to the samples treated with CO at 10^{-2} mbar pressure.

The catalytic activity of unsupported bulk gold, in form of gold powder with particle sizes between 0.5 μm and 2 μm, was determined. Pure gold was found to be generally active at temperatures above 570 K. Heating to 700 K in a 1:1 CO/O_2 mixture resulted in a conditioning effect, leading to higher catalytic activity of the gold powder. An activation energy of 53 kJ/mol for the CO oxidation reaction was determined from the temperature dependence of the reaction. Scanning electron microscopy and atomic force microscopy images revealed mesoscopic surface morphology changes caused by the catalytic, which seems to be associated with the conditioning of the catalyst.

Declaration

Herewith I state that no portion of the work referred in this thesis has been submitted in support of an application for another degree or qualification of this or any other university or other institute of learning.

Copyright Statement

(i) Copyright in text of this thesis rests with the author. Copies (by any process) either in full, or of extracts, may be made **only** in accordance with instrctions given by the author and lodged in the John Rylands University Library of Manchester. Details may be obtained from the Librarian. This page must form part of any such copies made. Further copies (by any process) of copies made in accordance with such instructions may not be made without the permission (in writing) of the author.

(ii) The ównership of any intellectual property rights which may be described in this thesis is vested in The University of Manchester, subject to any prior agreement to the contrary, and may not be made available for use by third parties without the written permission of the University, which will prescribe the terms and conditions of any such agreement.

(iii) Futher information on the conditions under which disclosures and exploition may take place is available from the Head of School of Chemistry.

Acknowledgment

For supervision and financial support as well as for giving me the opportunity to work in his group I do like to gratefully thank Sven Schroeder.

My deepest thanks goes to A. Murray Booth for designing with me the soft X-ray XAS cell as well as to the rest of my beamline crew including Agnes Coloumbanie-Dauvernge, Andy Ip and Hamid Esfahanian. Beamtimes without you would have been impossible especially by lending me a hand when I did let you, supplying the videos for the night shifts and granting me at least a few hours of sleep every now and then. I am also grateful for you sharing the office with me and helping me in general to prepare this thesis.

The beamline scientist of the CCLRC should be gratefully thanked for helping me finding parts for the experiments and especially John Purton, Ian Harvey, Tsu Hayama, Sunil Patel, Ian Kirkman and Bob Bilsborrow for helping me with their beamlines.

I would like to thank Dave Quin from the University of Southampton for the preparation of samples for soft X-ray XAS studies as well as Birgit Schumacher from the University of Ulm for the preparation of a sample that was used during *in situ* XPS studies at BESSY. Trevor Rayment from the University of Birmingham should be acknowledge for granting me permission to use his sample positioning system for several hard X-ray XAS studies.

I would like to mention the skilful work of the workshops of the School of Chemistry of the University of Manchester as well as of the CCLRC in Daresbury. This and a lot of helpful discussions were the requirements for most of the experiments.

Finally my family and friends in Berlin and Manchester deserve a special thank for helping me through the time.

1 Introduction

1.1 Aim of Study

The aim of this thesis was to study the low temperature oxidation of carbon monoxide, supported by gold catalyst. To this purpose, four model catalysts were prepared, each of them designed to study one particular property of the catalytic reaction.

The first system studied were gold particles supported on TiO_2 powder, which is one of the most common gold catalysts present in literature. This sample was studied by *in situ* XPS and the aim was to identify differences between a very low loaded catalyst (~ 0.5 wt% gold loading) and a high loaded catalyst as presented in this thesis (~ 3.3 wt%). The *in situ* XPS studies can also give indications about possible reaction intermediates and changes in the gold nanoparticles as well as in the support by analysing the corresponding elemental XPS peaks.

The second model was gold nanoparticles on a single crystal support, which can be studied by probe microscopy like AFM. Therefore a potential exists to better characterise changes in the gold particle shape than it is possible for powder supported catalysts. To mimic the preparation of gold nanoparticles on powder supports, single crystals supported gold nanoparticles were not prepared with "physical preparation methods" like chemical vapour deposition (CVD) or sputtering, but with a wet chemistry synthesis route very close to that used for powder catalysts. To characterise these samples with *in situ* spectroscopy a special measurement chamber was designed and the interaction of the particles with the different reactants was studied. It was also aimed for to analyse the catalytic activity of these catalysts.

Electrochemical oxidised gold was used to study the decomposition of these oxidised gold species under oxidising condition. The oxidising conditions are used to calcinate the gold catalysts. The oxidised species are also present when freshly prepared catalysts are used for the CO oxidation with excess amounts of oxygen. Also the interaction of oxidised gold species with CO was studied to achieve indications if oxidised species might be required or supportive for the catalytic reaction cycle of the CO oxidation.

The final model was macroscopic gold powder that was studied in terms to identify if bulk gold can be catalytic active and what are the potential differences to nanoparticular gold. This means also how much of a conversion for the CO oxidation could be expected from macroscopic gold in comparison to nanoparticular gold at room temperature.

Comparing the model with differences in complexity allows indication, which component of a catalyst is involved in which part of the catalytic reaction. E.g. it is argued if the TiO_2 support in gold catalysis is only responsible for supporting the gold nanoparticles or if either at the support or on defects sites of the catalyst the oxygen molecule is activated. Furthermore it is possible to study the difference between nanoparticular material and its crystalline counter part. Gold is therefore a very attractive candidate since it is generally believed that crystalline, bulk gold is catalytic inert, whereas nanoparticular gold shows very high catalytic activities. This difference between bulk and nanoparticular material is also known as "materials gap".

1.2 Catalysis with supported gold

1.2.1 History of gold catalysis

For a long time, gold was believed to be a poor material for applications as a heterogeneous catalyst. Also it was not known how to prepare highly dispersed gold particles on metal oxide supports. Since at least the 1920s [1], pure gold was known to be an efficient CO oxidation catalyst at temperatures above 300°C. It was often used in the form of sponges or other high surface forms [2, 3]. However Cu and Ag, as well as group VIII transition metals such as Rh, Ru, Ir, and Pd and Pt in particular, developed much higher activities for oxidation reactions when supported as small particles on oxides [4]. They also exhibited higher stability against sintering than gold, which has a significantly lower melting point and does not interact as strongly with catalyst support materials. For these reasons it was believed at least until the last two decades of the 20^{th} century that gold would not be of any use in heterogeneous catalysis.

In the 1970s gold was investigated as nanoparticles on different substrate [5, 6, 7]. Several research groups prepared, for the first time, supported catalyst by evaporating gold onto SiO_2 and Al and Al_2O_3, respectively. They investigated the particles with X-ray photoelectron spectroscopy (XPS) and showed that metallic gold nanoparticles could be formed by this method. Cocco and co-workers changed the preparation and impregnated η-Al_2O_3 and SiO_2 [8] in a procedure that is similar to the method now commonly known as the "Haruta method" (see below) [9]. However these researchers did not determine the catalytic potential of the gold nanoparticles. Finally, Haruta and co-workers carried out investigation in the late 1980s [10 -12]. The Haruta group has since been one of the most active research groups in the field of gold catalysis [13 - 18]. They tested different supports for the gold nanoparticles including TiO_2, Fe_2O_3, Al_2O_3 and Co_3O_4. They found that the nature of the support only has a small effect on the catalytic reactivity, however the properties of the gold clusters strongly influence the results. The preparation technique is also a determinant step affecting the activity of catalysts. When prepared by impregnation techniques, catalysts have generally poor activities. On the other hand, catalysts prepared by co-precipitation or deposition-precipitation give high activities for the CO oxidation (see the following section for more details). These two techniques are still the most common methods to prepare highly active gold catalysts. However several research groups involved in this field have developed slight variations to prepare the gold catalysts and these variations make it difficult to compare results. This difficulty in preparing a good catalyst, even if a recipe is given, might reflect the fact that catalysis is sometimes called "black magic" [19].

1.2.2 Preparation and application of gold catalysts

Gold catalysts can be prepared by deposition-precipitation [20]. The general route of the synthesis is given here but nearly each author uses slight variations to this route. First the gold is dissolved in a diluted aqueous solution. After adjusting the value of the pH, generally a value of greater than 8 is used, the support is added. The suspension is often stirred for some time (~ 1 hour), at different temperatures and finally the catalyst is separated from the solvent. Afterwards the catalyst is dried and

calcined, i.e. heated in reducing, inert or oxidising atmospheres. It was also reported that the catalyst could be used without calcinations.

Another technique involves co-precipitation [10]. Here the gold and support are precipitated out of the solution at the same time. Again several parameters can be varied, such as the solvent, the precipitation agent and general conditions like temperature, pH and the amount of gold in the solution.

A third technique is the impregnation of the support with the gold solution [14]. The gold is dissolved in a very small amount of solvent. The amount of solvent should be small enough to be fully absorbed by the support. After absorption of the solution, the catalyst has to be dried. However the catalytic activity is not as good as can be obtained by other preparation techniques.

It is possible to influence the amount of gold loaded onto the support but it is challenging to control the particle size distribution and the shape of the particles. A step forward is to precipitate gold nanoparticles in micelles, giving rise to a very narrow size distribution [21, 22]. The drawback of these "capped" nanoparticles is that the micelles surround the gold clusters even after the deposition. It is therefore difficult to activate the gold clusters for catalytic applications.

CO oxidation, catalysed by gold, can be applied to a wide range of applications [23]. CO is a highly toxic gas, which is produced via incomplete combustion of carbon containing species. For example, in low temperature fuel cells CO has to be removed from the gas steam. The gas stream, usually H_2 and O_2, contains small amounts of CO as the hydrogen is often produced by the water gas shift reaction (see below), which includes CO as one of the reactants. But CO tends to bind very strongly to the electrodes of the fuel cells, which means that small concentrations of CO can poison the cell very quickly and prevent it from working or lowering the efficiency. Therefore low partial pressures (in the ppm range) of CO have to be selectively removed from a stream of H_2 and O_2. These reaction conditions are also called PROX conditions and require that the catalyst is not only very active for the oxidation of CO, but should also not oxidize the hydrogen to water [24, 25]. The tested gold catalysts often show very good selectivity towards the CO oxidation under these conditions and the selectivity of the gold catalysts are better than for common oxidation, catalysts like Pt, Pd or Rh.

Removing CO from the environment is an ecological task, which becomes even more important in closed environments, as in submarines and on outer space missions. Since small quantities are so toxic to human beings it has to be removed from the air in these habitats to permit prolonged missions. CO can be removed by several chemical reactions but one of the simplest is by oxidation to CO_2, which lowers the toxic potential drastically. With gold catalysts this is possible at room temperature without the need for energy or any reactant inputs to the reaction, with the exception of oxygen, which will be present in the ambient air. This is important when energy and weight are limited as on outer space missions and therefore the use of gold catalysts is a very efficient way of dealing with the problem CO residues.
The oxidation of CO to CO_2 is also essential in closed-cycle CO_2-lasers [26 - 28]. In this case the CO_2 decomposes to carbon monoxide and oxygen when the laser is in operation. Both CO and O_2 tend to lower the efficiency of the laser and their amount should ideally be kept close to zero. This leads to the specific problem of oxidising small amounts of stoichiometric CO and 1/2 O_2 to CO_2, with CO_2 having a high partial pressure in the reaction mixture. A high amount of CO in the reaction mixture can lead to blocking of active sites on the catalyst. Hence low adsorption strength between CO_2 and support but high adsorption strength between CO, O_2 and support should be achieved.

Gold catalysts have been tested for other reactions as well (cf. table 1.1). The reaction of CO or CO_2 with hydrogen to methanol is industrially very important [17]. Methanol, as a simple alcohol, is one of the major feedstock in a very wide field of chemical reactions [29]. But it is important that no methane is formed beside methanol that would lower the profitability.

Table 1.1: Some catalytic reactions of Au/metal oxide.

Reaction	Reference
$CO + ½ O_2 \rightarrow CO_2$ (different conditions)	[24, 25]
$CO + 2 H_2 \rightarrow$ Methanol	[17]
$CO_2 + 3 H_2 \rightarrow$ Methanol + H_2O	[17]
Propylene + O_2 + $H_2 \rightarrow$ Propylene oxide + H_2O	[30]
Glycerol + $O_2 \rightarrow$ Glyceric acid	[31]
$2 NO \rightarrow N_2 + O_2$	[32]

The water gas shift reaction is one of the most important industrial reactions to produce hydrogen. Hydrogen itself is needed in industry for several hydrogenation reactions, for example, the production of formic acid [33]. Industrial catalysts, such as iron oxide-chromium oxide and copper oxide-zinc oxide, operate at temperatures between 200°C and 400°C [34]. The water gas shift reaction over gold catalysts in comparison can achieve good conversion at room temperature [33, 35].

The selective oxidation of propylene with oxygen and hydrogen to propylene oxide is industrially a very important step as well, for example, polyurethane is produced from propylene oxide. This epoxidation of propylene can be achieved with a variety of oxidation agents like peroxyacids [29], but is preferred to use molecular oxygen in industry. However to use molecular oxygen in a one-step reaction is not trivial and often results in unwanted side-products [30]. The one step synthesis would increase the profitability of the production. Supported gold nanoparticles seem to be a good candidate to resolve this problem, as the work of Hayashi et al. [30] showed very good selectivity of up to 90%.

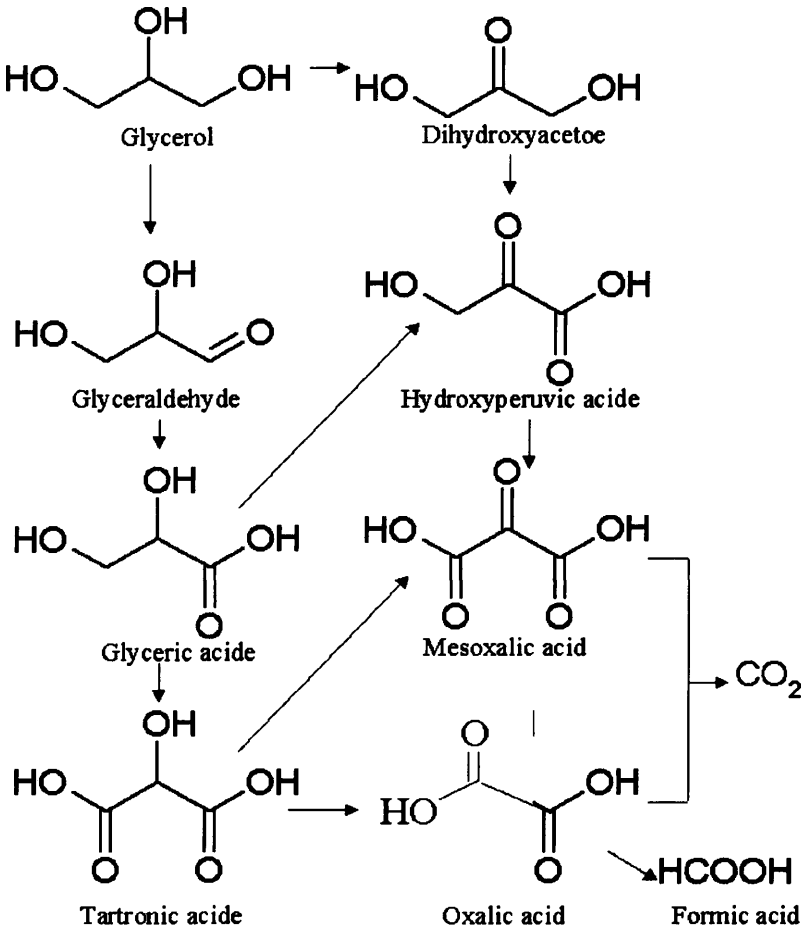

Fig. 1.1: Synthesis routes starting with glycerol for the stepwise oxidation (from [31]).

In recent years the use of gold as catalyst for the partial oxidation of polyols has attracted increasing interests. The polyols can be extracted from natural products such as rapeseed. The use of re-growing products is an essential step to an environmental friendly industry and is a point of increasing interest in recent years also driven by a drastically increasing oil price. The oxidation of polyols can lead to a variety of intermediates and products as fig. 1.1 on the example of glycerol shows [31]. As good as the wide variety of different products is, it makes it very difficult to design a catalyst that has a very high selectivity to only one of the possible products. The commonly used Pt and Pd based catalysts [36 - 38] show relative high selectivity but to some extent formic acid is formed as side product. This might happen by the

sequential oxidation of the C_3 products to oxalic acid and formic acid. For gold catalysts it can be shown that 100% selectivity to glyceric acid [31, 39] can be achieved that is a clear advantage over the Pt and Pd catalysts.

Beside the variety of (selective) oxidation of organic species by gold catalysts reactions involving nitrogen have been studied [32, 40]. As an example the decomposition of nitrogen oxide will be discussed in more details. NO is produced by car engines and its removal from the combustion gas is an important area for catalytic research [41]. A variety of catalysts have been tested for the decomposition of NO to N_2 and O_2. Generally the catalysts are either prone to a depression of steady state activity under the presence of oxygen, or lose activity when exposed to water vapour [32]. In lean-burn (oxygen rich) gasoline and diesel engines it is by definition a practice to work in excess of oxygen in the reaction mixture. This makes the first class of catalysts difficult to operate. The second class, sensitive to water, is also hard to operate in a car exhaust, because during the combustion of fuel water is also formed, which will deactivate the catalysts.
Gold nanoparticles tested on a model stream of nitrogen oxide, propane, oxygen and water show good conversion to N_2 [32]. But the catalyst often needs high temperatures (673 K) to reach high catalytic activities. Also tests in practical systems are missing so far, but these problems seem to be solvable and gold catalysts might help to reduce the pollution of cars in the near future.

1.2.3 Properties of Gold and TiO_2

To understand the catalytic activity of gold catalysts and the questions scientists discuss, a basic understanding of the two components of these catalysts is important. Therefore a general overview over gold and TiO_2, which was used as support in this study, is given in the following paragraph.
The yellowish colour of gold and its never changing brilliance are its most striking characteristics. These can be explained by the relativistic effect that is most dominant in gold [3, 42, 43]. Due to the heavy atomic core, the electrons with a high probability of being close to the core (s, p orbital electrons) are accelerated to relativistic velocities. This increases their mass and hence shrinks their orbitals and increases

their binding energy. It also increases the shielding of the nuclear charge for the d and f orbital electrons and leads to an increase in radius and decrease in binding energy for d and f orbitals. This means the outer most electrons (6s) are bonded more tightly and closer to the core than without the relativistic effect. The 5d and 4f electrons, which are not the valence electrons, instead lose a slight amount of binding energy. Overall the relativistic effects lead to a harder to ionize and therefore more "noble" electron shell for gold.

The first time gold not used as a bulk material was in producing red colour windows of churches and palaces [19, 44]. The red colour is due to nanoparticles of gold. This early use of "nanotechnology" makes it even more surprising that gold was thought to be uninteresting for any chemical reactions or catalysis until the very end of the 20th century.

For example gold has been used as a biomarker for viruses. Gold shows structures in the gas phase that were previously not observed for clusters in gas phase and gold – like carbon – has the ability to form nanorods. It is also possible to synthesise metal organic complexes with a gold core, which are stabilised with ligands to fulfil the 18-electron rule. The complexes give the possibility to arrange the gold atoms in a specific geometry and produce single crystals of the complexes. For example linear, two-coordinated gold(I) complexes with different gold chain length could be synthesised [45]. The complexes studied so far are either colourless or yellow, can form needles, plates or blocks and have monoclinic or orthorhombic crystal systems.

Because of its noble state in the bulk form gold is hard to oxidise and the only known gold oxide is Au_2O_3, in which gold has an oxidation state of +III [34, 46]. The oxygen atoms are arranged in a distorted square plane geometry around the gold atom (see fig. 1.2) [47 - 50] Oxidised gold can be produced in different ways, for instance electrochemical oxidation [51] and hydrothermal synthesis [49]. The electrochemical oxidation was used in this study and is explained in detail in the techniques chapter. In brief, a gold foil is placed into an electrolyte (here perchloric acid) and a current will flow between the gold foil and a second electrode by applying a potential difference between them.

In the hydrothermal synthesis a tetrachloroauroric acid ($HAuCl_4 \cdot n\ H_2O$) solution is kept at a high pressure (several kbar) and elevated temperatures (several hundred K)

in an autoclave. This synthesis results in crystalline Au_2O_3, which can be mixed with metallic gold [46, 49].

Oxidised gold species, e.g. Au_2O_3, $Au(OH)_3$, $Au(OH)_3 \cdot nH_2O$ and AuOOH, are of interest because they are often found on the gold catalysts after electrochemical preparation [52, 53]. This result is not too surprising since the gold catalysts are often prepared by using tetrachloroauric acid. A solution of the gold acid is then usually increased in pH (values above 8 are usual) before the gold is allowed to adsorb on the support. The increase in pH results in the formation of $[Au(OH)_xCl_{4-x}]^-$ complexes [54] (for more details see the techniques chapter), which have values of 3 to 4 for X at high pH. After depositing the gold complexes and separating the catalyst from the solvent the complexes can then transform into oxidised gold by releasing mainly water. The oxidised gold is then transformed into gold by calcining [52, 53] or under reaction conditions [53]. To understand this final step of preparing the catalyst and whether oxidised gold species might be important for the reaction cycle or not (see section 1.2.3), it is essential to study the decomposition of Au_2O_3 and other oxidised gold species. Therefore electrochemically prepared gold oxides were favoured in this work since not only crystalline Au_2O_3, as present after hydrothermal preparation is present, but also other oxidised gold species can be prepared. The composition of the gold species can be also influenced with the electrochemical route, by choosing different potentials for the oxidation process for example.

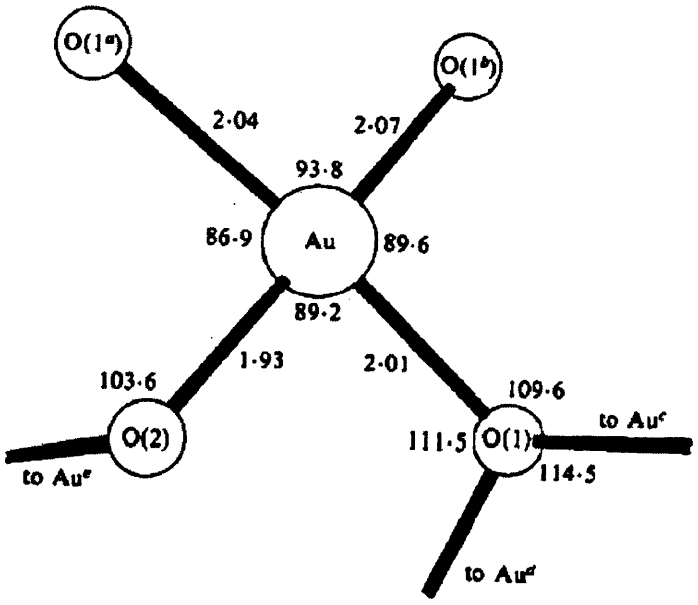

Fig. 1.2: The AuO_4 cell of Au_2O_3 [47]. Unique angles: O(1)-Au-O(1^a) 174.8°, O(2)-Au-O(1^b) 173.1.

TiO_2 is an "everyday" product and is used as a white pigment in paints and cosmetics, as a photocatalyst and as an interface for medical implants due to its good biocompatibility [55].

In surface science TiO_2 is one of the best-studied metal oxides [55 - 60]. It crystallises in three forms of rutile, anatase and brookite. Rutile is thermodynamically the most stable form but it is often found in mixtures with anatase. Rutile and anatase have a tetragonal crystal structure, whereas brookite is rhombohedral. The electronic structure of titanium oxide is well characterised and rutile(110) has the lowest surface energy. Further, it acts as a model system for other metal oxides: "The rutile TiO_2(110) surface has emerged as the leading prototypical system for fundamental surface science studies on transition metal oxides" [56].

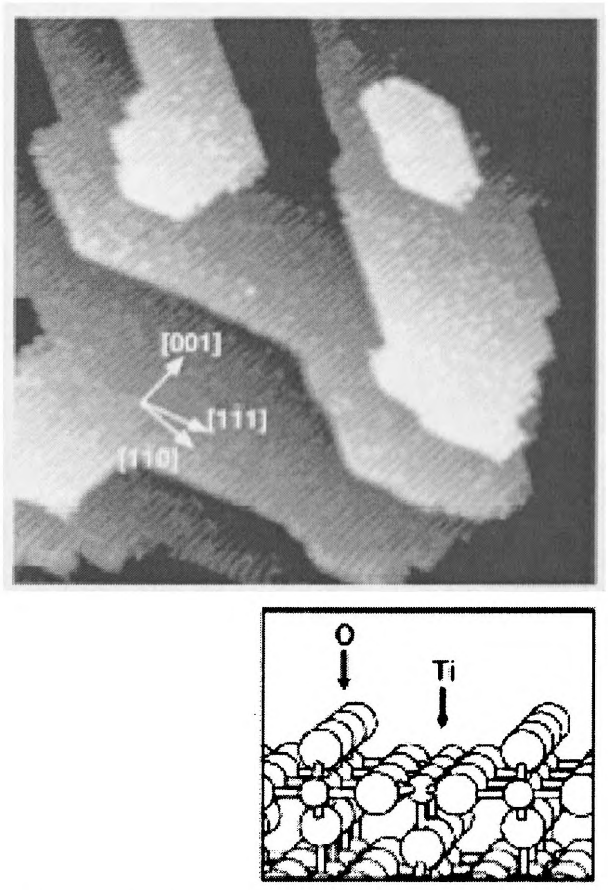

Fig. 1.3: STM image (40nm x 40 nm, top) and model of the $TiO_2(110)(1x1)$ surface (from [56, 63]). This is the surface of a light blue crystal, which was prepared by sputtering and annealing in ultrahigh vacuum. Bright and dark rows in the STM image correspond to positions of fivefold- coordinated Ti and twofold-coordinated O atoms (residing ~ 1 Å above the surface), respectively. The surface is flat, with step edges running parallel to the $\langle 1\bar{1}1 \rangle$ and $\langle 001 \rangle$ directions.

The surface and bulk stoichiometry of TiO_2 can be modified by different techniques [60 - 63]. Heating clear and defect free rutile crystals in either vacuum or a reducing atmosphere to temperatures between 1273 K and 1450 K results in variety of different coloured crystals [63]. The colour of the crystals depends more on the heating temperature than on the heating time. The colour varies from colourless over yellowish, pinkish to light and dark blue. The colour of the crystals correlates to the amount of defects introduced in the crystal with the darkest crystals containing the

most defects. The samples can also be reoxidised by heating in air to similar temperatures as used during reduction. The resulting samples are (almost) clear crystals.

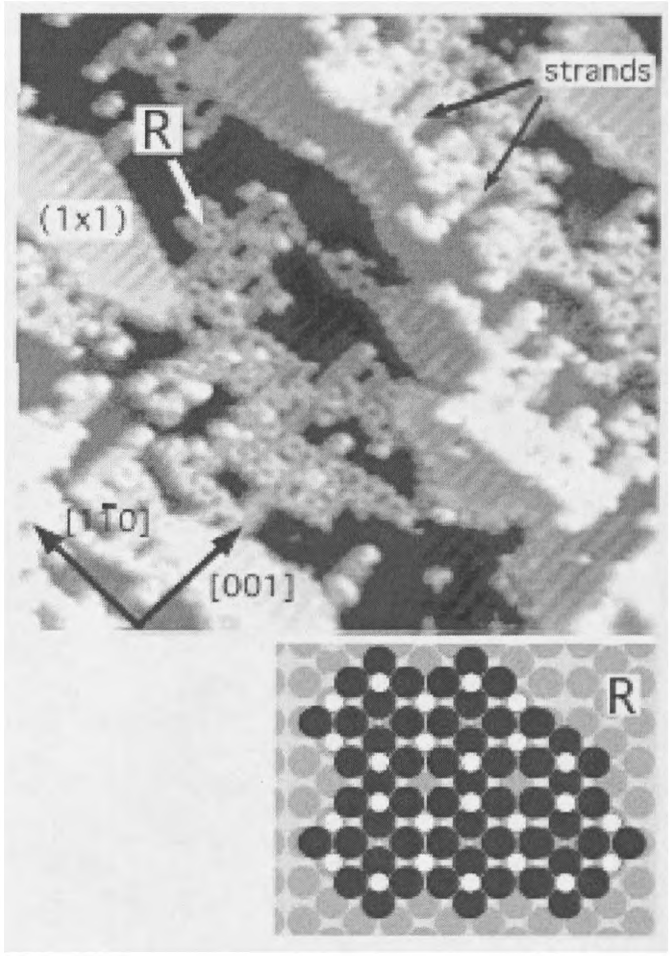

Fig. 1.4: STM image (30nm x 30 nm) after annealing a (1x1)-terminated TiO_2(110) surface in O_2 ($1 \cdot 10^{-6}$ mbar, 550 K, 20 min). Reoxidation of the reduced buk causes formation of irregular networks of pseudohecagonal rosettes ("R") added small (1 x 1) islands and strands (from [63]).

To modify the surface of the crystals, sputtering can be used. A bright TiO_2 crystal with a relative perfect surface as shown in fig 1.3 with alternating bright (Ti-atoms) and dark (O-atoms) rows and large terraces, can be altered to a dark crystal with a surface as shown in fig. 1.4 [63]. The STM image in fig. 1.3 shows a total of 7

terraces. All terraces show brighter colours to their left than to their right end and stack from the bottom left to the top right hand of the image. The inset in fig. 1.3 shows the surface termination of a perfect free TiO_2(110)(1x1) surface. This surface termination is also know as bulk-terminated since only some relaxation are expected to happen on the surface in comparison to the bulk crystal structure.

The dark sample in fig. 1.4 shows three surface atoms at three different heights levels (blackish, greyish and whitish). This sample does not show large areas of terraces but contains several islands and atoms [64]. Also the formation of pseudohexagonal rosettes indicated with "R" in the STM image was observed and a schematic drawing of the structure is given in the inset of fig. 1.4 (white and black balls being O and Ti atoms respectively). The changes in the surface morphology are important also for catalysis, since defect sites on the support are under discussion to play an important role (for more details see section 1.2.4).

A different way of modifying the surface of TiO_2 is by exposing it to intense ultra-violet (UV) light [61, 62]. The normally oleophilic and hydrophobic TiO_2 surface becomes amphiphilic, which was studied by the contact angle of water (74°), ethylene glycol (44°), tetralin (12°) and hexadecane (7°). After UV light exposure the contact angle for all 4 fluids decreases to 0°, this means all fluids wet the surface [61] (cf. fig. 1.5). This amphiphilic behaviour was explained by hydrophilic and oleophilic domains on the surface that have been found by friction-force microscopy and Fourier transform infrared spectroscopy (FTIR) [65]. The loss of the amphiphilc character of the sample was studied as well and showed an increase of contact angle to about 15° after 2 h and to 30° after 12 h of storage in air [61].

Despite the relative good understanding of the macroscopic effect of water wetting TiO_2, theoretical and experimental results show some discrepancies. Experimental results agree that water adsorbs on rutile(110) molecular and only dissociates at defect sites. Theoretical calculations thus predict that water will dissociate also on defect free rutile(110) [57].

The reconstruction of the surface is another point that shows some differences between theory and experiment [57]. For example surface X-ray diffraction (SXRD) and ion scattering experiments reveal relative strong relaxation of the surface atoms in comparison to the bulk. Theoretical calculations on the other hand indicated only small relaxations between surface and bulk. But it has to be taken into account that the theoretical calculations are performed for T = 0. Experiments are always performed at

a finite temperature and therefore some thermal energy is present. The thermal energy can lead to some differences between experimental and theoretical results, because it might be possible for atoms to overcome energetic barriers in the experiment, so that other configurations are possible other than those being calculated [57].

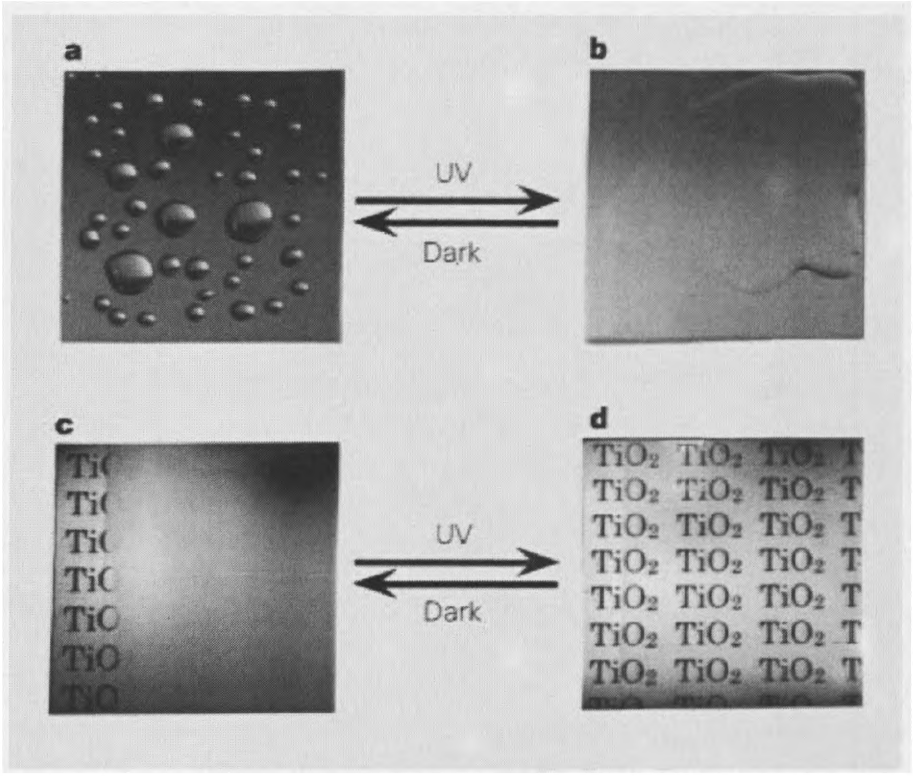

Fig. 1.5: Increased wettability of TiO_2 upon UV light (right images) exposure on a rutile single crystal (from [62]). a, A hydrophobic surface before ultraviolet irradiation. b, A highly hydrophilic surface on ultra-violet irradiation. c, Exposure of a hydrophobic TiO_2-coated glass to water vapour. The formation of fog (small water droplets) hindered the view of the text on paper placed behind the glass. d, Creation by ultra-violet irradiation of an antifogging surface. The high hydrophilicity prevents the formation of water droplets, making the text clearly visible.

1.3 Reaction mechanism of the CO oxidation

This section will give an overview of the problems to explain the reactivity of gold cluster in the CO oxidation. First of all two common reaction mechanisms in the CO oxidation over noble metals will be discussed. The Langmuir-Hinshelwood (LH) mechanism is accepted as the general reaction mechanism for the CO oxidation over Pt, Pd, Rh and Ir [66 - 70]. For ruthenium it seems that the Eley-Rideal (ER) and Langmuir-Hinshelwood (LH) mechanism are competing with each other and the reaction conditions appear to determining which mechanism is observed [71, 72]. The close relation of these metals to each other and to gold makes it possible that the catalytic reaction mechanism for gold is similar to either the LH or the ER mechanism.

1.3.1 Langmuir-Hinshelwood mechanism

A very simple reaction mechanism for gases on surfaces is the Langmuir-Hinshelwood mechanism (LH) in which (assuming only two reactants A and B) both reactants adsorb on the surface (see fig. 1.6). The LH mechanism also assumes that each surface site has the same adsorption energy for the adsorbates and that the adsorption of either reactant A or B does not influence the adsorption possibility for the remaining "free" adsorption sites. Furthermore the LH mechanism assumes that reactants, adsorbed on the surface, can freely move on the surface independent of the concentration of the reactants (and products). Therefore the reactants can move and "find" each other on the surface and then react to give the adsorbed product AB. In the final step the product desorbs into the gas phase again [73]. Due to this reaction mechanism the reaction rate depends on the concentration of both reactants A and B.

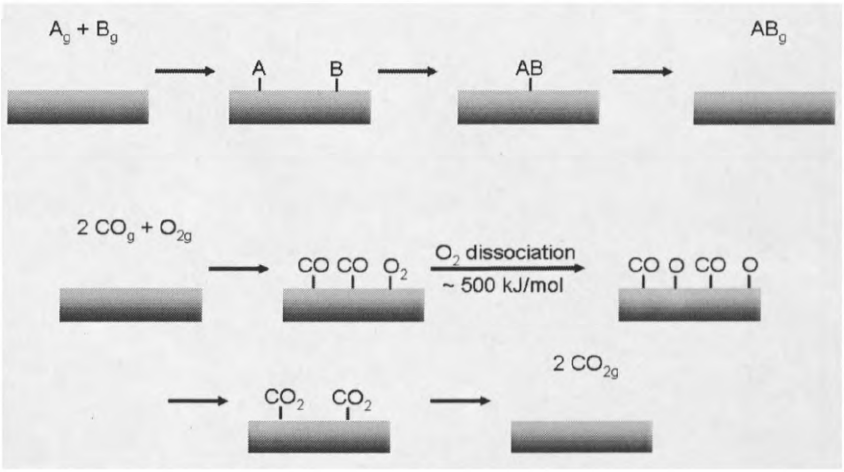

Fig. 1.6: Langmuir-Hinshelwood reaction mechanism in general (top) and schematically for the CO oxidation.

For CO oxidation this mechanism has to be slightly modified because CO has to react with "O" and not with molecular O_2. The splitting of the O_2 molecule requires energy where the bond enthalpy of O_2 is about 498 kJ/mol [74]. This energy is a high activation barrier and can only be overcome at high temperatures. Hence noble metal catalysts for CO oxidation normally work at temperatures above 500 K. It is also generally accepted that for these catalysts the oxygen dissociates on the metal surface before it oxidises the CO molecule [66]. Hence a simplified mechanism as shown in fig. 1.6 can be seen as a general scheme for the CO oxidation over e.g. Pt, Pd, Ir and Rh.

For gold, on the other hand, the reaction conditions usually do not exceed 400 K and are often close to or below room temperature. Hence it is often argued that the O_2 bond is weakened at specific spots on the catalyst [43, 75 - 78]. But this would mean a much stronger activation of the oxygen molecular on the gold catalysts than on other common CO oxidation catalysts.

1.3.2 Eley-Rideal mechanism

The Eley-Rideal (ER) mechanism is another very simple reaction mechanism for describing the reaction of gases on surfaces (cf. fig. 1.7). In the ER mechanism one of the two reactants A or B adsorbs on the surface, assuming A adsorbs. The other

reactant, B, reacts directly out of the gas phase to form the adsorbed product AB, which in the final step desorbs from the surface. For this mechanism the reaction rate only depends on the concentration of the adsorbed reactant. The reactant B can also be weakly adsorbed, physisorbed, on the surface. In this state B quasi freely moves on the surface, which is assumed to be like the gas phase.

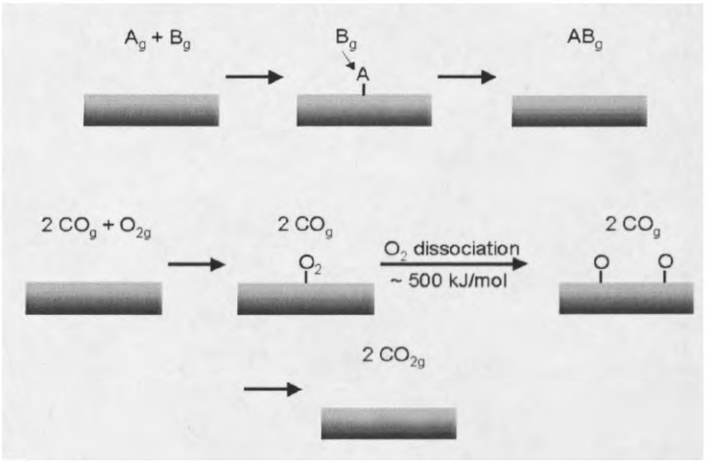

Fig. 1.7: Eley-Rideal reaction mechanism in general (top) and schematically for the CO oxidation.

The LH and ER mechanism are very similar and can compete against each other. This can be seen in the CO oxidation over Ru. In this case the reaction conditions determine if the CO is oxidized by the ER mechanism (oxidising conditions, CO/O_2 ratio ≈ 1) or the LH mechanism (reducing conditions, $CO/O_2 > 2$) [71]. The similarity between the LH and the ER mechanism for the CO oxidation was also confirmed by theoretical studies by Stampf and Scheffler [72] (cf. fig. 1.8), on the Ru(0001) surface as used by [71]. In both cases the O_2 molecule first adsorbs on the surface and dissociates. In the ER mechanism the CO molecule reacts out of the gas phase under the formation of CO_2 with the release of a relative large amount of potential energy. In the LH mechanism the CO molecule coadsorbs, followed by the formation of the CO_2 molecule and the potential energy is released in a two-step process.

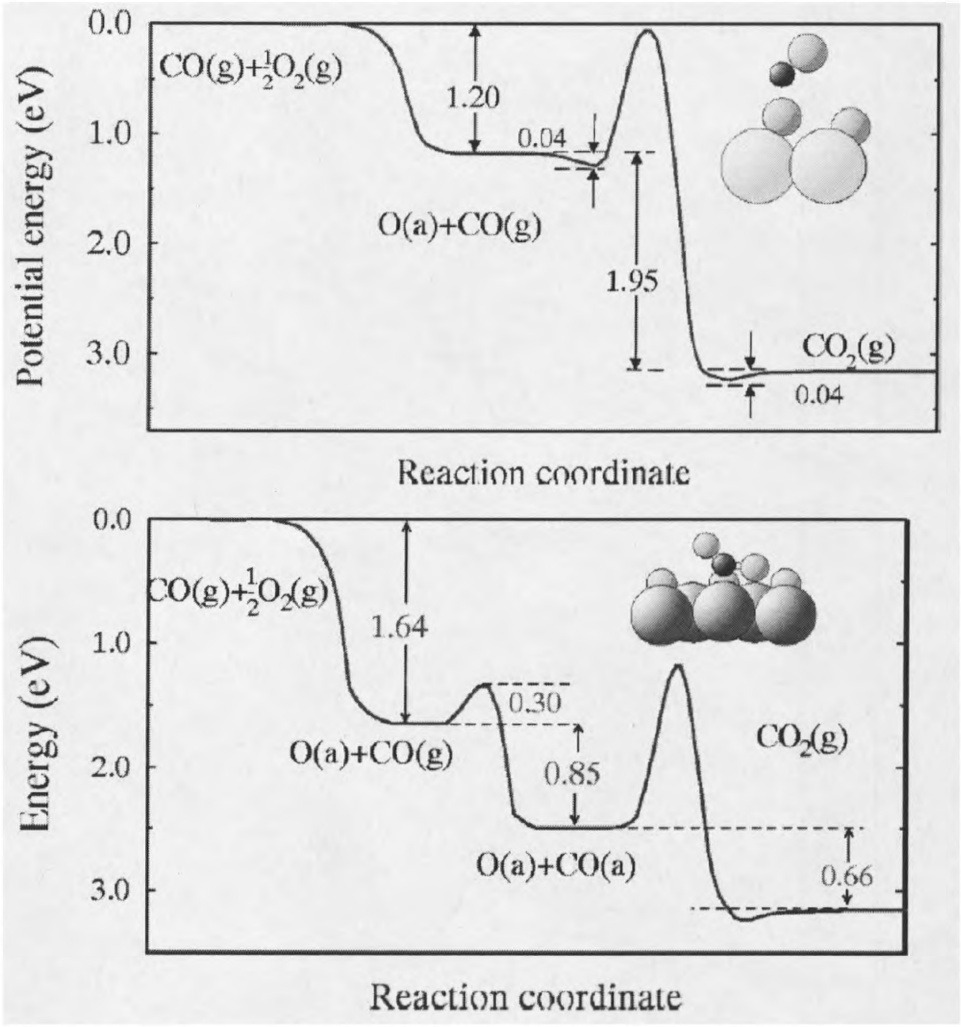

Fig. 1.8: Calculated energy diagram for the ER (top) and LH (bottom) mechanism of the CO oxidation at Ru(0001). The transition state geometry is indicated to the right in each diagram. The large, small and small darker circles represent Ru, O and C atoms, respectively (from [72]).

1.3.3 Mechanistic studies of CO oxidation over gold

The actual reaction mechanism and the adsorption behaviour of the reactants on gold catalysts are still controversially discussed in the literature [15, 16, 20, 30, 57, 79 - 84]. The following paragraphs give a brief overview over the most fundamental questions and will address the problems of the activation of oxygen, the site of

oxygen activation, the morphology, size and chemical state of supported gold particle, and the influence of the support on the reaction.

1.3.3.1 Size selected gold clusters in gas phase

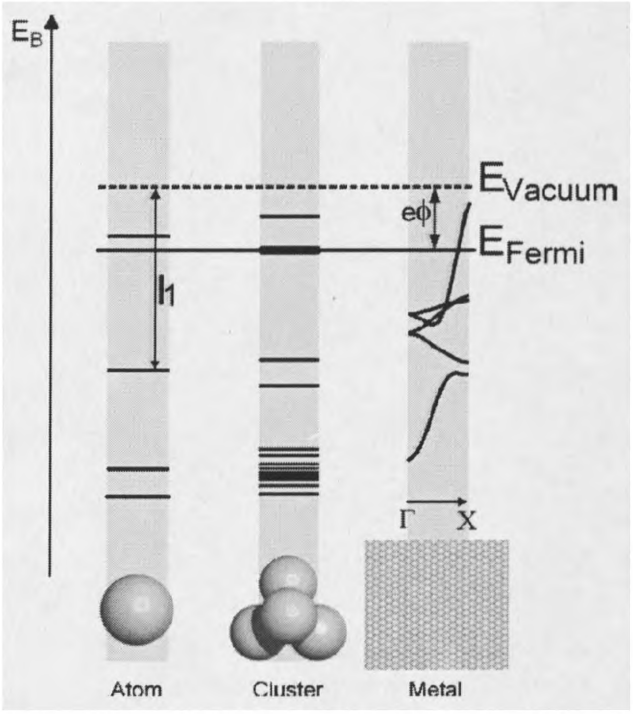

Fig. 1.9: Changes in the orbital levels from an atom to bulk material (from [19]).

Mass selected gold clusters are a good model to study the influence of the cluster size on the reactivity. The cluster size influences the orbital structure and changes from atomic orbitals (Au_1) over molecular orbitals to the band structure as in bulk gold (cf. fig 1.9). When studying these clusters in the gas phase it is possible to study neutral, positively and negatively charged clusters [85]. Also the few atoms that are incorporated in these clusters allow the study with the help of computers theoretically and compare experimental results and theoretical calculations [86 - 90].

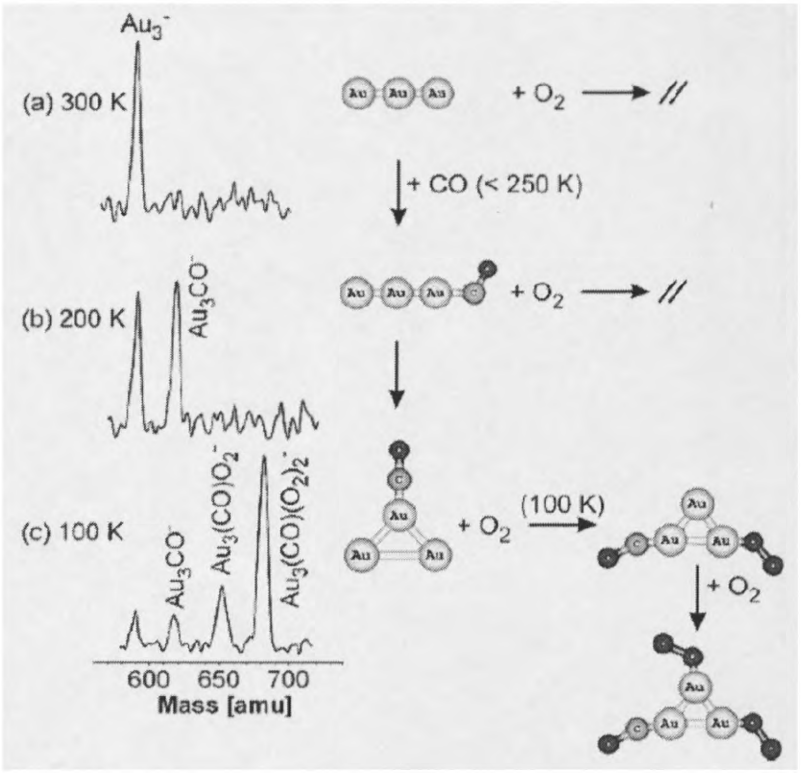

Fig. 1.10: Proposed change in cluster shape upon dosing CO on a Au_3-cluster in gas phase (from [90]). "//" indicates that the reactants did not react.

Probably, the most interesting cluster size is Au_{20}^-. This cluster binds O_2 nearly as strongly as Au_2 and Au_4 [91]. The intermediate even clusters bind O_2 only weakly (Au_{16} does not bind O_2 at all). In contrast is the neutral complex of Au_{20} even more "noble" than gold. It cannot be oxidised even with ozone [44]. The special behaviour of Au_{20} appears to be due to two reasons: Firstly this cluster has a closed electron shell resulting in a very wide HOMO-LUMO-gap (1.77 eV). Secondly, theoretical calculations showed that this cluster nucleates as a tetrahedral structure, which has the highest symmetry after the octahedral geometry [44] and increases the stability.

Studying the interaction of gold-clusters with CO and oxygen is interesting, because the neutral and positively charged clusters are in a size range of up to 20 atoms essentially that are unreactive to molecular oxygen [92, 93]. But negatively charged clusters show a strong odd-even alteration in the interaction with oxygen [91, 92, 94 -

99]. Au_1 is the only odd numbered anionic gold cluster that binds to oxygen, but in this case the dosed molecular oxygen dissociates [91]. On the even number cluster the oxygen does not dissociate and binds molecular [91, 97, 98, 99]. The interaction of these gold cluster ions with carbon monoxide has been studied as well [86, 95, 100 - 103]. In contrast to the interaction with oxygen the gold cluster do not show a strong odd-even alternation [86, 95], but a strong size dependency exists.

The adsorption possibility of carbon monoxide and oxygen on several gold clusters when dosed sequentially was studied as well [86, 87, 104]. It could be shown that CO and O_2 have synergetic effects on these clusters, meaning that more of the secondary dosed reactant could be adsorbed by the gold clusters, than when dosing onto a Au_n^--cluster. This cooperative behaviour was studied theoretically [90] and indicated a change in the gold cluster electronic structure by the σ-donation π-back-donation interaction of the gold cluster and the CO molecule [85, 105]. This change in electronic structure might also lead to a change in the cluster shape as proposed for the Au_3^-cluster [90] (cf. fig. 1.10). The initially linear Au_3^--cluster that was studied by femtosecond laser spectroscopy undergoes bending motions upon the adsorption of CO. But the linear Au_3^- gold clusters (with or without CO adsorbed) do not adsorb O_2, which can be concluded from theoretical calculations that show that these complexes are energetically disfavoured. Therefore the authors concluded that the former linear Au_3-CO^- complex undergoes a configuration change to a triangular gold cluster at temperature of about 100 K. Onto the triangular cluster up to two oxygen molecules can adsorb sequentially.

The formation of CO_2 could be observed on several gold clusters, which lead to a proposed catalytic cycle involving $Au_n(CO)_2O_2$ and $Au_n(CO)O + CO_2$ [86] for a sequential dosing of CO and O_2.

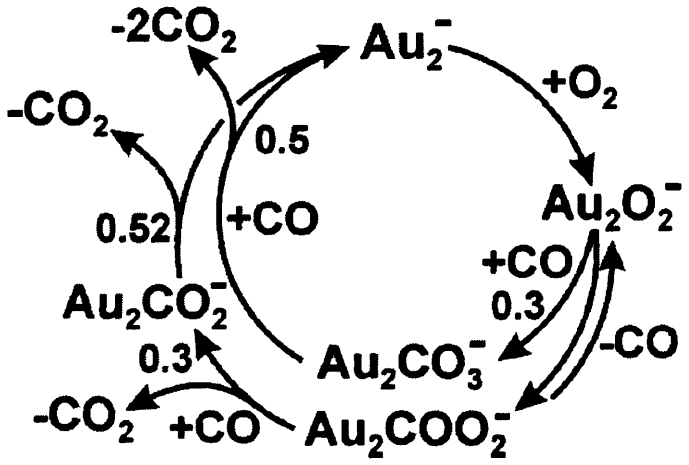

Fig. 1.11: Proposed catalytic cycle for the CO oxidation on a Au_2-cluster in gas phase (form [87]). The numbers given in the figure indicate the theoretically calculated barriers for the corresponding reaction step in eV.

For dosing CO and O_2 simultaneously onto an Au_2-cluster a slightly different catalytic cycle has been proposed [87, 89] (cf. fig. 1.11). This catalytic cycle involves post-adsorption of O_2 and CO that forms either a peroxyformate-like ($Au_2COO_2^-$) or a carbonate complex ($Au_2CO_3^-$). The peroxyformate-like species would release a CO_2 molecule and form with another carbon monoxide molecule a gold carboxyl species ($Au_2CO_2^-$). The carbonate species on the other hand would form with a CO molecule directly to two carbon dioxide molecules. To identify the more likely processes was not possible so far.

1.3.3.2 Reactivity of supported size selected gold cluster

To bridge between gas phase catalysis and supported catalysts mass selected Au_8 clusters were deposited on defective and defect free MgO(001) [88, 106]. The Au_8-clusters supported by defect-rich MgO show a much higher activity towards the production of CO_2 for a sequential dosing of CO and O_2 than that of Au_8-clusters supported by defect-poor MgO. Hence it was argued, under the support of theoretical calculations, that the MgO transfers electron density into the Au-cluster *via* its F-centres. F-centres, from the German Farbzentrum (English colour-centre), are missing

negative ions in an ionic crystal structure. In these defect states electrons can be captured that often lead to a change from colourless to colourful materials.

Therefore the transferred electron density from the F-centre can then stabilise the electron back-donation of the Au-clusters into the CO $2\pi^*$ orbital. It is further predicted that the oxygen is adsorbed in a peroxo or superoxo state [88] on the gold cluster, which again is stabilised by the increased electron density in the gold clusters on F-centres. This leads to a catalytic activity of the Au_8-clusters bond to a F-centre but being inactive when supported by defect free MgO [106, 107].

In recent studies Lee et al. used size selected gold clusters deposited on $TiO_2(110)$ crystals [108, 109]. The results showed that clusters with sizes of 7, 6 and 3 atoms are the most reactive Au_n (n = 1-7) clusters. The activity of these small gold clusters is in contrast to studies on MgO that revealed no catalytic activity for Au_n-cluster with $n < 8$ [107]. Au_1 and Au_2 clusters supported on TiO_2 are inactive and even reduce the very small CO activity of TiO_2 [60, 108]. The reduced activity of the TiO_2 supported Au_1 and Au_2 is assumed to be due to blocking of defect sites on the TiO_2 crystal by the clusters. The Au_1 and Au_2 clusters are therefore catalytic inactive, or could be even considered as an inhibitor or poison, which is in contrast to gas phase Au_2-clusters (see above). Annealing Au_1 clusters to 400 K results in a shift in XPS binding energy from 85.8 eV (Au_1 on vacant free TiO_2) and 85.4 eV (Au_1 on F-centre in TiO_2) to 84.5 eV. These samples show catalytic activity and hence the binding energy of 84.5 eV was assigned to gold clusters. This is also in agreement with ion scattering (ISS) results that indicate the beginning of agglomeration for these clusters at annealing temperatures of 400 K.

The effect of the support on the agglomeration of gold was studied by Lee et al. [110]. In their studies they deposited Au_1, Au_3 and Au_4 clusters on Al_2O_3 and TiO_2. The authors found that the gold clusters are less likely to sinter and are thus less prone to the removal by sputtering on the TiO_2 support than on the Al_2O_3 when prepared under the same conditions. In agreement with studies of Au/MgO [88, 106, 107] samples to which the gold clusters prepared on Al_2O_3 do not show any CO oxidation activity nor it seems that they interact with CO. Furthermore it was found that Au_1 is less likely to sinter then the Au_3 and Au_4 clusters, which is against the idea that cluster should diffuse less than isolated atoms.

A theoretical study by Chrétien and Metiu [111] discussed the effect of the gold cluster size, in the range between 1 and 7 gold atoms supported on partially reduced TiO_2, on the possible charge transfer between support and gold cluster. In contrast to gold cluster in the gas phase no simple odd-even relationship could be found for the charge transfer. The most stable configuration of the Au_1 and Au_3 clusters gaining charge density, Au_5 and Au_7 clusters lose charge density from defect states in the support and Au_2, Au_4 and Au_6 clusters do not change. For the second most stable configuration this changes as Au_1, Au_2, Au_3, Au_5 and Au_7 cluster are negatively charged on the support whereas Au_4 and Au_6 stays unchanged. This result does not correlate with the ionization potential of electron affinity of the clusters. But the shape of the molecular orbitals of the gas-phase clusters can be used to predict the charging of the adsorbed gold clusters.

1.3.3.3 Mechanistic models for supported gold cluster

For practical catalysts it becomes even more difficult to understand the reaction mechanism and several questions have not been resolved up to this date. One of the most urgent questions is the activation of oxygen and this problem has been formulated by Gottfried and co-workers [112] as follows: "How is the dioxygen molecule activated? What are the reactive oxygen species formed on a gold surface, and what is their role in the CO oxidation reaction?"
A number of different hypothetical reaction paths or activation possibilities for the oxygen have been proposed [3, 14, 43, 77, 86, 113 - 118].

To achieve a first idea of the reaction mechanism the reaction order can be determined, which was done for Au/TiO_2 catalyst [12, 80, 119]. The reaction rate (R) for the CO oxidation can be generally determined by:

$$R \propto [CO]^a [O_2]^b \qquad 1.1$$

with a and b being the reaction order for CO and O_2, respectively. The data reported vary relative strongly, for CO a reaction order between 0.05 [12] and 0.4 to 0.5 [12, 119] was found. For oxygen Bollinger et al. found a reaction order close to zero [80], Haruta et al. determined a reaction order of 0.24 [12] and Lin et al. reported values between 0.2 and 0.4 depending on the reaction conditions [119]. The variations in

value might be interpreted that the reaction mechanism is depended on the reaction conditions, but Bolling et al. pointed out that their results could be only fitted with a Langmuir-Hinshelwood type mechanism. The authors thus could not determine if oxygen and carbon monoxide adsorb competitively or non-competitively. Generally for a Langmuir-Hinshelwood type mechanism reaction orders of 1 for both CO and O_2 are expected. Therefore these results do not suggest a Langmuir-Hinshelwood reaction meachnism. Also an Eley-Rideal type mechanism seems unlikely since it would be expected that the reaction order of the species adsorbed would be 1 and for the species supplied from the gas phase 0.

One of the first attempts to examine the reaction mechanism in more detail and find an explanation for the high catalytic activity of clustered gold was done by Boccuzzi, who conducted several studies on the CO oxidation over gold catalysis, also in cooperation with Haruta, used FTIR as one of their main techniques [52, 81, 120, 121]. The FTIR results provide information about the adsorption site of several species present on the catalyst during the catalytic process. Hence by changing the preparation or calcinations temperature of the catalyst the amount of CO adsorbed on different sites of the catalysts could be followed. Adsorption sites for CO on the catalyst were found to be step sites (2103 cm^{-1} and 2098 cm^{-1}) on the gold particles and hydroxyl groups present on the support (2154 cm^{-1}, cf. fig. 1.12). The variation in observed wavelength between CO adsorbed on the support and the gold particle is large and makes the identification of these two groups easy.

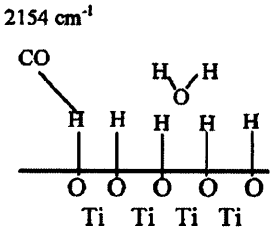

Fig. 1.12: Adsorption site of CO on TiO_2 for gold catalysts supported by TiO_2 powder, proposed by [52]. The moisture (H_2O) is required to from hydroxyl groups on the surface of the TiO_2 with which the CO-molecule interacts (indicated by a line in the drawing).

explain the good catalytic activity of gold catalysts at low temperatures, because the molecular oxygen would not need to be dissociated. The dissociation barrier of oxygen is the major activation barrier in the CO oxidation and it is controversially, how this activation barrier is overcome in the catalytic cycle. But at present carbonate species are widely believed not to be part of the catalytic cycle but a spectator species [24, 77, 122] or even inhibitors for the CO oxidation [123, 124] and be the reason for the deactivation of the catalysts in long time experiments. The strong bonding or close proximity to catalytic active sites explains the deactivation of catalysts by carbonate species. Hence the carbonate blocks these sites and the reactants CO and O_2 cannot adsorb and react. This means the more carbonate is present the more catalytic centres will be deactivated and therefore the catalytic activity will decrease. This blocking of active sites by carbonate species does not have to be irreversible as opposed to some groups. The catalytic activity can be regained by e.g. dosing water into the reactant stream [118]. The water is expected to decompose the carbonate by the possible formation of CO_2 and a superoxide-like (O_2^-) species.

The oxidation of CO by lattice oxygen was proposed by [75] (cf. fig. 1.13), which is based on the result that a Au/TiO_2 catalyst showed activity for the CO oxidation also in the absence of oxygen in the gas stream. The CO oxidation activity decreases over time but it could be re-established by mixing oxygen into the gas stream. Hence the authors postulated that lattice oxygen, most likely at the gold/support interface, of the TiO_2 must be involved in the reaction. The gas phase oxygen reoxidises the support in this reaction mechanism but is not directly oxidizing the CO.

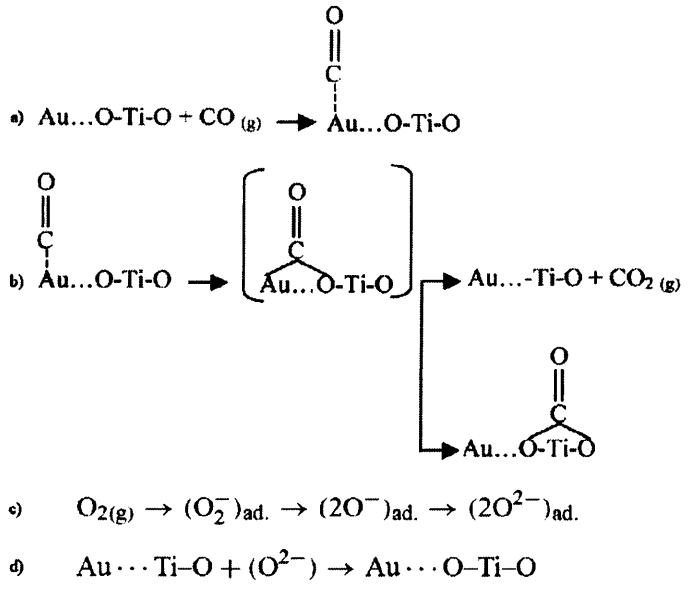

Fig. 1.13: Reaction mechanism proposed for the CO oxidation over gold by [75]. a) Adsorption of the CO on the gold particle. b) The adsorbed CO is transferred to the gold-support interface and can either react with oxygen from the TiO_2 lattice to CO_2 and desorbed or form a surface carbonate species. c) Molecular oxygen is adsorbed on defect sides of the catalyst and forms, after receiving four charges, O^{2-}. d) The O^{2-} species is incorporated into the defect site left by the former CO oxidation.

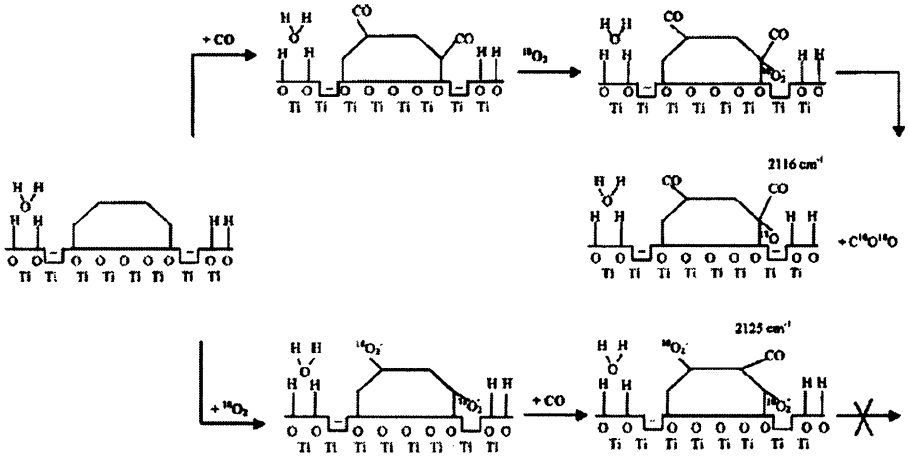

Fig. 1.14: Reaction mechanism proposed for the CO oxidation over gold by [52].

Other studies [52, 77] suggested that oxygen can be activated at the gold/support interface by oxygen defects in the support (cf. fig. 1.14 and 1.15). FTIR spectra show a band at 2100 cm^{-1} for CO dosed at 90 K on the catalyst, which was assigned to CO chemisorbed on the gold cluster. When dosing CO and O_2 sequentially this band shifts to 2116 cm^{-1} and 2125 cm^{-1} for CO respectively O_2 being dosed first. The shift in comparison to CO only present on the catalyst was assigned to a $O_2^{\delta-}$-$Au^{\delta+}$-CO (ν_{CO} = 2125 cm^{-1}, molecular oxygen) and a $O^{\delta-}$-$Au^{\delta+}$-CO (ν_{CO} = 2116 cm^{-1}, atomic oxygen) complex, whereas the oxygen interacts with a defect site in the support. The authors also suggested that only the atomic oxygen complex ($O^{\delta-}$-$Au^{\delta+}$-CO) should lead to the formation of CO_2 but not the molecular complex ($O_2^{\delta-}$-$Au^{\delta+}$-CO). In a recent study by Henao et al. [125] the IR bands around 2110 cm^{-1} were found as well but only shortly after CO had been titrated with oxygen. These authors concluded that these bands are both due to CO that slowly reacts to CO_2 and suggested that CO with an IR band at 2090 cm^{-1} is responsible for the fast reaction to CO_2. Henao et al. also stated that metallic gold does not adsorb much oxygen, but the oxygen that is adsorbed reacts rapidly with CO.

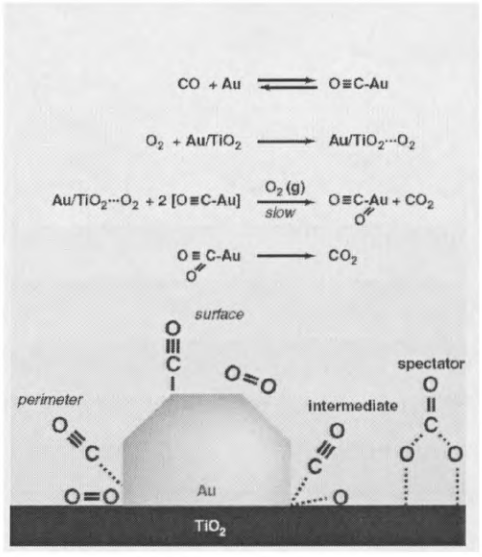

Fig. 1.15: Reaction mechanism proposed for the CO oxidation over gold by [77].

These two proposals are contradicted by isotope experiments with isotopically marked O_2, which indicate that no exchange of lattice oxygen takes place during the catalytic process [50, 52, 113, 114, 120, 126 - 128]. It could also be shown that the CO oxidation also works on non-reductive metal oxide [116] and metal carbonates [129] supports. This makes it very questionable whether the oxygen is supplied from the support in the CO oxidation.

Isotope studies also reveal that adsorbed oxygen molecules do not exchange O-atoms with each other. It also seems that coadsorbed CO and O_2 do not exchange oxygen atoms with each other, since in both case no oxygen molecules with mixed isotopes where present in the gas stream. For CO_2 and O_2 on the other hand it was shown that these molecules exchange oxygen atoms with each other. CO has been found not to dissociate during the oxidation to CO_2, but the presence of molecular oxygen in the reaction cycle is not ruled out [122, 126].

Another idea that has been put forward is the activation of the O_2 by water to a superoxide or similar states [22, 52, 77, 129]. Theoretical calculations prove that water and oxygen can interact on a TiO_2 support [127, 130]. Also some experimental results show that the water vapour pressure in the reactor during reaction has a crucial influence on maximum activity. However recent studies suggested that the water is responsible for the removal of carbonates that poison the catalyst and are formed during the reaction [118, 131].

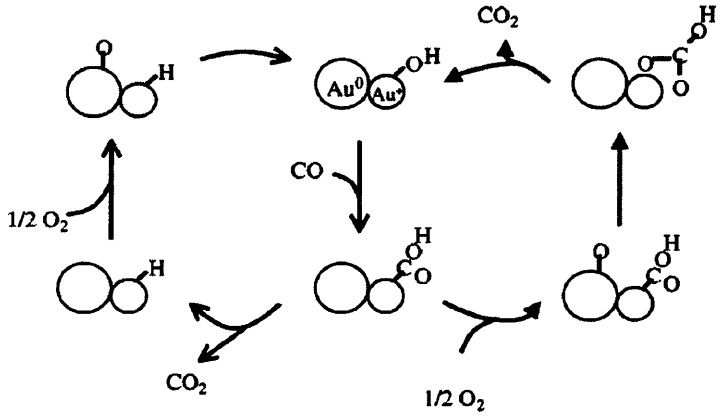

Fig. 1.16: Reaction mechanism proposed for the CO oxidation over gold by [116].

Costello et al. [116] proposed a reaction mechanism on mixed metallic and cationic gold clusters (cf. fig. 1.16) including two pathways for the CO oxidation. In both cases the molecular oxygen is activated at metallic gold domains and CO is oxidised to an adsorbed carboxylic species on the cationic gold. The carboxylic group can then form of CO_2. The remaining proton reforms a hydroxyl group with "activated" oxygen on the cationic gold. The other pathway includes the oxidation of the carboxylic group by activated oxygen to a carbonate group, which decomposes into CO_2 and a hydroxyl group. The authors also pointed out that water vapour is important in the reaction mixture to stabilise the cationic gold domains and for the formation of the hydroxyl group on the catalyst.

It has also been suggested that defect sites in the support transfer electrons into the gold nanoclusters [88, 132]. The electrons are then "transferred" by the gold clusters onto the oxygen and hence weaken the O=O double bond.

Theoretical calculations of the CO oxidation on supported gold catalysts reveal two active sites for the oxidation. In the work of Molina et al. the reaction site is close to the interface between an infinite 1-dimensional long gold rod (an endlessly long and 1 gold atom thick wire) and the support [133]. Remediakis et al. found that for finite gold clusters (approximated diameter of 0.7 nm) the reaction site is, in contrast to the infinite gold "cluster", in other words bulk gold, on top of the gold cluster [134, 135]. This theoretical finding might point out one of the reasons why different reaction mechanisms are proposed for different gold catalysts. Since the size of the gold particles might lead to different reaction channels the size of the clusters will be very important but varies from study to study.

These theoretical studies could also prove that the defect sides in the support are essential to stabilise the gold cluster on the support [134] as it has been shown by STM measurements [136] as well. But no influence of the defects sites on the reaction path could be found in the theoretical studies.

This leaves the question open where and how the oxygen is activated in the low temperature CO oxidation.

The adsorption of CO on gold has also been investigated, both on single crystals [137, 138] and on supported Au nanoparticles [139, 140]. These studies show that CO adsorbs best on nanoparticles and on roughened single crystal surfaces. The adsorption of CO on ordered gold surfaces is rather weak but still significantly

142]. The question remains what causes the improved adsorption on the imperfect surfaces. Lemire and co-worker [139] found in studies of Au/FeO_x systems that the CO adsorption/desorption is independent of the cluster size. Hence quantum effects cannot play a role in CO adsorption but it is suggested that low coordinated gold atoms, like those on terraces and edges, preferably adsorb CO. This would be presumably due to a better back-donation capability of the low coordinated gold atoms into the CO molecule, as also discussed for size selected gold clusters [85, 88, 105, 106]. Especially the theoretical work by Lopez and Norskov [143] on unsupported Au_{10} cluster suggests that low coordinated gold atoms are essential for the high catalytic activity of gold nanoparticles. The studies revealed two possible reaction pathways after the coadsorption of CO and O_2 on the cluster. The first path is the direct formation of CO_2 and O by a spillover of one of the oxygen atoms. The other path includes the dissociation of the oxygen molecule on the gold cluster with the following reaction of one oxygen atom and the CO molecule. Both ways have been found to have a low reaction barrier of less then 0.4 eV, which indicates a reaction possibility even under room temperatures. This study also pointed out that the dissociation of oxygen is extremely favoured on the gold cluster, contrary to a Au(111) surface.

1.3.3.4 Chemical state of the active gold cluster

A further point, which is highly controversial, is the chemical state of the active gold. The recent literature comprises claims that the Au nanoparticles are positively charged ("Au^{+I}-oxide") [116, 144, 145, 146, 147, 148, 149], Au^{+III} (gold-oxide) [150], negatively charged [91, 132] or neutral [125, 151].

The main reason why it is believed that the Au clusters are positively charged results from XPS measurements [144]. These measurements were carried out under UHV conditions after preparation and leeching of the metallic gold particles. Hence the postulated partially oxidised gold (Au^{I}) would be stable under laboratory conditions. This is in contradiction to our knowledge about gold oxides. No evidence has been found that it is possible to synthesise gold oxides other than Au_2O_3 [34, 46] and the analysis of Au/Fe_2O_3 catalysts with Mössbauer spectroscopy revealed only Au^0 and Au^{3+} states in the particles [118, 131]. Furthermore it has been also shown that a

higher photo-electron binding energy does not always indicate a higher oxidation state as can be seen in the oxides of lead (PbO and PbO_2) [5]. A recent study by Lee et al. on mass selected gold clusters on $TiO_2(110)$ also indicated a very wide range of BE, between 84 eV and 85.8 eV, for very small neutral gold clusters [109, 110]. This indicates that the BE shifts measured by [144] are due to Coulomb effects in small clusters [6] and not due to the formation of Au^{I}-oxides (this effect will be discussed in more detail in the technique chapter). This argument was also followed by Willneff et al. [152], who assigned the binding energy shift in *in* situ XPS studies to different sized gold cluster assemblies. The results presented by Gates et al. [145 - 147] that also point to Au^{I}-oxides do not provide enough detail to follow the data processing and analysis procedure. Also a recent publication by the same group showed clearly that gold catalysts prepared by $Au(CH_3)_2(C_5H_7O_2)$ are highly active and contain only Au^{+III} (in an mononuclear state) but neither Au^{+I} nor Au^{0}. This makes it difficult to follow the arguments of these authors.

1.3.3.5 Size and morphology of the active gold cluster

The shape of the Au nanoparticle can be a critical factor and is influenced by the support [153]. To determine the shape of the Au nanoparticle on powder catalysts, transmission electron microscopy (TEM) is mostly used [12, 154, 155]. But some problems have to be considered.

The catalyst powder is usually brought into a suspension and then dropped onto a carbon-coated copper grid. Therefore weakly adsorbed particles can be washed off the powder or some suspension can remain adsorbed on the sample. This can alter the measured particle size and shape in the TEM images. Also TEM is an *ex situ* technique, meaning that the images are taken under vacuum conditions. This leads to the problem that the reaction mechanism and catalyst can change under vacuum and normal pressure [156]. This phenomenon is often called "pressure-gap" [157] and has to be bridged to gain knowledge about the catalyst under "industrial" conditions (atmospheric pressure and above). TEM is also not the only technique facing this problem; all vacuum techniques e.g. scanning electron microscopy (SEM), X-ray photoelectron spectroscopy (XPS), Auger electron spectroscopy (AES) and low energy electron diffraction (LEED) are prone to this critique (for more details see the following section).

A further disadvantage of TEM is the limited resolution (High Resolution TEM ~ 1nm). This leads to a variation of the predicated sizes and shapes for the (mostly) catalytic active nanoparticles. The size of the active particles ranges from below 1 nm [144] to about 2 to 3 nm [25, 158].

To improve the resolution scanning tunnelling microscopy (STM) was used successfully on flat model catalysts [84, 139, 140, 159]. This allows the study of gold cluster also beneath 1 nm and gave some very interesting results. First of all gold nanoparticles are affected by Ostwald ripening, meaning bigger particles grow by consuming material from small particles (see fig. 1.17) [160]. The change in particle sizes could be introduced by heating in UHV [136, 137, 161], by dosing CO [160] or a CO/O_2 mixture [162]. In all cases particles with sizes around or below 1 nm and particles with several nanometers could be observed after the Ostwald ripening. When dosing O_2 only (about 10^{-3} torr) a reduction in the interaction between gold clusters and TiO_2 support could be observed by an easier "pick up" off the gold clusters by the STM tip [163]. This indicates that the F-centres in the support are essential for good sticking of the gold. It was also pointed out that these are the major points on which evaporated gold adsorbs on TiO_2 [136].

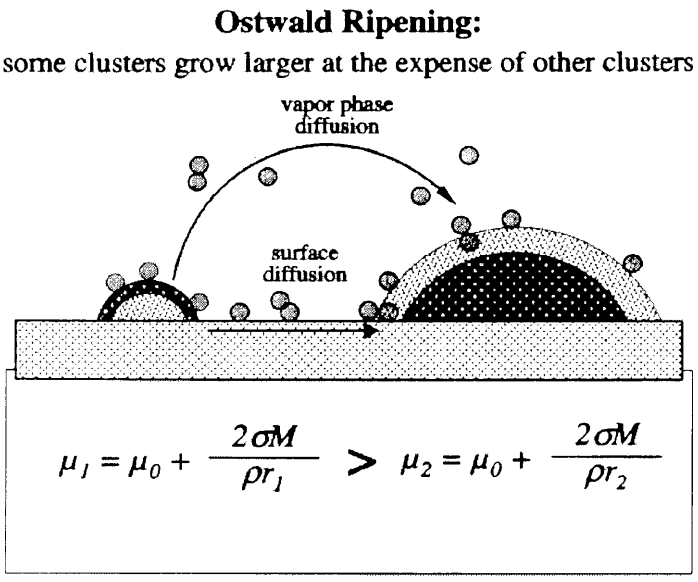

Fig. 1.17: Ostwald ripening in particles (from [160]).

Analysing the shape of the gold particles revealed two different shapes. One being smaller particles those grow in a quasi-2D shape (disc or hemielliptical like) with maximum heights of 2 atom layer (~ 0.6 nm) and a diameter of below 1 nm. For bigger particles a 3D growth was observed resulting in a more hemispherical or spherical shape of the gold particles [159]. The change in shape also corresponds to a change in conductivity measured by scanning tunnelling spectroscopy (STS). For gold particles with a maximum of 2 atom layer heights a non-metallic (non-conducting) behaviour was found. For bigger clusters this changes to a conducting or metallic behaviour [84, 132, 159]. The change from metallic to non-metallic gold was often postulated to relate to an increased CO oxidation [47, 84, 159] and an increase in adsorption heat for CO on the non-metallic gold clusters has been found [23].

The adsorption site of the gold clusters on the support might be important for the catalytic activity as well. Santra et al. [164] showed that for gold sputtered onto TiO_2 the clusters have a high possibility at low coverage (0.17 ML) to populate step sites on the support. These sites are quickly filled and gold clusters start to populate terrace sites only. Comparing the size of the clusters on steps and terraces shows that the gold clusters on steps are at the lowest coverage of 0.17 ML all ready bigger (diameter ~ 4.2 nm, heights ~ 0.60 nm) than clusters on terraces at coverage of 0.86 ML (diameter ~ 3.4 nm, heights ~ 0.45 nm).

The disadvantages of STM are the requirements to the sample, so powders and other not particular flat samples can be studied. But powders or other high surface materials that carry the catalytic active material "inside" are usually used as support. Therefore the catalytic active material is shielded from the STM tip and cannot be accessed. Hence it is not possible or only in very few cases to study industrially used catalysts with STM and the catalyst has to be a model on a flat support as e.g. single crystals. STM also requires the sample to be conducting or semi-conducting, where as a large number of catalysts supports are metal oxides that are usually non-conducting. This means that the sample preparation for model catalysts mimicking these supports is relative challenging.

1.3.4 Correlating model studies to practical catalysts – bridging gaps

The fundamental problem of catalysis science is the complexity of the problem, which is reflected by the controversial discussion for most catalytic systems, even though heterogeneous catalysts have been studied for more than 100 years now [4, 165]. This is because catalysis is the combination of two complex fields, namely the studies of the catalyst itself and of the reaction of the adsorbed reactants on the catalyst, which both can influence each other.

To start with the catalyst itself, it is a combination of materials that can be classified as support, the catalytic active material, and in most cases structural promoters and washcoats [4, 19, 165]. In fig. 1.18 a Au/TiO_2 powder catalyst is shown, indicating support and catalytic active material (gold partical). The support is in terms of volume and weight in most catalysts the absolute major component, but it only acts as the framework to hold the catalytic active material in position. To do so very porous materials, often powder, are used as support. But the support is often not part of the catalytic cycle. The catalytic active material is usually only a few weight percent of the catalyst and is present in small particles (few nanometers). But it is the part of the catalyst that is in contact with the reactants during their reaction and of the main interests when studying the catalytic mechanism. Structural promoters are usually use to keep the catalytic active material in a certain "form", e.g. crystal structure and the washcoat is often use for a better adhesion between active phase and support. The structural promoters and washcoats are generally not used in gold catalysis and therefore the reader is pointed to the literature [4, 165] for more information about them.

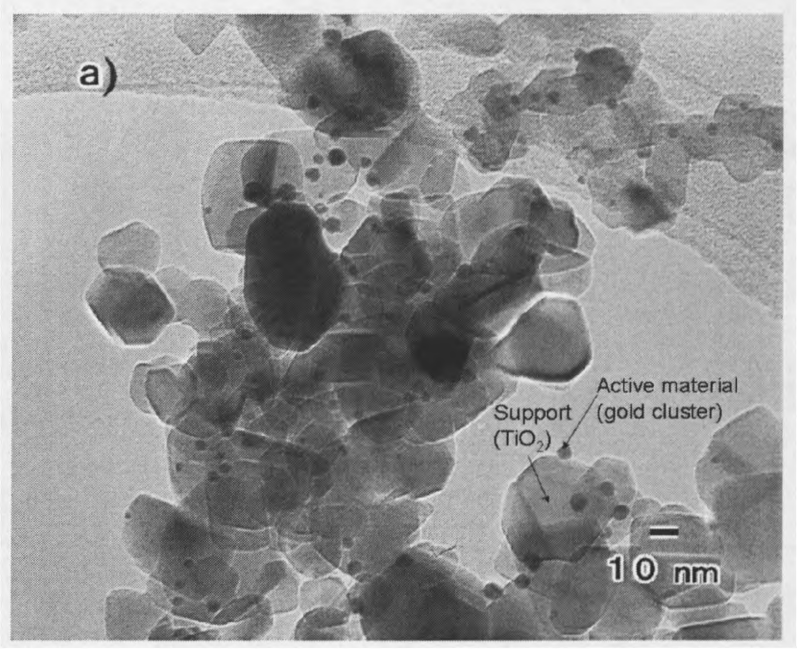

Fig. 1.18: TEM of a Au/TiO_2 catalyst (from [154]). The support and catalytic active material are indicated.

The complexity of catalysts makes it difficult to study them and to understand the reactions on a molecular basis. Hence model systems with a decreased complexity are used. The first model systems that have been used were single crystals of the active material, which can be easily studied by surface science techniques. On single crystals the surface is easily accessible and the sample is very homogenous, which makes it possible to assume that results found on one part of the sample are also correct for the rest of the sample.

But the difference between this model and real systems can be very dramatic, e.g., gold is seen as catalytically inactive as long as it is a single crystal with "bulk material" properties (meaning in a homogenous state) [3]. The activity of gold drastically changes as it becomes a nanomaterial and cannot be seen as a "homogenous" material anymore. The inhomogeneity of small gold particles, or gold clusters, can be seen in the similar amount of steps, kinks, edges and face atoms at the surface. All these different atoms can have different properties and therefore their behaviour has to be studied individually. On single crystals the majority of surface

atoms are face atoms and therefore no differentiation has to be taken into account. Also the nanoparticles are supported making the material, as a whole, inhomogenous. Another effect that might affect the activity of a catalyst is the cluster effect; meaning that the electronic structure in the nanoparticles is not the same as in a bulk material. This is due to the finite number of atoms leading to a finite number of states. This contrasts with bulk material, where an infinite number of atoms and states are found. Hence the band structure evolved for bulk material breaks down in nanoparticles [19] (cf. fig. 1.9). This general problem to understand the relation between single crystal and nanoparticle or catalytic active material is known as the material gap [157, 166].
In recent years different types of models have been evaluated to bridge this gap and two models, namely electrochemically oxidised gold foil and gold nanoparticles supported on flat TiO_2, will be studied in this thesis.
The approach to use single crystal supports for the catalytic active material has been performed before. Different preparation methods have been tested to mimic the real catalytic behaviour the best, including chemical vapour deposition (CVD) [15], sputtering [159] and spin coating [167 - 170]. The use of a flat support instead of a powder, as in practical catalysts, gives the advantage that techniques, which have been established in studying single crystals, like STM and AFM, can be used on these models as well [159].

As discussed in the previous section, the work on these models gave a very good insight into the shape and size of the gold catalyst. But reaction tests performed by Goodman et al. [79, 160] also indicated that, even though this model system is very close to practical gold catalysts, some differences still exist. They found that cluster size and catalytic activity are similar between model and practical system (cf. fig. 1.19). But the measured activity of the single crystal is initially very high, in this case even higher than the reference catalyst, but the catalysts deactivate very rapidly in the first 180 minutes of their activity. The high catalytic activity measured for the model catalysts might be also a problem in detecting the small amounts of products created by flat model catalysts, which is due to the small surface area of flat catalysts (see also chapter 3.3.2 for a more detailed discussion). But this is hard to judge because no detailed information on the reactor is given. The rapid deactivation thus indicates that still some differences between the used model catalysts and the practical catalysts exist and that a (small) material gap is present.

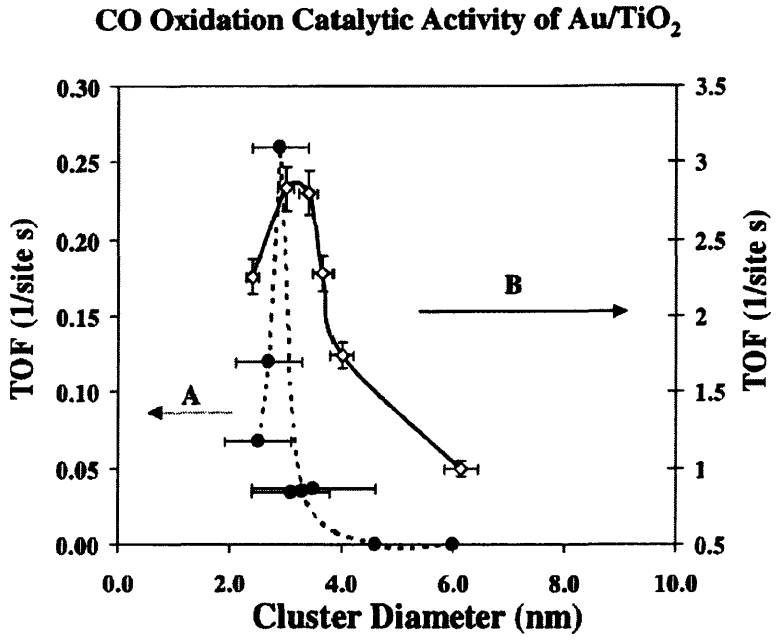

Fig. 1.19: CO oxidation turn over frequencies (TOF's) as a function of Au cluster size supported on TiO_2 (from [160]). A) (filled circles) practical powder catalysts, B) (empty circles) flat model catalysts.

When studying surfaces the low amount of atoms on a surface (~10^{15} atoms/cm^2) in comparison to bulk material ($6 \cdot 10^{23}$ atoms/mol) has to be considered, because an ideal surface is only 2-dimensional and the bulk is 3-dimensional (never the less the Avogadro number is the same). This means small amounts of impurities can have massive influence on the result. This is one of the reasons why first surface science studies in the 1960s were conducted under ultra high vacuum conditions (>10^{-6} mbar). In the pressure range under 10^{-6} mbar the adsorption of molecules from the sample chamber atmosphere becomes slow enough (at 10^{-6} mbar about 1 s to cover a free surface completely) to study the surface of the sample and preventing too many impurities impinging on the surface.

Another reason to use vacuum in the earlier years was that most techniques in surface science require vacuum to operate. Techniques developed for the vacuum use are SEM, TEM, LEED, STM, XPS, soft X-ray XAS, etc. Only in recent years it has been that these techniques have been adapted to keep the sample in atmosphere [23, 43, 79, 152], so that the interaction between adsorbents and surface can be studied as well.

The use of these techniques at different pressure ranges also pointed out that it is not trivial to study catalytic processes under vacuum conditions and correlate the results to studies taken under atmospherically or elevated pressures. The problem evolves from the different amount of adsorbents on the catalysts under the different pressure conditions. Under ultra high vacuum conditions the surface can be considered as nearly adsorbent free and the reactions partners will have to move on the surface to find each other. On the other hand all adsorbents are free to move since their next neighbour will be far away, because the surface is empty. This also means all kinds of adsorption sites are available for the adsorbents under vacuum conditions.
For the non-vacuum case, the opposite is the case. The surface is fully covered by adsorbents. This means reaction partners might not have to find each other on the surface but if so then the movement is strongly hindered. Also not all adsorption sites are freely available and the adsorbents will have to compete to adsorb on the different sites by their adsorption strength to the different sites. Finally another problem is present under non-vacuum conditions, because no reactant stream is 100% clean, small amounts of impurities (in the ppm region) can lead to the adsorption of adsorbents that are not considered to be the reactants. This can lead to poisoning of certain adsorption sites of the catalysts and therefore lead to a different reaction channel. In general this phenomenon is known as the pressure gap in catalysis [4, 157, 166].

To overcome these problems it has become common practice to use different types of catalyst systems under conditions close to operational conditions (*in situ* experiments), which was also an aim of this work.

References

[1] Bone, W. A.; Andrew, G. W.; Proceedings of the Royal Society A, **1925**, *109*, 459.
[2] N. W., Cant; P. W., Fredrickson; Journal of Catalysis, **1975**, *37*, 531-539.
[3] Bond, G. C.; Thompson, D. T.; Catalysis Reviews - Science and Engineering; **1999**, *41*, 319-388.
[4] Ertl, G.; Knözinger, H.; Weitkamp, J. (Eds.); *Handbook of Heterogenous Catalysis*, Wiley-VCH Verlagsgesellschaft mbH, Weinhaim, **1997**.
[5] Kim, K. S.; Winograd, N.; Chemical Physics Letters, **1975**, *30*, 91-95.

[6] Liang, K. S.; Salaneck, W. R.; Aksay, I. A.; Solid State Communications; **1976**, *19*, 329-334.

[7] Bond, G. C.; Semon, P. A.; Gold Bulletin, **1973**, *6*, 102-105.

[8] Cocco, G., Enzo, S., Fagherazzi, G., Schiffini, L., Bassi, I. W., Vlaic, G., Galvagno, S., Parravano, G.; Journal of Physical Chemistry, **1979**, *83*, 2527-2538.

[9] Haruta, M.; Kobayashi, T.; Sano, N.; Yamada, N.; Chemistry Letters; **1987**, 405.

[10] Haruta, M.; Yamada, N.; Kobayashi, T.; Iijima, S.; Journal of Catalysis, **1989**, *115*, 301-309.

[11] Kobayashi, T.; Haruta, M.; Sano, H.; Nakane, M.; Sensors and Actuators, **1988**, *13*, 339-349.

[12] Haruta, M.; Tsubota, S.; Kobayashi, T.; Kageyama, H.; Genet, M. J.; Delmon, B.; Journal of Catalysis; **1993**, *144*, 175-192.

[13] Haruta, M.; Catalysis Surveys from Japan, **1997**, *1*, 61-73.

[14] Bamwenda, G. R.; Tsubota, S.; Nakamura, T.; Haruta, M.; Catalysis Letters, **1997**, *44*, 83-87.

[15] Okumura, M.; Nakamura, S.; Tsubota, S.; Nakamura, T.; Azuma, M.; Haruta, M.; Catalysis Letters, **1998**, *51*, 53-58.

[16] Haruta, M.; Catalysis Today, **1997**, *36*, 153-166.

[17] Sakurai, H.; Haruta, M.; Applied Catalysis, A, **1995**, *127*, 93-105.

[18] Iizuka, Y.; Fujiki, H.; Yamauchi, N.; Chijiiwa, T.; Arai, S.; Tsubota, S.; Haruta, M.; Catalysis Today, **1997**, *36*, 115-123.

[19] Freund, H. J.; Surface Science, **2002**, *500*, 271-299.

[20] Dekkers, M. A. P.; Lippits, M. J.; Nieuwenhuys, B. E.; Catalysis Letters, **1998**, *56*, 195-197.

[21] Maye, M. M.; Luo, J.; Han, L.; Kariuki, N. N.; Zhong, C. J.; Gold Bulletin, **2003**, *36*, 75-82.

[22] Grunwaldt, J. D.; Kiener, C.; Wogerbauer, C.; Baiker, A.; Journal of Catalysis, **1999**, *181*, 223-232.

[23] Meier, D. C.; Goodman, D. W.; Journal of the American Chemical Society; **2004**, *126*, 1892-1899.

[24] Schumacher, B.; Denkwitz, Y.; Plzak, V.; Kinne, M. Behm, R. J.; Journal of Catalysis, **2004**, *224*, 449-462.

[25] Schubert, M. M.; Kahlich, M. J.; Gasteiger, H. A.; Behm, R. J.; Journal of Power Sources, **1999**, *84*, 175-182.

[26] Jagow, R. B.; Lamparter, R. A.; Katan, T.; Ray, C. D.; American Society of Mechanical Engineering, **1977**, *77-ENAs-28*, 16.

[27] Gardner, S. D.; Hoflund, G. B.; Upchurch, B. T.; Schryer, D. R.; Kielin, E. J.; Schryer, J.; Journal of Catalysis, **1991**, *129*, 114-120.

[28] Atkins, P. W.; *Physical Chemistry 6th edition*, Oxford University Press, **1999**.

[29] Smith, M. B.; March, J.; *March's Advanced Organic Chemistry: reactions, mechanisms and structure 5th edition*, Wiley-Interscience, **2001**.

[30] Hayashi, T.; T., K.; Haruta, M.; Journal of Catalysis, **1998**, *178*, 566-575.

[31] Carrettin, S.; McMorn, P.; Johnston, P.; Griffin, K.; Kiely, C. J.; Physical Chemistry Chemical Physics; **2003**, *5*, 1329-1336.

[32] Ueda, A.; Oshima, T.; Haruta, M.; Applied Catalysis, B: Environmental, **1997**, *12*, 81-93.

[33] Andreeva, D.; Idakiev, V.; Tabakova, T.; Andreev, A.; Giovanoli, R.; Applied Catalysis, A: General, **1996**, *134*, 275-283.

[34] Riedel, E.; *Anorganische Chemie Ed. 4*, de Gruyter, **1999**.

[35] Mohamed, M. M.; Ichikawa, M.; Journal of Colloid and Interface Science, **2000**, *232*, 381-388.

[36] Garcia, R.; Besson, M.; Gallezot, P.; Applied Catalysis, A: General, **1995**, 127, 165-176.

[37] Gallezot, P.; Catalysis Today, **1997**, *37*, 405-418.

[38] Kimura, H.; Applied Catalysis A, **1993**, *105*, 143-169.

[39] Carrettin, S.; McMorn, P.; Johnston, P.; Griffin, K.; Hutchings, G. J.; Chemical Communications, **2002**, 696-697.

[40] Gluhoi, A. C.; Dekkers, M. A. P.; Nieuwenhuys, B. E.; Journal of Catalysis, **2003**, *219*, 197-205.

[41] Silver, R. G.; Sawyer, J. E.; Summers, J. C.; (Eds.); *Catalytic Control of Air Pollution: Mobile and Stationary Sources*, ACS Symposium Series 495, Washington, **1991**, 98.

[42] Bartlett, N.; Gold Bulletin; **1998**, *31*, 22-25.

[43] Meyer, R.; Lemire, C.; Shaikhutdinov, S. K.; Freund, H. J.; Gold Bulletin, **2004**, *37*, 72-124.

[44] Li, J.; Li, X.; Zhai, H. J.; Wang, L. S.; Science, **2003**, *299*, 864-867.

[45] Blach, A. L.; Gold Bulletin, **2004**, *37*, 45-50.

[46] Weiher, N.; *Dissertation*, FU Berlin, **2003**.

[47] Jones, P. G.; Rumpel, H.; Schwarzmann, E.; Sheldrick, G. M.; Paulus, H.; Acta Crystallographica, Section B: Structural Crystallography and Crystal Chemistry, **1979**, *B35*, 1435-1437.

[48] Gmelin, L.; *Gmelin Handbook of Inorganic and Organometallic Chemistry, Gold Suppelement*, Volume 1, Springer Verlag, **1992**.

[49] Jansen, M; Mudring, A. V.; *The Chemistry of Gold Oxides*, John Wiley & Sons Ltd, **1999**.

[50] Olea, M.; Kunitake, M.; Shido, T.; Iwasawa, Y.; Physical Chemistry Chemical Physics, **2001**, *4*, 627-631.

[51] Peuckert, M.; Coenen, F. P.; Bonzel, H. P.; Surface Science, **1984**, *141*, 515-532.

[52] Boccuzzi, F.; Chiorino, A.; Manzoli, M.; Lu, P.; Akita, T.; Ichikawa, S.; Haruta, M.; Journal of Catalysis, **2001**, *202*, 256-267.

[53] Yang, J. H.; Henao, J. D.; Raphulu, M. C.; Wang, Y.; Caputo, T.; Groszek, A. J.; Kung, M. C.; Scurrell, M. S.; Miller, J. T.; Kung, H. H.; Journal of Physical Chemistry B, **2005**, *109*, 10319-10326.

[54] Moreau, F.; Bond, G. C.; Taylor, A. O.; Journal of Catalysis, **2005**, *231*, 105-114.

[55] Stone, P.; Bennett, R. A.; Bowker, M.; New Journal of Physics, **1999**, *1*, 1.1-1.12.

[56] Diebold, U.; Lehman, J.; Mahmoud, T.; Kuhn, M.; Leonardelli, G.; Hebenstreit, W.; Schmid, M.; Varga, P.; Surface Science, **1998**, *411*, 137-153.

[57]Zhang, L.; Persaud, R.; Madey, T. E. ;Physical Review B, **1997**, *56*, 10549-10557.

[58] Wahlström, E.; Vestergaard, E. K.; Schaub, R.; Ronnau, A.; Vestergaard, M.; Laegsgaard, E.; Stensgaard, I.; Besenbacher, F.; Science, **2004**, *303*, 511-513.

[59] Diebold, U.; Applied Physics A, **2003**, *76*, 681-687.

[60] Diebold, U.; Surface Science Reports, **2003**, *48*, 53-229.

[61] Wang, R.; Sakai, N.; Fujishima, A.; Watanabe, T.; Hashimoto, K.; Journal of Physical Chemistry B, **1999**, *103*, 2188-2194.

[62] Wang, R.; Hashimoto, K.; Fujishima, A.; Chikuni, M.; Kojima, E.; Kitamura, A.; Shimohigoshi, M.; Watanabe, Toshiya; Nature, **1997**, *388*, 431-432.

[63] Diebold, U.; Li, M.; Dulub, O.; Hebenstreit, E. L. D.; Hebenstreit, W.; Surface Review and Letters; **2000**, *7*, 613-617.

[64] Li, M.; Hebenstreit, W.; Diebold, U.; Physical Review, **2000**, *B61*, 4926.

[65] Wang, R.; Hashimoto, K.; Fujishima, A.; Chikuni, M.; Kojima, E.; Kitamura, A.; Shimohigoshi, M.; Watanabe, T.; Advanced Materials, **1998**, *10*, 135-138.

[66] Engel, T.; Ertl, G.; Advances in Catalysis, **1979**, *28*, 1-78.

[67] Nakao, K.; Ito, S. I.; Tomishige, K.; Kunimori, K.; Catalysis Today, **2006**, *111*, 316-321.

[68] Mhadeshwar, A. B.; Vlachos, D. G.; Combustion and Flame, **2005**, *142*, 289-298.

[69] Bowker, M.; Guo, Q.; Joyner, R. W.; Surface Science, **1993**, *280*, 50-62.

[70] Dwyer, D. J.; Hoffmann, F. M. (Eds.); *Surface Science of Catalysis: In situ Probes and Reaction Kinetics*; American Chemical Society, Washington D.C.; **1992.**

[71] Peden, C. H. F.; Goodman, D. W.; Weisel, M. D.; Hoffmann, F. M.; Surface Science, **1991**, *253*, 44-58.

[72] Stampfl, C.; Scheffler, M.; Surface Science, **1999**, *433-435*, 119-126.

[73] http://www.iupac.org/goldbook/L03451.pdf

[74] http://www.webelements.com/webelements/elements/print/O/enth.html.

[75] Konova, P.; Naydenov, A.; Venkov, C.; Mehandjiev, D.; Andreeva, D.; Tabakova, T.; Journal of Molecular Catalysis A: Chemical; **2004**, *213*, 235-240.

[76] Debaila, M.; Wells, R.; Anderson, J.; Journal of Catalysis, **2006**, *239* 162-172.

[77] Haruta, M.; Cattech, **2002**, *6*, 102-115.

[78] Stiehl, J.; Kim, T.; McClure, S.; Mullins, C.; Journal of the American Chemical Society, **2004**, *126*, 13574-13575.

[79] Valden, M.; Pak, S.; Lai, X.; Goodman, D. W.; Catalysis Letters, **1998**, *56*, 7-10.

[80] Bollinger, M. A.; Vannice, M. A.; Applied Catalysis, B: Environmental, **1996**, *8*, 417-443.

[81] Boccuzzi, F.; Chiorino, A.; Catalysis Letters, **1994**, *29*, 225-234.

[82] Liu, Z. M.; Vannice, M. A.; Catalysis Letters, **1997**, *43*, 51-54.

[83] Grunwaldt, J. D.; Baiker, A.; Journal of Physical Chemistry B, **1999**, *103*, 1002-1012.

[84] Valden, M.; Lai, X.; Goodman, D. W.; Science, **1998**, *281*, 1647-1650.

[85] Bernhardt, T. M.; International Journal of Mass Spectrometry, **2005**, *243*, 1-29.

[86] Wallace, William T.; Whetten, Robert L.; Journal of the American Chemical Society; **2002**, *124*, 7499-7505.

[87] Socaciu, L. D.; Hagen, J., Bernhardt, T. M.; Woeste, L.; Heiz, U., Haekkinen, H.; Landman, U.; Journal of the American Chemical Society, **2003**, *125*, 10437-10445.

[88] Yoon, B.; Hakkinen, H.; Landman, U.; Worz, A. S.; Antonietti, J. M.; Abbet, S.; Judai, K.; Heiz, U.; Science, **2005**, *307*, 403-407.

[89] Häkkinen, H.; Landman, U.; Journal of the American Chemical Society, **2001**, *123*, 9704-9705.

[90] Yuan, D. W.; Zeng, Z.; Journal of Chemical Physics, **2004**, *120*, 6574-6584.

[91] Kim, Y. D.; Fischer, M.; Gantefor, G.; Chemical Physics Letters, **2003**, *377*, 170-176.

[92] Cox, D. M.; Brickman, R. O.; Creegan, K.; Kaldor, A.; Materials Research Society Symposium Proceedings, **1991**, *206*, 43-48.

[93] Kimble, M. L.; Castleman, A. W.; International Journal of Mass Spectrometry; **2004**, *233*, 99-101.

[94] Cox, D. M.; Brickman, R.; Creegan, K.; Kaldor, A.; Zeitschrift fuer Physik D: Atoms, Molecules and Clusters; **1991**, *19*, 353-355.

[95] Lee, T. H.; Ervin, K. M.; Journal of Physical Chemistry, **1994**, *98*, 10023-10031.

[96] Salisbury, B. E.; Wallace, W. T.; Whetten, R. L.; Chemical Physics, **2000**, *262*, 131-141.

[97] Stolcic, D.; Fischer, M.; Gantefoer, G.; Kim, Y. D.; Sun, Q.; Jena, P.; Journal of the American Chemical Society, **2003**, *125*, 2848-2849.

[98] Kim, Y. D; International Journal of Mass Spectrometry, **2004**, *238*, 17-31.

[99] Sun, Q.; Jena, P.; Kim, Y. D.; Fischer, M.; Gantefor, G.; Journal of Chemical

[100] Nygren, M. A.; Siegbahn, P. E. M.; Jin, C.; Guo, T.; Smalley, R. E.; Journal of Chemical Physics, **1991**, *95*, 6181-6184.

[101] Wallace, W. T.; Whetten, R. L.; Journal of Physical Chemistry B, **2000**, *104*, 10964-10968.

[102] Wallace, W. T.; Whetten, R. L.; European Physical Journal D: Atomic, Molecular and Optical Physics, **2001**, *16*, 123-126.

[103] Balteanu, I.; Balaj, O. P.; Fox, B. S.; Beyer, M. K.; Bastl, Z.; Bondybey, V. E.; Physical Chemistry Chemical Physics, **2003**, *5*, 1213-1218.

[104] Hagen, J.; Socaciu, L. D.; Elijazyfer, M.; Heiz, U.; Bernhardt, T. M.; Woeste, L.; Physical Chemistry Chemical Physics, **2002**, *4*, 1707-1709.

[105] Elschenbroich, Salzer, A.; *Organometallics*, VCH, Weinheim, **1989**.

[106] Sanchez, A.; Abbet, S.; Heiz, U.; Schneider, W. D.; Häkkinen, H.; Barnett, R. N.; Landman, Uzi; Journal of Physical Chemistry A; **1999**, *103*, 9573-9578.

[107] Häkkinen, Hannu; Abbet, Stephane; Sanchez, Antonio; Heiz, Ulrich; Landman, Uzi; Angewandte Chemie, International Edition, **2003**, *42*, 1297-1300.

[108] Lee, S.; Fan, C.; Wu, T.; Anderson, S. L.; Journal of Chemical Physics, **2005**, *123*, 124710/1-124710/13.

[109] Lee, S.; Fan, C.; Wu, T.; Anderson, S. L.; Journal of Physical Chemistry B, **2005**, *578*, 5-19.

[110] Lee, S.; Fan, C.; Wu, T.; Anderson, S. L.; Journal of Physical Chemistry B, **2005**, *109*, 11340-11347.

[111] Chrétien, S.; Metiu, H.; The Journal of Chemical Physics, **2007**, *126*, 104701.

[112] Gottfried, J. M.; Schmidt, K. J.; Schroeder, S. L. M.; Christmann, K.; Surface Science, **2002**, *511*, 65-82.

[113] Olea, M.; Iwasawa, Y.; Applied Catalysis, A: General; **2004**, *275*, 35-42.

[114] Stiehl, J. D.; Kim, T. S.; McClure, S. M.; Mullins, C. B.; Journal of the American Chemical Society; **2004**, *126*, 13574-13575.

[115] Iizuka, Y.; Tode, T.; Takao, T.; Yatsu, K.; Takeuchi, T.; Tsubota, S.; Haruta, M.; Journal of Catalysis, **1999**, *187*, 50-58.

[116] Costello, C. K.; Kung, M. C.; Oh, H. S.; Wang, Y.; Kung, H. H.; Applied Catalysis, A: General, **2002**, *232*, 159-168.

[117] Bondzie, V. A.; Parker, S. C.; Campbell, C. T.; Catalysis Letters, **1999**, *63*, 143-151.

[118] Daniells, S. T.; Overweg, A. R.; Makkee, M.; Moulijn, J. A.; Journal of Catalysis, **2005**, *230*, 52-65.

[119] Lin, S. D.; Bollinger, M.; Vannice, M. A.; Catalysis Letters, **1993**, *17*, 245-262.

[120] Boccuzzi, F.; Chiorino, A.; Tsubota, S.; Haruta, M.; Journal of Physical Chemistry, **1996**, *100*, 3625-3631.

[121] Boccuzzi, F.; Chiorino, A.; Manzoli, M.; Surface Science, **2002**, *502-503*, 513-518.

[122] Schubert, M. M.; Hackenberg, S.; van Veen, A. C.; Muhler, M.; Plzak, V.; Behm, R. J.; Journal of Catalysis, **2001**, *197*, 113-122.

[123] Moreau, F; Bond, G. C.; Applied Catalysis, A: General, **2006**, *302*, 110-117.

[124] Zou, X.; Qi, S.; Suo, Z.; An, L.; Li, F.; Catalysis Communications, **2007**, *8*, 784-788.

[125] Henao, J. D.; Caputo, T.; Yang, J. H.; Kung, M. C.; Kung, H. H.; Journal of Physical Chemistry B, **2006**, *110*, 8689-8700.

[126] Calla, J. T.; Davis, R. J.; Journal of Catalysis, **2006**, *241*, 407-416.

[127] Liu, L. M.; McAllister, B.; Ye, H. Q.; Hu, P.; Journal of the American Chemical Society; **2006**, *128*, 4017-4022.

[128] Liu, H.; Kozlov, A. I.; Kozlova, A. P.; Shido, T.; Asakura, K.; Iwasawa, Y.; Journal of Catalysis, **1999**, *185*, 252-264.

[129] Lian, H.; Jia, M.; Pan, W.; Li, Y.; Zhang, W.; Jiang, D.; Catalysis Communications, **2005**, *6*, 47-51.

[130] Bongiorno, A.; Landman, U.; Physical Review Letters; **2005**, *95*, 106102/1-106102/4.

[131] Daniells, S. T.; Makkee, M.; Moulijn, J. A.; Catalysis Letters, **2005**, *100*, 39-47.

[132] Maeda, Y.; Okumura, M.; Tsubota, S.; Kohyama, M.; Haruta, M.; Applied Surface Science, **2004**, *222*, 409-414.

[133] Molina, L. M.; Rasmussen, M. D.; Hammer, B.; Journal of Chemical Physics, **2005**, *120*, 7673-7680.

[134] Remediakis, I. N.; Lopez, N.; Norskov, J. K.; Angewandte Chemie, International Edition, **2005**, *44*, 1824-1826.

[135] Remediakis, I. N.; Lopez, N.; Norskov, J. K.; Applied Catalysis, A: General, **2005**, *291*, 13-20.

[136] Wahlström, E.; Lopez, N.; Schaub, R.; Thostrup, P.; Ronnau, A.; Africh, C.; Laegsgaard, E.; Norskov, J. K.; Besenbacher, F.; Physical Review Letters, **2003**, *90*, 026101/1-026101/4.

[137] Gottfried, J. M.; Schmidt, K. J.; Schroeder, S. L. M.; Christmann, K.; Surface Science, **2003**, *536*, 206-224.

[138] Jugnet, Y.; Cadete Santos Aires, F. J.; Deranlot, C.; Piccolo, L.; Bertolini, J. C.; Surface Science, **2002**, *521*, L639-L644.

[139] Lemire, C.; Meyer, R.; Shaikhutdinov, S.; Freund, H. J.; Angewandte Chemie, International Edition, **2004**, *43*, 118-121.

[140] Shaikhutdinov, S. K.; Meyer, R.; Naschitzki, M.; Bäumer, M.; Freund, H. J.; Catalysis Letters; **2003**, *86*, 211-219.

[141] Gottfried, J. M.; Schmidt, K. J.; Schroeder, S. L. M.; Christmann, K.; Surface Science, **2003**, *525*, 197-206.

[142] Gottfried, J. M.; Schmidt, K. J.; Schroeder, S. L. M.; Christmann, K.; Surface Science, **2003**, *525*, 184-196.

[143] Lopez, N.; Norskov, J. K.; Journal of the American Chemical Society, **2002**, *124*, 11262-11263.

[144] Fu, Q.; Saltsburg, H.; Flytzani-Stephanopoulos, M.; Science, **2003**, *301*, 935-938.

[145] Guzman, J.; Gates, B. C.; Journal of Physical Chemistry B, **2003**, *107*, 2242-2248.

[146] Guzman, J.; Gates, B. C.; Journal of the American Chemical Society; **2004**, *126*, 2672-2673.

[147] Guzman, J.; Gates, B. C.; Journal of Physical Chemistry B, **2002**, *106*, 7659-7665.

[148] Mihaylov, M.; Gates, B. C.; Fierro-Gonzalez, J. C.; Hadjiivanov, K.; Knözinger, H.; Journal of Physical Chemistry, **2007**, *111*, 2548-2556.

[149] Manzoli, M.; Boccuzzi, F.; Chiorino, A.; Vindigni, F.; Deng, W.; Flytzani-Stephanopoulos, M.; Journal of Catalysis, **2007**, *245*, 308-315.

[150] Fierro-Gonzalez, J. C.; Bhirud, V. A.; Gates, B. C.; Chemical Communications, **2005**, *42*, 5275-5277.

[151] Lin, H. Y.; Chen, Y. W.; Industrial & Engineering Chemistry Research, **2005**, *44*, 4569-4576.

[152] Willneff, E. A.; Braun, S.; Rosenthal, D.; Bluhm, H.; Haevecker, M.; Kleimenov, E.; Knop-Gericke, A.; Schloegl, R.; Schroeder, S. L. M.; Journal of the American Chemical Society, **2006**, *128*, 12052-12053.

[153] Comotti, M.; Li, W.; Spliethoff, B.; Schueth, F.; Journal of the American Chemical Society, **2006**, *128*, 917-924.

[154] Tsubota, S.; Nakamura, T.; Tanaka, K.; Haruta, M.; Catalysis Letters; **1998**, *56*, 131-135.

[155] Fan, L.; Ichikuni, N.; Shimazu, S.; Uematsu, T.; Applied Catalysis, A; **2003**, *246*, 87-95.

[156] Marsh, Anderson L.; Burnett, Daniel J.; Fischer, Daniel A.; Gland, John L.; Journal of Physical Chemistry B, **2004**, *108*, 605-611.

[157] Bukhtiyarov, V. I.; Kinetics and Catalysis, **2003**, *44*, 420-431.

[158] Haruta, M.; Ueda, A.; Tsubota, S.; Torres Sanchez, R. M.; Catalysis Today, **1996**, *29*, 443-447.

[159] Lai, X.; St. Clair, T. P.; Valden, M.; Goodman, D. W.; Progress in Surface Science, **1998**, *59*, 25-52.

[160] Lai, X.; Goodman, D. W.; Journal of Molecular Catalysis A: Chemical, **2000**, *162*, 33-50.

[161] Mitchell, C. E. J.; Howard, A.; Carney, M.; Egdell, R. G.; Surface Science, **2001**, *490*, 196-210.

[162] Kolmakov, A.; Goodman, D. W.; Surface Science, **2001**, *490*, L597-L601.

[163] Kolmakov, A.; Goodman, D. W.; Catalysis Letters, **2000**, *70*, 93-97.

[164] Santra, A. K.; Kolmakov, A.; Yang, F.; Goodman, D. W.; Japanese Journal of Applied Physics, Part 1: Regular Papers, Short Notes & Review Papers, **2003**, *42*, 4795-4798.

[165]: Anderson J. R.; Boudart, M. (eds.); *Catalysis, Science and Technology*, Springer-Verlag, Volume 4, **1983**.

[166] Schlögl, R., Angewandte Chemie International Edition, **1993**, *32*, 381-383.

[167] Braun, S.; *Diploma Thesis*, FU Berlin, **2003**.

[168] van Hardeveld, R. M.; Gunter, P. L. J.; van IJzendoorn, L. J.; Wieldraaijer, W.; Kuipers, E. W.; Niemantsverdriet, J. W.; Applied Surface Science, **1995**, *84*, 339-346.

[169] Muijsers, J. C.; Weber, T.; van Hardeveld, R. M.; Zandberg, H. W.; Niemantsverdriet, J. W.; Journal of Catalysis, **1995**, *157*, 698-705.

[170] Brinie III, D. P.; Zelinski, B. J. J.; Perry, D. L.; Optical Engineering, **1995**, *34*, 1782-1788.

2 Techniques

2.1 X-ray spectroscopy

X-rays are used for characterising both the bulk and the surface of a wide range of materials. The main fields using X-rays include chemistry, physics, material science, biology, and geology, which use techniques such as X-ray photoelectron spectroscopy (XPS), Auger electron spectroscopy (AES), X-ray absorption spectroscopy (XAS) and X-ray absorption fine structure (XAFS) spectroscopy. X-ray diffraction (XRD) is a scattering based technique and will be not discussed further.

The general mechanism of absorption of an X-ray photon by an atom is represented in fig. 2.1. When an atom absorbs a photon, the energy excites an electron. The energy level of which the electron is excited depends on the energy of the incident photon and on the nature of the atom. If a core electron is excited, a hole is created, which is filled by an electron from an outer shell (the atom relaxes). Relaxation can occur by two different mechanisms. The system can release a photon when a valence electron is used to fill a core hole in a process called fluorescence, or by releasing a secondary electron, called an Auger electron.

X-ray fluorescence and Auger process are concurrent mechanisms. In the case of light atoms, fluorescence is predominant, whereas heavier atoms tend to relax by the Auger process.

If an electron is excited, it can either populate an unoccupied orbital or enter into a vacuum (ionised), which is called the final state. When the electron enters the vacuum it is called a photoelectron, which is probed by XPS. If the electron occupies an orbital after excitation, it will relax after a certain time and emit a photon. In the first case the state is, on a spectroscopic time scale, stable and the electron has to be restored to the atom by grounding the sample. This is usually achieved by connecting the sample to the sample chamber, which transfers the emitted electrons through the sample holder back into the sample, and from there into the probed states.

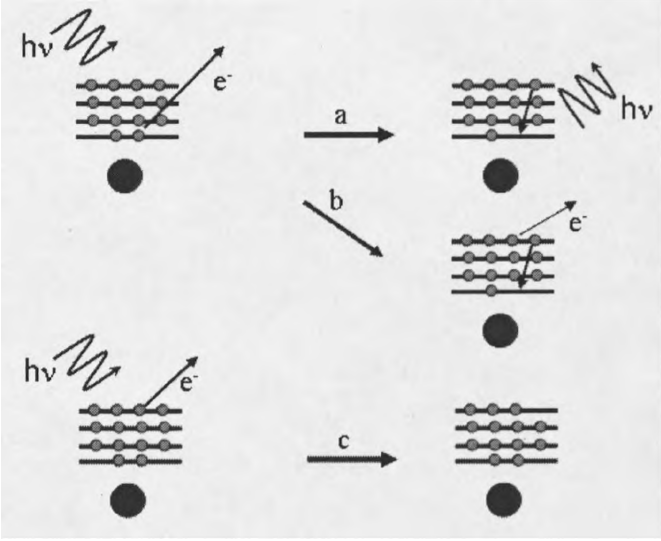

Fig. 2.1: Basic mechanisms in X-ray photon spectroscopy. a) X-ray fluorescence. b) Auger electron of a core-excited electron. c) Excitation of a valance electron.

For the excitation of an electron, the sample has to absorb incident light. The Beer-Lambert law describes the amount of photons that a material absorbs.

$$A = \lg\left(\frac{I_o}{I}\right) \text{ or } I = I_0 \cdot e^{\mu(E)\cdot d} \qquad 2.1$$

Where absorption (A) is equal to the logarithm of the initial light (I_0) divided by the transmitted light (I). It can be also expressed by considering the absorption coefficient (μ) at a specific light energy (E) and the thickness of the sample (d).

By tuning the incident light energy, the absorption coefficient of the material changes and an absorption spectrum can be measured. Significant absorption will occur when the energy of the incident light beam is equal to the energy needed for exciting an electron into an excited state or the vacuum. An approximation for that behaviour is given by Fermi's golden rule:

$$W_{fi} = \frac{2\pi}{\eta}\left|\langle f|H^{\text{int}}|i\rangle\right|^2 \delta(E_f - E_i - \eta\omega) \qquad 2.2$$

This gives the transition possibility (W_{fi}) between the initial (i) and final state (f), while the interaction between the initial and final state is given in the bracket notation and H^{int} is the Hamiltonian. The corresponding energies for the states are given by E_f and E_i and

$\eta\omega$ the light energy. ω is the light frequency and η is Planck's constant, divided by 2π. δ is the Dirac delta function, which in theory gives only a transition possibility if the photon energy is the difference between the energies of finial and initial state ($\delta(x)$ is 0 for all values except for $\delta(0)$ where it is unity).

If the energy of the incident photons is tuned in the X-ray region, the absorption coefficient will drastically increase when the energy is sufficient to excite an electron out of its shell into an unoccupied shell or into the vacuum. Hence this technique is called X-ray absorption spectroscopy (XAS) or X-ray absorption fine structure (XAFS) spectroscopy (see chapter 2.1.2).

Electrons that are excited from the same orbital and element will have the same kinetic energy, assuming the photon energy is constant. The kinetic energy can be analysed and the resulting technique is X-ray photoelectron spectroscopy (XPS). Auger electron spectroscopy (AES) is very similar to XPS but the electrons that are analysed are those from the Auger process. Since these electrons receive their energy from an electron that is "falling" down from a specific shell into a lower specific shell, their kinetic energy is independent of the X-ray energy applied to the atom. Therefore, if different photon energies are applied (e.g. Al K_α and Mg K_α) the kinetic energy of the Auger electron does not change. The kinetic energy of the primary electron will change when changing the excitation energy. This method is able to differentiate between both types of emitted electrons.

2.1.1 X-ray photoelectron spectroscopy (XPS)

As only the first few nanometers of the sample are probed due to the short mean free path of an electron in solids, XPS is an ideal candidate for surface analysis. A number of textbooks are available that discuss this technique [1].

The basic principle of XPS is that (soft) monochromatic X-ray radiation is used to ionise atoms by the excitation of photoelectrons (fig. 2.2). The emitted electrons are then analysed according to their kinetic energy.

The kinetic energy of the electron after leaving the atom can be expressed as:

$$E_{kin} = E_{excitation} - E_{bin}\,. \qquad 2.3$$

Where E_{kin} is the kinetic energy of the electron after leaving the atom, $E_{excitation}$ is the energy of the incident X-ray photon and E_{bin} is the binding energy of the electron in its specific binding state. This equation assumes the applicability of Koopman's theorem, i.e. the initial states can be supposed to be equal to the final states. This means that no relaxation of the atom, and therefore no change of the energy levels, occurs on a similar time scale as the photoelectron is emitted. This can be assumed since the impulse of the light photon is large enough to accelerate the electron out of the electronic shell, but will barely influence the atom core due to the much larger mass of the atom core in comparison to an electron.

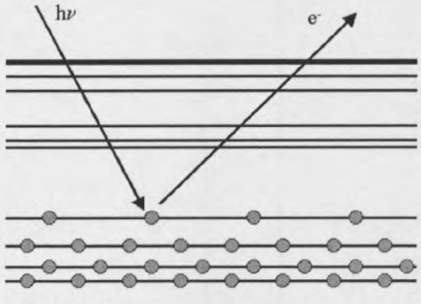

Fig. 2.2: Principle of the electron excitation.

E_{bin} is also influenced not only by the Binding Energy (BE) but also by other effects, which will be discussed in section 2.1.2.

The kinetic energy of the electron is commonly analysed by electrostatic analysers, e.g. with a hemispherical analyser (see fig 2.3). A magnetic lens focuses the electrons that are excited from the sample before entering the hemisphere to give a better energy resolution. When entering the hemisphere the electrons are forced into a curve by a homogeneous electrostatic field between the inner and outer hemisphere. The radius of the electron flight path between the hemispheres depends on the electrons kinetic energy and the field strength. Varying the strength of the field between the hemispheres enables all energies of the electrons to be scanned. Other techniques to analyse the kinetic energy of electrons and charged particles are given e.g. in [1].

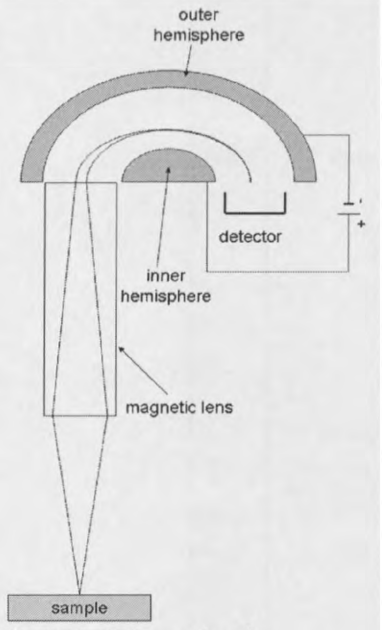

Fig. 2.3: Schematic of a hemispherical analyser.

It is possible to calculate the binding energy of the electron in the atom using formula 2.3 and entering the excitation energy and the kinetic energy of the electron.

The binding energy of the electron is related (mainly) to three factors: the probed atom as well as the chemical state and local environment. The probed atom influences the binding energy, since for heavier atoms electrons of the same state are more strongly bound by the higher charge of the core. Atoms in solids are not separated and the atoms surrounding them can distribute electrons to them. The surrounding electron band can screen ("fill") the electron holes created in one atom. The tendency of these atoms to screen depends strongly on their electron affinity, in other words the oxidation state of the probed atom.

Peaks in an XPS spectrum are named according to the atomic orbital, e.g., C 1s, O 1s, Ti 2p, Au 4f, etc. Since photoelectron emission is sensitive to spin orbit coupling, it is also common practice to extend the labelling for the p, d, and f states and report the corresponding term symbols as in Ti $2p_{3/2}$, Ti $2p_{1/2}$, Au $4f_{7/2}$ and Au $4f_{5/2}$.

The chemical state and local environment of the atom has a small, but important influence on the binding energy, resulting in chemical shifts of the photoemission lines. Generally the higher the oxidation state of an atom, the higher the binding energy (section 2.1.2 gives a discussion of cases where this simple initial statement breaks down).

Essentially, XPS is often used to identify the chemical composition of a sample (surface) and even small traces of impurities (a few % of a monatomic layer) can be detected. Hence it is also known as electron spectroscopy for chemical analysis (ESCA).

So far an atom has been considered to be isolated, but in a solid material this is not the case. This means for an atom that is not at the surface, the electron can be scattered by the electron shells of the other atoms en-route from the bulk to the surface (fig. 2.4). This scattering can basically happen in four ways: the electron is scattered elastically but in a

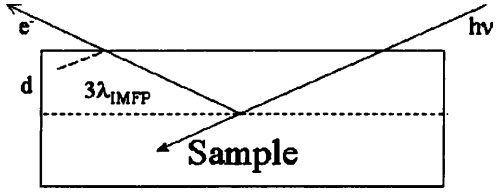

Fig. 2.4: Angle dependence of the escape depth of electrons.

direction to leave the bulk (2.3.b), the electron is inelastically scattered, but can still leave the bulk (2.3.c), the electron is scattered into the bulk (2.3.d) or the electron is absorbed (2.3.e). Electrons from deep inside the bulk have a higher probability of being scattered before leaving the sample than electrons originating at, or very near the surface. Therefore it is less likely that the former escape because they are either absorbed or they lose energy by inelastic scattering (this means the kinetic energy differs, and the electrons appears in the spectral background of an XP spectrum).

The inelastic mean free path (IMFP) quantifies these effects. This is the average distance an electron with a specific energy travels in the bulk between two inelastic scattering processes (for definition see [2]). The IMFP increases with kinetic energy, but it is normally not longer than a few nanometers. This means that only the topmost atomic layers in the sample are probed.

The actual surface sensitivity (i.e., the depth from which the electrons escape) can be varied by basically two different methods. First, by altering the energy of the exciting photons (only practical using a synchrotron light source), secondly one can vary the angle between the sample surface and the electron analyser. The detection angle dependence of the IMFP is approximately described by the following formula [1] (fig. 2.4): 2.4

$$d = 3\lambda_{IMPF} \sin\alpha .$$

The depth d describes the distance from the surface to the bulk from which 95 % of the electrons escape. λ_{IMPF} is the mean free path and α the angle between analyser and the beam (90° gives the maximum depth).

2.1.2 XPS of small particles

In X-ray photoelectron spectroscopy (XPS) many different factors can affect the binding energy (BE) of an element. These effects can be classified into initial and final state effects.

Starting with the initial state effects, the best known is the change in oxidation state, which results, as a first approximation, in a higher BE with higher oxidation states (exceptions include Pb_2O and PbO). Differences between surface and bulk atoms can be detected. Citrin *et al.* [3] showed that by varying the angle between the gold surface and

the detector, a shoulder to lower BE appears. This shoulder can be assigned to surface atoms on bulk gold. Furthermore Zhang and Sham [4] point out that the localisation of states in small clusters might affect the binding energy.

The term "final state effect" is very general and includes the ionisation process and the passage of the electron through the bulk. The mainly discussed effect is the distribution and neutralisation of the charge created in the sample by the leaving electron. The most obvious effect is known as sample charging or surface photovoltage [5]. This describes the positive charge on the whole sample, which is created by the bombardment of the sample with X-rays and the emission of electrons. Insulating and semi-conducting samples normally show a strong tendency for this.

A further charging effect is known as the coulomb effect. This effect appears in small clusters and thin films. These small "particles" only have a very limited number of neighbouring atoms over which the charge can delocalise. The hole created upon electron ionisation within the atom cannot be screened as well as in bulk material. This leads to a lower kinetic energy of electrons leaving these clusters. Hence a higher BE is detected for atoms in small clusters, although this does not mean that their initial state has a different energy to equivalent atoms in bulk material.

It has been shown before that supported metal clusters and metals in alloys can show a significant shift in BE in XPS, which is not related to a change of oxidation state in these metals [3, 6 - 10] (see also table 2.1 for BE shifts reported in the literature). Instead it is a size effect of the particles, related to their relaxation. This is expressed by the formula:

$$\Delta E_B^F(Q:X,Y) = \Delta E_V^B - \Delta\phi = \Delta q/r - \Delta V - \Delta E_R - \Delta\phi, \qquad 2.5$$

$\Delta E_B^F(Q:X,Y)$ is the final binding energy difference between the common ion Q in the crystals X and Y. ΔE_V^B is the binding energy of the electron with reference to vacuum level and $\Delta\phi$ is the work function correction. It can also be stated that the binding energy is dependent on the oxidation state or "chemical shift" ($\Delta q/r$) of the probed atom. Changes in the crystal structure (ΔV), e.g. between different morphologies, can change the BE of the atom. Furthermore, the possibility to replenish electrons to the electron hole by the surrounding electrons (ΔE_R) is essential for the measured binding energy, since the

electron leaving the atom is attracted by the remaining positive charge on its former host atom. This is known as the Coulomb effect, or the screening ability of the surrounding atoms. This effect occurs often in small clusters of metals because the surface atoms are highly uncoordinated. The band structure of the metals breaks down in the clusters and electron density cannot be transported easily to the probed atom as in a bulk metal.

Table 2.1: Binding energy shifts of the Au 4f state in gold clusters and alloys compared to bulk gold.

Gold system	Binding energy shift	Reference
Au(surface)	-0.4 eV	[3]
Au/TiO_2 (gold layer of 1.1 Å)	+0.4 eV	[11]
Au_1/TiO_2 (atomically dispersed)	+1.3 eV	[12]
Au_1/Al_2O_3 (atomically dispersed)	+ 0.7 eV	[13]
$AuAl_2$-alloy	+ 1.5 eV	[9]
Au/Al (gold thickness dependent)	> 1 eV	[9]
Au/Al_2O_3	+1.1 eV	[10]
Au/SiO_2	+1.3 eV	[10]
Au/SiO_2-alloy	+1.1 eV	[6]
Au/Ag-alloy	+0.3 eV	[6]
Au/C	+1.0 eV	[10]

The same effect is seen in alkane chains. Mårtensson and Nilsson [14] showed that with increasing chain length the BE of the centroid carbon decreases. This is due to the better charge screening effect in longer alkane chains.

2.1.3 Experimental settings for X-ray photoelectron spectroscopy (XPS)

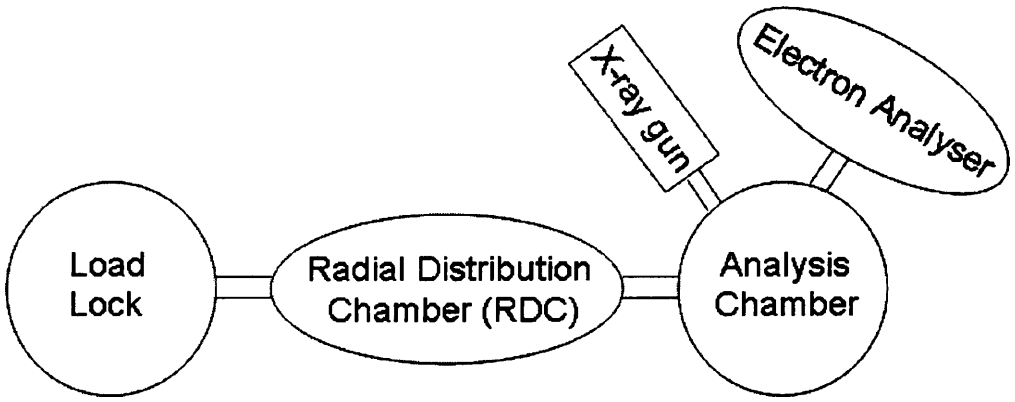

Fig. 2.5: Schematic view of the XPS apparatus for analysis of samples *ex situ.*

For *ex situ* XPS studies a Kratos Axis Ultra with a radial distribution chamber and load lock for sample loading was used (fig.2.5).

The samples were prepared on a stainless steel holder and several samples (between 4 and 15, depending on size) could be loaded simultaneously. Carbon sticky tape was used to hold the samples in place. Transferring a sample from the ambient conditions in the laboratory into the measurement chamber took approximately two hours including the pump down time of the sample to, normally, 1×10^{-9} mbar in the measurement chamber. For all measurements reported in this work, a monochromated Al K_α source was used, operating with an anode voltage of 15 keV and a cathode current of 10 mA. The pass energy of the hemispherical electron analyser during acquisition of survey spectra was 80 eV. For high resolution spectra of individual emission lines it was set to 20 eV. A non-monochromated Al K_α and a non-monochromated Mg K_α source were fitted as well, but have not been used in this study.

The measurement parameters for the different types of samples are summarised in table 2.2. The scan time for a spot on the gold nanoparticles on TiO_2 single crystals was approximately 12 h if the Au 4f signal was recorded. This was necessary to achieve a reasonable signal to noise ratio. All parameters that are given in table 2.2 were optimised

to give a good signal to noise ratio in an optimum of time for the corresponding sample type on representative samples.

Table 2.2: Parameters of typical XPS measurements of the different sample types.

Element	Au/TiO_2			Au oxide foils		
	Step width	Scan Time	Sweeps	Step width	Scan Time	Sweeps
survey	0.25 eV	400 ms	1	0.25 eV	400 ms	1
O 1s/Ti 2s	0.10 eV	300 ms	3	0.10 eV	600 ms	6
Ti 2p	0.10 eV	300 ms	3	---	---	---
C 1s	0.10 eV	300 ms	3	0.10 eV	300 ms	3
Cl 2p	---	---	---	0.10 eV	600 ms	6
Au 4f	0.10 eV	3000 ms	64	0.10 eV	300 ms	3
Na 2s/VB	0.10 eV	300 ms	5	0.10 eV	300 ms	3

2.1.4 X-ray absorption fine structure (XAFS) spectroscopy

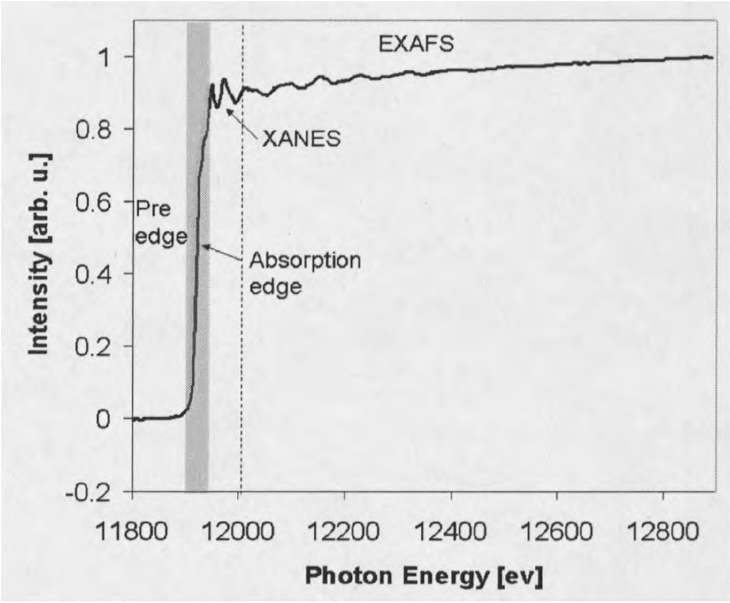

Fig. 2.6: Region explanation of an X-ray absorption spectrum on a gold L_{III}-edge spectrum.

The spectrum is separated into four regions (cf. fig. 2.6).

1. The pre-edge is the region (~50 eV) prior to the sharp increase in absorption. In this region the energy of the photons is not high enough to ionize an electron from the state that is probed.

2. The absorption edge, which is the sharp increase in absorption in the spectrum. At this point the photons have just enough energy to excite the electron from its state.

3. Up to 100 eV after the absorption edge the region is called X-ray absorption near edge structure (XANES) and is due to transition into unoccupied states (often it is referred to as NEXAFS, Near edge X-ray absorption fine structure).

4. For several 100 eV or even some keV beyond the absorption edge the extended X-ray absorption fine structure (EXAFS, not to be confused with XAFS, which is the whole spectrum) is located. The structure in this region is due to multiple scattering of the escaping electron.

2.1.4.1 X-ray absorption near edge spectroscopy

X-ray absorption near edge spectroscopy (XANES) defines the region above the absorption edge. In this region the electrons have enough energy to enter unoccupied states of the material and therefore it is probing the chemical environment of the excited atom. The resulting, mostly very sharp, structures occur over the first roughly 100 eV above the absorption edge.

At specific photon energy, the electron will be able to reach the lowest unoccupied shell (in molecules it would be the lowest unoccupied molecular orbital [LUMO], see fig 2.7). At this point the absorption edge is reached. Upon further increase of excitation energy, the electrons can be promoted to higher unoccupied levels of the sample, which will result in an increase in the amount of X-ray absorbed by the material. Thus the electronic structure of the unoccupied orbitals in an atom or a molecule can be probed. For metals, it is probing the band structure since no separate states are present.

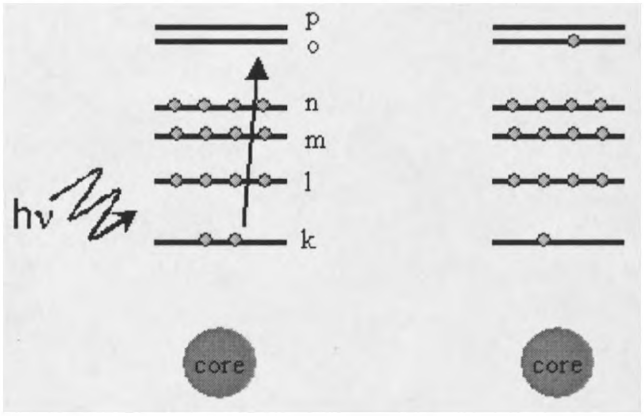

Fig. 2.7: Model of the electron excitement out of the k-shell into the lowest unoccupied molecular orbital (LUMO), induced by a photon.

The unoccupied states in an atom are very sensitive to changes in the oxidation state of that atom. Therefore XANES spectra often give a very clear differentiation between different oxidation states, as can be seen for gold(0) and gold(+III)-oxide as shown in fig. 2.8. For metallic gold, the absorption edge increases to roughly the intensity level behind the edge. For gold-oxide the absorption at the edge increases to a much higher value than the intensity level behind the edge. This feature is called near edge resonance, or historically, "white line".

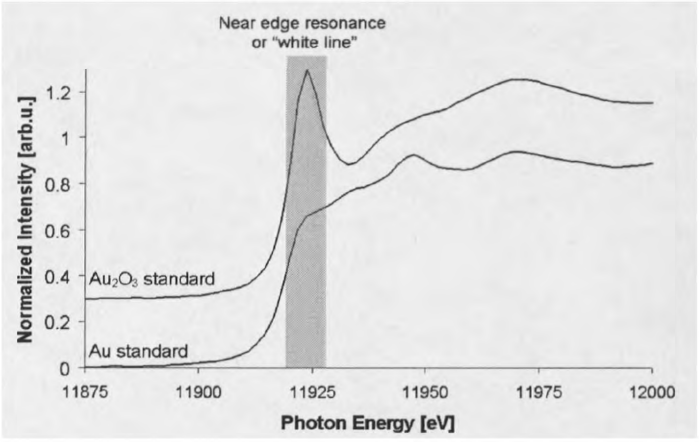

Fig. 2.8: NEXAFS spectra of gold and gold-oxide.

Analysing the near edge structure can separate different types of hybridisation. This is particularly important in carbon C K-edge (C K-edge) spectra and is subject of the following section.

2.1.4.2 Soft X-ray building block theory

The building block theory was introduced for analysing data gained from large molecules with soft X-ray C K-edge XANES. This theory will be introduced here as it is needed to understand the results of the *in situ* experiments. One of the major groups in this field is that of Stöhr [15].

The major assumption of building block theory is that large molecules are built up from diatomic molecules that are linked to each other. For a detailed analysis of a single group it is further expected that no interaction between these groups is present; this means that the molecule does not contain delocalised molecular orbital (MO's). This would exclude a large group of aromatic molecules from the theory. But if no detailed analysis is required it is, with some care, also possible to study molecules with delocalised MO's.

The C K-edge NEXAFS spectra can be separated into two major regions: The transitions of the C 1s (K-shell) electron into π^* (between 284 and 290 eV) and into σ^* resonances (above 290 eV). A further transition that is seen for most organic molecules is the Rydberg resonance transition of sp^3 carbon and excitation into C-H σ^* states that are below 290 eV.

For further refinement the specific groups in the molecule have to be analysed. This is done by the hybridisation of the carbon atoms (sp, sp^2 and sp^3) or bonds (triple, double and single). Both nomenclatures are common [15, 16]. Throughout this work the hybridisation nomenclature will be used here. In a molecule only containing C-C and C-H bonds, sp (triple bonds) hybridized states are excited at lower photon energies than sp^2 (double bond) and sp^3 (single bonds) states. The defined photon energy also depends on the oxidation state of the carbon atom. The higher the oxidation, the greater the photon energy needed to excite the electron into the corresponding state.

Table 2.3: XAS peaks of some materials with high carbon content.

Name	Peak position	Assignment	Ref.
Pentacene	285.8	$sp^2\ \pi^*$	[17]
	288.7	$sp^2\ \pi^*$	[17]
	~ 294	$sp^2\ \sigma^*$	[17]
	~ 300	$sp^2\ \sigma^*$	[17]
Hexaphenylbenzene	285.2	$sp^2\ \pi^*$	[17]
	288.6	$sp^2\ \pi^*$	[17]
	~ 293	$C\text{-}sp^2\ \sigma^*$	[17]
HOPG	285.5	$sp^2\ \pi^*$	[18]
	291-298	$sp^2\ \sigma^*$	[18]
	291.63	exciton	[18]
HOPG	285.4	$sp^2\ \pi^*$	[17]
	290	$sp^2\ \sigma^*$	[17]
Diamond(111)	289.5	1s exciton	[18]
	290-300	$sp^3\ \sigma^*$	[18]
	304-312	$sp^3\ \sigma^*$	[18]
Hydrofullerene	285	see ref.	[16]
	287	see ref.	[16]
	289	see ref.	[16]
	293	see ref.	[16]

For a proper analysis of the investigated molecule, the spectra of the designated building blocks are added to a full spectrum. This works very well for non-conjugated molecules as described by Stöhr [15]. For conjugated molecules, this method does not work as well, changes have to be expected between the building blocks and the total molecule spectrum in the π^* region. A similar conclusion has to be drawn for the σ^* states in saturated linear and cyclic molecules. Even though the same spectrum should be expected from the

building block theory, a huge difference especially for smaller rings (n<6) in comparison to their chain analogues is noticed [15].

For C K-edge spectra it is possible to have a closer look at the hybridization of the carbon atom. Thus sp^2-carbon atoms have an absorption peak around 285 eV whereas sp^3-carbon atoms have resonance a few eV higher. For an overview of some common samples see table 2.3.
The example of hydrofullerene shows that as long as only one hybridized form of carbon is present in the sample, an overlap between the different carbon states occurs [16]. In the case of hydrofullerene the contributions of the two carbon species could be calculated but if the problem becomes even more complex, e.g. different oxidation states of the carbon or an unknown sample, the limits of assigning the peak are reached.

2.1.4.3 Extended X-ray absorption fine structure (EXAFS)

By increasing the photon energy further, the electrons gain enough energy to leave the atom and ionise it. Electrons that have left may enter the vacuum. But before they do so there is a probability that they will be scattered by the electron shells of surrounding atoms. This gives the sinusoidal type oscillations, as observed in the spectrum beyond the XANES region and is called extended X-ray absorption fine structure (EXAFS). To explain this effect the electron in its waveform has to be understood. After the electron has left the atom it is "trapped" in a lattice of surrounding atoms, similar to a water wave in a pond in which stones stand out of the water, the electron will scatter on the neighbouring atoms and interfere with each other (see fig. 2.9). This can be seen in the slight variations in the absorption intensity in an EXAFS spectrum.

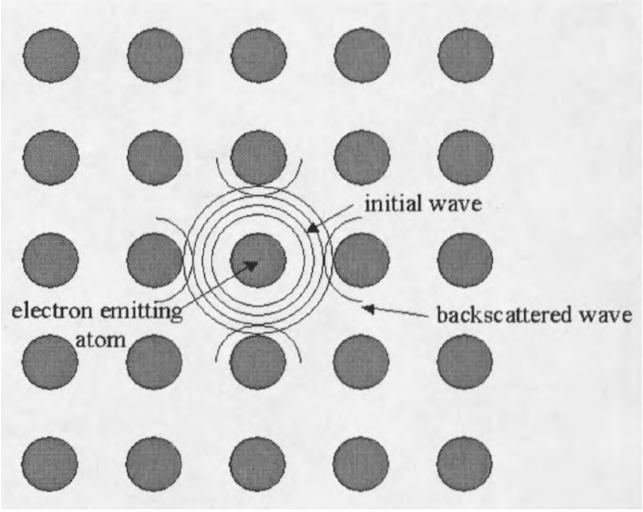

Fig. 2.9: Electron wave scattering model. The central atom emits the electron that is scattered at the surrounding atoms and the resulting interference will be present by the structure in the EXAFS spectrum.

Another effect that has to be considered in XA spectroscopy is that the excited atoms will reoccupy the lower energy states. Therefore a valence band electron falling into the hole left in the core states can excite another electron. If it is close to the Fermi level, this electron can be ejected (Auger process), otherwise the excess energy can appear as a photon (fluorescence) and is illustrated in fig. 2.10.
The emitted electrons and photons can be used to detect the XA spectrum (cf. 2.1.4.5). However, a problem evolves from the emitted electrons in the XANES region, because they can be scattered as well, and a clear separation between XANES and EXAFS is not possible.

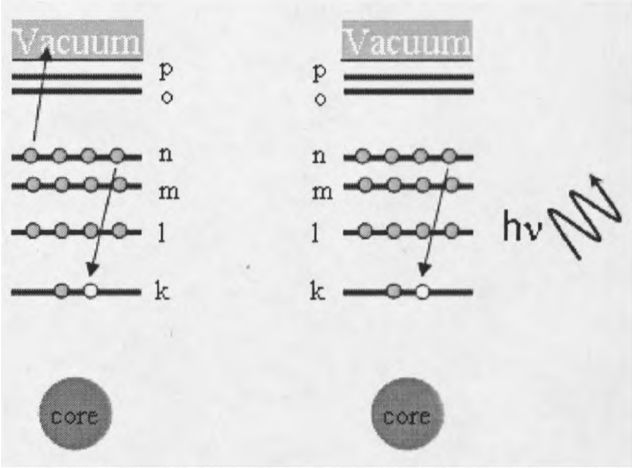

Fig. 2.10: MO schema of the Auger processes (left) and fluorescence (right) after an electron has been excited in the atom.

2.1.4.4 Use of soft and hard X-rays in XAS

Soft X-ray experiments (0 eV < wavelength (λ) < 1000 eV) have to be performed under vacuum conditions because soft X-rays ionise air and hence are absorbed. The soft X-ray beam can traverse a short path at elevated pressures (up to 10 mbar) without losing all its intensity, assuming the gas used does not contain many atoms per molecule (principally, the more atoms a molecule contains the higher its absorption coefficient for soft X-rays). Short distances of gaseous atmosphere, that the beam has to pass, can be used to fill the sample chamber with gases for *in situ* experiments and thin metal or metal oxide meshes with different coatings (also called windows) will separate the UHV from the sample chamber (for images see experimental part).

Using windows gives problems, due to non-linear absorption of the X-rays, especially in the C K-edge region from impurities (read carbon K-edge, meaning electrons emitted from the K-shell of carbon atoms). The main impurities on the window are carbon containing molecules, because the windows are usually stored and transported in air and the residuals are still present during measurements. Standard spectra have to be used to separate the spectrum of the sample from the "spectrum of the windows".

Experiments conducted with hard X-rays ($\lambda > 4000$ eV) do not require UHV setups since air does not absorb them. Therefore different parts of the experiment are built on a table without a vacuum line connecting them. This also makes the use of the atmosphere around the sample possible without taking any extra precaution than is necessary for the possible hazards of the gasses.

Another important difference between soft and hard X-ray beamlines is the type of mirrors and monochromators used. For soft X-rays experiments, equipment similar to those used for visible light, are needed. This also includes the use of gratings as monochromators. This is not possible for hard X-rays because the distance between the planes of the grating would be too small to manufacture. Hence the diffraction in single crystals is used as a monochromator. Si(111) and (220) are common but other elements and planes are also used.

2.1.4.5 Detection techniques used in XAS

Different techniques can be used for measuring XAS data. The most common ones are electron yield, fluorescence and absorption. These techniques can, in general, be used in both energy regions, soft and hard X-rays. The choice of technique depends on the experimental set up and the information depth of the sample that should be investigated.
Total electron yield: Total electron yield (TEY) in the soft X-ray region is a simple but effective method. The set up of the experiment requires a charged metal ring to which the electrons are accelerated. If the sample is contained in an atmosphere[1] a voltage of normally 40 V or more between sample and ring accelerates the electrons and the gas atoms or molecules are ionised (cf. fig. 2.11; for a complete electrical scheme see fig. 2.13). This works as a charge multiplier and the signal to noise ratio is, usually, very good.

[1] The atmosphere in experiments based on vacuum techniques like soft X-ray XAS or XPS is not allowed to rise above a certain level. This level is experiment dependent but is often found to be in or below the mbar region. The atmosphere itself can be a single gas, like CO or O_2, or a combination of gases.

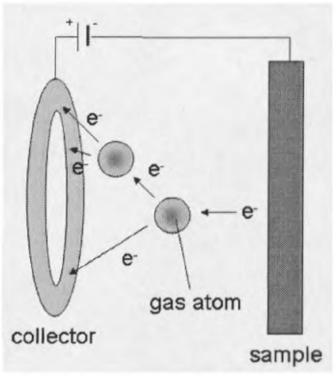

Fig. 2.11: Electron cascade of the electrons ejected from the sample and being attracted by the positively charge collector.

Two limitations have to be considered with soft X-rays. Firstly, the pressure drop over the window between beamline and sample chamber, which might lead to a window failure, and secondly, an elevated pressure drastically reduces the amount of X-rays reaching the sample.

TEY can be used for hard X-rays as well, but here the distance between sample and collector is critical, because the electrons that have left, have a very short mean free path at normal or even higher pressure. Hence if the distance is too wide (several cm) all electrons get absorbed.

Fluorescence: Electronically excited atoms have two ways of returning to their ground state. The first one is the Auger process, which releases an electron from the atom. This electron can be used in Auger electron spectroscopy (AES) and is also detected in TEY. The second possibility is the atom releases a photon. This is called fluorescence and is used in fluorescence yield (FY) measurements. The information gained from FY is much less surface sensitive then TEY because the mean free path of a photon in material is much longer then that of an electron. Hence combining both techniques can give information about the surface (TEY) and bulk (FY) structure of a sample.

Transmission: The transmission mode is mainly used for hard X-rays. For soft X-rays the sample would have to be very thin to allow the X-rays to partially penetrate the sample. For measuring the transmission, the intensity before the sample (I_0) and after the sample (I_t) is measured. The difference between both signals gives the sample signal. For hard X-

rays this is usually done with ionisation chambers that are filled with a mixture of noble gases. The X-ray ionises the noble gases and the current between two plate condensers is measured.

2.1.4.6 Soft X-ray XANES

A. M. Booth and S. Braun designed and constructed equipment based on DIN CF35-flanges for the soft XANES studies (fig. 2.12) [19, 20]. The sample chamber is based on standard CF35 stainless steel cubes (see below). The system can be seen as an assembly of 4 major parts. Part A is the measurement chamber, where the sample is held during experiments. Part B is the pumping system, which permits adjustment of the pressure in the measurement chamber and is coupled to the gas analysis system. Part C interfaces the sample chamber with the beamline, from which the X-ray beam enters the measurement chamber. Part D is a load lock system for changing samples. It also connects to the gas supply lines for *in situ* experiments.

Measurement Chamber - The measurement chamber is a DIN CF35 cube (Hositrad, CU35), with two view ports, mounted for aligning the sample in the beam and brief inspection of the state of the sample and electrical connections. A fluorescence detector can be mounted at an angle of 90° relative to the X-ray beam path (Part C). To the top of the cube the sample loading area is connected (Part D) and the pumping of the cube is done via Part B.

Pumping System - Part B contains a 4-way cross (Hositrad, FX 35/38R), which is mounted underneath the sample chamber. The mass spectrometer (MS, SRS RGA 100) is connected to this cross via a leak valve (Hositrad, VML 14CFR16). A pressure gauge (Pfeiffer, Compact FullRange™ BA Gauge PBR 260) is attached and a gate valve allows the adjustment of the pumping speed of the turbo pump (Pfeiffer, TMH 071 P, with MVP 015-2 backing pump).

Beamline Interface - The X-ray beam enters the sample chamber through part C from the left hand side into the sample chamber. The X-ray beam enters from the beamline and passes (in order) through a first DIN CF35 4-way cross (Hositrad, FX 35/38R) the first metal window, a second cross (Hositrad, FX 35/38R) and a second metal window. The

two metal windows are necessary to allow pressures of about 1 mbar in the sample chamber, whilst maintaining the pressure on the beamline side under 10^{-8} mbar. Pressure gauges (Pfeiffer, Compact FullRange™ BA Gauge PBR 260) are mounted on the crosses between the two windows to monitor the leak rate of the first and second window and to prevent them from bursting. The sections are each pumped by a turbo pump (Pfeiffer, TMH 071 P, with MVP 015-2 backing pump).

Load Lock System - The sample change is conducted in part D, which is connected via a gate valve (VAT, Series 10) with the sample chamber. The sample can be loaded in a second DIN CF35 cube (Hositrad, CU35). Two load locks are mounted on the cube (Caburn). The linear manipulator (Ferrovac, MD16 Series) is mounted on the top. The sample holder is mounted on the manipulator, and can be transferred between the load lock and the sample chamber. Furthermore it is possible to rotate the sample holder. On the sample holder itself a caddy is fitted that holds the sample (see below). A turbo pump (not shown) is also mounted on the cube, for pumping the load area after changing the sample without breaking the vacuum in the rest of the chamber. The gases can be dosed via the leak valves. The gases are supplied via disposable cans (CO: Linde 3.7; He: Air Liquide 5.0, O_2: Air Liquide 4.8).

Electrical feedthrough are mounted between the load area cube and the manipulator. The feedthrough is used for the drain current and as a thermocouple.

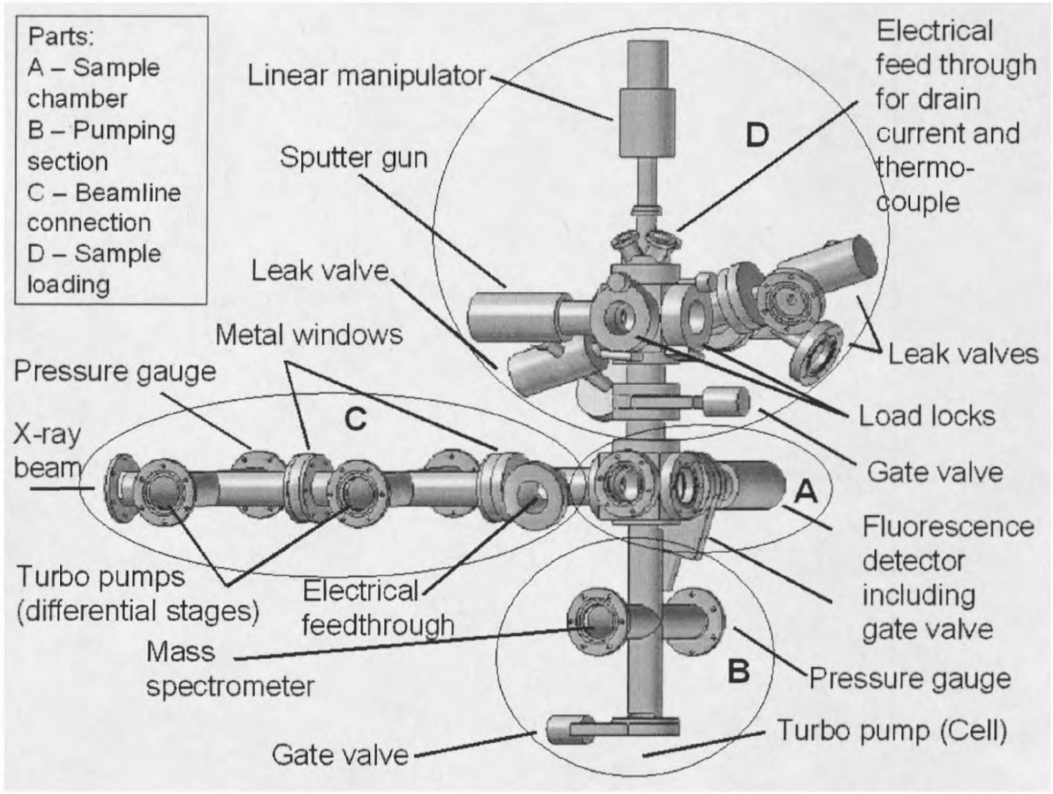

Fig. 2.12: Drawing of the general layout of the chamber used for soft NEXAFS measurements (adapted from reference [19, 20]).

A schematic drawing of the circuit underlying the soft X-ray TEY cell is shown in fig. 2.13. Both the drain and collector current are fed out of the sample chamber via electrical feed through and carried on with BNC-cables. The drain current is directly fed into a current amplifier (Keithley 427) before it is connected to the station electronics. Typical settings for the current amplifier are a gain of 10^{-9} V/A and a rise time of 300 ms.

The collector is connected to the anode of a Battery box that is charged (U=100 V(DC)). The voltage on the collector enables an electron cascade effect in the sample chamber. This means the electrons that are released from the sample are accelerated towards the collector. The accelerated electrons will collide with gas molecules (that are in the chamber under *in situ* conditions) and these excited molecules will release further electrons. This increases the current that is measured on the collector, and increases the

S/N ratio (signal to noise ratio). The current is then fed again into a current amplifier and from there into the beamline electronics.

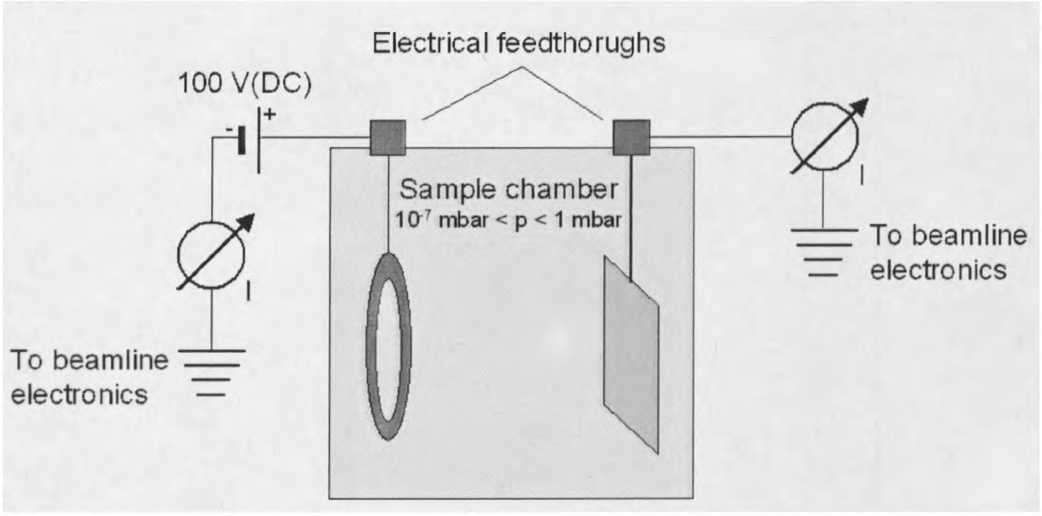

Fig. 2.13: Circuit for soft NEXAFS measurements by total electron-yield detection.

Fig. 2.14 shows the sample mounting environment, which allows the change of samples in the high vacuum chamber in less than 30 min (not including pumping). The set up contains three parts: the sample holder (i), the sample caddy (ii) – that actually carries the sample – and a boron electrical heater (iii, GE Advanced Ceramics HTR 1001)). The heater can be replaced by a Peltier element that allows cooling of the sample.

The sample holder (made of aluminium) is mounted onto the linear manipulator and stays in the apparatus for the entire experiment (including sample changes). The heater is mounted via M2 screws that are also used to supply the heater with the necessary current. The heater is electrically shielded from the holder and the rest of the apparatus using ceramic discs.

The caddy (made of aluminium) can slide onto the sample holder, and the heater and is attached firmly to the sample holder to allow heating in vacuum. The small hole at the end of the caddy is used to introduce a thermocouple underneath the sample to monitor the sample temperature. The wider hole on the other side of the caddy matches up with the hole in the sample holder, and is used to secure the caddy to the sample holder and to attach the drain current on a screw fitting into the hole.

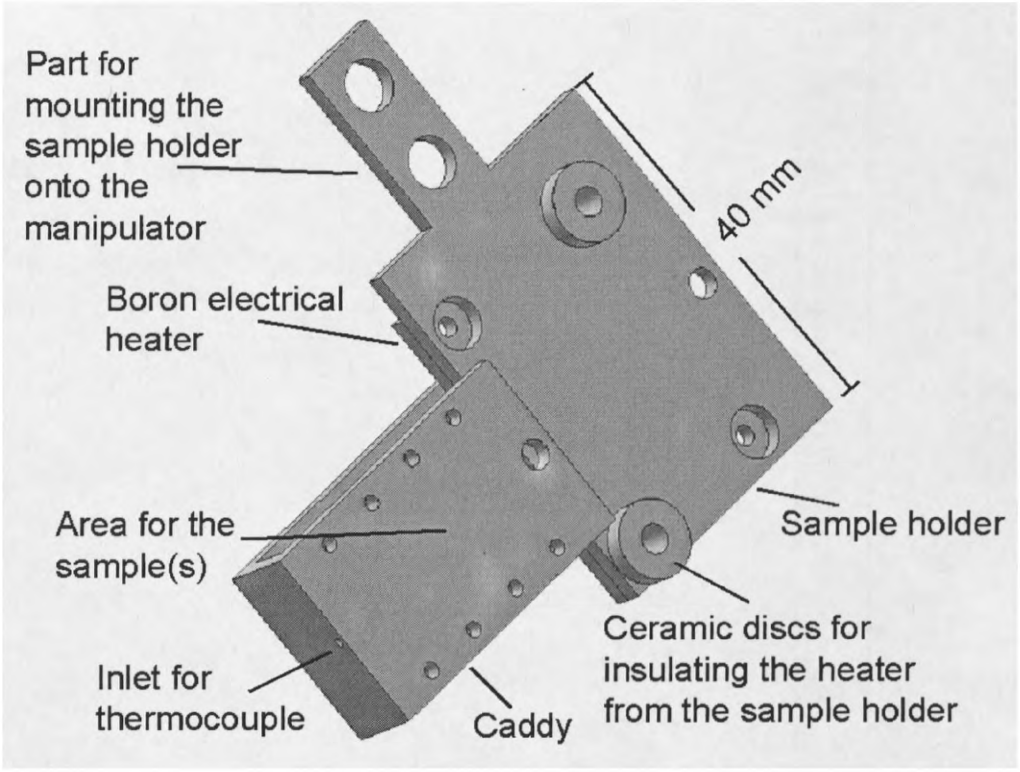

Fig. 2.14: Sample holder and caddy as used in the soft X-ray NEXAFS cell.

This setup was used at station 5U.1 at the CCLRC Daresbury Laboratory. The acquisition mode of the data was the total electron yield, due to the use of drain and collector current. The normal measurement geometry was with the sample surface 90° to the incident X-ray beam but spectra could also be gathered under different angles.

Due to carbon contamination of the beamline, and the used windows to separate the sample chamber from the beamline, the received C K-edge spectra had to be calibrated. To monitor the flux of photons reaching the sample, a gold foil was placed into the sample chamber. Before measuring the spectrum the foil was sputtered until no change in the C K-edge spectrum could be observed. This spectrum was then used to calibrate the sample spectrum, by either subtracting it or dividing it by a weighted gold foil spectrum. This calibration procedure did not have to be applied for the O K- and Ti L-edge.

2.1.4.7 Total reflection hard X-ray XAS of supported gold nanoparticles

For the model catalyst samples used in this work, the concentration of gold nanoparticles on TiO_2 single crystals is very low (below 1 monolayer on top of a 1 mm thick sample). Hence a standard transmission experiment to probe the gold cluster would give no detectable signal. To increase the signal, it is useful to use grazing incident of the beam so that the X-rays that hit the sample are reflected, increasing the possibility that the X-ray is inducing an electron absorption process. Furthermore, the background spectrum of the TiO_2 support is minimized since the sample is not fully illuminated.

The critical angle under which total reflection occurs in a specific material at a specific wavelength can be calculated using equation 2.6. [21]:

$$\gamma_c \approx \sqrt{2\sigma_c} = \lambda \cdot \sqrt{\frac{N_A r_0}{\pi} \cdot \sum_j \frac{\rho_j}{M_j}\left(Z_j + f_j'\right)}. \qquad 2.6$$

Where γ_c is the critical angle (in rad), σ_c the dispersive term of the complex refraction index, λ the wavelength, N_A the Avogadro constant, r_0 the Bohr radius, ρ_j the density of the material j, M_j the molar mass, Z_j the average number of electrons in the material per atom, and f_j' the correction factor for the material. The critical angle for TiO_2 is about 2 mrad or 0.1° at the Au L_{III} edge.

The beam heights can be calculated from the critical angle *via* the following fomula:

$$h = \frac{\sin(\gamma_c)}{\cos(\gamma_c)} * l \qquad 2.7$$

where h is the height of the beam, γ_c the calculated critical angle and l the length of the sample. Using 2.7, the beam height for a 10 mm long sample should be no higher than 20 μm for the Au L_{III}-edge (~ 12 keV).

The studies on the supported gold nanoparticles were conducted at station 9.3 of the CCLRC Daresbury Laboratory. The typical ring current was between 120 and 250 mA. The Au L_{III}-edge was chosen to test the grazing incident (0.1° to 1°) measurements on gold nanoparticles with different sizes on rutile(100) and (110) single crystals. The samples were put into the small dead volume cell (see construction part) and elevated with an Al-block. A small dome sealed with Kapton™ was used to enclose the sample in

the cell and the sample surface was elevated 0.5 mm into the dome. The use of a Be-window (K-Tek) was not possible since the window gave too much background noise.
Fig. 2.15 shows the schematic set-up of the experiment, with the X-ray beam coming out of the storage ring on the left, the fluorescence detector (12 elements) mounted vertically over the sample and the ionisation chambers for the initial intensity (I_0) and transmitted intensity (I_t) to the left and the right.

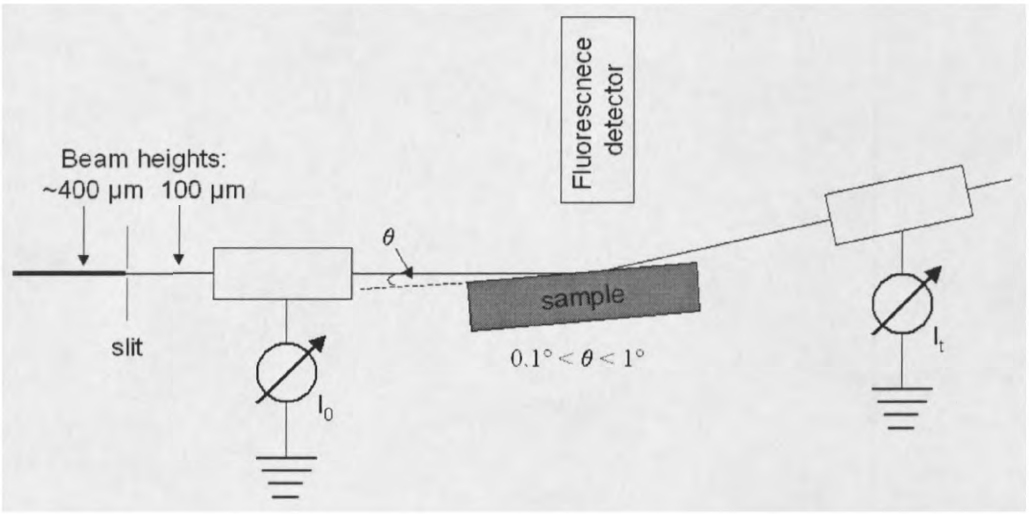

Fig 2.15: Schematic drawing of the grazing incident set-up used at station 9.3 of the CCLRC Daresbury Laboratory.

The beam height was reduced by the mirror system of station 9.3 down to 400 µm - which is the minimum height without losing unacceptable levels of signal. A further reduction of the beam heights to 100 µm was achieved by a slit in front of the I_0 chamber. This beam height illuminates not only the sample surface, but also the dome surface at the given angles. To only illuminate the sample surface, the beam would have to be even thinner. The beam heights needed for the given conditions can be calculated to 20 µm (see theoretical part). This is not practical since too much intensity would be cut off, and the X-ray beam will illuminate part of the chamber as well.

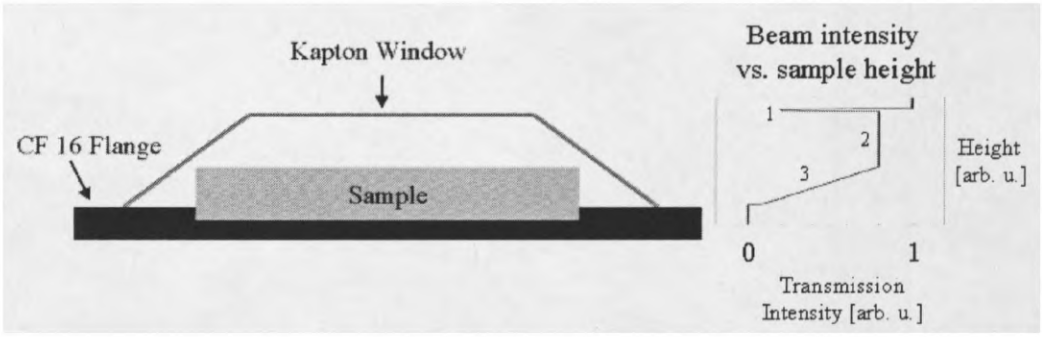

Fig 2.16: Schematic view of the sample underneath the dome for the *in situ* measurements. On the right hand side the principle graph of the beam intensity against the sample height is shown. At point 1 the beam penetrates the top of the Kapton™ window. At point 2 the beam moves through the window side until it hits the sample and gets slowly dampened by the sample (3).

The procedure described hereafter was found to be a simple, effective method to detect the sample signal. Nevertheless it can take a few hours before achieving a signal especially for the very diluted samples. The sample was first removed from the beam to give the total transmission intensity (see fig. 2.16 Intensity = 1). Moving the sample into the beam resulted in a sharp and quite strong drop in intensity as soon as the beam was at the height of the top of the Kapton Window. After passing the top, the intensity came back to roughly 80% as long as the beam was only passing through the Kapton foil at the front and back of the dome. Elevating the sample further resulted in a rather slow drop of the intensity when the beam was slowly penetrating the sample, until a full decay when the beam was totally in the sample or shadowed by the flange, which could not be specified.

In most cases it was found that the best S/N ratio for the Au L_{III} spectra was achieved when the sample was elevated into the beam so that the signal nearly vanished (~ 10%). Therefore this height was chosen as a starting height.

Afterwards the tilting angle was calibrated. The sample was rocked, and the maximum transmission was defined as 0 tilting. This means the sample was tilted about its

perpendicular axes to the beam. While tilting the angle a transmission diagram was captured.

Quick scans (about 15 min) over the edge (11900-11950 eV) were used to detect the fluorescence spectrum of the sample. The sample was tilted in 0.1° steps, and twisted in the positive direction (meaning the sample surface containing the nanoparticles) towards the beam. The best S/N ratio was determined by quick scans and the full spectra were gathered at this angle.

Taking roughly one hour-long scans and accumulating 8 to 20 spectra recorded the Au LIII-edge spectra. A scan time of one hour gave the opportunity to detect a spectrum, which allowed detecting failures, but did not give an acceptable S/N ratio.

In situ spectra were taken under static CO (Linde, 3.7) and static O_2 (Messer, 4.8) atmospheres. A MS monitored the purity of the atmosphere and the pressure (~1.5 bar) remained constant over the time of the experiment.

2.1.4.8 Decomposition of oxidised gold with hard X-ray absorption spectroscopy

Au L_{III}-edge measurements were performed at station 16.5 selecting the photon energy with a Si(220) mirror. The X-ray beam entered the chamber trough a Kapton™ window. The sample was mounted perpendicular to the beam and the X-ray absorption spectra were monitored with the collector and the drain current. Both currents were similar but the collector current gave the better S/N ratio.

After the electrochemical oxidation (see below) the samples were transported to the beamline and roughly 5x10 mm^2 pieces were mounted on the heating stage. It was possible to heat the samples with a BN heater and the gasses CO, O_2 and He could be dosed. A pressure of 1.5 bar was used in the air tight cell.

2.2 Atomic force microscopy

2.2.1 Background to AFM

Atomic force microscopy (AFM) uses a small tip to scan a sample and is therefore similar to scanning tunnelling microscopy (STM). The advantage of AFM is that no voltage between the sample and the tip is needed. However the resolution of an AFM is not atomic.

The general set up of an AFM is a laser, a probe and a photodiode array. The laser is reflected from the cantilever of the probe on to the photodiode, and can monitor structures in the Ångström region [22]. To scan the sample, it is moved by a *xyz* piezo crystal into position. Due to the difference in the sample structure, the cantilever is either bent to, or away from the sample and the laser is reflected at a different position on the photodiode array.

The probe itself is built up of three basic components (see fig. 2.17): The support, which is attached to the probe holder, a cantilever and the tip. The laser is focused on the upper side of the cantilever and is reflected from there via mirrors on the photodiode array. Due to the distance between cantilever and the first mirror, the movement of the cantilever is magnified by a large factor and thus small movements of the cantilever can be detected.

The cantilever is too thick to detect very small particles, hence a very small tip is mounted underneath the cantilever. The diameter of the tip is normally around 20 nm.

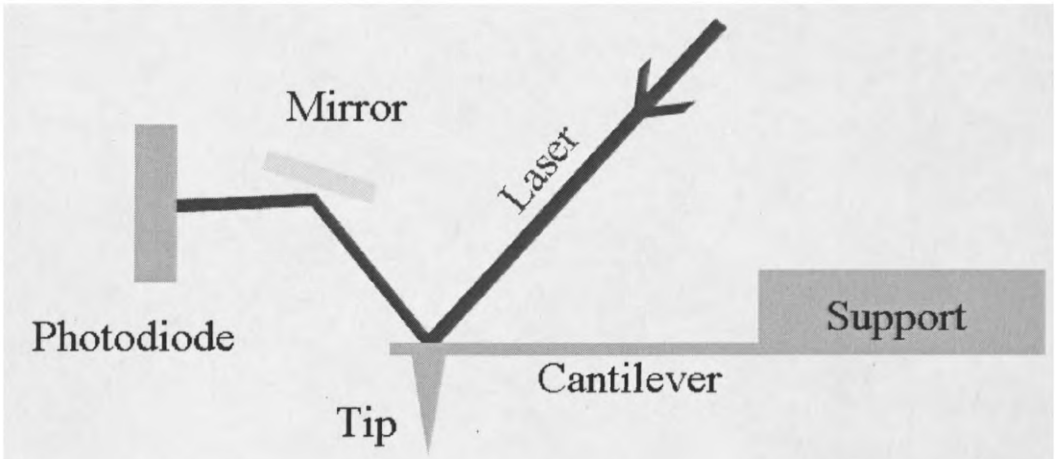

Fig. 2.17: Schematic layouts of an AFM probe.

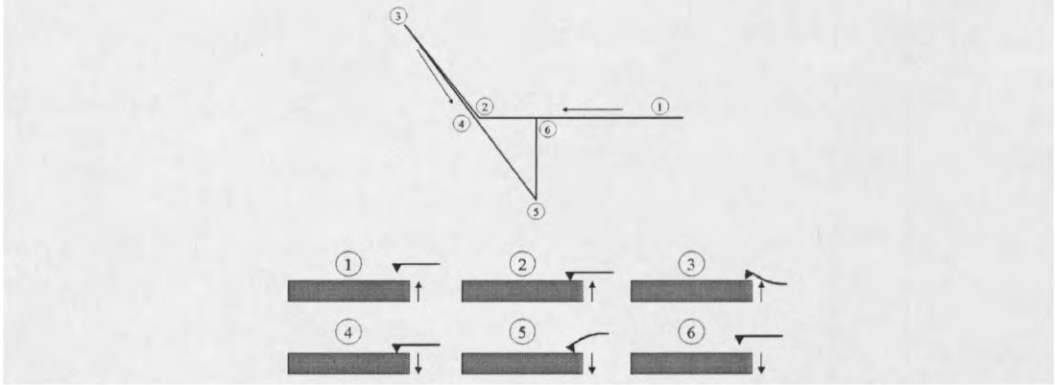

Fig. 2.18: Force mode of the AFM. 1) The surface approaches the tip, 2) The tip touches the surface, 3) The tip is repelled from the surface, 4) The tip is attached to the surface, 5) The tip is held by adhesion on the surface, 6) The tip is disengaged from the surface.

AFM probes the surface by the interaction between tip and surface; hence the tip has to be very close to the surface. When the tip engages the surface, changes in attraction between tip and surface occur. This interaction can be illustrated in a force scan, where the sample is moved up and down under the probe (see fig.2.18). First the tip is far from the surface (point 1). When the sample is moved towards the probe a point is reached where the tip hits the surface (point 2). As the sample is moved further, the tip is repelled

by the sample (point 3). Moving the sample away from the probe releases the repulsion until the tip is held on the surface by the adsorption forces only (point 4). The tip stays on the surface until the force applied to the probe is higher than the adsorption force (point 5) and the tip is released from the surface (point 6).

The most common scanning modes in AFM are: contact, non-contact and tapping mode. In contact mode the tip is "scratching" the surface. To avoid that the tip is being detached from the surface it is slightly forced onto the surface. Due to the small surface area of the tip, tremendous pressure is applied to the sample, and thus only hard samples can be used.

To understand the non-contact mode another step has to be added to the force curve. This is just before the tip hits the surface. At this point the Van-der-Waals interaction between tip and sample bend the cantilever towards to the surface. This can be used to monitor the surface structure without actually touching the surface of the sample. Otherwise it is pretty similar to contact mode, but it can be used for softer materials.

The tapping mode is, in principle, a combination of the non-contact and the force measurement. The cantilever is oscillating with its eigenfrequency. The influence of the adsorption force on the frequency is monitored, and regulated, so that the tip is not touching the surface. This technique enables height and amplitude profiles of the sample as well as a phase profile to be obtained. The phase profile is influenced by two different factors: the amplitude of the sample and the "properties" of the sample at the monitored position. The term "properties" is very broad and can be, for example, different materials (e.g. TiO_2 and Au) or different phases in a material (e.g. amorphous and crystalline structures).

2.2.2 Experimental settings for AFM

To collect AFM images a Veeco™ Nanoscope III in tapping mode was used. The tips used were Al-coated single cantilever tapping mode tips (Budget Sensors, Resonant Frequent: 300 kHz, Force Constant 40 N/m). A typical scan was done with an initial gain of 0.2, a proportional gain of 2.0, 512 lines/sample and a scan speed between 0.5 and 1

Hz. The scan range could be varied from 30 μm to 250 nm. At scan ranges less than 1 μm special care had to be taken to achieve a noise free image. The AFM was enclosed with a Plexiglas hood for the reduction of noise effects, and to have the option to maintain the sample under controlled conditions (N_2 atmosphere, BOC 2.2).

The samples with a TiO_2 single crystal could be placed directly under the tip. The gold and gold oxide foils were glued on carbon sticky tape (Agar), which was supported on AFM specimen disc (Agar).

2.3 Scanning electron microscopy

2.3.1 Background to SEM

SEM or scanning electron microscopy (cf. fig. 2.19) uses a focused electron beam, similar to a light microscope, to image a sample. The main advantage of SEM in comparison to light microscopy is the shorter wavelength of the electrons compared to visible light. Therefore much finer structures can be resolved than with a light microscope since the maximum resolution is the same as the wavelength of the probe to a first approximation.

The electrons that are needed for SEM are generated in the electron gun. Usually a filament (normally tungsten) is ionised to release the electrons. The filament is heated by applying a voltage to it, and an anode accelerates the emitted electrons in the direction of the sample (fig. 2.20).

The electron beam passing the anode is divergent and has to be focused on to the specimen, for this magnetic lenses are used. The field is shaped in a way that only electrons on the axis between the magnetic coils encounter a homogenous field from all sides (fig. 2.21). Electrons that are off-axis are forced into a spiral, and approach the axis by moving through the lenses. Finally the electrons will be focused and scanning coils fine-tune the electron beam for scanning the specimen *via* a raster.

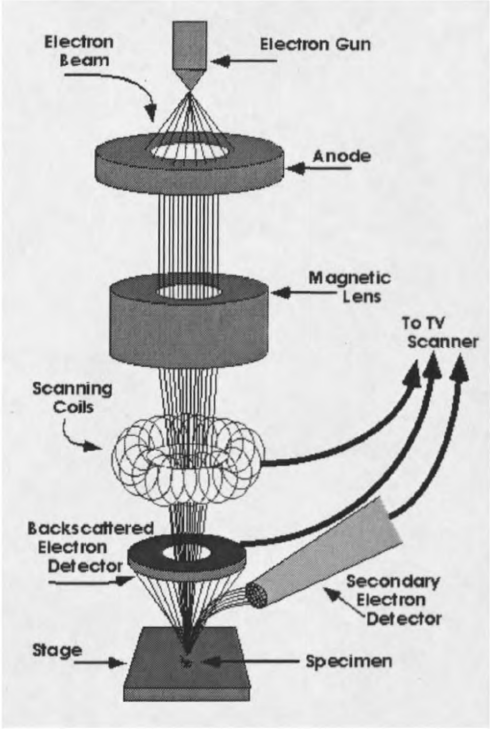

Fig. 2.19: Schematic set up of a scanning electron microscope [22a].

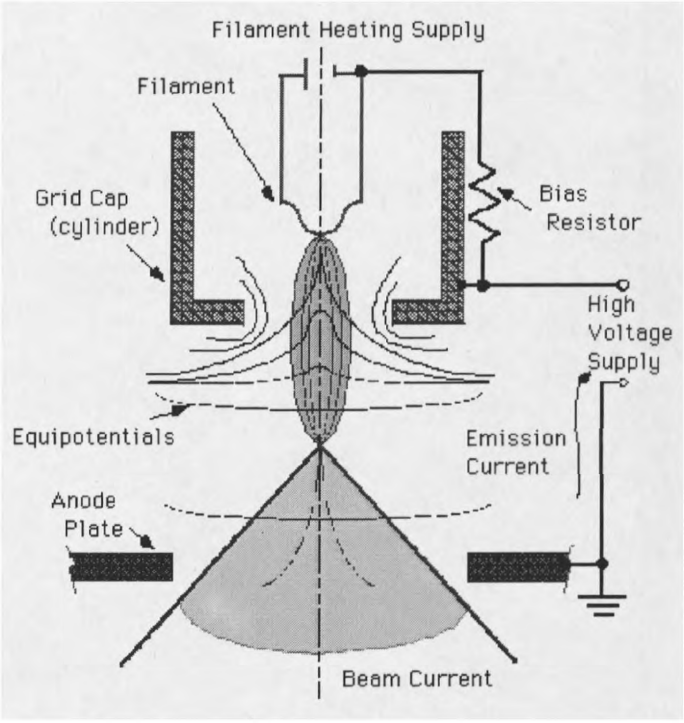

Fig. 2.20: Working principle of an electron gun [22a].

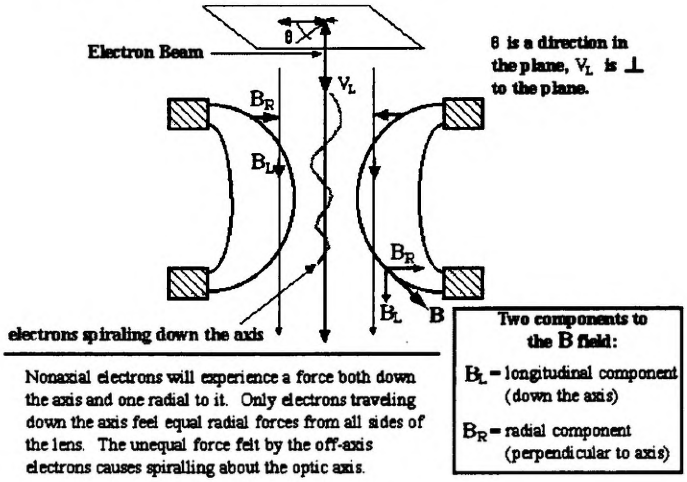

Fig. 2.21: Schema of the electron focusing in a SEM [22a].

The electrons hitting the specimen undergo two main events, either they transfer energy to the electrons of an atom, or they are backscattered (fig. 2.22). For the first case electrons can be ejected from the atom. These electrons are called secondary electrons. The other possibility is that the electron is backscattered by either the outer electron shell or the core of an atom in the specimen. The main difference between these two electrons is that the backscattered electrons have the same energy as they had before probing the sample, whereas the secondary electrons have a fraction of the initial electron energy.

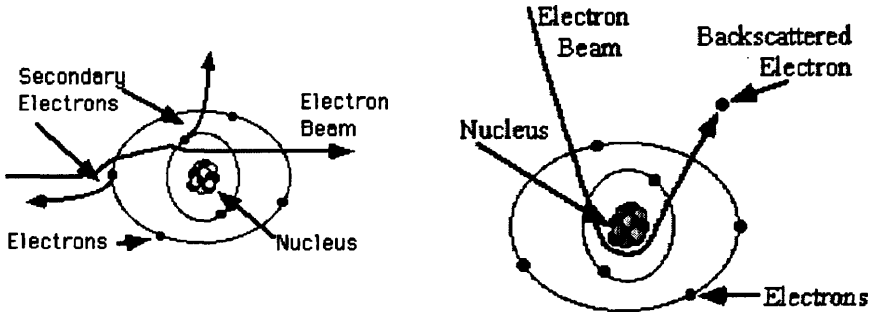

Fig. 2.22: Atomic model of the creation of secondary electrons (left) and the backscattering of an electron on an atom (right).

2.3.2 Experimental part to SEM

SEM images of the gold oxide foils and gold powder have been taken with a FEI Quanta 200 ESEM. The acceleration voltage of the electron beam was usually 30 keV and the high vacuum mode (~ 1×10^{-4} torr) has been used. The usual spot size of the electron beam was about 0.4 μm and secondary electron images are shown. For EDX measurements an EDAX Gensis analyser with an electron spot size of about 0.6 μm has been used. An ultra thin window had been used to separate the EDX from the SEM chamber.

To image the gold nanoparticles a FEI XL 30 ESEM FEG has been used. To reduce the charging effects on the sample the low vacuum mode had been used (~ 0.5 torr). Water

vapour (imaging gas) was dosed into the chamber. 30 keV was used as an acceleration voltage and secondary electrons were detected.

2.4 Electrochemistry

2.4.1 Background

A typical cyclic voltammogram (CV) obtained using a polycrystalline gold foil is shown in fig. 2.24. The electrochemical cell was a standard 3-electrode cell with an Ag/AgCl reference electrode (cf. fig. 2.23). The gold foil was oxidized in a 0.1 molar $HClO_4$ solution.

To understand the volatmmogram, the model of Peukert *et al.* [24] for the electrochemical oxidation of gold in acidic solution will be used (cf.. fig. 2.25). At low potentials (below 0.0 V vs. a standard hydrogen electrode (SHE) or –0.2 V vs. Ag/AgCl) water is the main adsorbate on the surface, and hydrogen is formed by proton diffusion to, and oxidation at the electrode. At potentials between 0.0 V and 1.3 V vs. SHE (-0.2 V and 1.1 V vs. Ag/AgCl) the main adsorbate is again water molecules, but no hydrogen formation takes place. This is equal to the formation of an electric double layer.

At a potential of 1.3 V and 1.5 V vs. SHE (1.1 V and 1.3 V Ag/AgCl) the adsorbed water molecules get oxidised and form a layer of adsorbed hydroxyl groups:

$$Au \cdot H_2O_{ad} \rightarrow AuOH_{ad} + H^+ + e^-. \qquad 2.8$$

At even higher potentials the gold is oxidised:

$$AuOH_{ad} + 2\ H_2O \rightarrow Au(OH)_3 + 2\ H^+ + 2e^-. \qquad 2.9$$

At first a monolayer of oxidised gold species is formed by the oxidation, and then multilayers of oxidised gold species are formed. The formation of other species than $Au(OH)_3$ is possible as well, and beside the formation of an hydroxydic state, an oxidic and an aqueous/hydrous state were postulated [25].

Decreasing the potential after oxidising the gold foil results in the reduction of the formed species at a potential of 1.1 vs. SHE or 0.9 vs. Ag/AgCl. The potential at which the oxidised gold species are reduced depends on the maximum oxidation potential. The higher the oxidation potential, the lower the potential required to reduce the oxidised

species [24]. This was again assigned to the formation of different oxidised gold species with different degrees of hydration.

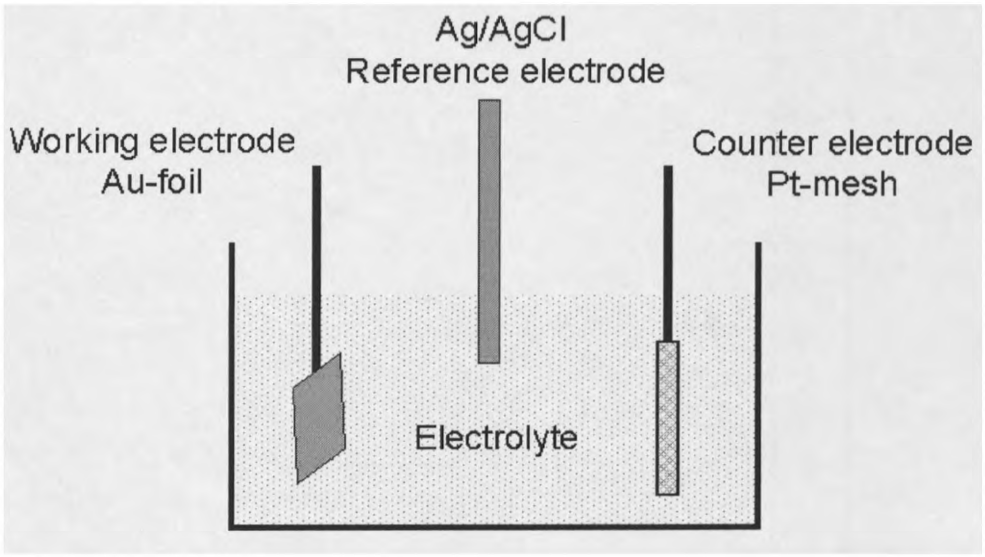

Fig. 2.23: Schematic set up of a simple electrochemical cell.

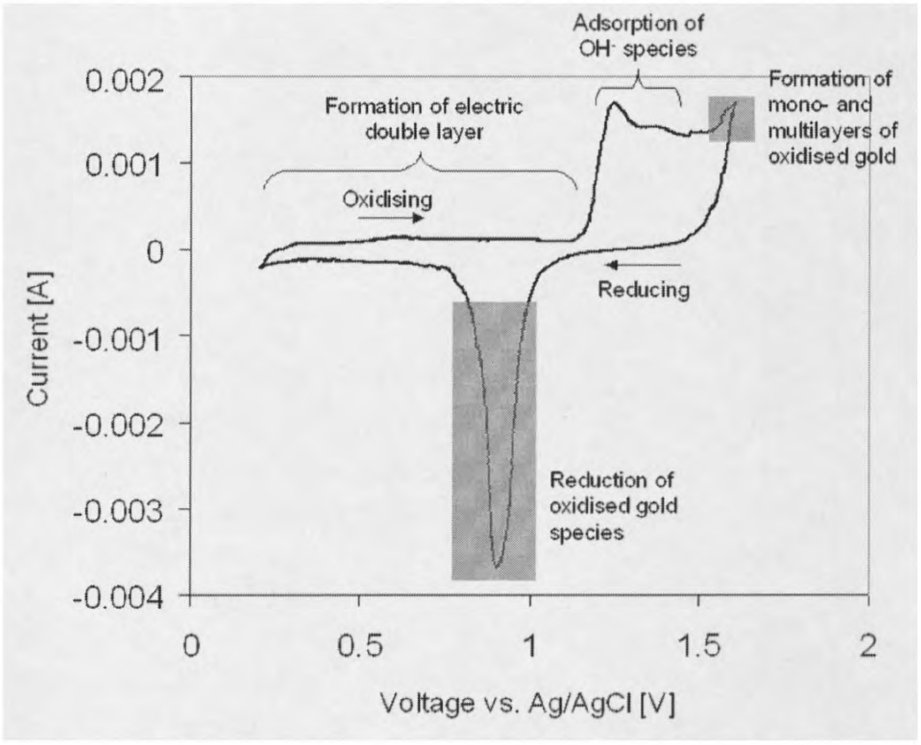

Fig. 2.24: Cyclic voltammogram of a gold foil in $HClO_4$ with a Ag/AgCl reference electrode.

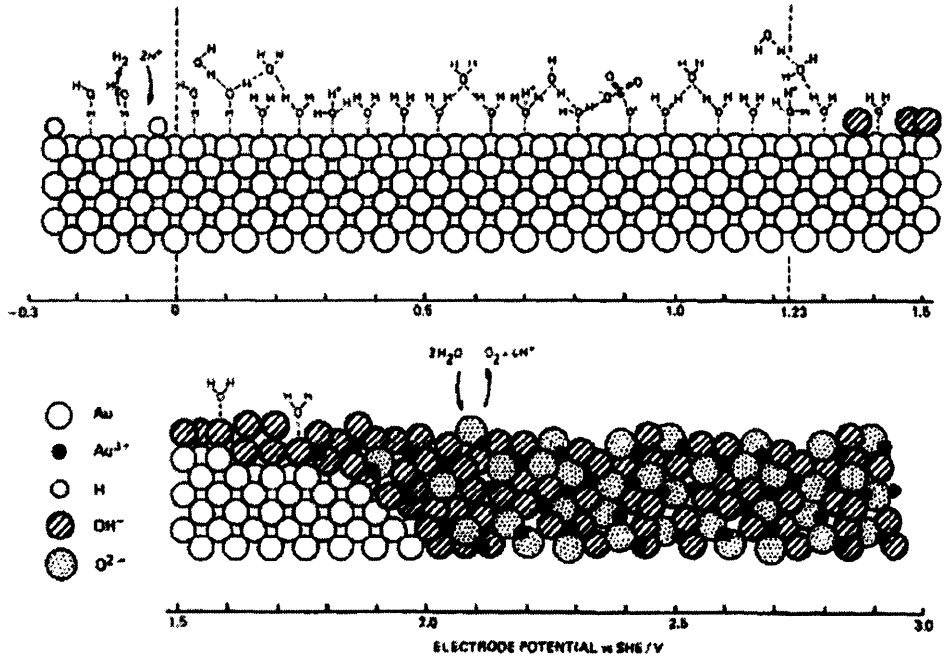

Fig. 2.25: Model for the surface composition of gold electrode in acid electrolyte as a function of applied potential; data shown vs. a standard hydrogen electrode (SHE) [24].

2.4.2 Preparation of electrochemical oxidized gold foil

The electrochemical oxidation was done as described below; D. Quin prepared initial samples for soft X-ray XAS studies.

All glassware, the gold foil and electrodes (with the exception of the counter electrode) were cleaned with concentrated HNO_3 prior to use and rinsed with deionized water. The deionized water was prepared with an ELGA PURELAB Option Q or ELGA UHQ and the resistance was 18.2 MΩ cm. Carbon contaminations were removed by UV light treatment. Storage times have been kept below one week.

The electrolyte solution was prepared by diluting 855 µl 70% perchloric acid (Merck, pro analysis, φ=1.68 g/ml) in a 50 ml graduated flask with deionized H_2O. The solution was not stored for more than one week.

Pt-Mesh was used as the counter electrode. The reference electrode was a Ag/AgCl (CH Instruments Inc.). For controlling the applied voltage an Amel 2051 Potentiostat was used, computer controlled via an Amel 7800 interface.

Before the electrochemical oxidation was started, cyclic voltammograms (CVs) were recorded as references. The settings for the CVs are shown in table 2.4.

Table 2.4: Electrochemical parameters for cyclic voltammograms (CV's).

Initial potential vs. Ag/AgCl [V]	0.2
Final potential vs. Ag/AgCl [V]	1.6
[mV/s]	50
Cycles	10 to 20
Resolution [Points/s]	50

After recording the CVs the electro-chemical oxidation was started. The settings for the oxidation depended on the desired thickness of the gold oxide layer.

2.5 Spin Coating

2.5.1 General overview

The spin coating process has been used since the 1920s to prepare thin layers on flat surfaces. Applications range from producing thin films of paint or vanish [26] to the production of the phosphoric layer in colour televisions [27] and, more recently, in producing the protecting layer on CDs and DVDs [28]. It is also used in computer chip production to prepare the photo resisting layer on the silicon-wafers. It was also shown in the literature that catalytically active materials can be prepared on flat supports by spin coating [29 - 31].

For the spin coating process, normally a rotating disk – know as chuck - is used with speeds between 500 and 6000 RPM. On the chuck, a flat substrate made out of any material that is neither rough, nor porous, can be fixed with a vacuum of about 20 mbar – the substrate is often called wafer. To apply the vacuum to the substrate different types of chucks are available. The simplest variation comprises of a hole in the middle of the chuck through which the vacuum is applied onto the substrate.

At the start, a small amount of the solution that contains the salt or polymer, which is supposed to build up the film, is brought onto the wafer. This can be done either with a non-rotating wafer, as was done in this study and in [32] among others, or with the disk rotating slowly as done e.g. by Lai [33]. With the start of the spinning process, a great amount of solution is spread off the wafer by centrifugal forces while the remaining amount wets the surface of the wafer. When the first fluid film is established the film thins further, but slower and much more homogenously than in the beginning. At this stage the resulting film gets its homogeneity. The thinning can be observed by the colour change of the wafer surface.

The thinning by centrifugal forces gets slower with time, and a second effect starts to dominate, the evaporation of the solvent. Due to solvent evaporation the solution gets more and more concentrated and the solvate, which builds up the solid film, precipitates.

To describe the physics of the spin coating process, it is useful to divide it into four different stages with different behaviour (deposition, spin-up, spin-off, evaporation) [34]

(see also table 2.5). Birnie and Manley [35] investigated the last three stages via optical interference and showed that initially, the kinematic viscosity has the biggest influence on the thinning processes, where as at the end, solvent volatility is dominant. The time taken for the film to thin varies (for organic solvents) between 1 s and 15 s for a spinning speed of 2000 RPM. The "thinning time" (for pure solvents) depends on the viscosity and the vapour pressure of the solvent.

Table 2.5: The four stages of spin coating.

Deposition	The solution is brought onto the wafer.
Spin-up	A lot of solution is spread off the wafer by centrifugal force.
Spin-off	The film thins by centrifugal forces.
Evaporation	The film thins by evaporation of the solvent.

There are a huge number of parameters that influence the resulting film. This is reflected by the quantity of literature, which is enormous for this theme. An overview of the most important effects and a short comparison of the literature are given in table 2.6.

It was also shown that the first two stages of the spin coating process (deposition and spin-up) [36] have little effect on the final film thickness. This is important with simplifying mathematic models describing the spin coating process. One can predict that the acceleration of the spin coater, as well as the amount of solution and how it is brought onto the wafer, is essentially insignificant for the thickness of the final film. But these two parameters can influence the homogeneity and defects of the film.

Table 2.6: Parameters for the spin coating and their effects.

Effect	Parameter
Thickness of the film	The main parameters are the concentration of the solvate [33, 37], the spinning speed [33, 37] and, less importantly, the solvent pressure in the atmosphere [38]
Film homogeneity	The spinning speed, the amount and the procedure of placing the solution on the wafer [36], the flow-behaviour of the solution

	and the evaporation rate of the solvent (see also defects) have the main influence on film homogeneity.
Defects	
Bénard cells	When the surface of the substrate is not homogenous (in terms of surface tension) Bénard cells can appear [39].
Radial striations	Evaporation of the solvent too quickly can result in this defect [35, 40] (see also Marangoni effect [41]).
Chuck-marks	These are induced by the chuck/substrate interface (The materials of the chuck and substrate are important for this defect) [42, 43].
Craters	Foreign substances on the surface of the wafer can built-up craters [39].

2.5.2 Theory about the spin coating process

Emslie and co-workers [27] undertook the first theoretical approach on the physical problem of "spin coating" in 1958. According to the separation drawn under point 2.5.1 they had only investigated the spin-off stage. They showed that a solution placed on a disk, which rotates round its vertical axis, gets thinner and more homogenous (if the solution is Newtonian) with time. Meyerhofer [44] then rewrote the formula given by Emslie and co-workers to:

$$h = h_0\left[1+\left(\frac{4\omega^2}{3\nu}\right)h_0^2 t\right]^{-1/2} \qquad 2.10$$

This formula shows that the height of the film over the wafer (h) depends on the time t of the spin coating process. So for t=0 the film has the initial height (h_0). If t is not equal to zero then the denominator is larger then 1 and the height (h) decreases. The speed with which h decreases depends on one spin coating parameter, the spinning speed (ω), and on one solution parameter, the kinematic viscosity (ν). The kinematic viscosity is defined by the viscosity of the liquid divided by its density ($\nu=\eta/\rho$).

But there is one great failing, namely the missing consideration of solvent evaporation. Without the evaporation, the concentration of the solution would not increase and the solvate would not precipitate to build up a solid film. Meyerhofer was the first to consider the evaporation. His assumption was quite simple, that the evaporation of the solvent is independent of the thinning by the centrifugal force. Therefore he added an evaporation constant (Φ) and derived the following formula:

$$h_f = c_0 \left(\frac{\Phi}{2(1-c_0)\frac{\rho\omega^2}{3\eta}} \right)^{1/3} \quad \text{, with } \Phi = C\omega^{\alpha}. \qquad 2.11$$

In comparison to formula 2.10 the initial film height (h_0) is replaced by the initial solvate concentration (c_0). Furthermore the final film height (h_f) depends on the evaporation rate Φ. The evaporation rate Φ has an exponential dependence α. This dependency is ½ for pure solvents and inorganic salt solutions and 0 for polymers [31]. This is due to the different evaporation behaviour of those solutions. The evaporation of a polymer solution is influenced by the mass transport of the solvent in the solution, and not by the spinning speed [31]. For the pure solution and the inorganic salt solution, the mass transport of the solvent from the solution into the gas phase, and its transport into the air, is the dominating influences on the evaporation [31]. Therefore, the dependency of the spinning speed of the final film height differs for the two different solutions. After insertion of the dependencies on the evaporation into formula 2.11 one gets, for the dependency of the final film height for the polymer solution:

$$h_f \propto \omega^{-2/3} \qquad 2.12$$

and for pure and salt solution the dependency:

$$h_f \propto \omega^{-1/2}. \qquad 2.13$$

An air stream enforces the evaporation over the disk due to its rotation. The air stream constantly transports "fresh" air over the liquid surface and thereby forces evaporation by moving the solvent away from the liquid-gas interface. This stream is named after its first investigator von Kármán [45] (see fig. 2.26).

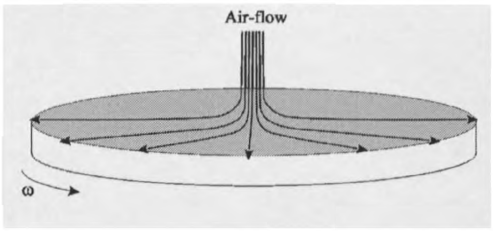

Fig. 2.26: Von Kármán flow of the air over the rotating disk.

2.5.3 Gold cluster formation on supports

The formation and adsorption of the gold clusters on the support is very important for the catalytic activity. This topic is just starting to be understood. The part that is well known is the behaviour of the often used gold acid ($HAuCl_4$ * n H_2O) [46 - 49] but some discrepancies for some species at specific pH values are still present. The recent work of Moreau *et al.* [46] will be cited and a figure regarding the changes of the gold complex at different pH is adopted in fig. 2.27. At pH 0 to 2 the $AuCl_4^-$ anion is mainly present. With increasing pH, hydroxyl and hydrate groups replace the Chlorine atoms sequentially until, at a pH of 10 to 11, only $Au(OH)_4^-$ ions are present. The replacement of the Chlorine atoms with OH^- or H_2O is essential, since Chlorine is a well known catalyst poison and its presence on the catalyst should be prevented [50, 51].

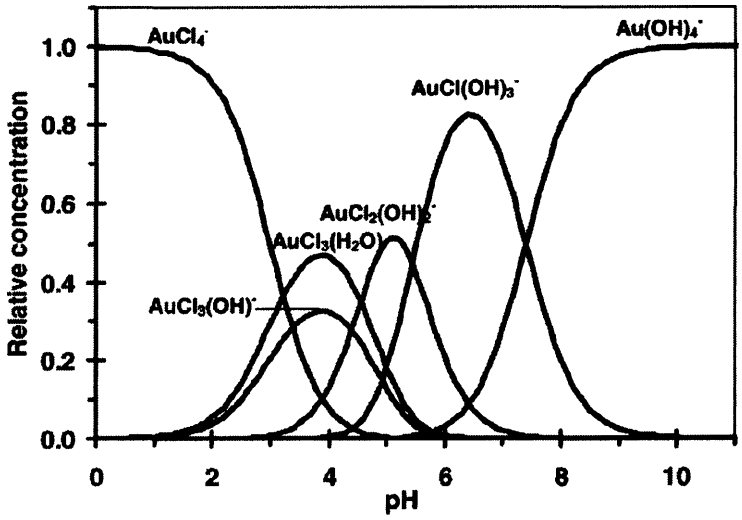

Fig. 2.27: pH dependence of the relative equilibrium concentration of gold complexes (from [46]).

After dissolving the gold acid, the formed nanoparticles have to be adsorbed on the support. If TiO_2 is used, the main attraction between the gold complexes and the support will be electrostatic [46]. Since all gold complexes are negatively charged, the support should have a positive charge, but the isoelectric point for TiO_2 is between 4.5 and 6.3 [52]. This leads to the problem that the pH for the gold cluster should be much higher to prevent the deposition of Chlorine on the catalyst. Higher pH e.g. 9 and above can be used, but the loading of the gold on the catalyst is not complete [46]. Moreau *et al.* also reported that at lower pH the loading of gold is essentially quantitative on the support, but catalyst performance is poor in comparison to catalysts prepared at higher pH.
The partial adsorption of the gold complexes on the negatively charged support at high pH has been explained by an equilibrium of gold complexes binding to the surface by hydratisation [46]. The gold complexes are, therefore, not irreversibly attached to the surface and can be re-dissolved.

In general, the spin coating process can be compared with the impregnation technique for the preparation of catalysts on porous materials. But impregnation gives, in the case of

gold catalysts, poor results, due to the fact that the gold particles are often too large and contaminated with chlorine atoms. To avoid this, two factors are important: Firstly and most importantly, a high pH of 9 or 10 is used for the solution, so that exclusively, or nearly, all gold atoms present in the solution are hydroxilated and do not have any chlorine ligands. Secondly the solution needs to be of very low concentration, so that the formed gold clusters cannot interact with each other, and therefore do not form bigger aggregates. The low concentration is also important to wash off HCl in the spin up and spin off process.

Therefore, the different steps of deposition precipitation and spin coating with low concentrated solutions can be compared (cf. fig. 2.28). Firstly, the support and the solution are brought together, either by adding the support to the stirred solution for powder catalysts or by dropping the solution on the support. In both cases the gold clusters will adsorb on the support, which is even increased by stirring the solution for some time in the case of powder catalysts. After adsorption, the powder catalyst is filtrated, which is similar to the spin up and spin off phase of the spin coating. In both cases the gold particles are washed with large quantities of solvent, and chlorine ions are eliminated from the catalyst. In the case of the flat support this is done by the very low concentration, so that the amount of chlorine solved in the solution is negligible.

Finally the catalyst needs to be dried. This is done by heating the powder catalysts to about 80°C, or in the evaporation phase of the spin coating process. A small difference exists in this step between the two techniques, since gold clusters that are still present in the solution are forced onto the support in the case of spin coating. This is an effect that is not present when preparing powder catalysts with precipitation-deposition.

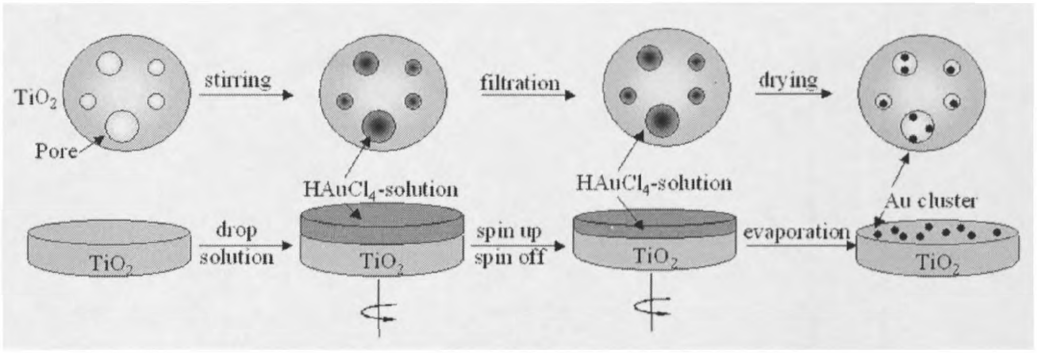

Fig 2.28: Comparison of the preparation of a catalyst with deposition-precipitation and spin coating with highly diluted solution.

2.5.4 Experimental, spin coating

Gold nanoparticles on TiO_2 single crystals (Crystal GmbH) were prepared by spin coating of a highly diluted $HAuCl_4$ solution onto the single crystals. The TiO_2 crystals were cleaned by rubbing them with a tissue and ethyl acetate, acetone and ethanol followed by an ultra sonic bath for 10 min in each solvent. In between each ultra sonic bath, the TiO_2 crystals were rinsed with distilled water (R ~ 18.2 MΩ cm, organic contaminations were removed by UV light treatment in the deionised water supply). Before the spin coating, the single crystal was irradiated with UV light (Ealing, 150 Xe/200 Hg light) for about 30 minutes and used directly afterwards.

A tetrachloro auroric acid solution ($HAuCl_4$) was obtained by dissolving 69.0 mg $HAuCl_4 \cdot H_2O$ (Sigmal Aldrich, ACS Reagent®) in 10 ml distilled water (R ~ 18.2 MΩ cm). This stock solution was then further diluted before the spin coating to the concentration indicated for the different samples, and was in the range between 2 mmol/l and 0.09 mmol/l. As for wet impregnation, a pH of ~9 was achieved by adding a few µl of concentrated NH_3 (BDH, AnalaR®) to the diluted solution. After a maximum of 90 s, the solution was added drop-wise onto the single crystal, and the spin coating was started (speed: 5000 rpm, acceleration: 5000 rpm/s, length: 120 s).

References

[1] Briggs, D.; Seah, M. P.; *Practical Surface Analysis*, John Wiley and Sons, **1983**.

[2] Jablonski, A.; Powell, C. J.; Surface Science Reports, **2002**, *47*, 33-91.

[3] Citrin, P. H.; Wertheim, G. K.; Baer, Y.; Physical Review Letters; **1978**, *41*, 1425-1428.

[4] Zhang, Peng; Sham, T. K.; Physical Review Letters, **2003**, *90*, 245502/1-245502/4.

[5] Widdra, W.; Brocker, D.; Giessel, T.; Hertel, I. V.; Kruger, W.; Liero, A.; Noack, F.; Petrov, V.; Pop, D.; Schmidt, P. M.; Weber, R.; Will, I.; Winter, B.; Surface Science, **2003**, *543*, 87-94.

[6] Kim, K. S.; Winograd, N.; Chemical Physics Letters, **1975**, *30*, 91-95.

[7] Egelhoff, W. F., Jr.; Journal of Vacuum Science and Technology, **1982**, *20*, 668-670.

[8] Wertheim, G. K.; DiCenzo, S. B.; Youngquist, S. E.; Physical Review Letters, **1983**, *51*, 2310-2313.

[9] Liang, K. S.; Salaneck, W. R.; Aksay, I. A.; Solid State Communications, **1976**, *19*, 329-334.

[10] Mason, M. G.; Physical Review B: Condensed Matter and Materials Physics, **1983**, *27*, 748-762.

[11] Zhang, L.; Persaud, R.; Madey, T. E.; Physical Review B: Condensed Matter, **1997**, *56*, 10549-10557.

[12] Lee, S.; Fan, C.; Wu, T.; Anderson, S. L.; Surface Science, **2005**, *578*, 5-19.

[13] Lee, S.; Fan, C.; Wu, T.; Anderson, S. L.; Journal of Physical Chemistry B, **2005**, *109*, 11340-11347.

[14] Mårtensson, N.; Nilsson, A.; Journal of Electron Spectroscopy and Related Phenomena, **1995**, *75*, 209-223.

[15] Stöhr, J.; *NEXAFS Spectroscopy*, Springer-Verlag, **1992**.

[16] Muramatsu, Y.; Ueno, Y.; Hayashi, T.; Grush, M. M.; Gullikson, E. M.; Perera, R. C. C.; Journal of Electron Spectroscopy and Related Phenomena, **2000**, *107*, 177-184.

[17] Shimada, H.; Imamura, M.; Matsubayashi, N.; Saito, T.; Tanaka, T.; Hayakawa, T.; Kure, S.; Topics in Catalysis; **2000**, *10*, 265-271.

[18] Coffman, F. L.; Cao, R.; Pianetta, P. A.; Kapoor, S.; Kelly, M.; Terminello, L. J.; Applied Physics Letters; **1996**, *69*, 568-570.

[19]: Booth, A. M.; Braun, S.; *et al.*; in preparation

[20] Booth, A. M.; *Dissertation*, The University of Manchester, **submitted 2007**.

[21] Weisbrod, U.; Gutschke, R.; Knoth, J.; Schwenke, H.; Applied Physics A: Solids and Surfaces, **1991**, *A53*, 449-456.

[22] *MultiMode™ SPM Intruction Manual*, Digital Instruments, **1996-1997**.

[22a]: http://www.mse.iastate.edu/microscopy/home.html.

[23] Hamann, C. H.; Vielstich, W,; *Elektrochemie*, Wiley-VCH, 3. Auflage, **1998**.

[24] Peuckert, M.; Coenen, F. P.; Bonzel, H. P.; Surface Science, **1984**, *141*, 515-532.

[25] Weiher, N.; *Combined in situ and ex situ Studies of an Electrochemical Interface – Investigation of Anodic Oxide Layers on Gold*, Dissertation, Freie Univerität Berlin, **2003**.

[26] Walker, P. H.; Thompson, J. G.; Proc. Am. Soc. Testing Materials, **1922**, *22 Part II*, 464.

[27] Emslie, A. G.; Bonner, F. T.; Peck, L.G.; Journal of Applied Physics, **1958**, *29*, 858-862.

[28] http://www.heise.de/newsticker/data/hag-12.03.03-000/

[29] Niemantsverdriet, J. W.; Engelen, A. F. P.; de Jong, A. M.; Wieldraaijer, W.; Kramer, G. J.; Appl. Surf. Sci., **1999**, *144-145*, 366-374.

[30] Muijsers, J. C.; Weber, Th.; van Hardeveld, R. M.; Zandbergen, H. W.; Niemantsverdriet, J. W.; Journal of Catalysis, **1995**, *157*, 698-705.

[31] van Hardeveld, R. M.; Gunter, P. L. J.; van IJzendoorn, L. J.; Wieldraaijer, W.; Kuipers, E. W.; Niemantsverdriet, J. W.; Applied Surface Science **1995**, *84*, 339-346.

[32] Kuipers, E. W.; Laszlo, C; Wieldraaijer, W.; Catalysis Letters, **1993**, *17*, 71-79.

[33] Lai, J. H.; Polymer Engineering and Science, **1979**, *19*, 1117-1121.

[34] Bornside, D. E.; Macosko, C. W.; Scriven, L. E.; J. Imag. Tech., **1987**, *13*, 122-130.

[35] Brinie III, D. P.; Manley, M.; Phys. Fluids, **1997**, *9*, 870-875.

[36] Daughton, W. J.; Givens, F. L.; J. Electrochem. Soc., **1982**, *129*, 173-179.

[37] Damon, G. F.; Applied Spectroscopy, **1972**, *26*, 36-43.

[38] Chen, B. T., Polymer Engineering and science **1983**, *23*, 399-403.

[39] Hansen, C. M.; Pierce, P. E.; Ind. Eng. Chem. Prod. Res. Develop., **1974**, *13*, 218-225.

[40] Du, X. M.; Orignac, X.; Almeida, R. M.; J. Am. Ceram. Soc., **1995**, *78*, 2254-2256.

[41] Scriven, L. E.; Sternling, C. V.; Nature, **1960**, *187*, 186-188.

[42] Birnie III, D. P.; Zelinski, B. J. J.; Marvel, S. P.; Melpolder, S. M; Roncone, R. L.; Opt.

[43] Birnie III, D. P.; Zelinski, B. J. J.; Perry, D. L.; Opt. Eng., **1995**, *34*, 1782-1788.

[44] Meyerhofer, D; Journal of Applied Physics, **1978**, *49*, 3993-3997.

[45] von Kármán, Zeitschrift für Angewandte Mathematik Mech., **1921**, *1*, 244.

[46] Moreau, F.; Bond, G. C.; Taylor, A. O.; Journal of Catalysis, **2005**, *231*, 105-114.

[47] Murphy, P. J.; LaGrange, M. S.; Geochimica et Cosmochimica Acta, **1998**, *62*, 3515-3526.

[48] Murphy, P. J.; Stevens, G.; LaGrange, M. S.; Geochimica et Cosmochimica Acta, **2000**, *64*, 479-494.

[49] Grisel, R. J. H.; Kooyman, P. J.; Nieuwenhuys, B. E.; Journal of Catalysis; **2000**, *191*, 430-437.

[50] Soares, J. M. C.; Hall, M.; Cristofolini, M.; Bowker, M.; Catalysis Letters, **2006**, *109*, 103-108.

[51] Yang, J. H.; Henao, J. D.; Costello, C.; Kung, M. C.; Kung, H. H.; Miller, J. T.; Kropf, A. J.; Kim, J. G.; Regalbuto, J. R.; Bore, M. T.; Pham, H. N.; Datye, A. K.; Laeger, J. D.; Kharas, K.; Applied Catalysis, A: General, **2005**, *291*. 73-84.

[52] Kosmulski, M.; Journal of Colloid and Interface Science, **2004**, *275*, 214-224.

3 Small volume cell for *in situ* measurements of flat samples

3.1 Abstract

This chapter describes the design and construction of a small dead volume reactor for the *in situ* spectroscopic characterisation of flat model catalysts. The reactor permits control of environmental conditions, including pressures from 100 mbar to several bars, and temperatures ranging from room temperature to approximately 150°C. *In situ* XAS and Raman spectroscopy have been performed to demonstrate the possibilities of the reactor when studying planar gold model catalysts.

3.2 Introduction

To study heterogeneous (gas/solid) catalytic reactions, it is necessary to gain molecular-level knowledge about the components involved in the reaction. These include, e.g., the catalyst itself, the reacting gas molecules, their adsorption and reaction on the catalyst, transition states and any reaction intermediates. This characterisation is best performed *in situ*, i.e., under reaction conditions, allowing experimentally determined information to be correlated to behaviour under practical conditions. Many different reactors for *in situ* studies of powder catalysts have previously been reported in the literature [1 - 15]. The techniques used for *in situ* probing have most prominently included X-ray diffraction (XRD), X-ray absorption fine structure (XAFS) and Fourier transform infrared spectroscopy (FTIR). The wide range of differences between previous designs is because it is effectively impossible to create a 'perfect' reactor, which is suitable for all types of gas/surface systems, reaction conditions and spectroscopic techniques. In the literature, the material used for the construction of the reactor has been quartz, metals or alloys. The former has the advantage of inertness for most gases and reactions, whereas the latter are more robust and, therefore, easier to handle. Some of the metal reactor vessels are

aluminium or different types of steel. Aluminium is a metal very simple to machine. It has a relatively low melting point, and therefore cannot be used when high temperatures (above 800 K) are required in the reactor. Stainless steel and other forms of steel have higher melting points than aluminium but the small amounts of other metals beside iron in these steels can be dissolve during the reaction. This can lead to the transport of catalytically active metals on to the catalyst, leading to a misinterpretation of the catalytic activity of the catalyst.

The window material used in cells for most spectroscopic investigations must be sufficiently transmitting in the energy region of the photons used. Quartz glass can be used when techniques utilise the UV and visible light region (~ 200 nm - 800 nm) such as light microscopy, Raman scattering, UV/visible spectroscopy, etc. It can also be used as the building material for view ports in UHV experiments, due to its good vacuum and overpressure stability. Quartz glass can also be heated to reasonable temperatures (~ 1300 K). For hard X-rays, either beryllium, or a polymer like Kapton™, is used. Beryllium has the advantage of being more pressure resistant compared to the polymers and will not deform during under- or overpressure. It is also possible to heat beryllium to higher temperatures (~ 1300 K) [16] than the polymers (~ 500 K). Beryllium however has the disadvantage of being highly toxic, and when it ruptures it often becomes a powder that can contaminate a wide area.

The gases, which are dosed during the *in situ* studies, must not damage the windows. Furthermore the geometric requirements for the positioning of the photon source, the sample and the detector have to be addressed when incorporating windows into the *in situ* cell. For example, in transmission XAFS the X-rays have to pass through the sample and the cell horizontally, as this is the geometry of virtually all X-ray sources suitable for XAFS [17]. In contrast, XRD measurements and fluorescence yield XAFS measurements usually utilise the same window for the incoming beam and the detected signal, requiring a larger window.

The cell design is also dependent on the conditions that the samples are to be studied under, e.g. pressure and temperature. Whereas most surface science techniques are designed for use under vacuum, industrial catalytic processes are conducted at several bars and, usually, at hundreds of °C. Therefore, a pressure and temperature range, under

which the experiments should be conducted, has to be defined and the design of the cell has to address these specifications. For example, polymers often cannot be heated to higher than 200°C without being damaged or decomposing.

Reaction rates are most commonly observed by analysing the gas mixture after it has flown over/through the catalyst. Either mass spectrometry (MS) or gas chromatography (GC) is used in most existing *in situ* cell designs. For single crystal catalysts the detection of the reaction products is a considerable problem in comparison to powder-based catalysts. This is due to the small surface area present in flat model catalysts (10^{-2} m^2) in comparison to powder catalysts (10^0 to 10^3 m^2/g). This leads to the production of small amounts of reaction products. Therefore very low flow rates (µl/min) are needed when studying single crystal catalysts, which cannot be achieved with common mass flow controllers. The low flow rates predict that the dead volume of the cell must be very small as well; otherwise a very long response time will be present.

Some attempts to study the reaction rates over small surface area catalysts in the mbar pressure range have been reported in the literature [18, 19]. Johansson *et al.* [18] constructed a reactor made from Pyrex (cf. fig. 3.1). The sample is pumped over a leak valve into a MS and a non-sealing Pyrex connection to an evacuated quartz tube. The reaction gas is applied over a capillary that is connected to the main stream of gas. This set up allows a flow rate of about 1.7 µl/s with the sample being at atmospheric pressure. However, this reactor does not allow simultaneous *in situ* spectroscopic studies.

Recently, Zhao *et al.* [19] presented a flow reactor that is capable of testing the catalytic activity of a flat catalyst and to perform *in situ* studies with IR spectroscopy (cf. fig. 3.2). The flow reactor for the flat samples is connected to a UHV system in which the samples can be prepared. In the measurement position the sample is sealed from the UHV system with Viton O-rings, which are differentially pumped. The gas is supplied *via* calibrated capillaries and the cell is connected to a MS and a pumping stage. The pressure of the gas supplying system regulates the flow rate in the cell. A KBr window is fitted on the cell to allow infrared spectroscopy.

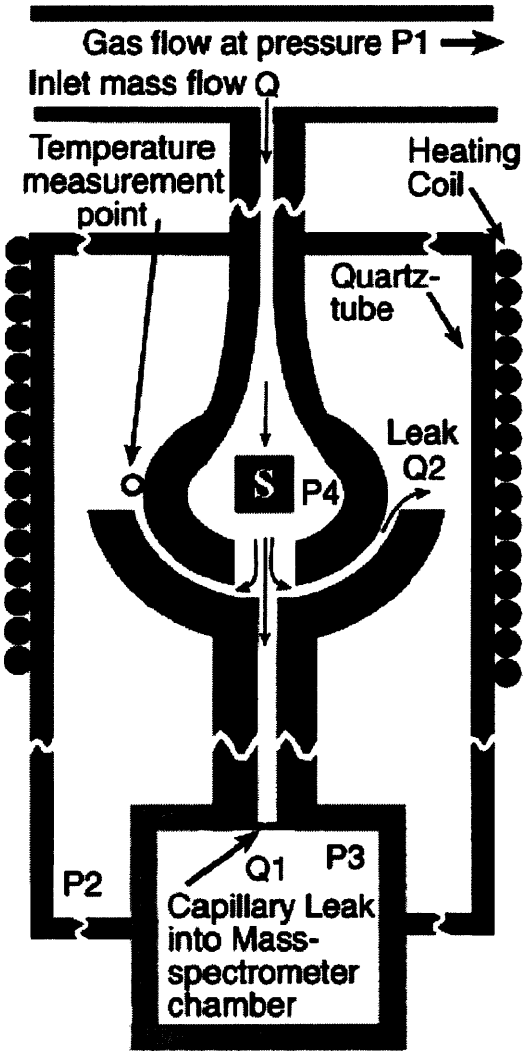

Fig. 3.1: Reactor design of Johansson *et al.* [18]. The model catalysts (S) are placed in the middle of the reactor and the different pressures (P1 - P4) in the reactor are indicated.

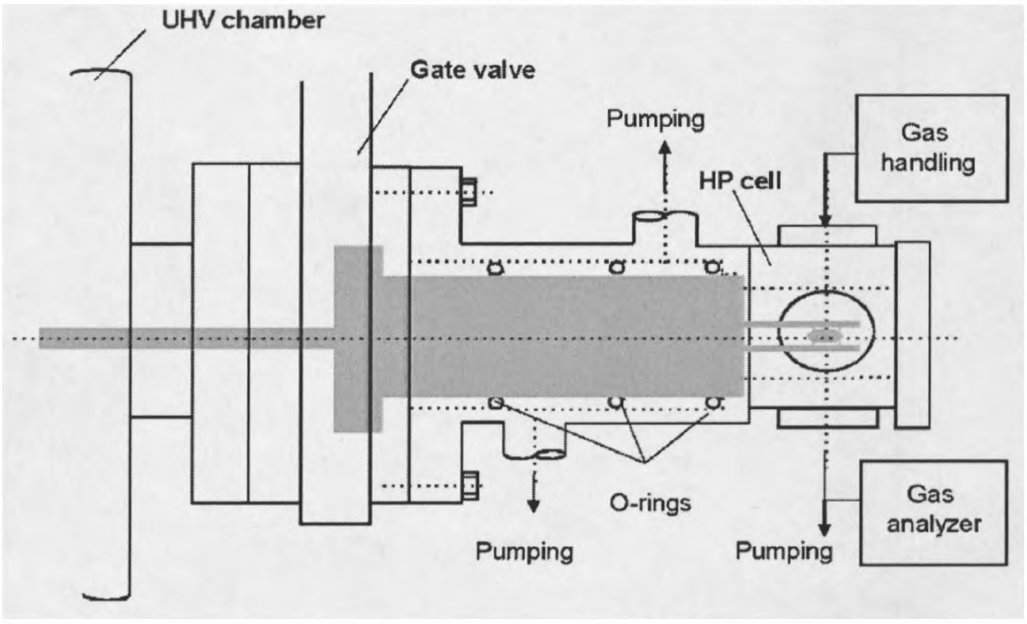

Fig. 3.2: Reactor design by Zhao *et al.* [19]. The sample is positioned in the high-pressure (HP) cell.

3.3 Design of a µl-flow reactor for *in situ* Raman spectroscopy and *in situ* XAS

3.3.1 Design considerations

The flow reaction chamber (RC) needed for *in situ* probing by Raman spectroscopy and XAS has to fulfil the following criteria:

1. The dead volume has to be small enough to permit probing of reaction rates, but large enough to ensure negligible influence of aliquots injected into the analysing probe (MS, GC).
2. Control of environmental conditions (p, T, gas flow rates).
3. The sample must be mechanically fixed in the chamber.

4. The sample surface has to be exposed only to the reactant gas, and protected from contamination by physical contact with other parts of the reaction chamber.
5. The reaction chamber and the surrounding parts have to be airtight to avoid contamination due to impurities from leaking of ambient laboratory air.
6. The system has to be transportable, for travelling to and from synchrotron sources.
7. To be able to use different *in situ* techniques, the window covering the sample has to be replaceable.

3.3.2 Dead volume considerations

Considering that an Au atom has a diameter of approximately 0.3 nm. It roughly covers a surface area of 0.3 nm × 0.3 nm = 0.09 nm². That means the maximum amount of atoms on the sample surface (10 × 10 mm² = 100 mm² = 1×10^{14} nm²) is:

1×10^{14} nm² / 0.09 nm² ≈ 1.1×10^{15} atoms.

If each atom is active and has a turnover frequency (TOF) of 1 s^{-1} (which is a reasonable activity of gold catalysts) 1.1×10^{15} molecules CO_2 or about 2×10^{-9} mol CO_2 are produced per second. Using the ideal gas theory, $pV=nRT$, it follows for normal pressure and room temperature:

$$V = \frac{nRT}{p} = \frac{2\times10^{-9}\,\text{mol}\times8.315\,\text{J/mol/K}\times293\text{K}}{1.013\text{hPa}} \approx 4\times10^{-8}\text{l} = 0.04\mu\text{l} \quad (3.1)$$

Under these absolute ideal conditions one would get about 0.04 µl/s or 2.5 µl/min CO_2. A flow in the ml/min region is too great for this system because the gas residence time would be too short to result in detectable traces of reaction products. A flow in the µl/min region would permit their detection. The reactor described in the following sections was thus designed for flow rates of 1 to 10 µl/min.

Usually, mass flow controllers are used to regulate the flow through catalytic reactors, but these controllers operate with flow rates in the ml/min regime. It was therefore decided to create a system where the flow rate is achieved by regulating the flow at the reactor outlet, using a system of UHV-compatible dosing valves that operate against vacuum (turbomolecular pump); this allows for very slow flow rates of 1×10^{-9} mbar·l/s.

The reproducibility of the experiment should also be considered. For these low flow rates (~1 μl/min) the reactor has to be completely leak tight, since even small leakage of air into the reactor would result in a N_2 detection at m/Z = 28 amu in the mass spectrum, which can easily become higher than the signal of CO. CO also has a m/Z of 28 amu, therefore a leak causes observation of the reaction to become impossible. Furthermore, impurities on a catalyst can either inhibit or accelerate the catalytic reaction; small amounts of impurities on the sample can affect the reaction rate disproportionately due to the small surface area. The impurities can also arise due to contact with air. Therefore the sample should be mounted in a glove box (point 5 above).
The dead volume is critical for the detection of the reaction products, since volume in the ml region would make the detection of the CO_2 very difficult and the response time of the system would be exceedingly slow (hours).

3.3.3 General design of the cell

A schematic set up that accommodates the requirements for an *in situ* spectroscopy cell is shown in fig. 3.3. This reaction cell was made in the workshops of the School of Chemistry and will be described in detail in section 3.3.4. The left part of the scheme in fig. 3.3 mostly contains standard Swagelok© parts, and is responsible for the gas supply to the reaction chamber (RC). The right part is used for the detection of the reaction gases. This part of the apparatus mainly contains standard UHV-parts with Conflat (CF) flanges.

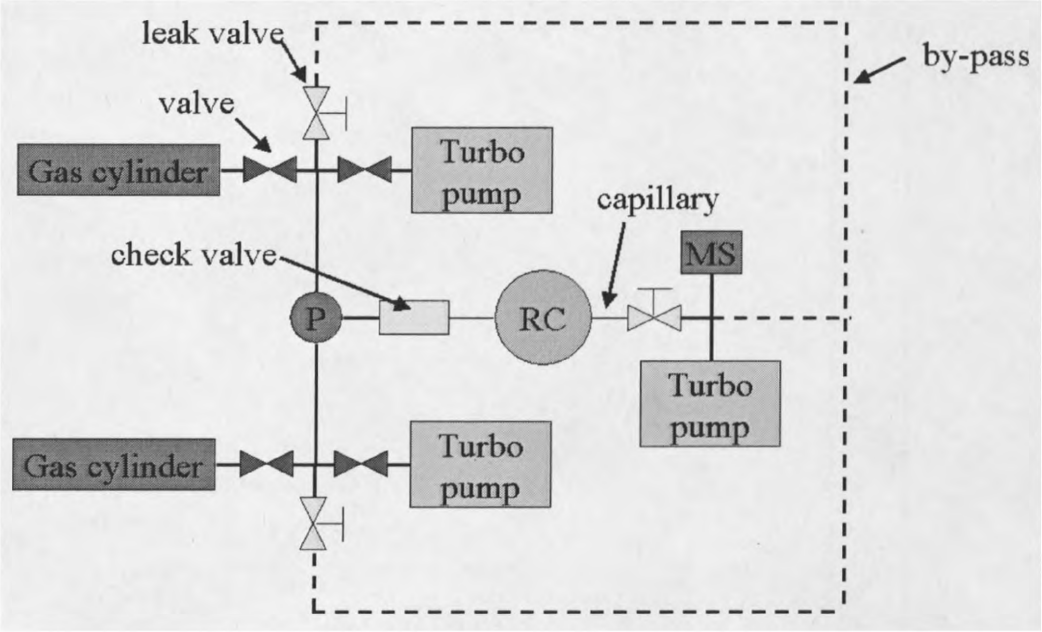

Fig. 3.3: Leak tight set up for the reaction monitoring of flat model catalysts. RC represents the reaction chamber and P refers to the pressure gauge used to determine the pressure in the reaction chamber.

Gas mixtures are dosed from small gas cylinders (Swagelok© 304L-HDF2-40), whereas the pressure in the gas cylinders determines the pressure in the reactor. With a manometer (label P; Keller Leo 3) in front of the reaction chamber, the pressure and flow rate can be determined. By operating the corresponding valves (Swagelok, SS-2H2) and leak valves (Hositrad VML14CF16) one of the two gas cylinders can be selected, it can be connected to a turbo pump (for emptying), the by-pass or the reaction chamber.

To analyse the gas mixture without any reaction, the bypass can be used. This is needed to determine the background signal of the CO_2 and estimate possible impurities in the gas mixture before the reaction. It is also possible to determine leaks in the gas supply. The turbo pumps (Leybold Vacuum TW70H) not connected to the RC are needed for the refilling process of the gas cylinders. The check valve (Swagelok© SS-2C2-1/3) is used to prevent back diffusion from the RC into the gas cylinders.

The reaction gases are analysed by a MS spectrometer (SRS RGA100) operating at a pressure of 10^{-6} mbar or lower. Therefore the reaction cell is connected *via* a leak valve (Hositrad VML14CF16) to a 6-way cross (only shown as 4-way cross, missing are the window and the gauge, Leybold Vacuum Ionivac ITR 90). To the 6-way cross, a turbo pump (Leybold Vacuum TW70H) is connected, allowing the pressure in the MS and the flow speed through the RC to be adjusted by controlling the leak valve and throttle.

3.3.4 Main reactor body

A small reactor with a dead volume of less than 100 µl was designed and constructed (see fig. 3.4). The material used for the reactor was aluminium. The sample inset is 10 mm × 10 mm × 1.5 mm, which holds the sample mechanically from the sides in position. The 1.0 mm high samples used have a distance of 0.5 mm to the ceiling, which is important in minimising the dead volume. To connect the reaction chamber (RC) to a gas system, 1/16" stainless steel capillaries with an inner diameter of 0.005" (0.127 mm) were fitted to the RC with Swagelok© NPT/tube fittings. For detecting the temperature of the RC, a 1 mm wide hole was drilled 1 mm below the sample to the centre of the sample into the aluminium body.

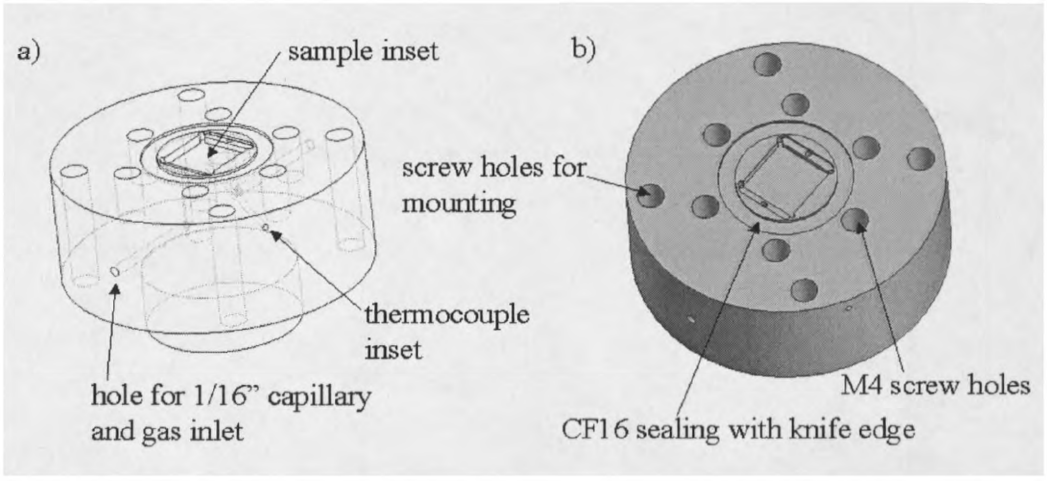

Fig. 3.4: Technical drawings of the reaction chamber. a) visible and hidden edges, b) shaded with visible edges.

On top of the RC, a standard DIN CF16 flange can be mounted, and sealed by Teflon™ rings. Modification of this flange provides the opportunity to use this cell with different kinds of *in situ* techniques, e.g., total reflection EXAFS (see results section) and Raman. Using a blank flange proves the sealing of the cell, since it is possible to pressurise the RC to at least 5 bar without any leakage. This was performed by placing the reaction chamber in water, while constantly applying 5 bar of He pressure from a gas cylinder to it. No gas bubbles could be seen, even after several minutes under these conditions.
The small design of the reactor body (it has a diameter of 50 mm) allows for easy transport - literally in the breast pocket, which is important for rapid transportation between different experiments. Assuming the presence of turbomolecular pumps at the experiment, the whole cell, including gas supply system, can be transported in a small box (~ 50x30x10 cm^3) and does not weigh more then a few kilogram.

Heating the sample directly was not possible due to the small design of the cell. Therefore a ceramic heater (GE Advanced Ceramics HTR 1001) was placed underneath the reaction chamber. By changing the applied voltage to the heater the temperature could be controlled.

3.3.5 Windows based on the CF 16 flange

To seal the cell, only a blank CF16 flange can be used, and the leak tightness of the set up should be tested. Possible influence of the *in situ* technique on the reaction can be investigated by comparing the reaction results under *in situ* conditions with the blank flange results (no outer influence on the reaction). Using the blank flange will also result in the smallest dead volume of the cell, and is therefore the best for kinetic measurements.
A simple modification of the blank flange is to insert a window of quartz glass (Caburn, CVP-16) or beryllium (K-Tek). The quartz window can be used e.g. for Raman and UV/Vis spectroscopy, or to monitor possible macroscopic changes in the catalyst by light microscopy. The beryllium window will in general allow XAFS spectroscopy and XRD.

However due to the very small Au particles, it will only be possible to inspect the TiO_2 support with both techniques under non-grazing incidence conditions. For small angle XRD (SAXRD) and grazing incidence XAFS a dome of beryllium (K-Tek) could be used. When using this dome for XAFS measurements it transpired that no fluorescence signal of the gold particles could be detected due to the absorption by the beryllium. Therefore a dome with a Kapton™ window was constructed (fig. 3.5). The Kapton™ foil is glued onto a 1 mm high socket. The sample is elevated from its normal position by a 6 mm high Al block and is ~ 0.7 mm below the Kapton™ window. This design gives only small losses in the intensity of the fluorescence signal of the gold particles compared to measuring without the window.

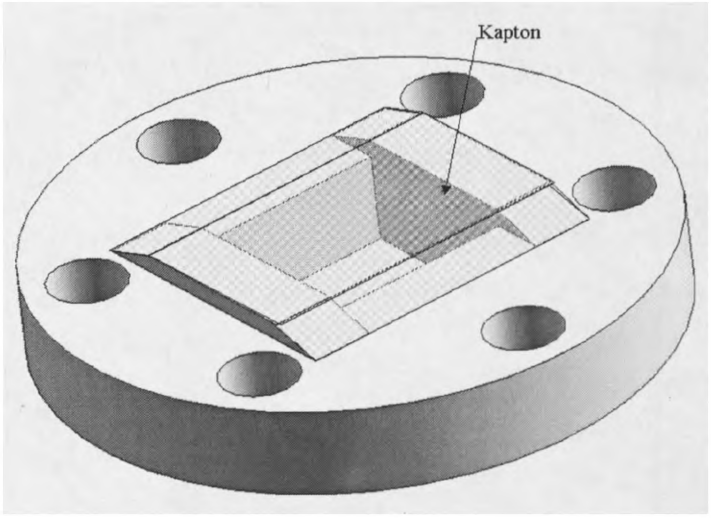

Fig. 3.5: CF 16 flange with Kapton™ window for total reflection EXAFS and SAXRD.

3.3.6 Holding plate for Raman scattering experiments

For *in situ* Raman scattering experiments (results not shown) it was required to manufacture an in-set plate for the optical table to fix the cell underneath the objective (cf. fig. 3.6). Through the central hole of this plate, the lower part of the cell is held in position. The two connected holes are for heating. The 6 holes around the central hole are for screwing the cell onto the plate and continually holding it in the horizontal position.

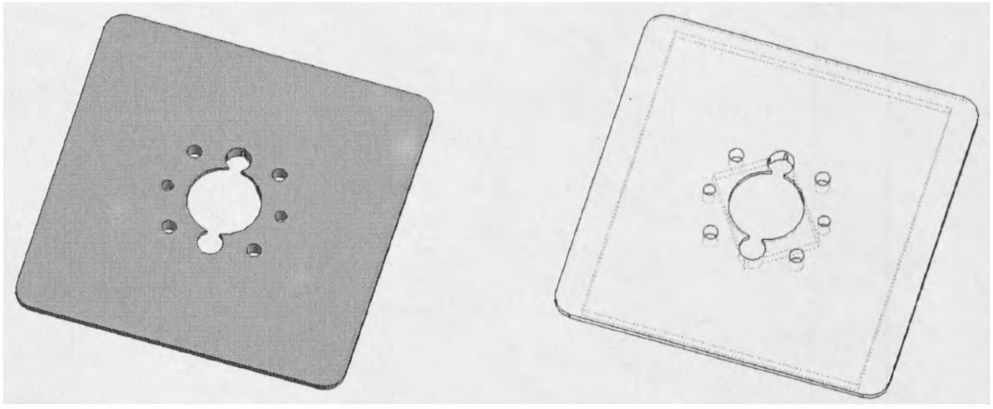

Fig. 3.6: Raman holding place for the *in situ* cell. In the clear image the in-set for the heater can be seen in the centre.

3.4 Results

3.4.1 Hard X-ray absorption spectroscopy

The cell was tested for *in situ* total reflection X-ray absorption spectroscopy (XAS) at station 9.3 of the CCLRC. It was shown that the cell presents a very good opportunity to the scientist to study flat samples under different conditions including temperatures between room temperature and 250°C as well as pressures of up to 1.5 bar. These spectra amongst others are discussed in chapter 4.1 as well as further details for the set up of the experiments.

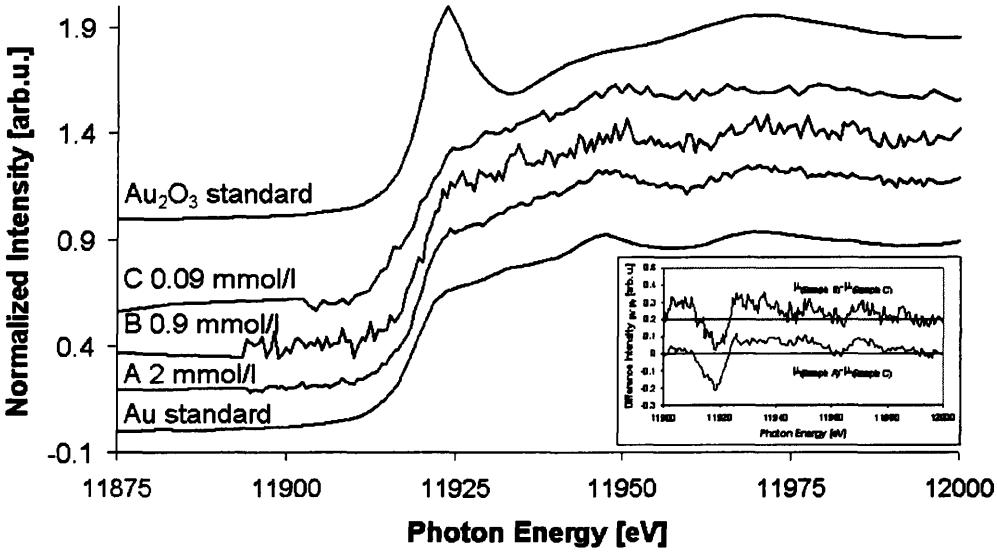

Fig. 3.7: Total reflection X-ray absorption spectra of different $Au/TiO_2(110)$ catalysts.

Measuring these spectra takes a considerable amount of time at a 2nd generation synchrotron light source. Besides setting up the experiment, which is described in the experimental part, the collection of the spectra shown here in fig. 3.7 and in chapter 4.1 takes several hours, up to 24 hours. The reasons are the low concentration of gold atoms on the sample (below 0.1 monolayer of gold), as calculated in chapter 4.1 from XPS results, and the very small beam heights required, which was calculated in the theory section. Performing these studies at a 3rd generation synchrotron light source will potentially reduce the required measurement time drastically. This is because the photon flux is generally much higher, and the beam can be more focused on a 3rd generation synchrotron light source.

This combination of very low "sample concentration" and low photon flux leads to a very weak gold signal and comparatively high background noise. Low gold concentrations on the samples are necessary, however, to achieve gold nano-clusters, which are commonly agreed to be the active phase [20]. Higher $HAuCl_4$ concentrations, and therefore higher gold concentrations, are not possible without producing bulk gold, at least with the present preparation conditions. Since XA spectra of a gold foil (bulk gold) and the sample prepared with 2 mmol/l $HAuCl_4$ concentration show a close similarity, formation of gold

particles with a diameter of a few nm can only be prepared with a lower $HAuCl_4$ concentration than 2 mmol/l (see also chapter 4.1.4).

The low photon flux on the sample is due to the grazing incidence measurements of the samples. Measuring the samples perpendicular to the beam would result in a very high background noise of the TiO_2 support and would make the detection of the gold absorption spectrum more complicated, if not impossible.

The grazing incidence measurements thus have high requirements to the beamline optics, since the beam has to be extremely focused in height. The required height of 20 μm could not be achieved with the optics of station 9.3 of the CCLRC without losing significant amounts of photon flux. Hence it was decided to focus the beam to a height of 400 μm. This beam height thus does not only cover the sample but also the sample chamber and therefore results in a high background signal. The beam height was further reduced with a slit to 100 μm, which still gave some background signal from the sample chamber, but reducing the beam height to 50 μm or 20 μm resulted in a very weak gold signal.

Finally, the character of the single crystal of the support has to be considered as well. By scanning the photon energy, the Bragg conditions can be fulfilled and the TiO_2 planes can reflect the X-ray beam into the fluorescence detector. This results in a peak that is extremely intense in comparison to the gold signal. If this peak is positioned at or close behind the absorption edge, the sample had to be turned around its vertical axis. This operation resulted in a shift of the Bragg peak and a configuration had to be found in which the Bragg peaks did not occur in the near edge region.

3.4.2 Mass spectroscopy of gas mixtures dosed in the reaction chamber

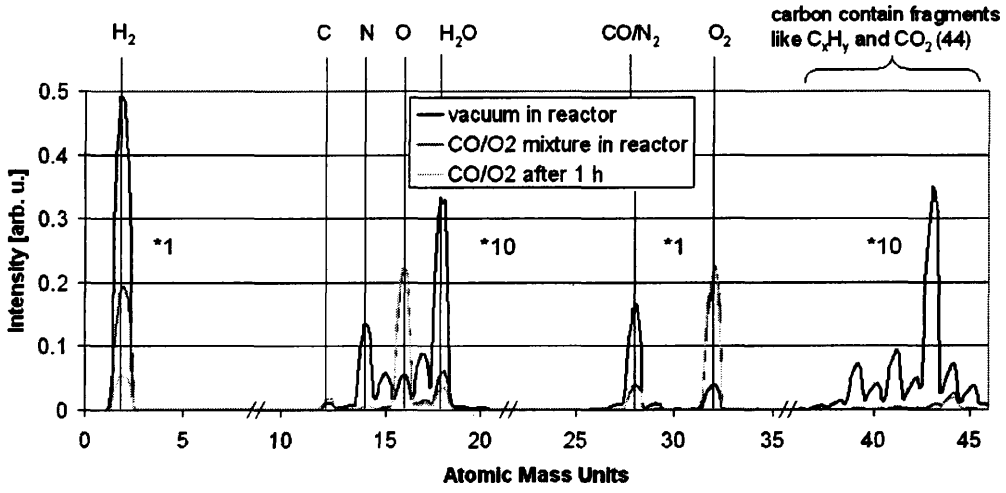

Fig. 3.8: Comparison of the MS trace of the reactor under vacuum (black line), after dosing a CO/O_2 mixture into the reactor (dark grey) and after leaving the reactor under these conditions for 1 h (light grey line).

To test the performance of the reactor under *in situ* conditions, a gas mixture of CO and O_2 was dosed in the reaction chamber. The lack of leakage and inertness to the CO oxidation of the reactor, as well as the possibility to detect impurities in the gas stream should be proven. Therefore the gas stream was analysed after dosing the gas, and after leaving the gas mixture in the reactor for 1 h (cf. fig. 3.8). For comparison a mass spectrum was taken before dosing gas into the evacuated reaction chamber (black line in fig. 3.8), with a pressure of $7 \cdot 10^{-6}$ mbar in the MS chamber. Connecting the reaction chamber directly to the mass spectrometer, by opening the leak valve between MS and reactor completely, allowed this. All mass spectra show the presence of hydrogen (H_2), carbon (C), nitrogen (N), oxygen (O, O_2), water (H_2O), carbon monoxide (CO) or nitrogen (N_2, both mass 28) and carbon containing molecules and their fragments (C_yH_x) as well as CO_2 (cf. table 3.1).

The mass spectrum (MS) of the evacuated reactor (pressure in the mass spectrometer $7 \cdot 10^{-6}$ mbar) shows a strong H_2 peak (at an atomic mass unit, or amu, of 2). This peak is

due to hydrogen in the mass spectrometer. The hydrogen gets oxidised by the oxygen, dosed later on in the experiment, to water and therefore can be better pumped and decreases with experiment time. The mass spectrum of the remaining atmosphere in the reactor under further vacuum contains some air, which can be seen by N (amu: 14), O (amu: 16), N_2 (amu: 28) and O_2 (amu: 32) peaks with a ratio of roughly 3:1 for the nitrogen to oxygen peaks. This is air adsorbed on the reactor walls, which is difficult to extract from the reactor by pumping alone, since the reactor is connected via a capillary to the mass spectrometer. This lowers the pumping ability of the turbomolecular pump on the reactor drastically and hence it takes a very long time to remove the last trace of air from the reactor without dosing other gases. The same is true for water remaining in the reactor as peaks at atomic mass units (amu) of 17 (OH) and 18 (H_2O) indicate. The atmosphere of the evacuated reactor also contains large amounts of carbon containing fragments. The high intensity of these fragments to the air peaks is a good indication that the reactor is leak tight and that only adsorbents from the reactor walls are slowly desorbing into the reactor atmosphere, which are monitored by the MS.

Table 3.1: MS intensities.

amu	Conditions								
	Vacuum			After dosing			1 h after dosing		
		$N_2^{\#}$	$CO^{\#}$		$N_2^{\#}$	$CO^{\#}$		$N_2^{\#}$	$CO^{\#}$
H_2 (2)	48.5	---	---	19.3	---	---	5.25	---	---
C(12)	0.105	---	---	0.177	---	---	0.160	---	---
N(14)	1.30	---	---	0.0531	---	---	0.0531	---	---
O(16)	0.528	---	---	2.21	---	---	2.2	---	---
H_2O(18)	3.29	---	---	0.559	---	---	0.258	---	---
N_2/CO (28)	16.6	15.9	0.7	3.80	0.88	2.92	3.96	0.99	2.97
O_2 (32)	3.92	---	---	21.9	---	---	21.9	---	---
Mass 44*	0.645	---	---	0.254	---	---	0.188	---	---

* Under vacuum condition this reflects carbon residuals; after dosing gases this will be mainly CO_2 produced at the filament

[#] The intensities of N_2 and CO have been calculated by comparing the relative intensities of the C and N signal; neglecting different fragmentation and ionisation potentials

After dosing a CO/O_2 mixture into the reaction chamber the leak valve was closed and a pressure of 5×10^{-6} mbar in the mass spectrometer chamber was used to monitor the gas composition. The dosing of the gases results in an increase in the oxygen peaks amu 16 and 32, but in a decreasing N_2/CO peak (amu: 28). This is due to a drastic decrease of nitrogen in the atmosphere, and the increasing amount of CO in the atmosphere, as comparison between the N (amu: 14) and C (amu: 12) peaks shows (cf. table 3.1). All values are stable over experiment time; only the level of nitrogen is increasing, by about 12%. But the total amount of nitrogen in the atmosphere is very low, about 2%, which explains the variations in the concentration of nitrogen. Also these values are only estimates and are calculated from 3 peaks. This does not indicate an air leak in the chamber because an increase of several times the nitrogen signal would be the result of a leak in the reaction chamber.

The water contained in the atmosphere is decreasing over time, because water adsorbed in the reaction chamber is slowly transported out of the system, and that the hydrogen in the mass spectrometer chamber is slowly pumped and therefore less hydrogen can react with oxygen to form water. The peaks in the region above 40 amu decrease drastically after dosing the CO/O_2 mixture, then more steadily with time (cf. fig. 3.9). This shows that the carbon containing fragments do not, or only slightly, desorb under atmospheric conditions. Also a change in the intensity distribution can be seen. Under vacuum conditions the peak at 43 amu is the strongest. When dosing the gas mixture, the peak at 44 amu becomes the strongest. Under vacuum this peak is only due to carbon containing fragments, but when CO and O_2 are dosed, small amounts are converted at the MS filament to CO_2. This means under these conditions this peak is mainly due to CO_2. That no CO is oxidized to CO_2 in the chamber can be seen by the fact that the CO_2 is not increasing over time but actually decreases. This decrease is due to the decreasing amount of carbon containing fragments, which were still present directly after dosing the gas mixture, but nearly vanishes after 1 hour, as hardly any fragments with an amu of 43 are detected.

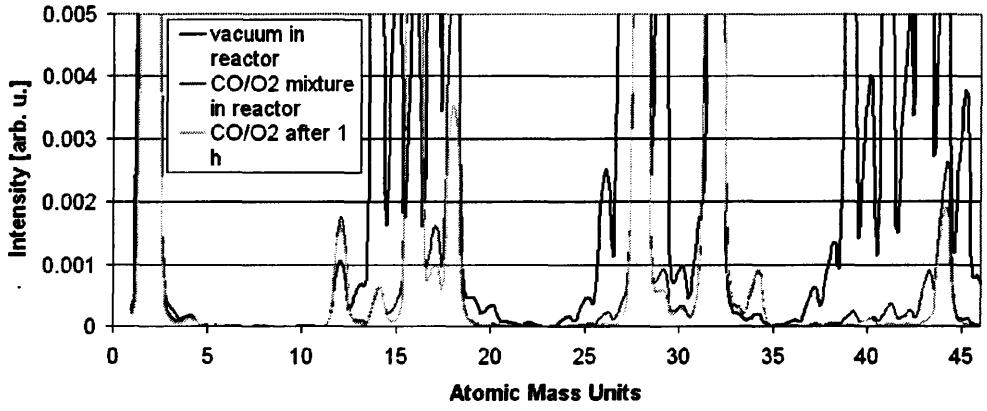

Fig. 3.9: Focus on the traces in the mass spectrum from fig. 3.8, with a scale increased by the factor 100.

3.5 Discussion

A small dead volume cell was constructed to study flat model catalysts with *in situ* spectroscopic techniques and kinetic measurements. The cell was tested with two different model systems (gold nanoparticles on TiO_2 and electrochemical oxidised gold foil) and *in situ* XAS that shows the potential of the cell (see also chapter 4.1). It is also possible to adapt the cell for further spectroscopic techniques like Raman scattering, Fourier Transformation Infrared (FTIR), UV/Vis and X-ray diffraction (XRD). This presents a much wider range of techniques than shown in previous studies [18, 19]. The compact design of the cell and the gas supplying system allows for easy transportation between experiments without the demand of a large UHV system at the experiment sites. The only requirements are a turbomolecular pump and a mass spectrometer, giving a great advantage over the cell presented by Zhao *et al.* [19] that requires a fully operating UHV chamber.

On the other hand the design of the cell makes it more difficult to obtain kinetic data compared to other systems [18, 19], since the dead volume could not be minimised to the level needed. The demand to a very small flow through the reaction chamber requires a very good leak tightness of the needle valve between the reaction chamber and the MS.

This could not always be obtained and is one reason why no kinetic data has been obtained so far. Nevertheless it was proven that the cell is completely sealed to the outer atmosphere as different experiments show. It is possible to pressurise the reaction chamber to 5 bar without any leakage, no impurities can be monitored when an atmosphere is dosed by means of mass spectrometry and the pressure inside the reaction chamber remains constant for more than 12 hours in both under- and overpressure conditions.

In situ spectroscopic experiments have been performed in the pressure range of 1 to 2 bar, but the cell was tested to be leak tight to at least the sub-mbar region, as no pressure changes over long time experiments (24 h) occurred. This means experiments in the mbar region as well as at several bar are possible. The temperature has been varied between 300 K and 420 K but using a cooling bath for the cell would allow experiments to be operated at lower temperatures than room temperature. Other designs [18, 19] are able to heat the sample to higher temperatures (1700 K [19]) but for the study of gold catalysts these temperatures are generally not needed. In most designs it is also common to heat the sample directly with a heater placed underneath the sample. This is not possible in the present design but it has the advantage that the sample and the gas have the temperature indicated by the thermocouple inside the reactor body. However, extra care has to be taken that the observed reaction is due to the sample and not an artefact of heating the reactor body. Under room temperature, it could be proven that the reactor does not catalyse the oxidation of CO.

The theoretical calculation showed that a dead volume of more then 1 ml and flow rates above the µl/min region would make catalytic measurements impossible. These requirements have not yet been fulfilled, and the catalytic activity of the used model catalysts has yet to be measured.

Reference

[1] Dalla Betta, R. A.; Boudart, M.; Foger, K.; Loffler, D. G.; Sanchez-Arrieta, J.; Review of Scientific Instruments, **1984**, *55*, 1910-1913.

[2] Clausen, B. S.; Steffensen, G.; Fabius, B.; Villadsen, J.; Feidenhans'l, R.; Topsoe, H.; Journal of Catalysis, **1991**, *132*, 524-535.

[3] Clausen, B. S.; Topsoe, H.; Catalysis Today, **1991**, *9*, 189-196.

[4] Grunwaldt, J. D.; Caravati, M.; Hannemann, S.; Baiker, A.; Physical Chemistry Chemical Physics, **2004**, *6*, 3037-3047.

[5] Jentoft, R. E.; Deutsch, S. E.; Gates, B. C.; Review of Scientific Instruments, **1996**, *67*, 2111-2112.

[6] Bare, S. R.; Mickelson, G. E.; Modica, F. S.; Ringwelski, A. Z.; Yang, N.; Review of Scientific Instruments, **2006**, *77*, 023105/1-023105/6.

[7] Kampers, F. W. H.; Mass, T. M. J.; van Grondelle, J.; Brinkgrave, P.; Koningsberger, D. C.; Review of Scientific Instruments, **1989**, *60*, 2635-2638.

[8] Sankar, G.; Thomas, J. M.; Rey, F.; Greaves, G. N.; Journal of the Chemical Society, Chemical Communications, **1995**, 2549-2550.

[9] Meitzner, G.; Bare, S. R.; Parker, D.; Woo, H.; Fischer, D. A.; Review of Scientific Instruments, **1998**, *69*, 2618-2621.

[10] Odzak, J. F.; Argo, A. M.; Lai, F. S.; Gates, B. C.; Pandya, K.; Feraria, L.; Review of Scientific Instruments, **2001**, *72*, 3943-3945.

[11] Moggridge, G. D.; Schroeder, S. L. M.; Lambert, R. M.; Rayment, T.; Nuclear Instruments & Methods in Physics Research, Section B: Beam Interactions with Materials and Atoms, **1995**, *97*, 28-32.

[12] van der Eerden, A. M. J.; van Bokhoven, J. A.; Smith, A. D.; Koningsberger, D. C.; Review of Scientific Instruments, **2000**, *71*, 3260-3266.

[13] Sullivan, V. S.; Jackson, S. D.; Stair, P. C.; Journal of Physical Chemistry B, **2005**, *109*, 352-356.

[14] Schneider, M. S.; Grunwaldt, J. D.; Burgi, T.; Baiker, A.; Review of Scientific Instruments, **2003**, *74*, 4121-4128.

[15] Drochner, A.; Fehlings, M.; Krauß, K.; Vogel, H.; Chemie-Ingenieur-Technik, **1999**, *71*, 861-864.

[16] http://brushwellman.com.

[17]

a) http://www.srs.ac.uk/srs/stations/station9.3.htm.

b) http://www.esrf.eu/UsersandScience/experiments/XASMS/BM29/overview.

[18] Johansson, S.; Fridell, E.; Kasemo, B.; Journal of Vacuum Science and Technology, **2000**, *18*, 1514-1519.

[19] Zhao, Z.; Diemant, T.; Häring, T:; Rauscher, H.; Behm, R. J.; Review of Scientific Instruments, **2005**, *76*, 123903/1-123903903/8.

[20] Haruta, M.; Cattech, **2002**, *6*, 102-115.

[21] Williams, K. A.; Pradhan, B. K.; Eklund, P. C.; Kostov, M. K.; Cole, M. W.; Physical Review Letters, **2002**, *88*, 165502/1-165502/4.

[22] Itoh, T.; Abe, K.; Dokko, K.; Mohamedi, M.; Uchida, I.; Kasuya, A.; Journal of The Electrochemical Society, **2004**, *151*, A2042-A2046.

[23] Yang, S.; Kondo, J. N.; Hayashi, K.; Hirano, M.; Domen, K.; Hosono, H.; Chemistry of Materials, **2004**, *16*, 104-110.

[24] Maynard, K. J.; Moskovits, M.; Chemical Physics Letters, **1987**, *142*, 298-301.

4 Results

4.1 Growth of Au nanoclusters on TiO_2(110) by spin coating

4.1.1 Abstract

Gold and oxidised gold nanoparticles were prepared by a wet chemical approach on a single crystal rutile(110) support by spin coating. The concentration used for the spin coating was varied, and gold clusters of different sizes (in the nm region) were prepared. These samples were characterised by both soft and hard X-ray absorption spectroscopy, probing the interaction of the gold (-oxide) particles with CO and O_2. The results show that CO adsorbs on the Au/TiO_2 sample. O_2 does not appear to influence the electronic structure of the gold particles significantly.

4.1.2 Introduction

Understanding the catalytic activity of nano-scale gold particles for the oxidation of CO has been the subject of a large number of recent publications [1 - 11]. CO oxidation at room temperature is an interesting application, e.g. to remove CO from the feed stream of a fuel cell, the purification of CO_2 gas in laser, or the oxidation of CO in closed environments [12]. This makes it an appropriate candidate for the study of the interaction of the educts with the gold nanoparticles. Although this system has been studied intensively since the early 1990s, the mechanism of the catalytic oxidation of CO by gold nanoparticles is still a controversial subject.

A more facile approach to understanding the reaction mechanism of catalysts is to study model catalysts with reduced complexity [13 - 15]. The application of surface science techniques often requires flat model systems without spectroscopically inaccessible particles hidden in pores. This has disadvantages, such as low surface area and very small amounts of active phase in comparison to powder catalysts (further discussion is given in chapter 3).

In this chapter, the synthesis of a gold model catalyst with Au supported on rutile(110) is described. To model practical catalysts the gold particles were prepared by means of wet chemistry, using spin coating. Spin coating is similar to the impregnation techniques used for the preparation of powder catalysts [16, 17] making it an interesting technique for the preparation of flat model catalysts. A detailed comparison between the preparation by spin coating and impregnation of powder catalysts was first given by Niemantsverdriet and co-workers [13]. An adapted version for the preparation of gold catalysts is given in fig. 4.1.1. The industrial catalyst and the flat model are shown in the upper row and lower row, respectively. In the first step the TiO_2-powder is added to the $HAuCl_4$-solution and stirred. For the model catalyst this is achieved by pouring the solution on the single crystal. Afterwards, spin coating results in the reduction of the amount of solution on the single crystal and dries the gold clusters on the support. For the powder catalyst the solvent is removed by heating the sample, which can be done directly if the sample is impregnated. If the sample is prepared by deposition-precipitation the catalyst has to first be separated from the solution by filtration, since evaporation of the volumes of solvent used would take too long.

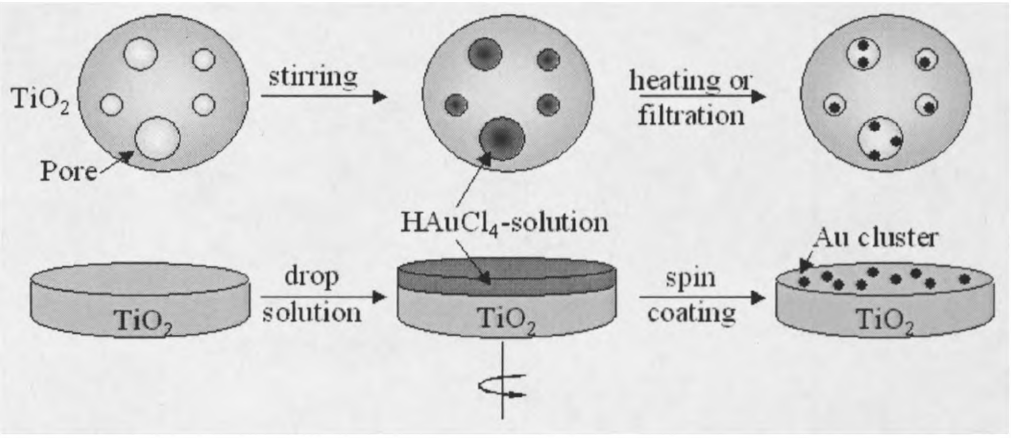

Fig. 4.1.1: Schematic comparison of the preparation of a powder (upper row) and a flat model catalyst. Based up on Niemantsverdriet et al. [13].

4.1.3 Experimental

4.1.3.1 Sample preparation

Gold nanoparticles on TiO_2 single crystals (Crystal GmbH) were prepared by spin coating of a highly diluted $HAuCl_4$ solution onto the single crystals. The TiO_2 crystals were cleaned by rubbing them with paper tissue and ethyl acetate, acetone and ethanol, followed by an ultra sonic cleaning for 10 min in each solvent. Between each ultra sonic cleaning the TiO_2 crystals were rinsed with distilled water (~ 18.2 MΩ). Before spin coating, the single crystal was irradiated with UV light (Ealing, 150 Xe/200 Hg light) for approximately 30 minutes and used immediately for spin coating.

A tetrachloroauric acid solution ($HAuCl_4$) was obtained by dissolving 69.0 mg $HAuCl_4 \cdot H_2O$ (Sigmal Aldrich, ACS Reagent®) in 10 ml distilled water (R ~ 18.2 MΩ). This stock solution was then further diluted before spin coating to the required concentration, range between 2 mmol/l and 0.09 mmol/l. For wet impregnation, a pH of ~9 was achieved by adding a few µl of concentrated NH_3 (BDH, AnalaR®) to the diluted solution. After (a maximum of) 90 s, the solution was positioned on the single crystal and the spin coating was started (speed: 5000 rpm, acceleration: 5000 rpm/s, length: 120 s).

For the XANES studies at the Au L_{III}-edge three different samples were prepared by diluting the stock solution to concentrations of 2 mmol/l, 0.9 mmol/l and 0.09 mmol/l and then spin coating onto rutile(110) single crystals (these samples will from now on be labelled Au/TiO_2-2, Au/TiO_2-0.9 and Au/TiO_2-0.09). For the soft X-ray XANES studies (O K- and Ti L-edge) a sample of 2 mmol/l concentration had been used.

Another type of sample was prepared by washing a spin-coated sample with a basic cyanide solution. The 2% cyanide solution was prepared with NaCN and was kept at pH ~12 using NaOH [18]. The Au/TiO_2 sample was placed in a beaker and washed for 1 minute with cyanide solution. The sample was then rinsed with distilled water. This sample is labelled Au/TiO_2-CN.

4.1.3.2 Soft X-ray absorption near edge structure

The X-ray Absorption Spectroscopy (XAS) experiments were carried out at beamline 5U.1 of the CCLRC Daresbury Laboratory. The ring current was typically between 120 mA and 250 mA. The sample chamber was separated from the beamline by two nickel mesh windows with a 120 nm boron coating (Luxel). The windows were pumped separately by turbo pumps. This set up allows for a pressure of roughly 1 mbar in the sample chamber without significant leakage of gas into the beamline (For more details see the techniques chapter).

For the CO adsorption experiments, sample Au/TiO_2-2 was mounted on an Aluminum holder with carbon sticky tape (Agar). The sample was positioned at 90° relative to the beam, but it could be rotated to measure under different incident angles. An untreated rutile(110) single crystal (Crystal GmbH) was mounted in the same way to obtain the Ti L-edge and O K-edge as standard.

The spectra were recorded in the total electron yield (TEY) mode by collecting the drain and collector sample current. The collector-ring for the electrons ejected from the sample was mounted opposite to the sample. The X-ray beam passed through the middle of the ring. To attract electrons, a voltage of approximately +90 Volts was applied to the collector. The collected currents were converted into voltage with a Keithley 427 Current Amplifier. The gain was typically set to 10^9 V/A and the amplifier rise time to 300 ms. The voltage was converted *via* a voltage-to-frequency (V/F) converter and read into the station software.

It was possible to obtain the Ti L-, O and C K-edge of the samples, but the C K-edge did not yield any useful information. Carbon contamination deposited on the sample during preparation, and storage in the laboratory environment was the only signal detectable. The Ti L- and O K-edge have been divided by the I_0 signal. No further subtraction was needed since there was no oxygen or titanium contamination present on the window material.

4.1.3.3 Grazing incidence hard X-ray absorption near edge structure (XANES)

XANES characterisation of the gold nanoparticles was conducted at station 9.3 of the CCLRC Daresbury Laboratory. The synchrotron storage ring current was between 120 and 250 mA. The samples were mounted into the cell described in the techniques chapter. The samples were elevated with an Al-block into the Al dome, which sealed the cell above the sample. The X-ray beam passed the Al dome through a cut out that was sealed with a Kapton™ window (cf. fig. 4.1.2).
The X-ray beam height was reduced to 400 μm by the mirror system of station 9.3. A further reduction of the beam height to 100 μm was achieved by mounting a slit in front of the I_0 chamber. A beam with this height will illuminate not only the sample surface but also the dome surface at the given angles. The Au L_{III}-edge spectrum of the sample was recorded with a 13-element solid-state fluorescence detector mounted vertically over the sample.

For the grazing incidence measurements, angles between 0.1° and 1° have been used (for determining the 0 angle and alignment see the experimental chapter). The angle to measure the sample was chosen by the greatest intensity recorded by the detector. Special care had to be taken that no Bragg-reflection of the TiO_2 support was present in the edge area. Roughly one-hour scans were taken and 8 to 20 spectra were accumulated for the given Au L_{III}-edge spectra. A scan time of one hour allowed collection of spectra for alignment but did not show an acceptable signal-to-noise (S/N) ratio. The total acquisition time for the spectra was between 8 h and 24 h, decreasing with increasing spin coating concentration.

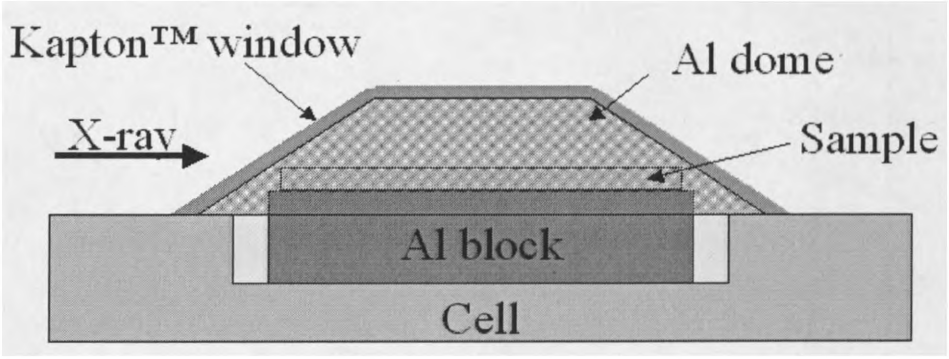

Fig. 4.1.2: Set up for the grazing incidence hard X-ray XANES analysis of Au/TiO_2 samples. The X-ray beam enters and leaves the Al dome through a cut out that also allows the measurement of the fluorescent signal with a detector above the sample. The cut out is covered with Kapton™-foil to give a pressure cell. For a more detail description see the techniques chapter.

In situ spectra were taken under static CO (Linde, 3.7) and static O_2 (Messer, 4.8) atmosphere. A quadrupole mass spectrometer monitored the purity of the atmosphere and the pressure (~1.5 bar) remained constant over the time of the experiment.

The resulting spectra were normalised with the IFEFFIT program Athena [19].

4.1.3.4 XPS

A Kratos AXIS Ultra system was used for the chemical analysis of the samples. Samples were loaded and pumped down *via* a load lock, and transferred into the sample chamber *via* a radial distribution chamber. The pressure during XPS measurements was better then 5×10^{-8} mbar and a base pressure of 1×10^{-9} mbar or better was used in the sample chamber.

For the calculation of the monolayer thickness of the gold atoms on the TiO_2 support, the surface atom per area has to be known. For the $TiO_2(110)$ surface this is

5.19×10^{14} (TiO_2 units)/cm^2 with a unit cell of 0.650 nm along the $[1\bar{1}0]$ direction and 0.296 nm along the [001] direction for the TiO_2(110) surface [20]:

$$N_{Substrate} = N_{TiO_2} = \frac{1}{l(1\bar{1}0)\times l(001)} = \frac{1}{0.650\text{nm}\times 0.296\text{nm}} = 5.19\times10^{14}\,\frac{1}{\text{cm}} \quad 4.1.1$$

For the gold monolayer the Au(100) surface with 1.20610^{15} (Au atoms)/cm^2 was used as an approximation to the maximum coverage of the substrate surface. The coverage Θ follows from: 4.1.2

$$\Theta = \frac{N_{Adsorbate}}{N_{Substrate}}$$

Where $N_{Adsorbate}$ is the surface number density of the Au atoms and $N_{Substrate}$ is the surface number density of atoms on TiO_2(110). This gives a value of 2.32 for the system gold surface on TiO_2(110), which corresponds to 2.32 gold atoms per (unit cell) of TiO_2. This value reflects one monolayer (Φ=1) of Au on the TiO_2(110) surface.

For calculating the monolayer thickness from XPS intensities the following formula should be used [21, 22]:

$$\Phi = \frac{1}{\frac{I_{Sub}N_{Ad}S_{Ad}}{I_{Ad}N_{Sub}S_{Sub}}\left[1-\exp\left(-\frac{a_{Ad}}{\lambda_M(E_{Ad})\cos\theta}\right)+1-\exp\left(-\frac{a_{Ad}}{\lambda_M(E_{Sub})\cos\theta}\right)\right]}\cdot \quad 4.1.3$$

For calculating the monolayer Φ of the adsorbent on the substrate, the intensities of the adsorbent and substrate emission in the XPS (I_{Ad} and I_{sub}), the surface number densities (N_{ad} and N_{Sub}) as well as the relative atomic sensitivity factors (RSF, S_{Ad} and S_{Sub}) are needed. Furthermore, the diameter of the adsorbents atoms (a_{ad}) and the angle θ under which the sample was taken are required. The mean free path (λ) of the electrons in the adsorbent and substrate have been calculated according to:

$$\lambda_M = 0.41\cdot a^{3/2}\cdot\sqrt{E_{Kin}}\,. \quad 4.1.4$$

The diameter (a) in this equation means the diameter of a gold atom for calculating the mean free path in the adsorbent. For the mean free path in the substrate the diameter was calculated as the average of the titanium diameter and the 2 oxygen diameters.

4.1.3.5 SEM

SEM images of the gold nanoparticles have been taken with a FEI XL 30 ESEM FEG. The acceleration voltage of the electron beam was usually 30 keV. The usual spot size of the electron beam was about 0.4 µm, and secondary electrons were recorded for the images. To reduce the charging effects on the sample low vacuum mode was used (~ 0.5 torr). Water vapour (imaging gas) was used as the dosing gas.

4.1.3.6 AFM

To collect AFM images a Veeco™ Nanoscope III in tapping mode was used. The tips used were Al-coated single cantilever tapping mode tips (Budget Sensors, Resonant Frequent: 300 kHz, Force Constant 40 N/m). A typical scan was done with an initial gain of 0.2, a proportional gain of 2.0, 512 lines/sample and a scan speed between 0.5 and 1 Hz. The scan range could be varied from 30 µm to 250 nm. At scan ranges less than 1 µm special care had to be taken to achieve a noise free image. The AFM was enclosed with a Plexiglas hood for the reduction of noise effects, and to have the option to keep the sample under controlled conditions (N_2 atmosphere, BOC 2.2).

4.1.4 Results

4.1.4.1 Morphology

A series of SEM images for a sample prepared with a $HAuCl_4$-concentration of 2 mmol/l is given in fig. 4.1.3. The SEM images were taken after analysing the sample with XPS and storage of approximately 3 months. The overview image (4.1.3.I) shows only very few white particles. Dark spots and shades in the image are charging effects from the

electron bombardment of the isolating sample. These spots are not present in images with higher magnification. In fig. 4.1.3.II a large particle is shown, which has a length of about 1 μm. However, such particles are very rare on the sample (less than 5 were observed while searching the whole sample). The chemical analysis with Energy Dispersive X-ray Analysis (EDX) resolved that this particle only contains carbon.

Besides some larger particles with diameter between 50 and 100 nm, a small amount of tiny particles with diameters of 20-40 nm can be seen in figs. 4.1.3.III and 4.1.3.IV. SEM is not capable of resolving particles smaller than 20 nm. Images with higher magnification (fig. 4.1.3.V and IV) reveal the spatial resolution limitation of Field Emission Microscopy Scanning Electron Microscopy (FEM-SEM) for the characterisation of nanoparticles on TiO_2, since the contrast of even the bigger 20 nm particles becomes unsatisfactory. In fig. 4.1.3.VII an agglomerate of particles is shown, which is about 150 nm long and contains about 11 particles.

Energy Dispersive X-ray Analysis (EDX) could not resolve the chemical composition of all particles because EDX probes approximately 2 μm into the material. Hence only titanium and oxygen signals from the support were detected. It was impossible to determine whether a specific cluster was gold, oxidic gold or a surface contamination. An exception was the large particle in fig. 4.1.3.II, which is composed of carbon, as revealed by EDX.

AFM images of the different $Au/TiO_2(110)$ samples and the $TiO_2(110)$ support are shown in fig. 4.1.4. In general terms, all five samples show a very high similarity. The surfaces contain large amounts of small elevations with diameters around 35 nm and heights of 1.5 nm. Even though a chemical analysis of these elevations was not possible, the heights indicate that these particles are TiO_2 islands that are presumably (1x1) terminal TiO_2. Similar islands have been reported when defect free TiO_2 was annealed in $1 \cdot 10^{-6}$ mbar O_2 [20, 23] and are most likely formed by the polishing and storage of the samples.

After spin coating, some bigger particles are also visible on all samples with diameters of up to 125 nm and heights of about 10 nm. It is unlikely that these particles are gold particles since they are still present on the cyanide-leached sample (Au/TiO_2-CN). XPS analysis revealed that the cyanide leached sample is gold free and therefore these

particles are likely either carbon contaminations or even bigger reconstructions of the TiO_2 surface induced by the spin coating process.

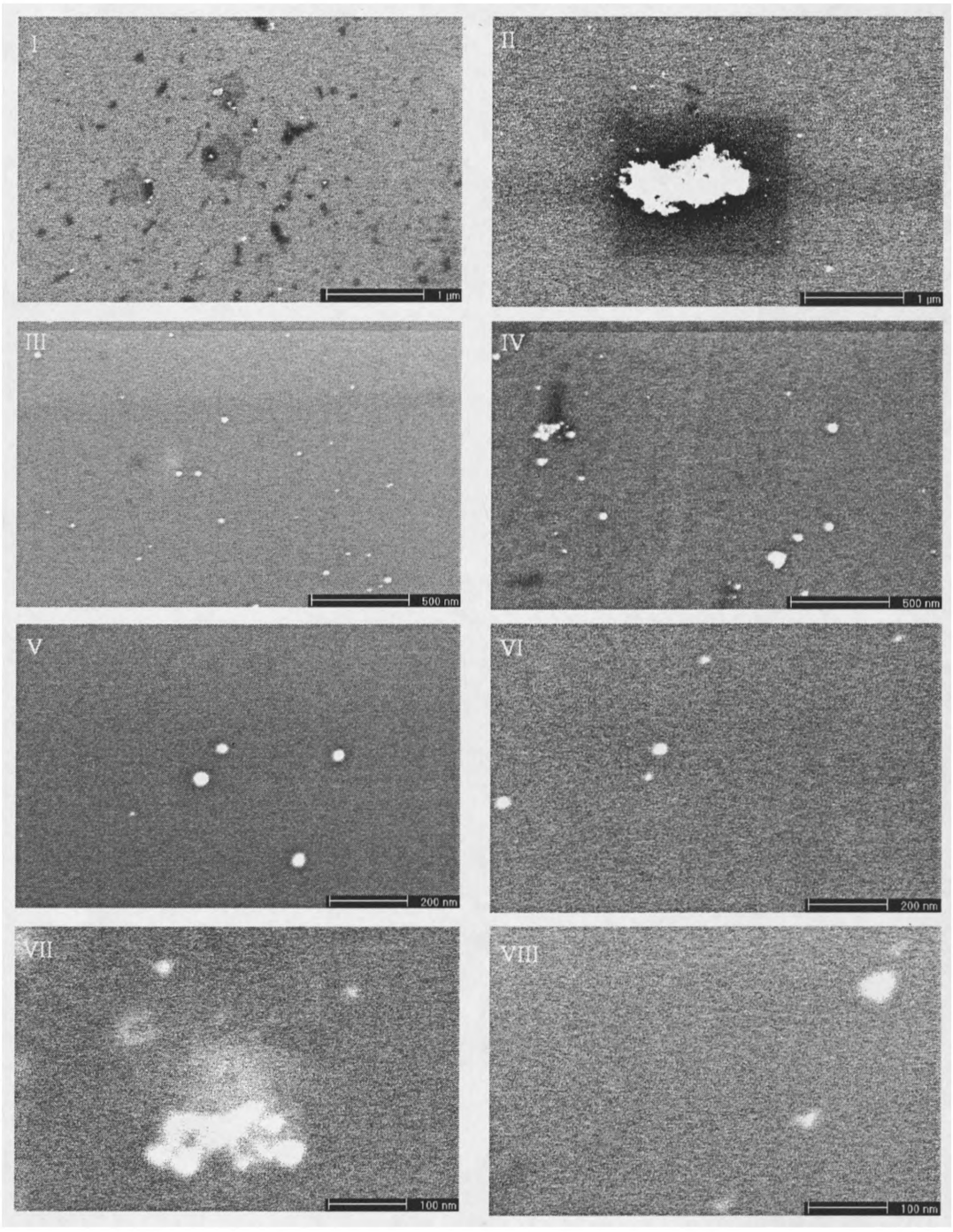

Fig. 4.1.3: SEM images of the surface of rutile(110) single crystal after spin coating with a $HAuCl_4$ solution (2 mmol/l).

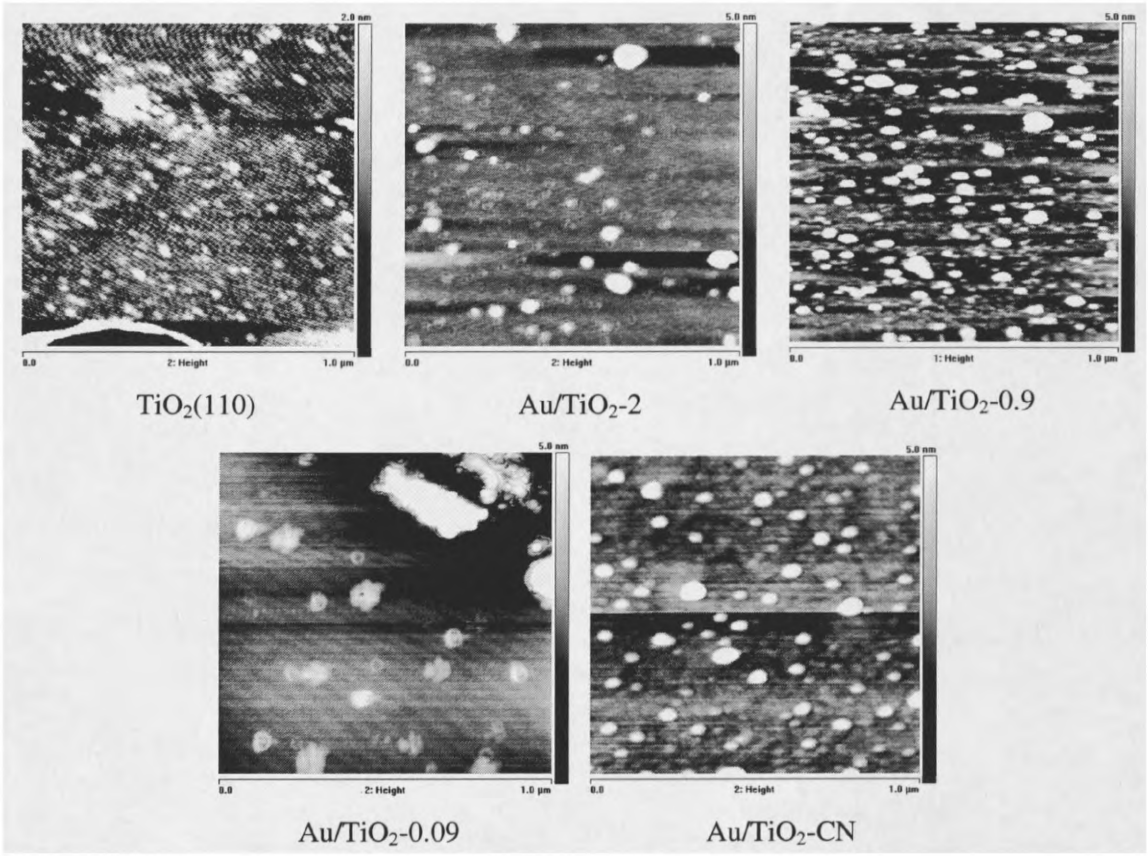

Fig. 4.1.4: AFM images of $TiO_2(110)$ and four samples spin coated with a $HAuCl_4$ solution of 2 mmol/l, 0.9 mmol/l, 0.09 mmol/l and after leaching a sample with basic cyanide solution (Au/TiO_2-CN).

4.1.4.2 Total reflection XANES studies

In fig. 4.1.5 the Au L_{III}-edge spectra of the three samples (Au/TiO_2-2, Au/TiO_2-0.9, Au/TiO_2-0.09, spin coated with $HAuCl_4$ concentrations of 2 mmol/l, 0.9 mmol/l and 0.09 mmol/l, respectively) are shown. For comparison, spectra of gold metal and Au_2O_3 are presented as well. All spectra have an edge position of 11919±1 eV. The spectra of the $Au/TiO_2(110)$ samples show no distinct near-edge resonance in this region, which indicates that the majority of the oxidised gold species was reduced. Oxidised gold

species are formed during the preparation step when ammonia is added to the $HAuCl_4$-solution (for more details see the techniques chapter).

The difference spectra of the samples (see inset of fig. 4.1.5) were calculated by subtracting the spectrum of sample Au/TiO_2-0.09 from the others, and reveal a dip around the absorption edge (11920 eV). This means an increased intensity for sample Au/TiO_2-0.09 in this region. This suggests that either more Au^{3+} species are present in the gold clusters of this sample or that a change in the electronic structure of the gold clusters occurs with small $HAuCl_4$ concentrations. A further indication for a change in the gold clusters by lowering the $HAuCl_4$ concentration is given by the damping of the EXAFS structure, indicative of smaller gold particles.

The differences in the whole spectra (fig. 4.1.6) and the different regions of the spectra, as indicated in fig. 4.1.6, are shown in detail in fig. 4.1.7, 4.1.8 and 4.1.9. As a reference point a gold catalyst with a gold loading of 0.5 wt% was included as reference as well [24]. All spectra of the model gold catalysts show the same differences from the gold standard spectrum as the powder catalyst with low coordinated gold atoms.

The fine structure in the near-edge region of all Au/TiO_2 samples is attenuated, which indicates that, in comparison to bulk metallic gold (cf. fig. 4.1.22), a band structure has not been fully developed. The weak EXAFS also indicates that the atoms have a low coordination number and hence must be associated with small or strongly disordered gold clusters. The damping increases towards lower spin coating concentrations and results in nearly no structure beyond the edge for sample Au/TiO_2-0.09. The damped structure indicates that the first shell coordination numbers are significantly lower than the value of 12 in crystalline bulk gold. Although a direct calculation of the CN from the EXAFS data was not possible, since the S/N ratio was not good enough, a comparison with similar prepared gold catalysts allows to come to this conclusion [25]. This conclusion is especially true for sample Au/TiO_2-0.09.

Significantly reduced coordination numbers indicate the presence of gold particles with diameters of a few nm. In this size range, particles will only contain a few layers of Au. For gold evaporated onto TiO_2 it was observed previously that the gold particles only grow quasi-2-dimensional [26].

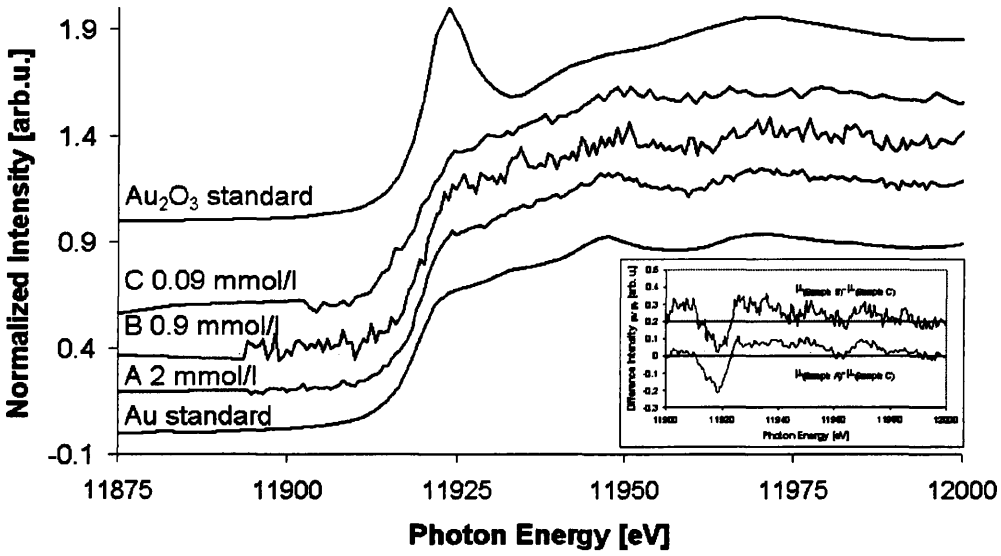

Fig. 4.1.5: XANES spectra of Au/TiO_2 model catalysts prepared using different HAuCl4-solutions (A: Au/TiO_2-2, B: Au/TiO_2-0.9, C: Au/TiO_2-0.09). The time required to obtain these spectra are 8 h, 12 h and 24 h, respectively. As Au standard a gold foil and for the Au_2O_3 and oxidised gold foil was used. The inset shows the difference between the XAS spectra of samples prepared with 2 mmol/l and 0.9 mmol/l with 0.09 mmol/l.

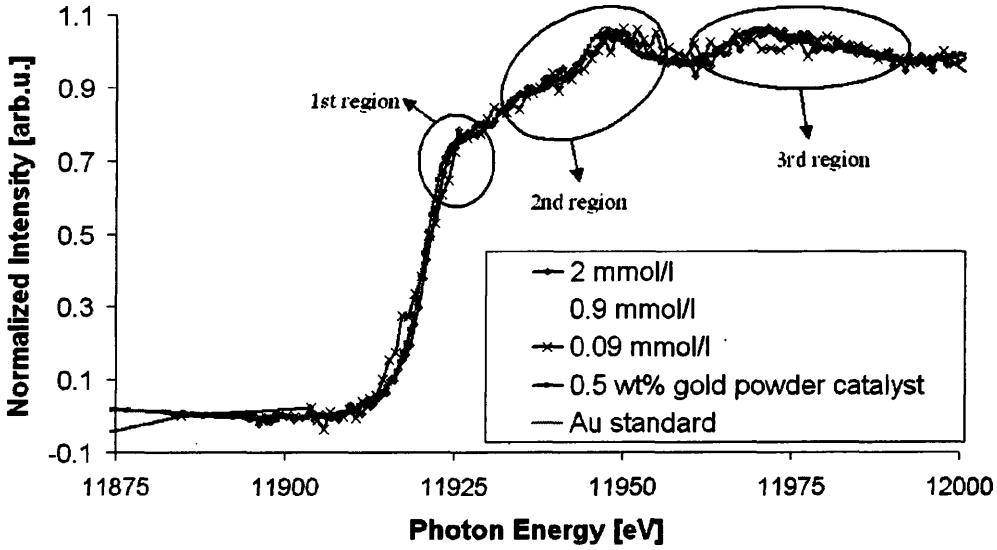

Fig. 4.1.6: XANES data of a gold foil (Au standard), a 0.5 wt% gold powder catalyst supported on P25 and the samples prepared with 2 mmol/l and 0.09 mmol/ $HAuCl_4$ solution. The sample prepared with 0.9 mmol/l $HAuCl_4$-concetration is not shown for sake of clarity. The indicated regions in the figure are shown in the figures 4.1.7, 4.1.8 and 4.1.9 respectively.

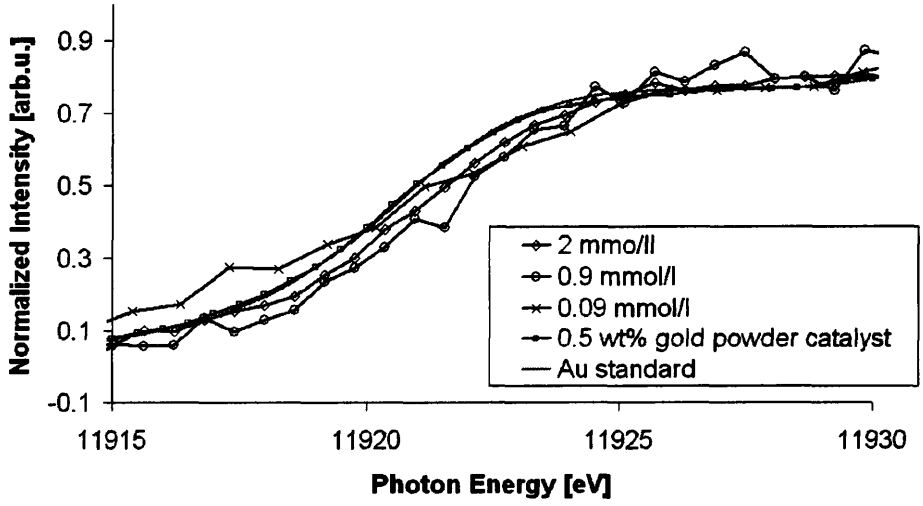

Fig. 4.1.7: XANES data (near edge region) of a gold foil (Au standard), a 0.5 wt% gold powder catalyst supported on P25 and the samples prepared with 2 mmol/l 0.9 mmol/l and 0.09 mmol/ $HAuCl_4$ solution.

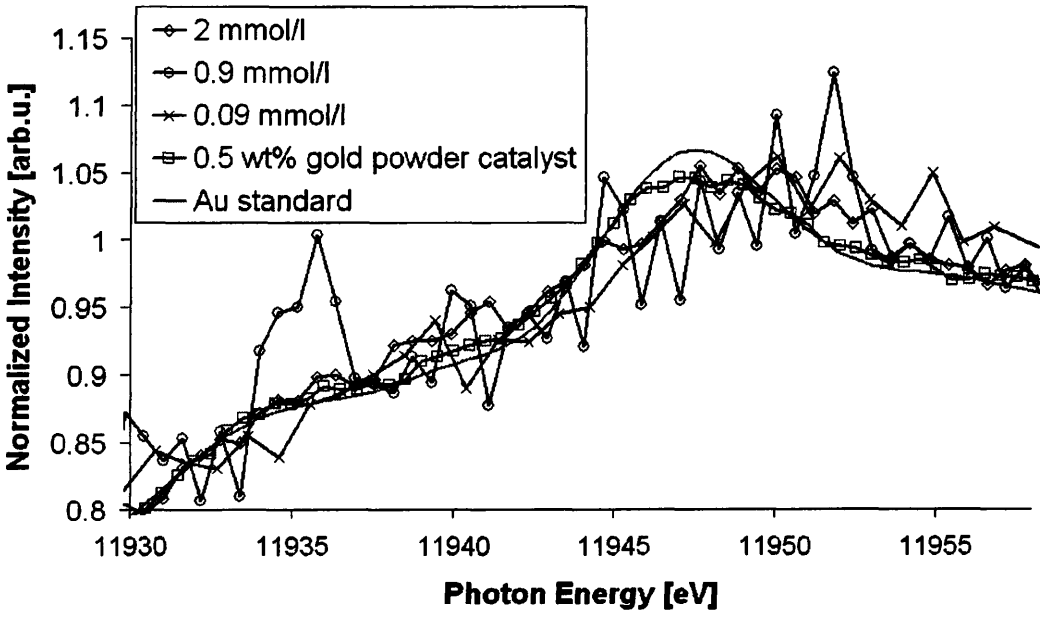

Fig. 4.1.8: XANES data (region 11930 eV to 11960 eV) of a gold foil (Au standard), a 0.5 wt% gold powder catalyst supported on P25 and the samples prepared with 2 mmol/l 0.9 mmol/l and 0.09 mmol/ $HAuCl_4$ solution.

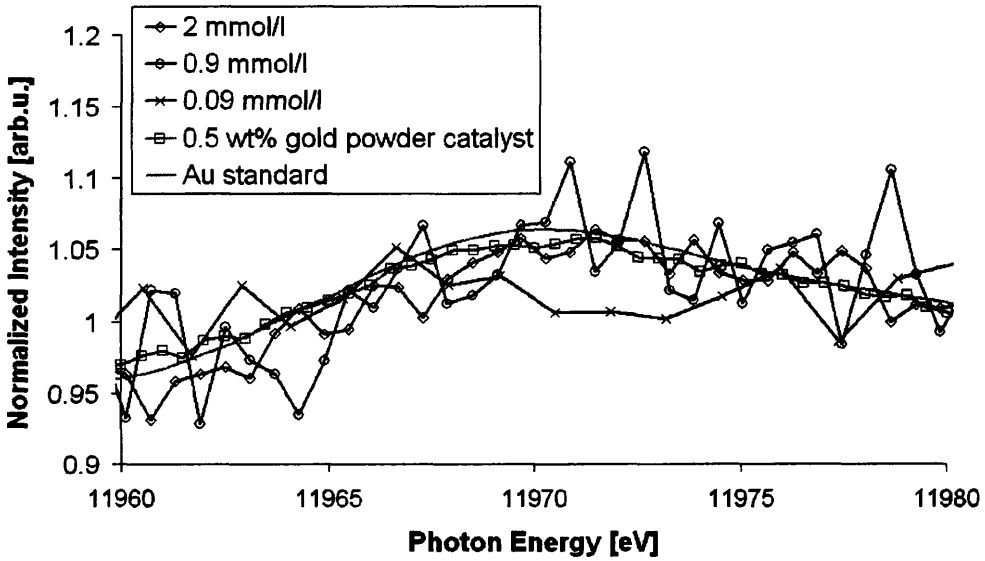

Fig. 4.1.9: XANES data (region 11960 eV to 11980 eV) of a gold foil (Au standard), a 0.5 wt% gold powder catalyst supported on P25 and the samples prepared with 2 mmol/l 0.9 mmol/l and 0.09 mmol/ $HAuCl_4$ solution.

Spectra of sample Au/TiO_2-0.9 at 25°C and 150°C in air (cf. fig. 4.1.10) show a high similarity. However, the spectrum subtraction reveals that at 25°C, a slight pre-edge is present that vanishes at 150°C. This might indicate a clustering effect of the smaller clusters on the sample and result in a narrower cluster size distribution. But better signal to noise ratio, and a spectrum taken after heating would be needed to prove this. Unfortunately, this was not possible with the allocated beamtime since a measurement time of 8 hours resulted in the spectrum represented at 25°C.

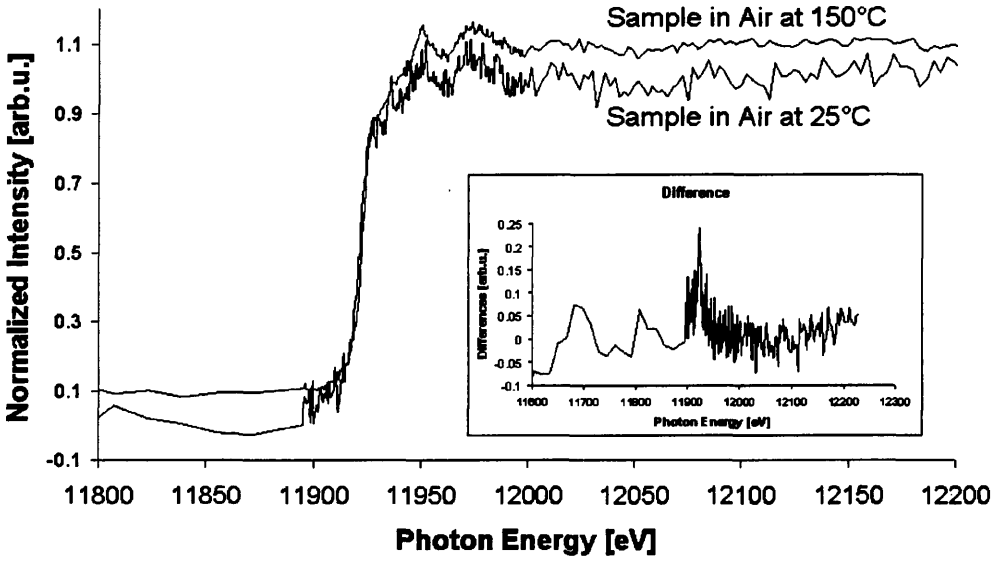

Fig. 4.1.10: XANES spectra of sample Au/TiO_2-0.9 taken at different temperatures. The spectra are stacked. The inset shows the difference between both spectra.

In situ experiments conducted on sample Au/TiO_2-0.9 should reveal any observable interaction of the atmosphere with the gold nanoparticles. This sample was chosen, because the amount of gold is still high enough to give a reasonable XANES spectrum in about 12 h measuring time, but should contain only a very limited number of larger gold clusters.

The resulting spectra of sample Au/TiO_2-0.9 in pure CO and O_2 atmosphere are presented in fig. 4.1.11. Again the damped XANES and EXAFS structure of the gold particles is

present and only small oscillations in the first 100 eV behind the edge can be seen. In general the spectra show no differences (cf. inset of 4.1.7), but from 11924 eV to 11935 eV the absorption of the X-rays is increased under CO conditions. This increase indicates the interaction of the CO with the gold nanoparticles, as a similar effect on dispersed Au/TiO_2 catalysts [27] show.

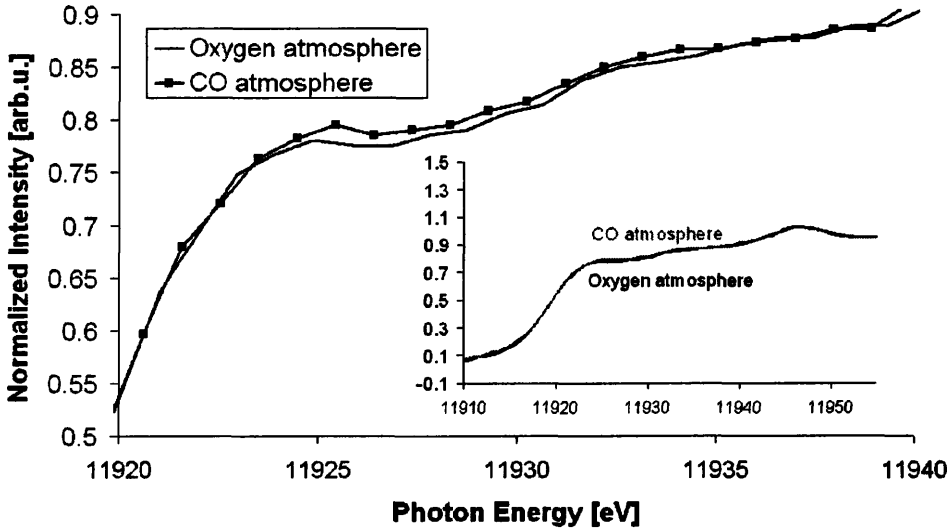

Fig. 4.1.11: Au L_{III}-edge of gold nanoparticles on rutile(110) (Au/TiO_2-0.9) in CO and O_2 atmosphere at 1.5 bar. The inset shows the total XANES region.

4.1.4.3 Soft X-ray XANES studies

In fig. 4.1.12 the O K-edge spectra of a Au/TiO_2 sample prepared with 2 mmol/l $HAuCl_4$-solution under different CO pressures are presented. To compare the different conditions with each other, the normalisation region (0.5 eV to 20 eV behind the edge) for the spectra had to be chosen close to the absorption edge (531 eV). However this results in a slightly different shape of the spectra compared to those in the literature [28, 29].

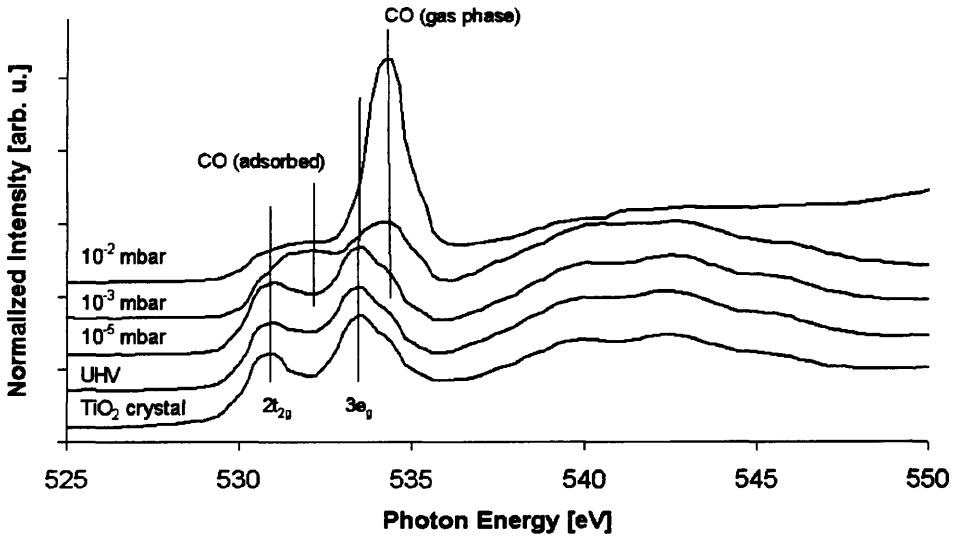

Fig. 4.1.12: O K-edge spectra of a Au/TiO_2(110) sample prepared with 2 mmol/l $HAuCl_4$-solution at different CO pressures.

The TiO_2 crystal – as well as the sample Au/TiO_2-2 under vacuum condition – shows a typical O K-edge spectrum of rutile (see e.g. [28]). The two main areas of the spectra are due to the interaction of the O 2s and 2p states with the Ti 3d (530 eV – 535 eV), Ti 4s and 4p (536 eV – 550 eV) states to form the empty states into which the electrons of the O K-shell are promoted (cf. table 4.1.1). Due to the tetrahedral crystal structure of rutile these orbitals split up again and result in the O 1s – Ti 3d combination in an energetic lower Ti 3d $2t_{2g}$ (Ti 3d; O 2pπ) and a Ti 3d $3e_g$ (Ti 3d; O 2pσ) peak. The O 1s interaction with the Ti 4sp orbitals results in a Ti 4sp $3a_{1g}$ (Ti 4s; O 2p) and a Ti 4sp $4t_{1u}$ (Ti 4p; O 2p) state (cf. fig. 4.1.13) [29].

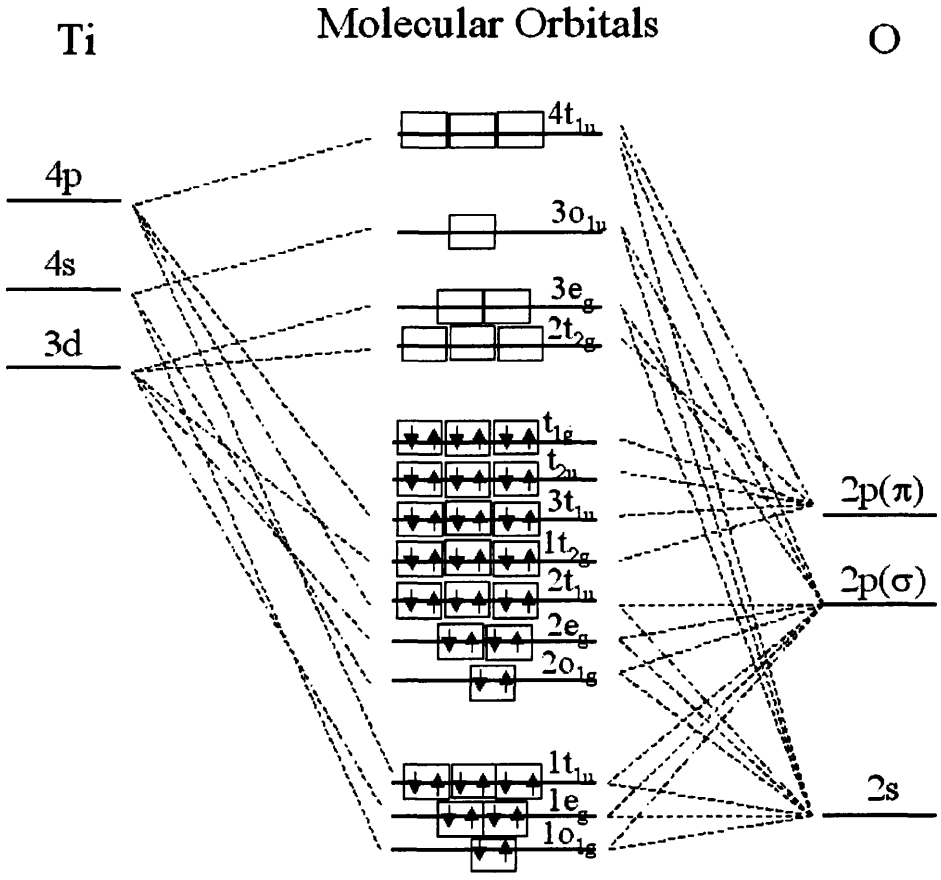

Fig. 4.1.13: Schematics of molecular orbitals of TiO_2 with an octahedral symmetry. The molecular orbitals are derived from a linear combination of the atomic orbitals (LCAO) [29]. Not drawn to scale.

At higher CO pressure (10^{-3} and 10^{-2} mbar) the Ti 3d peaks get partially covered by the CO peaks, and their exact position is not reliably detectable anymore.
Comparing the photon energies of the O K-edge for TiO_2 and gaseous CO with the literature data [28, 30] a very good agreement between the two "standards" was shown (cf. table 4.1.1).

The contribution of the CO at elevated pressures can also be seen. The main CO peak at (534.2 eV) is from gas phase CO (see chapter 4.2 and ref. [30]). That no further peaks

above 538 eV are present – for gas phase CO – can be explained by the relatively low intensity of these peaks. A further contribution of CO can be seen at pressures of 10^{-3} mbar and above. This peak, around 532.2 eV, indicates the presence of CO adsorbed on the sample. CO adsorption studies on nickel [31, 32] and tungsten [33] revealed photon energies for chemically adsorbed CO that are lower than for free, or physically adsorbed CO [30, 34].

Comparing the O K-edge of the same sample at different temperatures and under vacuum, as well as 10^{-3} mbar CO pressure, is shown in fig. 4.1.14 and 4.1.15. Under both conditions the increase of the temperature does not have an influence on the TiO_2 structure, as no differences are observed. Furthermore no increase in the possibility of adsorbing CO by the sample is indicated, since no CO peak appears in the spectra at elevated temperatures.

Table 4.1.1: Comparison of the different states in the O K-edge spectra of sample Au/TiO_2-2 at different CO pressure.

	Ti 3d $2t_{2g}$	$CO_{adsorbed}$	Ti 3d $3e_g$	$CO_{gasphase}$	Ti 4sp $3a_{1g}$	Ti 4sp $4t_{1u}$
10^{-2} mbar	(530.8 eV)	532.0 eV	-	534.2 eV		
10^{-3} mbar	530.8 eV	532.2 eV	-	534.2 eV	540.0 eV	542.6 eV
10^{-5} mbar	531.0 eV	-	533.6 eV	(534.2 eV)	539.8 eV	542.6 eV
UHV	531.0 eV	-	533.4 eV	-	539.8 eV	542.4 eV
rutile	530.8 eV	-	533.4 eV	-	540.0 eV	542.6 eV
Kucheyev (and ref.)	530.9 eV	-	533.9 eV	-	-	-
Lusvardi	531.3	-	534.0	-	540.3	543.5
Stevens CO on W	-	533.5 eV	-	-	-	-
Tillborg CO on Ni	-	~533.5 eV	-	-	-	-
Domke (EELS)	-	-	-	534.2 eV	-	-

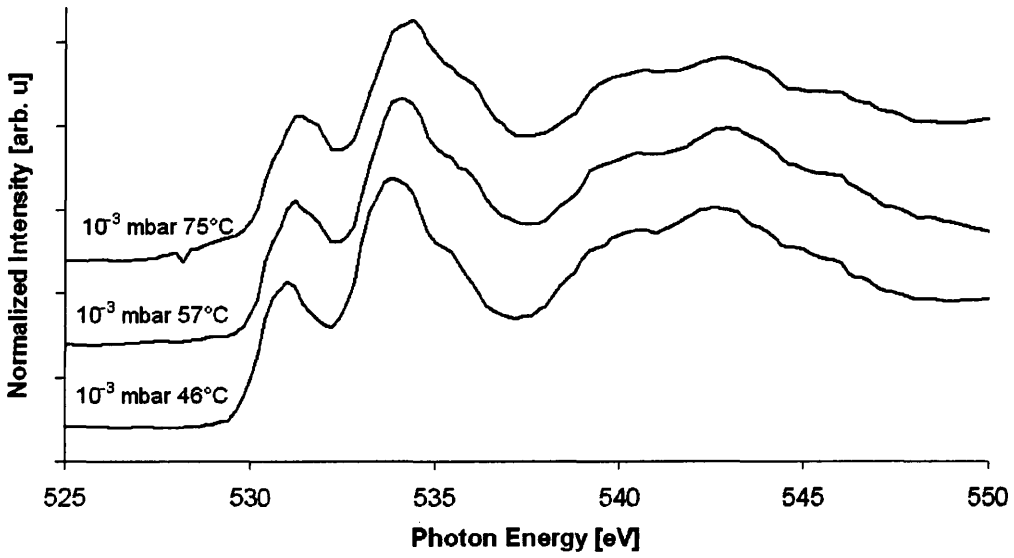

Fig. 4.1.14: O K-edge spectra of a $Au/TiO_2(110)$ sample at 10^{-3} mbar CO pressures at different temperatures.

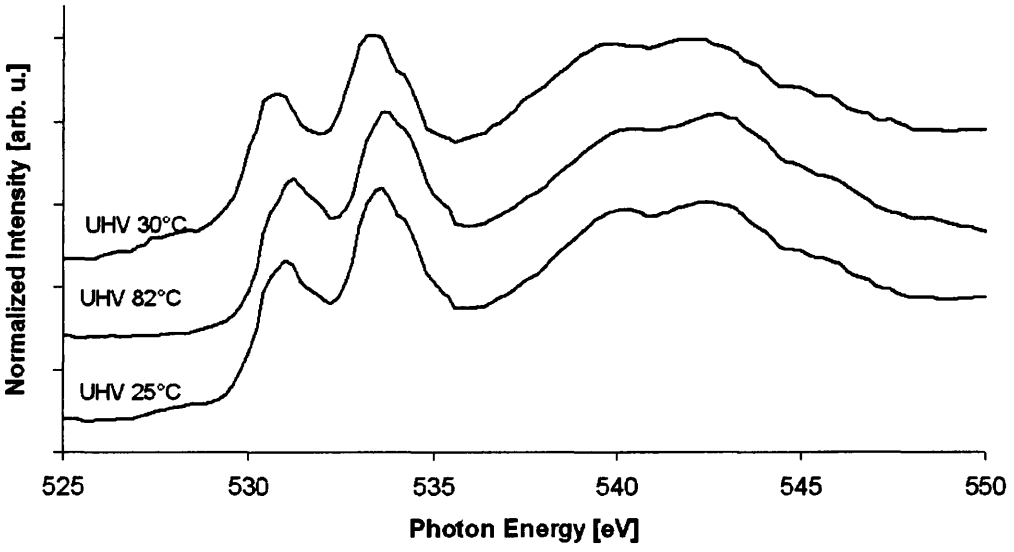

Fig. 4.1.15: O K-edge spectra of a $Au/TiO_2(110)$ sample under UHV conditions (10^{-6} mbar) at different temperatures.

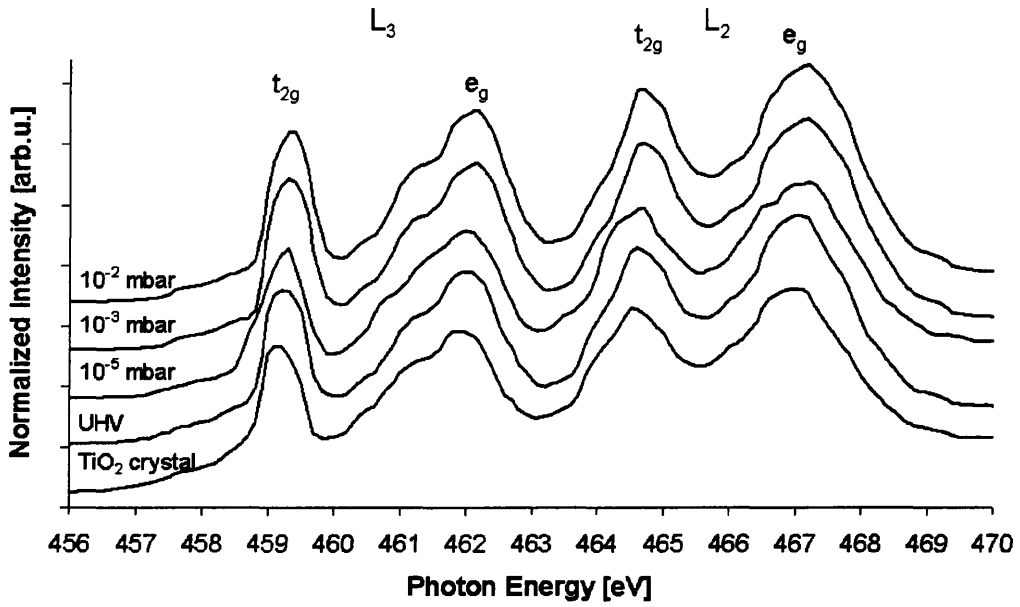

Fig. 4.1.16: Ti L-edge spectra of a Au/TiO_2(110) sample at different CO pressures.

In fig. 4.1.16 the Ti L-edge of the sample prepared with a $HAuCl_4$-concentration of 2 mmol/l at different CO pressure and a "pure" rutile single crystal are compared. All spectra show the L_{III} and L_{II}-edge, and the typical splitting of these peaks into a t_{2g} and e_g branch by the crystal field of the rutile [28, 35]. The spectra do not show strong differences between each other, and are also comparable to literature spectra of rutile single crystals (see also table 4.1.2). This indicates that the gold nanoparticles on the sample prepared with a $HAuCl_4$-concentration of 2 mmol/l have no influence on the crystal structure of the support.

Nevertheless, a change in the surface layer of the TiO_2 crystal cannot be ruled out, since the XAS data will probe the first 5 to (maybe) 10 unit cells deep of the crystal. Hence, very small changes in the crystal structure might be not resolved in the spectra.

Table 4.1.2: Ti L-edge positions of the sample prepared with a $HAuCl_4$-concentration of 2 mmol/l under different CO pressures and literature data.

	L_3 t_{2g}	L_3 e_g	L_2 t_{2g}	L_2 e_g
10^{-2} mbar	458.3 eV	461.2 eV	463.7 eV	466.2 eV
10^{-3} mbar	458.3 eV	461.2 eV	463.7 eV	466.1 eV
10^{-5} mbar	458.3 eV	461.0 eV	463.6 eV	466.2 eV
UHV	458.3 eV	461.0 eV	463.6 eV	466.0 eV
Rutile	458.2 eV	461.0 eV	463.6 eV	466.0 eV
Kucheyev	458.2 eV	461.1 eV	463.8	-

4.1.4.4 XPS

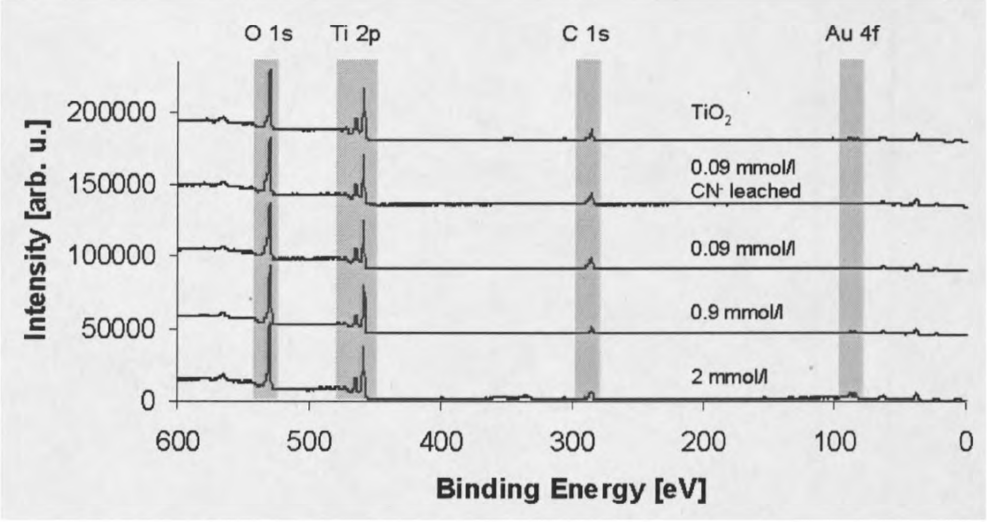

Fig. 4.1.17: XPS survey scans of $Au/TiO_2(110)$ samples with the indicated $HAuCl_4$ concentrations used during spin coating.

The survey scans of the different gold catalysts show the elemental composition of Au, C, Ti and O (cf. fig. 4.1.18 and table 4.1.3). Whereas, a notable Au 4f signal is only visible for the samples prepared with a $HAuCl_4$-concentration of 2 mmol/l and 0.9 mmol/l, a carbon signal can be identified in all spectra. When comparing the intensities of the C 1s and Au 4f peak it should be remembered that gold has a relative atomic sensitivity factor (RSF) approximately 16 times higher than that of carbon. This means for the sample

prepared with a $HAuCl_4$-concentration of 2 mmol/l the amount of gold on the sample is roughly 1/16 of that of carbon, even though the intensities are approximately the same. This confirms that there are only small amounts of gold on the samples.

The change in the carbon intensities between the different samples can be explained by different storage times for the samples, and the adsorption of carbonaceous contamination. For the sample prepared with a $HAuCl_4$ concentration of 0.09 mmol/l this has been tested by scanning the sample 1 day after preparation, followed by storage of 2 months. The amount of carbon clearly increases during storage from around 5% to about 13%. Also the Ti 2p and the Au 4f intensities decrease slightly, by the shielding of these signals from the formed carbon overlayer. The oxygen intensity remains roughly constant, which indicates that the carbon residuals also include some oxygen groups.

Table 4.1.3: XPS intensity (without RSF) comparison for the used supported gold nanoparticle model catalysts.

Catalyst	Storage time	Intensity			
		Au 4f	C 1s	Ti 2p	O 1s
Au/TiO_2-2	2 days	9.2%	8.9%	41.9%	40.0%
Au/TiO_2-0.9	2 days	4.1%	6.6%	44.8%	44.4%
Au/TiO_2-0.09	1 day	~1%*	5.0%	48.5%	45.5%
Au/TiO_2-0.09	2 month	~1%*	12.9%	40.1%	46.2%
Au/TiO_2-0.09CN	1 week after leaching	0%	9.8%	42.9%	47.3%
TiO_2	1 week after cleaning	0%	9.1%	44.9%	46.0%

*The Au 4f peak is very close to the noise level and a reliable value cannot be obtained from the survey scan

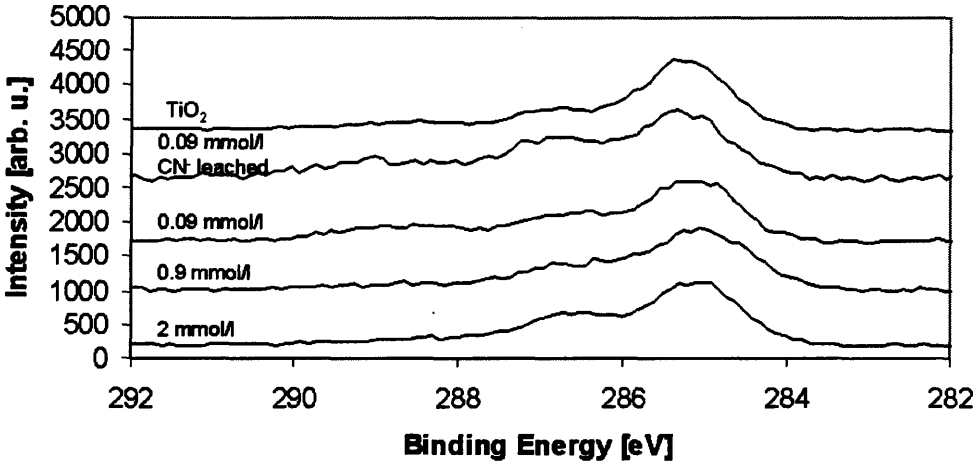

Fig. 4.1.18: C 1s XP spectra of $Au/TiO_2(110)$ samples with the indicated $HAuCl_4$ concentrations used during spin coating.

In fig 4.1.18 and 4.1.19 the C 1s and O 1s XP spectra of the different samples are shown. The C 1s spectrum contains, for all spectra, 2 peaks, one at 285 eV, assigned to C-C and C-H groups and one at 286.5 eV, assigned to C-O groups [36]. The O 1s spectra show only one peak at 530 eV, which is from the TiO_2 support [20]. The absence of a change in the line shape of both spectra indicates that the carbonaceous contamination is similar for all samples.

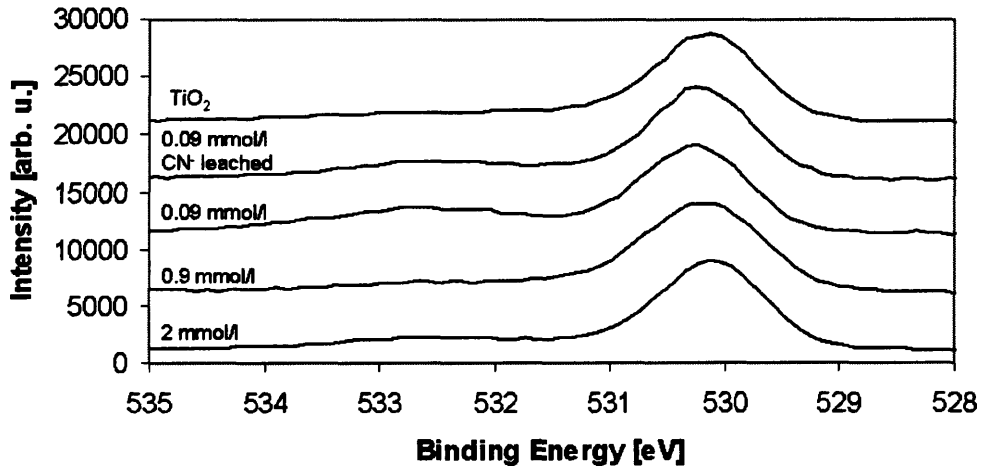

Fig. 4.1.19: O 1s XP spectra of $Au/TiO_2(110)$ samples with the indicated $HAuCl_4$ concentrations used during spin coating.

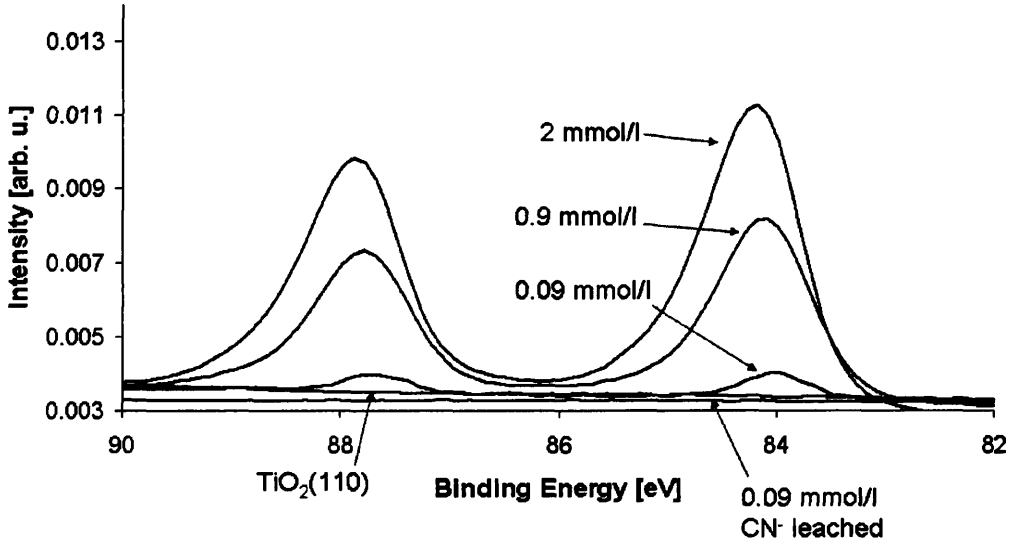

Fig. 4.1.20: XP Au 4f spectra of the different Au/TiO_2 samples.

The XPS results shown in fig. 4.1.20 show the increase of gold concentration on the sample with increasing spin coating concentration. For the sample prepared with a $HAuCl_4$ concentration of 2 mmol/l and the sample prepared with a $HAuCl_4$ concentration

of 0.9 mmol/l two clear Au 4f spectra can be seen. The BE of ~84 eV indicates that only Au^0 is present. Possible Au^{3+} species could not be detected, which might be due to the fact that Au^{3+} are light sensitive, and can be reduced by X-rays. For the sample prepared with a $HAuCl_4$-concentration of 0.09 mmol/l the gold signal is already drastically reduced, but again, only Au^0 can be seen. After leaching the sample prepared with a $HAuCl_4$-concentration of 0.09 mmol/l with a basic cyanide solution, no gold can be detected, and the spectrum is similar to a spectrum of untreated TiO_2.

The fitting for the Au 4f peaks with one and two components is shown for the sample prepared with a $HAuCl_4$-concentration of 2 mmol/l in fig. 4.1.21. The fit with only one gold component (bottom) shows a slight asymmetry of the gold peaks to higher binding energy (BE). This asymmetry (cf. table 4.1.4) is due to gold clusters adsorbed on different positions on the single crystal (marked as Au^0(I) and Au^0(II) for the two different BEs). This effect has also been found by Lee et al. [37] for mass selected gold clusters on TiO_2(110). The effect is due to the adsorption of the gold clusters on different adsorption sites like steps and terraces. The different adsorption sites have influence on the screening of the electron hole in the gold clusters induced by the X-ray absorption. This affects the final state of the gold clusters and leads to different BEs of the clusters and is also known as Coulomb effect (cf. techniques section and [38]).

Table 4.1.4: XPS Au 4f fitting peaks for sample Au/TiO_2-2.

Assignment	Position [eV]	FWHM [eV]
1 component		
Au^0 $4f_{7/2}$	84.0	1.11
Au^0 $4f_{5/2}$	87.7	1.11
2 components		
Au^0(I) $4f_{7/2}$	83.9	0.80
Au^0(II) $4f_{7/2}$	84.3	1.47
Au^0(I) $4f_{5/2}$	87.6	0.80
Au^0(II) $4f_{5/2}$	87.8	1.47

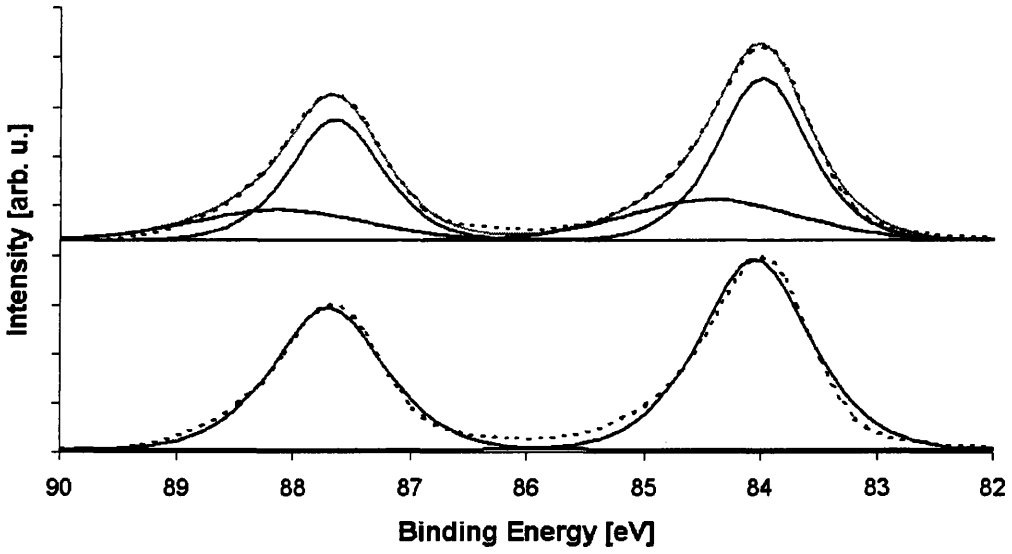

Fig. 4.1.21: XPS Au 4f fits for sample Au/TiO_2-2. Top with two components, bottom with one. The doted lines are the experimental data; the black lines are the fitted components; the grey line is the fit.

The hypothetical monolayer thickness, which can be obtained by using equation 4.1.3, gives an indication of the amount of gold on the substrate. Therefore the relative intensities between the Ti 3s and Au 4f peaks were used and are represented in table 4.1.5. As fig. 4.1.20 suggests the monolayer thickness (ϕ) decreases with decreasing spin coating concentration. From the long accumulation time of the XPS and XAS experiments, it would be expected the amount of monolayers on the samples is very small and does not exceed 0.1 monolayer even for the "high" concentrated sample.

Table 4.1.5: Calculated gold monolayers (ϕ) on the Au/TiO_2 samples.

Spin coating concentration	$I_{Au\ 4f}$	$RSF_{Au\ 4f}$	$I_{Ti\ 2p}$	$RSF_{Ti\ 2p}$	Θ	ϕ
2 mmol	3.0	17.4	1.0	0.408	0.19	0.084
0.9 mmol	0.64	17.4	1.0	0.408	0.10	0.044
0.09 mmol	0.069 ($4f_{7/2}$)	9.79 ($4f_{7/2}$)	1.0	0.408	0.080	0.034

4.1.5 Discussion

4.1.5.1 Morphology of the sample

The amount, and size, of the gold particles prepared by spin coating was studied with AFM and SEM. The resolution of SEM was not high enough to be able to detect any gold particles on the sample. The smallest particles visible in SEM were about 20 nm in diameter and are presumably carbon contamination. A chemical analysis of the small particles with EDX was not possible, since the probing depth is too deep and only Ti and O could be detected in the spectrum. The AFM images showed more details of the surface, but revealed that it is difficult to determine small particles on the reconstructed TiO_2(110) surface.

To clarify whether a certain particle is comprised of gold or carbon, STM measurements in combination with STS could be a very useful tool. Unfortunately, the TiO_2 support used in this work is not conductive enough to allow an engagement with an STM-tip. To overcome this problem, Goodman et al. [39, 40] prepared TiO_2 layers on metal single crystals to achieve the required conductivity. Another method would be to induce defects in the single crystal to increase the conductivity. This can be done e.g. by heating of the TiO_2-crystal [20]. But this can only be done before the preparation of the gold particles on the crystal, since the required temperatures would lead to massive clustering of the gold particles.

This leaves the question of the particle size and size distribution open. An estimation of the particle size can be given by the XANES data and they reveal that the particles must have, in all cases, nm sizes, with most likely no particle diameter wider than 3 nm. This shows that the aimed particle size of about 1 nm was, at least, nearly reached for the given samples.

4.1.5.2 XANES

In fig. 4.1.22 experimental and theoretical data of supported gold nanoparticles with low coordination numbers are given. Both show, in the XANES region, a dampening of the

structure. Very similar results are present in the XANES data obtained on the gold particles supported on flat TiO_2 (fig. 4.1.10 to 4.1.13). The theoretical calculations indicate that coordination numbers of maximum 10 to 9 are required to see the dampening of the structure. From this, it can be concluded that the gold particles supported on the flat TiO_2 prepared with a $HAuCl_4$-concentration of 0.09 mmol/l have a coordination number (CN) of 9 at the maximum. This CN, on the other hand, can only be achieved with a non-3D growth of the particles. From STM studies, it is known that gold particles with a diameter of more than a few nm grow 3 dimensionally, and hence the diameter of the formed gold particles must be nanoparticlular with diameters of maximum 3 nm.

But the longer measurement times also show that – at least with the preparation method used at the present study – the measurements take an unreasonably long time at a 2nd generation synchrotron (about 24 h for one condition).

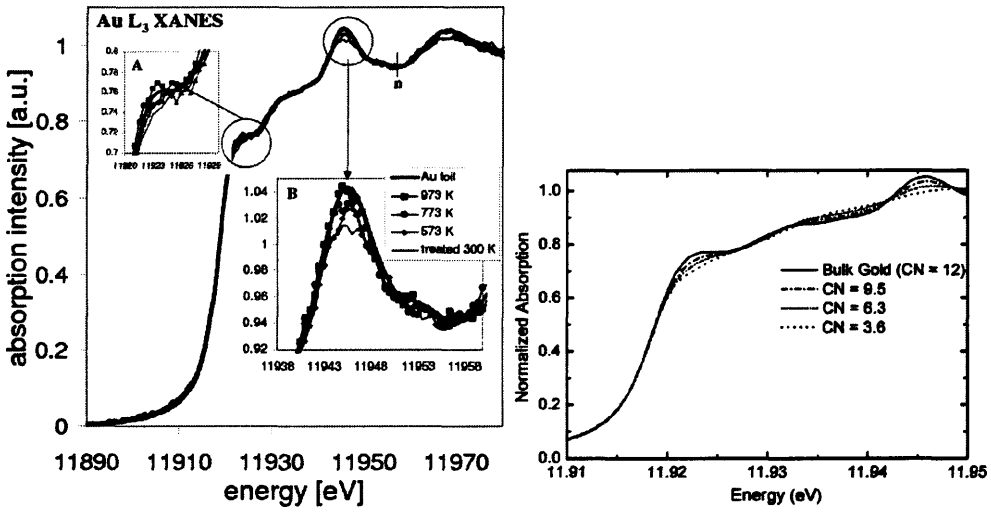

Fig. 4.1.22: Left figure shows XANES data of a 0.5 wt% Au/TiO_2 catalyst that has been differently calcinated [24]. With increasing calcinations temperature, the particle size of the gold clusters increase, therefore the coordination number of the gold atoms increases, and the dampening of the XANES structure is decreasing, becoming close to metallic gold for the sample heated to 973 K. The right figure shows theoretically calculated

XANES spectra for gold clusters with coordination numbers of 9.5, 6.3 and 3.6 respectively [41].

A clear difference between the gold nanoparticles supported on the flat rutile(110) crystals and the powder supported ones is the oxidation state after the preparation. Whereas most of the gold nanoparticles on the powder particles [1, 42 - 44] are Au^{3+} (and are often reduced to Au^0 by calcining); XANES and XPS measurements indicate that the nanoparticles on the flat support are nearly all reduced to Au^0 after preparation. It is often reported that the Au^{3+} particles have a high sensitivity to light and can be reduced by photo-induction. This might have happened under the long measurement times of these samples.

Comparing the preparation methods, the only differences are that the solution is normally heated to about 80°C for the powder impregnation, and that the gold particles are allowed to adsorb on the support for about 1 h. In the flat model case this is not possible, because heating of the solution would lead to a non-uniform film [45]. The lack of heating may not be a problem, however, Moreau et al. [46] could not find any indication that heating beyond room temperature led to any change in their generated catalyst. The influence of the different adsorption times must remain unanswered. It seems unlikely that the adsorption time would have an influence on the chemical state of the particles.

It should be finally addressed that most of the TiO_2 powder supports used in gold catalysis (like the commonly used Degussa P25) contain anatase besides rutile. This mixture cannot be simulated by a single crystal support, and might have an influence on the stability of the oxidised gold species.

Dosing CO on gold nanoparticles supported on rutile single crystal gives similar results in the hard Au L_{III}-edge and the soft O K-edge XANES spectra. The Au L_{III}-edge spectra show a slight electronic change in the gold particles, visible in a slight near edge resonance as also recently reported by Henao *et al.* [47]. The soft X-ray absorption results confirm that CO adsorbs on such samples. This leads to the conclusion that at least a part of the CO adsorbs on the gold particles. It has been found before that CO can adsorb on

either pure gold [48] or on supported gold nanoparticles [49, 50]. It could be shown as well that CO prefers to adsorb on low coordinated gold atoms.

An interaction between O_2 and the sample prepared with a $HAuCl_4$-concentration of 0.9 mmol/l in the Au L_{III}-edge has not been found. This agrees with gold single crystal studies [51, 52] in which the oxygen has to be "activated" by e.g. low temperature electron bombardment [53] or by using atomic oxygen [52] to be able to chemisorb on the gold surface. This indicates that the O_2 is likely to be adsorbed on the TiO_2 support and would be supplied to the gold particles on a CO oxidation as recent theoretical calculations show [54]. It is important to note the influence of water for this, and might explain the difference in the literature about reaction mechanism and the role of water in the catalytic oxidation of CO [1, 55].

The O K-edge spectra gained for TiO_2 and gas phase CO correlate very well with the data known from literature [28, 30, 56]. The exception is the Ti 4sp $4t_{1u}$, which is about 1 eV shifted to lower photon energy in our case. The difference can be explained by the short measurement range in this study, which made it necessary to choose the normalization area of the spectra closer to the absorption edge than is known from literature spectra. This gives a slightly different background shape for the spectra and results in an increased uncertainty for the peak position at photon energies above 540 eV.

Beside gas phase CO, adsorbed CO could be identified. The values differ from the values given by Stevens *et al.* [33] and Tillborg *et al.* [32] by 1.3 eV to 1.5 eV. But due to the double referencing to the TiO_2 and CO gas phase peak we are very confident that our value is at the right position. Tillborg *et al.* also reported that under certain conditions a splitting of the CO peaks is present when H_2 is coadsorbed on the Ni(110) sample. This results in a peak at ~532 eV and ~534 eV and shows the variation potential of the adsorbed CO peak.

It should also be considered that the literature data are experiments on "perfect" single crystal surfaces, with a high coordination number for the surface atoms and a full underlying conduction band. In the present gold nanoparticle study this is not the case. Also Björneholm *et al.* [34] showed that small changes in the adsorption site or geometry of the CO molecule on single crystal samples can lead to a shift of the photon energy of

several tenth of eV. This indicates that the difference in the photon energies must be related to the different types of samples.

4.1.6 Conclusions

It has been shown that the concentration of the $HAuCl_4$ solution used during the spin coating process has a crucial effect on the particle size of the formed gold clusters. All samples show a trend to non-bulk behaviour, whereas the sample with the lowest concentration (0.09 mmol/l) has a clear nanoparticle Au L_{III}-edge XANES pattern. The experiments further show that cluster size influences reducibility. Samples with large Au clusters (2 mmol/l and 0.9 mmol/l $HAuCl_4$-concentration) show only a very small near edge resonance. The sample prepared with a $HAuCl_4$-concentration of 0.09 mmol/l has a slightly increased near edge resonance, which can be interpreted as either Au^{3+} present on the sample or a change from metallic to non-metallic behaviour of the gold cluster.
In situ high-pressure XANES spectroscopy on flat model Au catalysts was carried out successfully with soft and hard X-rays. The *in situ* O K-edge spectra show, beside the presence of gas phase CO, some CO adsorption is found on the sample. The *in situ* Au L_{III}-edge spectra prove that the CO interacts with the gold nanoparticles. The Ti L-edge indicates that CO also interacts with the support.

References

[1] Haruta, M.; Cattech, **2002**, *6*, 102-115.

[2] Wallace, William T.; Whetten, Robert L.; Journal of the American Chemical Society; **2002**, *124*, 7499-7505.

[3] Bond, G. C.; Thompson, D. T.; Catalysis Reviews - Science and Engineering; **1999**, *41*, 319-388.

[4] Olea, M.; Iwasawa, Y.; Applied Catalysis, A: General; **2004**, *275*, 35-42.

[5] Stiehl, J. D.; Kim, T. S.; McClure, S. M.; Mullins, C. B.; Journal of the American Chemical Society; **2004**, *126*, 13574-13575.

[6] Iizuka, Y.; Tode, T.; Takao, T.; Yatsu, K.; Takeuchi, T.; Tsubota, S.; Haruta, M.; Journal of Catalysis, **1999**, *187*, 50-58.

[7] Meyer, R.; Lemire, C.; Shaikhutdinov, S. K.; Freund, H. J.; Gold Bulletin, **2004**, *37*, 72-124.

[8] Costello, C. K.; Kung, M. C.; Oh, H. S.; Wang, Y.; Kung, H. H.; Applied Catalysis, A: General, **2002**, *232*, 159-168.

[9] Bondzie, V. A.; Parker, S. C.; Campbell, C. T.; Catalysis Letters, **1999**, *63*, 143-151.

[10] Haruta, M.; Catalysis Surveys from Japan, **1997**, *1*, 61-73.

[11] Daniells, S. T.; Overweg, A. R.; Makkee, M.; Moulijn, J. A.; Journal of Catalysis, **2005**, *230*, 52-65.

[12] Bond, G. C.; Thompson, D. T.; Gold Bulletin; **2004**, *126*, 1892-1899.

[13] Niemantsverdriet, J. W.; Engelen, A. F. P.; de Jong, A. M.; Wieldraaijer, W.; Kramer, G. J.; Applied Surface Science, **1999**, *144-145* , 366-374.

[14] Sanders, A. F. H.; de Jong, A. M.; de Beer, V. H. J. ; van Veen, J. A. R.; Niemantsverdriet, J. M.; Applied Surface Science, **1999**, *144-145*, 380-384.

[15] Kuipers, E. W.; Doornkamp, C.; Wieldraaijer, W.; van den Berg, R. E.; Chemical Materials, *1993*, **5**, 1367-1369.

[16] Niemantsverdriet, J. W.; Engelen, A. F. P.; de Jong, A. M.; Wieldraaijer, W.; Kramer, G. J.; Applied Surface Science, **1999**, *144-145*, 366-374.

[17] Braun, S.; *Diploma Thesis*, Freie Universität Berlin, **2003**.

[18] Fu, Q.; Saltsburg, H.; Flytzani-Stephanopoulos, M.; Science, **2003**, *301*, 935-938.

[19] http://cars9.uchicago.edu/ifeffit/

[20] Diebold, U.; Surface Science Reports, **2003**, *48*, 53-229.

[21] Schroeder, S. L. M.; *Diploma Thesis*, Freie Universität Berlin, **1991**.

[22] Briggs, D.; Seah, M. P.; *Practical Surface Analysis - 2nd edition*, John Wiley & Sons, **1990**.

[23] Li, M.; Hebenstreit, W.; Gross, L.; Diebold, U.; Henderson, M. A.; Jennison, D. R.; Schultz, P. A.; Sears, M. P.; Surface Science, **1999**, *437*, 173.

[24]: Willneff, E. A.; *PhD Thesis*, University of Manchester, **2007**.

[25] Zhang, P.; Sham, T. K.; Physical Review Letters, **2003**, *90*, 245502-1 – 245502-4.

[26] Chusuei; C. C.; Lai, X.; Luo, K.; Goodman, D. W.; Topics in Catalysis, **2001**, *14*, 71-83.

[27] Henao, J. D.; Caputo, T.; Yang, J. H.; Kung, M. C.; Kung, H. H.; Journal of Physical Chemistry B, **2006**, *110*, 8689-8700.

[28] Kucheyev, S. O.; van Buuren, T.; Baumann, T. F.; Satcher, J. H., Jr.; Willey, T. M.; Meulenberg, R. W.; Felter, T. E.; Poco, J. F.; Gammon, S. A.; Terminello, L. J.; Physical Review B: Condensed Matter and Materials Physics, **2004**, *69*, 245102/1-245102/7.

[29] Chen, J. G.; Surface Science Reports, **1997**, *30*, 1-152.

[30] Domke, M.; Xue, C.; Puschmann, A.; Mandel, T.; Hudson, E.; Shirley, D. A.; Kaindl, G.; Chemical Physics Letters, **1990**, *173*, 122-128. Domke, M.; Xue, C.; Puschmann, A.; Mandel, T.; Hudson, E.; Shirley, D. A.; Kaindl, G.;Chemical Physics Letters, **1990**, *174*, 668.

[31] Illing, D.; Heskett, D.; Plummer, E. W.; Freund, H. J.; Somers, J.; Lindner, T.; Bradshaw, A. M.; Buskotte, U.; Neumann, M.; Starke, U.; Heinz, K.; De Andres, P. L.; Saldin, D.; Pendry, J. B.; Surface Science, **1988**, *206*, 1-19.

[32] Tillborg, H.; Nilsson, A.; Maartensson, N.; Andersen, J. N.; Physical Review B: Condensed Matter and Materials Physics, **1993**, *47*, 1699-1702.

[33] Stevens, P. A.; Madix, R. J.; Friend, C. M.; Surface Science, **1988**, *205*, 187-206.

[34] Björneholm, O.; Nilsson, A.; Zdansky, E. O. F.; Sandell, A.; Hernnaes, B.; Tillborg, H.; Andersen, J. N.; Maartensson, N.; Physical Review B: Condensed Matter and Materials Physics; **1992**, *46*, 10353-10365.

[35] Mallick, K.; Witcomb, M. J.; Scurrell, M. S.; Applied Catalysis, A: General, **2004**, *259*, 163-168.

[36] Beamson, G.; Briggs, D.; *The XPS of Polymers Database*, **2000**, SurfaceSpectra Ltd.

[37] Lee, S.; Fan, C.; Wu, T.; Anderson, S. L.; Surface Science, **2005**, *578*, 5-19.

[38] Yang, Z.; Wu, R.; Physical Review B: Condensed Matter and Materials Physics, **2003**, *67*, 081403/1-081403/4.

[39] Valden, M.; Lai, X.; Goodman, D. W.; Science, **1998**, *281*, 1647-1650.

[40] Lai, X.; St. Clair, T. P.; Valden, M.; Goodman, D. W.; Progress in Surface Science, **1998**, *59*, 25-52.

[41]: van Bokhoven, J. A.; Miller, J. T.; Journal of Physical Chemistry C, **2007**, *111*, 9245-9249.

[42] Moreau, F.; Bond, G. C.; Taylor, A. O.; Journal of Catalysis, **2005**, *231*, 105-114.

[43] Minico, S.; Scire, S.; Crisafulli, C.; Galvagno, S.; Applied Catalysis, B: Environmental, **2001**, *34*, 277-285.

[44] Park, E. D.; Lee, J. S.; Journal of Catalysis, **1999**, *186*, 1-11.

[45] Brinie III, D. P.; Zelinski, B. J. J.; Marvel, S. P.; Melpolder, S. M.; Roncone, R. L.; Optical Engineering, **1992**, *31*, 2012-2020.

[46] Moreau, F.; Bond, G. C.; Applied Catalysis A: General, **2006**, *302*, 110-117.

[47] Henao, J. D.; Caputo, T.; Yang, J. H.; Kung, M. C.; Kung, H. H.; Journal of Physical Chemistry B, **2006**, *110*, 8689-8700.

[48] Gottfried, J. M.; Schmidt, K. J.; Schroeder, S. L. M.; Christmann, K.; Surface Science, **2003**, *536*, 206-224.

[49] Dekkers, M. A. P.; Lippits, M. J.; Nieuwenhuys, B. E.; Catalysis Letters, **1998**, *56*, 195-197.

[50] Dekkers, M. A. P.; Lippits, M. J.; Nieuwenhuys, B. E.; Catalysis Today; **1999**, *54*, 381-390.

[51] Gottfried, J. M.; Schmidt, K. J.; Schroeder, S. L. M.; Christmann, K.; Surface Science, **2003**, *525*, 184-196.

[52] Gottfried, J. M.; Schmidt, K. J.; Schroeder, S. L. M.; Christmann, K.; Surface Science, **2003**, *525*, 197-206.

[53] Gottfried, J. M.; Schmidt, K. J.; Schroeder, S. L. M.; Christmann, K.; Surface Science, **2002**, *511*, 65-82.

[54] Liu, L. M.; McAllister, B.; Ye, H. Q.; Hu, P.; Journal of the American Chemical Society, **2006**, *128*, 4017-4022.

[55] Debeila, M. A.; Wells, R. P. K.; Anderson, J. A.; Journal of Catalysis; **2006**, *239*, 162-172.

[56] Lusvardi, V. S.; Barteau, M. A.; Chen, J. G.; Eng, J., Jr.; Fruhberger, B.; Teplyakov, A.; Surface Science, **1998**, *397*, 237-250.

4.2 *In situ* studies of oxidised gold under different environmental conditions

4.2.1 Abstract

Thin oxidised gold films prepared by anodic oxidation of gold have been studied with *in situ* C K-edge and Au L_{III}-edge spectroscopy. The oxidised gold has been decomposed under an oxygen atmosphere at elevated temperatures. The bulk oxidised gold decomposed at a temperature of 433 K completely, as *in situ* XA spectra revealed. XP spectra taken after the treatment showed remaining oxidised gold species near the surface, even though the sample was heated further to 573 K in oxygen. The surface morphology was studied with SEM, and no macroscopic defects are present on the surface prior to the decomposition. After heating in oxygen the surfaces contain small, rough islands.

The soft X-ray studies revealed the formation of a graphite like overlayer on the sample upon dosing CO into the measurement chamber. The graphite overlayer might have been formed by a Boudouard-like reaction on the sample under these conditions. XPS data taken after CO dosing revealed that some superficial gold(+III) species have remained after the reduction in CO at room temperature.

4.2.2 Introduction

For more then a decade it has been known that dispersed gold nanoparticles have extraordinarily high catalytic activities, whereas bulk gold is practically inert to any catalytic reaction. Most research into these systems has focused on the mechanism of the low-temperature CO oxidation reaction, which was first discovered by Haruta [1]. Besides being of scientific interest, these low-temperature catalysts, if sufficiently stable, could be useful for addressing CO removal from engine exhausts during the cold start phase, or to neutralise noxious gases in poorly ventilated environments (e.g. offices,

toilets but also during space exploration or in submarines). Another, more specialised application, would be in CO_2 lasers where re-oxidation of CO could enhance efficiency.

The mechanism underpinning the intriguing low-temperature activity of gold catalysts, as well as the optimum methods for the preparation of active and stable catalysts are controversial subjects [2 - 9]. Investigations of model catalysts are an aid to resolving the required mechanistic details [10, 11]. For supported Au catalysts, model studies have so far included investigations of gold single crystal surfaces [12 - 17], nanoparticles supported on well-defined single crystalline oxide supports [18 - 24] and unsupported gold clusters [25 - 28]. To be able to compare to practical systems, it is essential to conduct the characterisation of these systems *in situ*, mimicking conditions as closely as possible to practical catalysts. Many surface analysis techniques are traditionally operated under ultra-high vacuum conditions, but the latest developments in instrumentation permit characterisation at atmospheric presssures and thus avoid the complications arising from the 'pressure gap' [29].

This work aims to address the parameters that influence the formation and structure of gold nanoparticles from oxidic and hydroxidic gold species by reduction with CO at elevated temperatures. Better insight into the reduction process is needed to improve understanding of the process for practical Au catalyst preparation. The most commonly used method is deposition-precipitation, which starts with the deposition of Au hydroxo complexes that are prepared by adding a base (commonly used are NaOH and NH_3) to aqueous solutions of $HAuCl_4$. These complexes are then allowed to chemically anchor on the oxidic catalyst support material. After drying of the resulting catalyst precursors, the deposited oxide/hydroxide layers are reduced by heating (calcination) or by exposing to a reducing agent such as CO or H_2. A model system for this process is electrochemically prepared oxidic and hydroxidic Au films. The chemical composition of electrochemically prepared anodic oxide layers on gold electrodes, which can be summarily described as $AuO_x(OH)_{3-2x}\cdot nH_2O$ [$0 \leq x \leq 1.5$], is very similar to that of the overlayers generated in the deposition precipitation process. However, investigations of the anodic oxide permits studies of $AuO_x(OH)_{3-2x}$-reduction in a less complex parametric space than the practical catalysts. The absence of (i) the influence of chloride species in $HAuCl_4$ solutions and (ii) the surface reactivity of the oxide support is expected to lead to a better understanding of

$AuO_x(OH)_{3-2x}$ reactivity, and subsequently an assesssment of oxide support and chloride effects in practical systems.

This work studies the electrochemically prepared $AuO_x(OH)_{3-2x}$ layers in the presence of different gas compositions and temperatures *in situ* by near-edge X-ray absorption fine-structure (NEXAFS) measurements. The measurements are performed in a cell that permits closing of the 'pressure gap' [29] between ultra-high vacuum and atmospheric pressure in the soft X-ray region of the electromagnetic spectrum, i.e., in the photon energy range of the C, N and O K-edges (from approcimately 250 eV to 600 eV). The use of the C K-edge to monitor transformations of a sample in the presence of a carbon containing reactant has not been performed often. Over the last decade the study of polymers and other carbon containing samples with soft x-ray NEXAFS increased [30 - 37]. As discussed below, the C K-edge NEXAFS studies as a function of partial CO pressure reveal how the CO chemically interacts with the precursor. Additional Au L-edge experiments in the hard X-ray range similarly reveal changes in the oxidised gold composition under different conditions.

4.2.3 Experimental

4.2.3.1 Sample preparation

Prior to the electrochemical oxidation, the gold foil (0.5 mm thick) and all glassware was washed with 69% HNO_3 for 10 min to remove residuals of Cu from the production process. Afterwards all parts were rinsed with deionised water. The deionised water was prepared with an ELGA PURELAB Option Q or ELGA UHQ and the resistance was 18.2 MΩ cm. Carbon contaminations were removed by UV light treatment. Storage times prior to experiment were less than one week.

The electrolyte solution was prepared by diluting 855 µl 70% perchloric acid (Merck,

Table 4.2.1: Electrochemical parameters for cyclic voltammograms (CV's).

Initial potential vs. Ag/AgCl [V]	0.2
Final potential vs. Ag/AgCl [V]	1.6
[mV/s]	50
Cycles	10 to 20
Resolution [Points/s]	50

pro analysis, φ=1.68 g/ml) in a 50 ml graduated flask with deionised H_2O. The solution was not stored for more than one week.

A Pt mesh was used as the counter electrode. The reference electrode was Ag/AgCl (CH Instruments Inc.). An Amel 2051 Potentiostat, which was computer controlled *via* an Amel 7800 interface, was employed to provide the required voltages. Before the electrochemical oxidation was started, cyclic voltammograms (CVs) were recorded as references (cf. table 4.2.1). The oxidised gold layer was achieved by oxidising the sample for 60-90 min with a current of 20 mA in a 0.1 molar $HClO_4$ solution. This treatment should give a 1-2 μm thick overlayer of oxidised gold on bulk gold [38].

4.2.3.2 C K-edge NEXAFS Measurements

XAS experiments were carried out at beamline 5U.1 at the CCLRC Daresbury Laboratory. The sample chamber, in brief (for more details see chapter 2 and [39]), contains four different modules that are based on CF35 flanges. On top of the load lock section, the linear manipulator is mounted and samples can be transferred between the load lock and the measurment chamber without breaking the vacuum. In order to dose gases into the measurement chamber, the chamber was separated from the beamline by two Nickel mesh windows with a 120 nm Boron coating (Luxel). The volume between the windows was pumped separately by a turbomolecular pump. This setup allows a pressure of roughly 1 mbar in the sample chamber without significant leakage on the beamline side. Gases used were supplied *via* disposable cans (CO: Linde 3.7; He: Air Liquide 5.0, O_2: Air Liquide 4.8).

The electrochemically oxidised gold foils were mounted on an aluminium sample holder and were fixed into position with a tantalum strip. The sample was positioned at 90° relative to the beam, which could be turned as well to measure under different incident angles. The sample holder was designed by Booth and Braun and is described in chapter 2 and [40].

The spectra were recorded in the total electron yield (TEY) mode by accumulating both the drain and collector sample current. The collector for the electrons ejected from the

sample was a ring mounted in front of the sample, where the X-ray beam passed through it. A DC voltage of +90 Volts was applied to the collector to establish an accelerating electric field for the collection of electrons from the sample. Keithley 427 current amplifiers converted currents into voltages. The gain was typically set to 10^9 V/A and a rise time of 300 ms was used. The voltage was converted to a proportional count rate *via* a voltage-frequency converter and then read into the station software *via* counter cards.
Due to the carbon contamination of the beamline, and the windows used, the measured C K-edge spectra had to be carefully calibrated against a standard spectrum. To monitor the flux of photons reaching the sample a gold foil was placed into the sample chamber. Before measuring this standard spectrum, the gold foil was sputtered until no change in the C K-edge spectrum was observed. This spectrum was used to calibrate the sample spectra by either division or subtraction of a scaled gold foil spectrum.
The resulting spectra were normalised with the IFEFFIT program Athena [41]. Typical settings for the normalisation were 278 eV to 282 eV for the region before the edge (285.0 eV) and 300 eV to 305 eV past the edge.

4.2.3.3 Au L_3-edge XAFS measurements

Au L_{III}-edge measurements were performed at station 16.5 of CCLRC Daresbury Laborator using a Si(220) monochromator. Storage ring current was between 150 mA and 250 mA. The X-ray absorption spectra were recorded in total electron-yield mode using collector and drain current. Both currents were similar but the collector current gave a better S/N ratio and was therefore used for the data analysis. The sample was mounted with carbon tape on an Al holder which could be heated from the back with a BN heater (cf. chapter 4.2.3.2). The temperature of the sample was recorded with a K-type thermocouple inserted in the Al holder about 0.5 mm underneath the sample. Once applied, the temperature was stable to ±1 K for the duration of the spectrum. The gas line setup allowed dosing of CO, O_2 and He in different stoichiometries between pressures of 0.5 bar and 2 bar. All spectra shown are measured at 1.5 bar.
The photon energy was calibrated by measuring a gold foil before the experiment. To align the spectra with respect to small photon energy shifts during the measurement, the

peak at 11970 eV was used and spectra were shifted to have their maximum at the region on top of each other.

4.2.3.4 XPS

A Kratos AXIS Ultra system was used for the surface analysis of the samples. Samples were loaded and pumped down *via* a load lock and transferred into the sample chamber *via* a radial distribution chamber (cf. chapter 2). The pressure during acquisition of XP spectra was better than $5 \cdot 10^{-8}$ mbar. The base pressure in the sample chamber was 10^{-9} mbar or lower. The monochromatised Al K_α X-ray source was operated at 150 W power, with an acceleration voltage of 15 kV and a filament emission current of 10 mA. The pass energy of the hemispherical electron analyser during acquisition of survey spectra was 80 eV. For high-resolution spectra of individual emission lines, it was set to 20 eV. For the analysis of the Au 4f spectra the intensity ratio of the $4f_{7/2}$ to $4f_{5/2}$ peaks was fixed to 4:3 and the FWHM was set equal for the corresponding $4f_{7/2}$ and $4f_{5/2}$. All samples used for the Au L_{III}-edge XAFS measurements were divided into two halves to permit analysis both before and after treatments with CO and at elevated temperatures.

4.2.3.5 SEM

SEM images of the oxidised gold foils were taken with a FEI Quanta 200 ESEM. The acceleration voltage of the electron beam was usually 30 keV and the high vacuum mode ($\sim 1 \cdot 10^{-4}$ torr) was used. The usual spot size of the electron beam was about 0.4 μm. Only images collected from secondary electrons are shown. For EDX measurements an EDAX Gensis analyser with an electron spot size of about 0.6 μm was used. An ultra thin window was used to separate the EDX from the SEM chamber.

4.2.4 Results

4.2.4.1 Adsorption of CO on oxidised gold

4.2.4.1.a C K-edge NEXAFS

In fig. 4.2.1 the C K-edge spectra of an electrochemically oxidised gold foil in the presence of CO is shown. The spectra are stacked according to increasing CO pressure from bottom to top with the initial spectrum – before dosing any gases – at the bottom. All spectra are taken under the indicated pressures (black lines) and after pumping the chamber to 10^{-6} mbar (grey lines). All peaks appear above photon energies of 285 eV. Some pre-edge structure is visible in the region lower than 285 eV. At higher photon energies a slightly structured tail (293-300 eV) is present as well.
All spectra taken after dosing CO into the chamber are different from the initial spectrum. The main absorption edge is centred at 285.6 eV. Apart from the absorption edge, no prominent features except a long tail can be seen. When the CO pressure increases to 10^{-2} mbar another peak appears at 287.4 eV. This peak gains intensity when the pressure is further increased to 10^{-1} mbar. Small features appear in the region between 292 eV to 296 eV. These features vanish after evacuating the chamber. A comparison with the data taken by Kaindl *et al.* [42, 43] reveal that these peaks likely originated from gas phase CO (cf. 5.2.1). All other features show no change between CO pressure and vacuum and must be attributed to stable adsorbed species.

Since all data of the carbon deposits are of an unknown species, the building block theory will be used to gain more details on this species [36]. The building block theory, in short, assumes that for the C K-edge spectrum the molecule can be separated into blocks of 2 atoms. The electrons between these blocks do not interact with further bonds in the molecule, this means there are no delocalised electrons. Therefore, the gained C K-edge spectrum should be a superposition of the different two atomic building block spectra.

The photon energy at which the electron is excited in a C K-edge spectrum is mainly due to the hybridisation, and the oxidation, state of the carbon atoms and the type of bond they are excited from (σ or π bond). For more details see chapter 2 and [36].
In general, two main types of assigment of the spectra are used. One is referred to the actual bond from which the electron is excited (single, double, triple bond) [36], the other uses the hybridisation of (at least) one of the atoms involved in the bond [33]. The first method might be more accurate in terms of the actual nature of the electron excited from, but the second seems to be more useful in this case since it is not clear if the bonds are always C-C bond.

Using the building block theory, the described peaks can be assigned to specific C states. The result of this is given in table 4.2.2. As a summary all peaks below 286 eV will be ascribed to electrons excited from the 1s level of sp^2 C atoms into π^* states. The peaks between 286 eV and 290 eV will either originate from sp^2 hybridised C into π^* states or from Rydberg states of sp^3 C. Peaks above 290 eV are due to transitions of sp^2 C into σ^* states. The CO peak is a transition of the sp^2 C from the 1s orbital into a π^* state.
The assignments to the different types of carbon were done according to calculations by Muramatsu *et al.* [33] on hydrofullerene and assignments given for carbon-based compounds given by [44, 45] (cf. fig. 4.2.2).

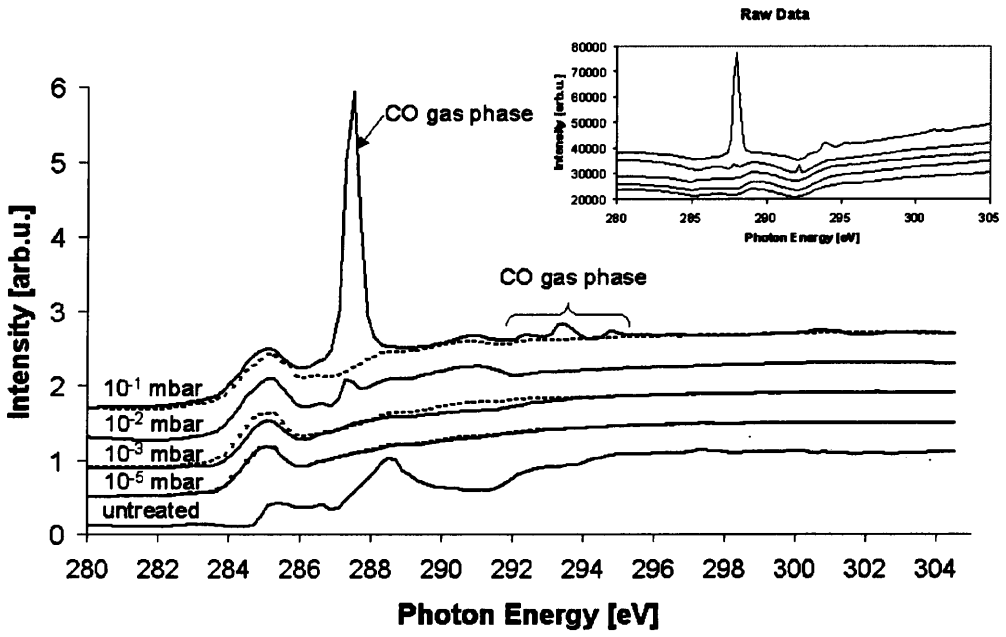

Fig. 4.2.1: C K-edge spectra of CO dosed on a oxidised gold foil. The full line is at the pressure indicated in the figure the dotted line after pumping the CO out of the chamber. The inset shows the raw data of the spectra under the conditions given in the main figure.

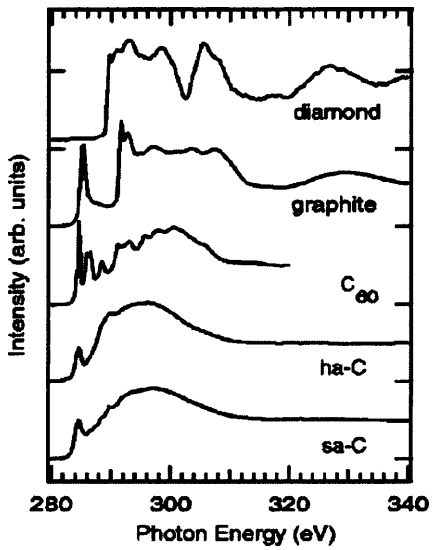

Fig.4.2.2: C K-edge NEXAFS of Díaz et al. showing the respective spectra of diamond, graphite, C_{60}, and two different amorphous graphites (ha, sa) [30].

Table 4.2.2: Peak positions of the C K-edge spectra taken under different CO pressures.

	1 sπ* sp² C	1 sπ* sp² C	1 sπ* sp²/sp³ C	1 sπ* sp²/sp³ C	1 sπ* CO	1sσ* sp² C
UV	-	285.8	287.0	289.0	-	293.4
10^{-5} mbar CO	283.7	285.6	-		-	-
After 10^{-5} mbar CO	283.6	285.6	287.3 (pl)	289.4 (pl)	-	-
10^{-3} mbar CO	283.6	285.6	-		-	-
After 10^{-3} mbar CO	283.5	285.6	287.3	289.4 (pl)	-	-
10^{-2} mbar CO	283.6	285.7	287.1	-	287.8	-
10^{-1} mbar CO	283.6	285.6	287.0	-	287.9	-
After 10^{-1} mbar CO	283.6	285.7	287.1	289.1	-	291.5
Kaindl et al. [42, 43]	-	-	-	-	287.4 (EELS)	-

4.2.4.1.b XPS

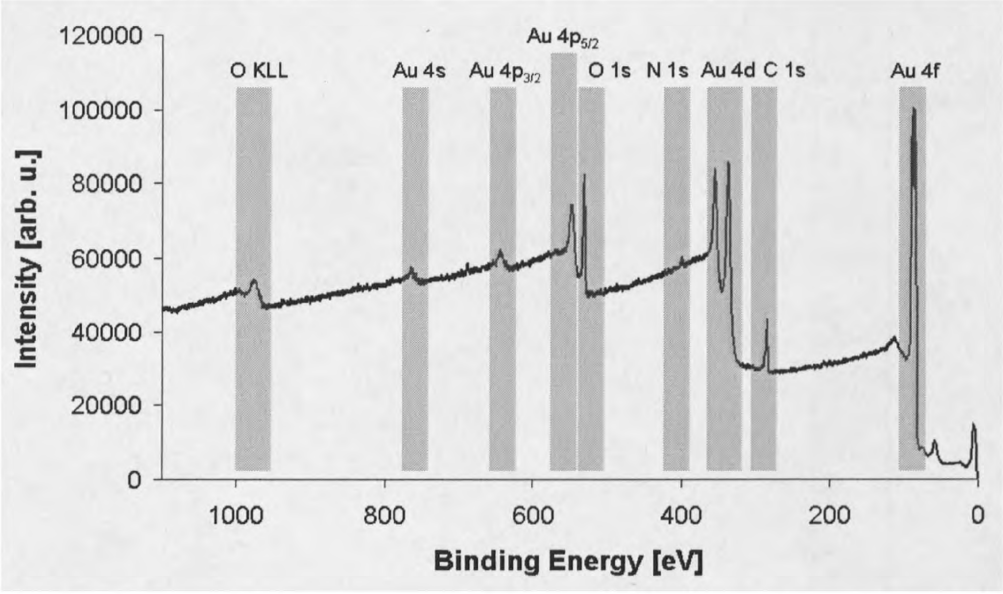

Fig. 4.2.3: Survey XPS scan of an electrochemically oxidised gold foil after CO adsorption.

X-ray photoemission (XP) spectra of the sample taken after the NEXAFS studies, off the beamline with an *ex situ* (ultra high vacuum) XPS, reveal an elemental composition of carbon, gold, oxygen and nitrogen on the surface of the sample (cf. fig. 4.2.3). The Au 4f spectrum (fig. 4.2.4) contains 4 peaks in total, of which two belong to metallic Au^0 and two to oxidic Au^{3+}. The peak of the $4f_{7/2}$ emission from Au^0 was calibrated to a binding energy (BE) of 84.0 eV. This results in a position of 85.5 eV for the $Au4f_{7/2}$. peak, indicating the presence of Au^{3+} [46]. For the $4f_{5/2}$ states the peaks are positioned at 87.7 eV and 89.4 eV, corresponding to Au^0 and Au^{3+}, respectively. The intensity distribution is 35.2%, 22.0%, 26.4% and 16.5%, corresponding nominally to a composition of 61.5% Au^0 and 38.5% Au^{3+}. This suggests that the oxidised gold has not been fully reduced in a pure CO atmosphere at pressures up to 10^{-1} mbar. The data are also compared in table 4.2.3.

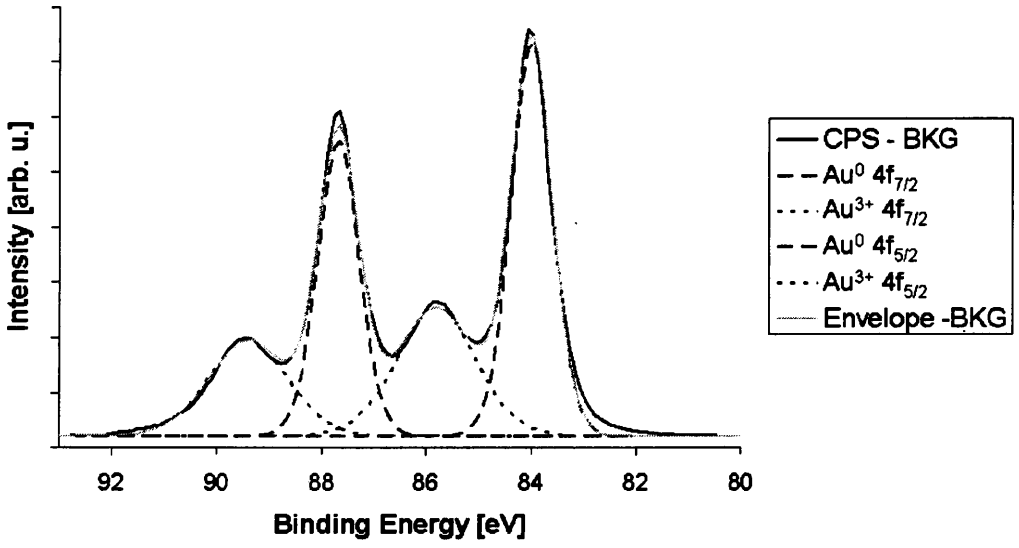

Fig. 4.2.4: XPS of the oxidised gold sample after dosing different CO partial pressures. CPS: Counts per second; BKG: Background.

Table 4.2.3: Energy of the Au4f peaks of the electrochamicaly oxidised Au foil used in the soft X-ray absorption studies. The binding energy (BE) is given and the lowest Au 4f peak has been calibrated to a BE of 84.0 eV.

Assignment	Energy [eV]	FWHM [eV]	% [Au^0:Au^{III}]
Au(0) $4f_{7/2}$	84.00	0.92	35.2 [61.5 %]
Au(+III) $4f_{7/2}$	85.81	1.75	22.0 [38.5 %]
Au(0) $4f_{5/2}$	87.68	0.92	26.4 [61.5 %]
Au(+III) $4f_{5/2}$	89.40	1.75	16.5 [38.5 %]

4.2.4.2 Decomposition of electrochemically formed oxide layers

4.2.4.2.a Thermal-decomposition in oxygen: XPS and *in situ* Au L_3-edge measurements

All XANES spectra of the electrochemically oxidised foil in O_2 atmosphere are very similar (fig. 4.2.5) and resemble no intense 'white line' feature in the region of the Au d-band, even at the beginning of the experiment. This was quite surprising since the electrochemical oxidation conditions should have resulted in a rather thick oxide layer. Nevertheless the XP spectra taken of the same sample before and after the beamtime show clearly that both samples contain oxidised gold in their top layer (fig. 4.2.6). Obviously the amount of the oxidised gold was reduced after treatment during the beamtime, but still a detectable amount of oxidised gold was present in the top 1 to 2 nm of the sample (cf. table 4.2.4 and 4.2.5).

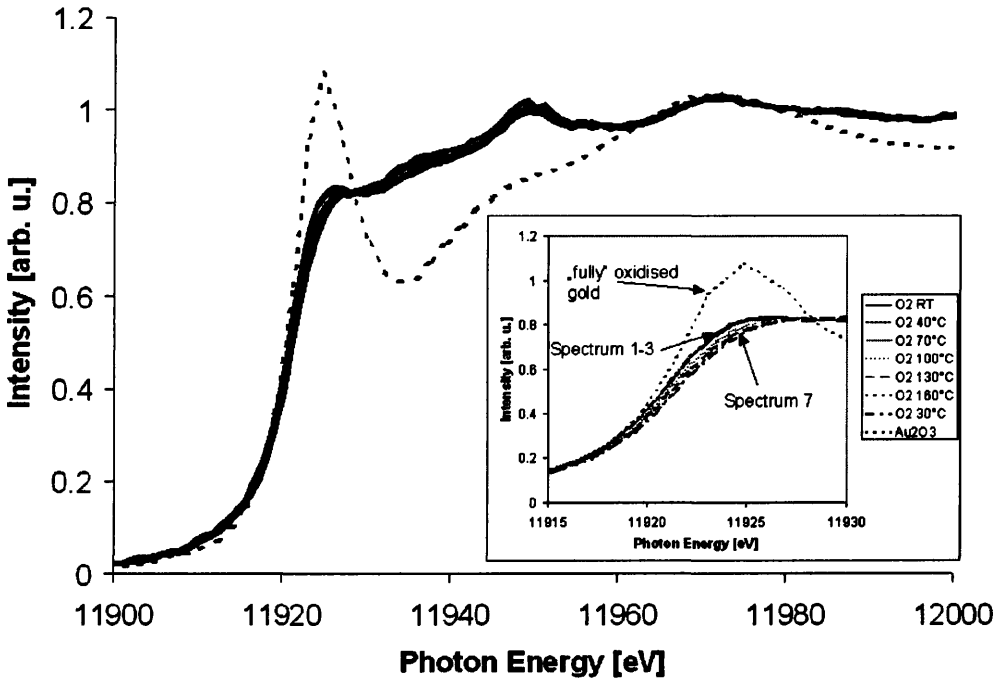

Fig. 4.2.5: Au L_{III}-edge total electron-yield spectra of an electrochemically oxidised gold foil in oxygen at different temperatures. The inset shows the area close to the absorption edge The temperatures, at which the spectra a measured are given in the legend of the inset with the first spectrum at the top and the last at the bottom.

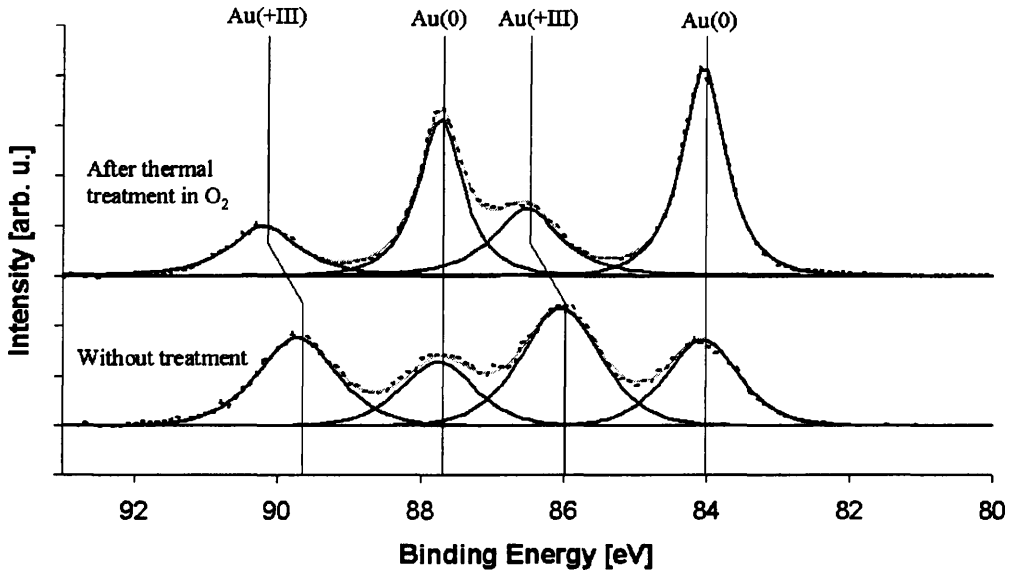

Fig. 4.2.6: Au 4f XP spectra of an electrochemically oxidised gold foil. The lower spectrum shows the sample before treatment during the Au L_3-edge measurement; the upper one after treatment in oxygen.

Table 4.2.4: XPS data of the sample before decomposing in oxygen at elevated temperatures.

Assignment	Energy [eV]	FWHM [eV]	% [Au(0):Au(+III)]
Au(0) $4f_{7/2}$	84.06	1.19	22.9 [40.1%]
Au(+III) $4f_{7/2}$	86.04	1.30	34.2 [59.9%]
Au(0) $4f_{5/2}$	87.75	1.19	17.2 [40.1%]
Au(+III) $4f_{5/2}$	89.72	1.30	25.7 [59.9%]

Table 4.2.5: XPS data of the sample after decomposing in oxygen at elevated temperatures.

Assignment	Energy [eV]	FWHM [eV]	% [Au(0):Au(+III)]
Au(0) $4f_{7/2}$	84.06	0.73	38.4 [67.1%]
Au(+III) $4f_{7/2}$	86.53	1.10	18.8 [32.9%]
Au(0) $4f_{5/2}$	87.73	0.73	28.8 [67.1%]
Au(+III) $4f_{5/2}$	90.19	1.10	14.0 [32.9%]

Small differences in the edge of XANES spectra taken at different temperatures can still be seen (see inset of fig. 4.2.5). At the beginning of the series, a small 'white line' was present, which is gradually reduced when the temperature was increased. To elucidate this effect, difference spectra were determined, using the last spectrum in the series (in O_2 at 30°C) as a reference spectrum (fig. 4.2.7). This approach revealed that the reduction of the oxide film commences at temperatures above 100°C. At 160°C the reduction is complete and irreversible, as cooling down to RT reveals. Further heating to 300°C and spectra taken at 220°C did not result in a further reduction (not shown).

The XP spectra of both samples - with and without treatment - were taken in one experimental run, under identical conditions. The resulting spectra (fig. 4.2.6) reveal two gold species resulting in four peaks, two each for the $4f_{7/2}$ and $4f_{5/2}$ state. The lowest in binding energy (BE) of these peaks is the Au(0) $4f_{7/2}$ from metallic gold and was set to 84.0 eV. The next highest peak – between 86 eV and 87 eV – is of the Au $4f_{7/2}$ of a Au(+III) state (table 4.2.4) as comparision with literature reveals [46]. After the thermal reduction in O_2, the Au(+III) $4f_{7/2}$ peak is shifted +0.5 eV in BE compared to the Au(0) $4f_{7/2}$ (table 4.2.5). A similar behaviour can be seen for the Au $4f_{5/2}$ peaks and shows the correctness of the fit. Furthermore, the full width at half maximum (FWHM) is reduced from 1.2 eV and 1.3 eV to 0.7 eV and 1.1 eV respectively for the Au(0) and Au(+III) state (the FWHM is restricted to the same value for the corresponding Au $4f_{7/2}$ and $4f_{5/2}$ peaks). That a reduction of the sample occurred in the outer most layer of the sample can be seen if the intensities are compared. Without treatment the Au(+III) state yields roughly 60% of the total Au 4f signal. After treatment this value is reduced to about 33%.

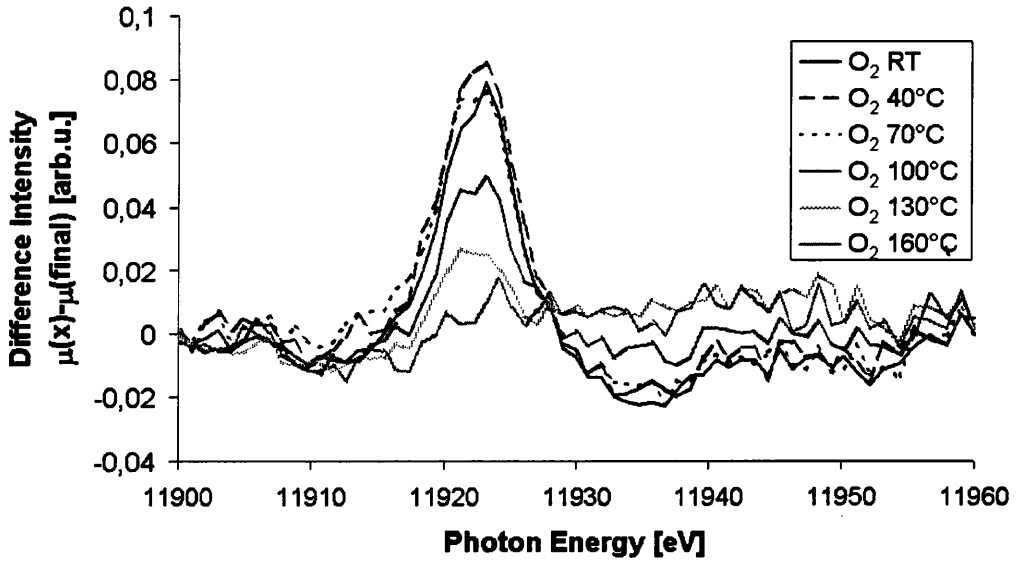

Fig. 4.2.7: Difference spectra of the data shown in fig. 4.2.1. The last spectrum in fig. 4.2.5, that was taken at 30°C in oxygen, is the standard for all difference spectra.

The O1s peak (fig. 4.2.8) provides more details on the gold(+III) species as it is easier to differentiate between oxidic, hydrous and aqueous species than in the Au 4f spectra. Weiher [38] prepared electrochemical films similar to the ones used in this work. However, much higher intensities of the emission due to Au^{3+} were observed. One major difference between Weiher's study and the present study is that the films in the former were prepared in a chamber directly attached to a UHV system, which allowed the transfer of the sample to the measurement chamber without exposure to air. The transport through laboratory environment might lead to a reaction of the less stable aqueous/hydrous species to the oxidic species.

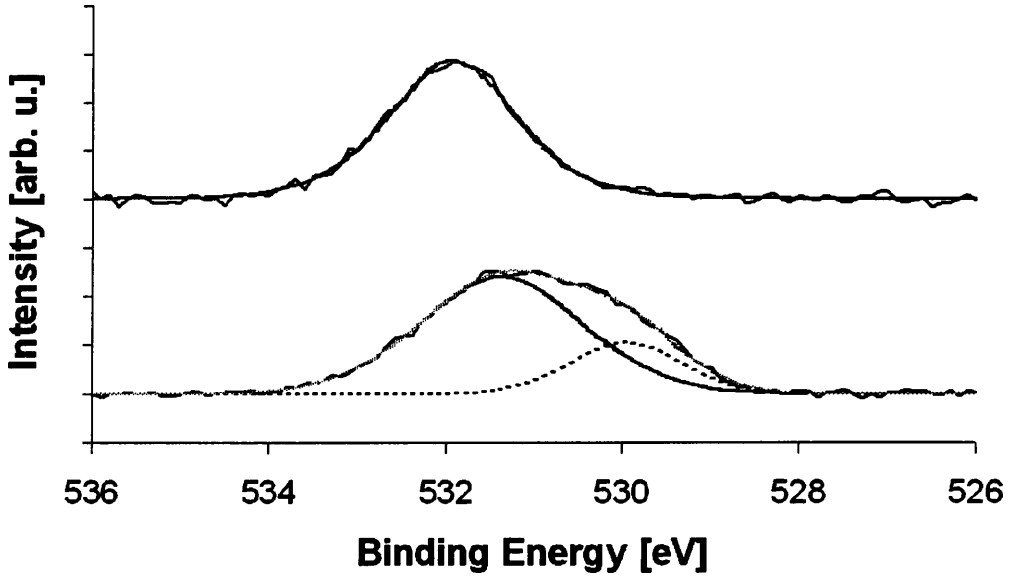

Fig. 4.2.8: O 1s XPS of a gold foil reduced in oxygen at elevated temperatures (upper spectrum). For comparison the sample without treatment is shown as well (lower spectrum).

In the O 1s XP spectrum of the untreated sample (fig. 4.2.8, lower spectrum, table 4.2.6) an oxidic (529.9 eV) and a hydroxidic (531.4 eV) species are present, similar to those previously [38] observed. An aqueous/hydrous species as reported by Weiher [38] could not be detected. This might occur since this species is relatively unstable and is likely to be removed by the storage of the sample under ambient conditions in a laboratory for roughly 1 week. In the reduced sample, only a hydroxidic sample is present (531.9 eV), which is also shifted by 0.5 eV to higher binding energies.

The O1s peak (fig. 4.2.8) provides more details on the gold(+III) species by having larger differences in binding energy than the Au 4f peaks for the oxidic, hydroxidic and aqueous/hydrous species. In the O 1s XP spectrum of the untreated sample (fig. 4.2.9, lower spectrum, table 4.2.7) an oxidic (529.9 eV) and a hydroxidic (531.4 eV) species are present, similar to those previously [38] observed. An aqueous/hydrous species as reported by Weiher [38] could not be detected and is likely due to the storage of the sample under ambient conditions of a laboratory for roughly 1 week. In the reduced

sample only a hydroxidic species is present (531.9 eV), which is also shifted by 0.5 eV to higher binding energies.

Table 4.2.6: O 1s XPS of a oxidised gold foil reduced in oxygen at elevated temperatures.

Assignment	Position [eV]	FWHM [eV]	%
O 1s oxidic (without treatment)	529.94	1.48	22.8
O 1s hydroxidic (without treatment)	531.37	2.18	77.2
O 1s hydroxidic	531.94	1.70	100

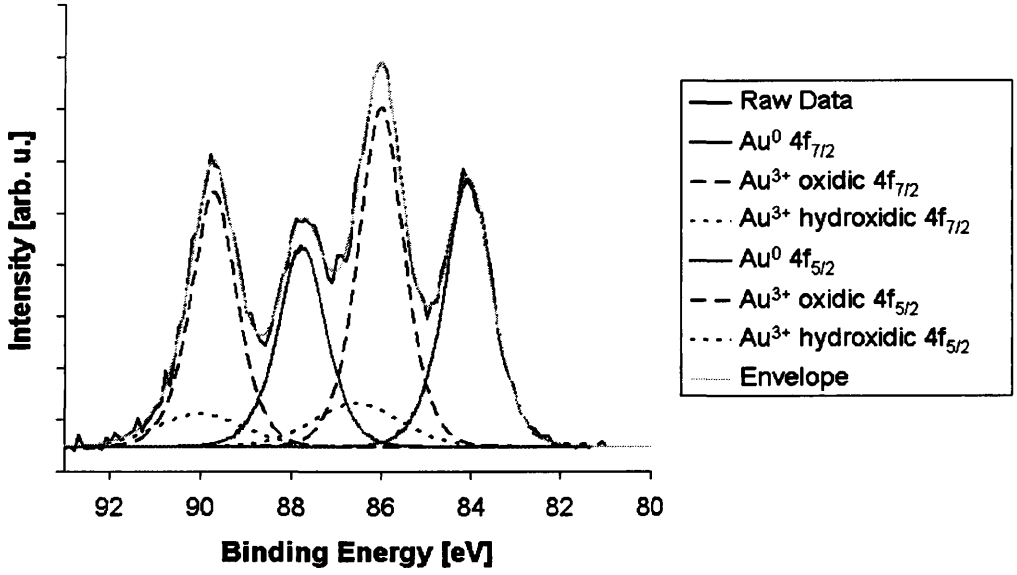

Fig. 4.2.9: Au 4f XP spectrum of the untreated sample for the oxygen reduction, including a metallic, oxidic and hydroxidic gold component.

Table 4.2.7: Au 4f XP spectrum of the untreated sample for the oxygen reduction including a metallic, oxidic and hydroxidic gold component.

Assignment	Position [eV]	FWHM [eV]	% [$4f_{total}$]
Au(0) $4f_{7/2}$	84.07	1.23	22.9 [40.1]
Au(+III) hydroxidic $4f_{7/2}$	86.01	1.17	27.8 [48.7]
Au(+III) oxidic $4f_{7/2}$	86.54	2.20	6.4 [11.2]
Au(0) $4f_{5/2}$	87.76	1.23	17.2 [40.1]
Au(+III) hydroxidic $4f_{5/2}$	89.71	1.17	20.9 [48.7]
Au(+III) oxidic $4f_{5/2}$	89.99	2.20	4.8 [11.2]

From the O 1s results, 3 species (metallic, oxidic, hydroxidic) would be expected in the Au 4f spectrum. A fit with this assumption is shown in fig. 4.2.9; the corresponding data are given in table 4.2.7. The peaks for the hydroxidic species are rather broad and had to be set to a maximum value of 2.2 eV FWHM. The energy difference between the Au $4f_{7/2}$ and Au $4f_{5/2}$ peak is slightly smaller than expected (3.4 eV, the Au $4f_{7/2}$ and $4f_{5/2}$ peaks are usually separated by 3.7 eV [46]). Considering the relatively low intensity of the hydroxidic peak in the total gold spectrum it shows the possibility of the existence of this peak.

When comparing the shifts of the (hypothetical) hydroxidic components in the O 1s and the Au 4f XP spectra, it shows that the O 1s peak is shifted by 0.6 eV to higher BE after the reduction but the Au 4f peaks seem to be rather stationary (±0.0 eV and -0.2 eV for the Au $4f_{7/2}$ and $4f_{5/2}$ peaks). But a change in the crystal structure might lead to different screening effects on the gold and oxygen atoms in the different spectra, and hence give slightly different shifts for the O 1s and Au 4f binding states. It could also be possible that the peak position of the hydroxidic peaks in the Au 4f spectrum before thermal treatment is not correctly resolved. This would be due to the overlap of the hydroxidic and oxidic peaks in the Au 4f spectrum, which makes this a challenging task.

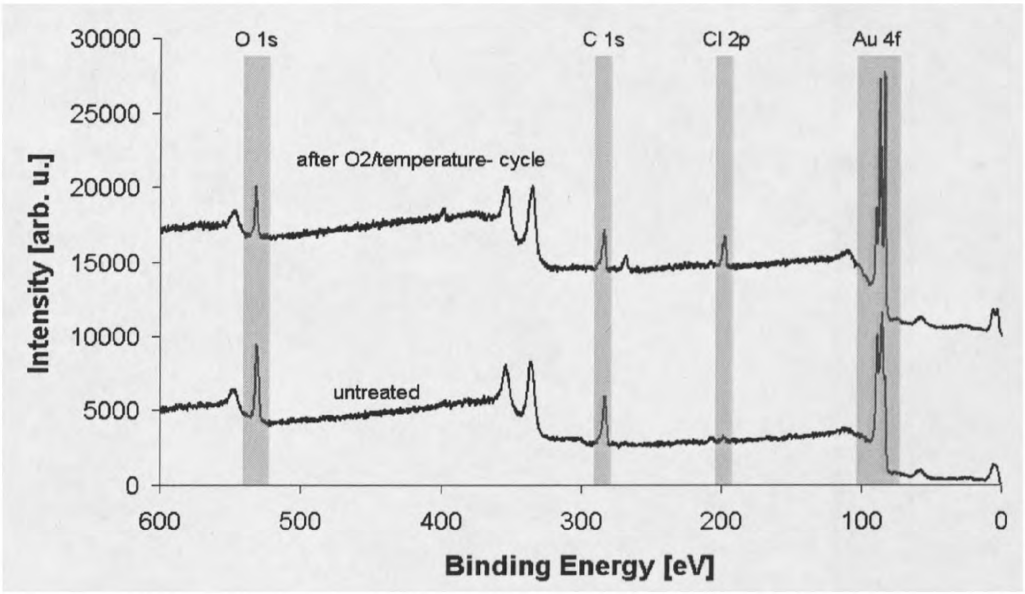

Fig. 4.2.10: XPS survey scans of a oxidised gold foil before and after heating it in O_2.

The elemental composition of the sample before and after the O_2/temperature cycle is shown in fig. 4.2.10. The amounts of carbon and oxygen on the sample surface are only slightly reduced after the treatment (see table 4.2.8). The Au 4f intensity is increased and shows that some of the carbon must have been removed during the treatment from the sample.

It should be noted that the amount of chlorine on the surface is increased after this treatment, as the appearance of the Cl 2p peak indicates. The chlorine can be deposited on the surface by the handling and transport between the NEXAFS and XPS experiment, although extra precautions were taken to prevent any contamination of the sample. Another source could be the electrochemical oxidation, which could have deposited some chlorine underneath the sample surface. By heating in O_2, this chlorine might have migrated to the surface. This is in contrast to the sample treated in the CO/O_2-cycle, that does not show any indication for chlorine on the surface upon treatment.

Table 4.2.8: XPS survey scans of a oxidised gold sample before and after heating it in O_2.

Region	Untreated		After heating in O_2	
	Counts per s	%	Counts per s	%
Au 4f	9964	68.3	11446	83.7
C 1s	1918	13.1	1099	8.0
O 1s	2700	18.5	1125	8.2

4.2.4.2.b Thermal-reduction in oxygen: SEM Imaging

SEM images of an electrochemically oxidised gold foil are shown in fig. 4.2.11 with images of an untreated surface on the left (images I to III) and images of the surface after heating the sample in oxygen on the right side (images IV to VI). With a small magnification (1000x, image 4.2.10.I) the homogeneity of the sample can be seen, and the surface appears to be quite smooth. However, fine cracks running from top to bottom are visible as well. One of them is shown in more detail at the magnification of 10000x in image 4.2.10II. Furthermore small particles can be seen on the surface. At the maximal magnification of 40000x (image 4.2.10.III) the surface shows a porous structure, which breaks up into small islands, separated by small cracks. This is the expected surface structure of an electrochemically prepared gold sample. Some of the gold on the surface will dissolve in the $HClO_4$-solution by the electrochemical process. This induces a roughening in the surface since the gold is not fully homogenously dissolved over the whole sample.

After heating, the top layer of the sample peels off from the supporting gold and results in cracks of about 5 µm width and up to several 100 µm length (image 4.2.10.IV). The small cracks seen in the untreated sample cannot be observed anymore and are most likely the fracture points where the overlayer cracks during heating. At the point where the upper layer is bent horizontally up from the surface, the thickness of the overlayer can be estimated (image 4.2.10.V). This is approximately the maximum thickness for the oxidation of gold with an electrochemical process under the given conditions [38].

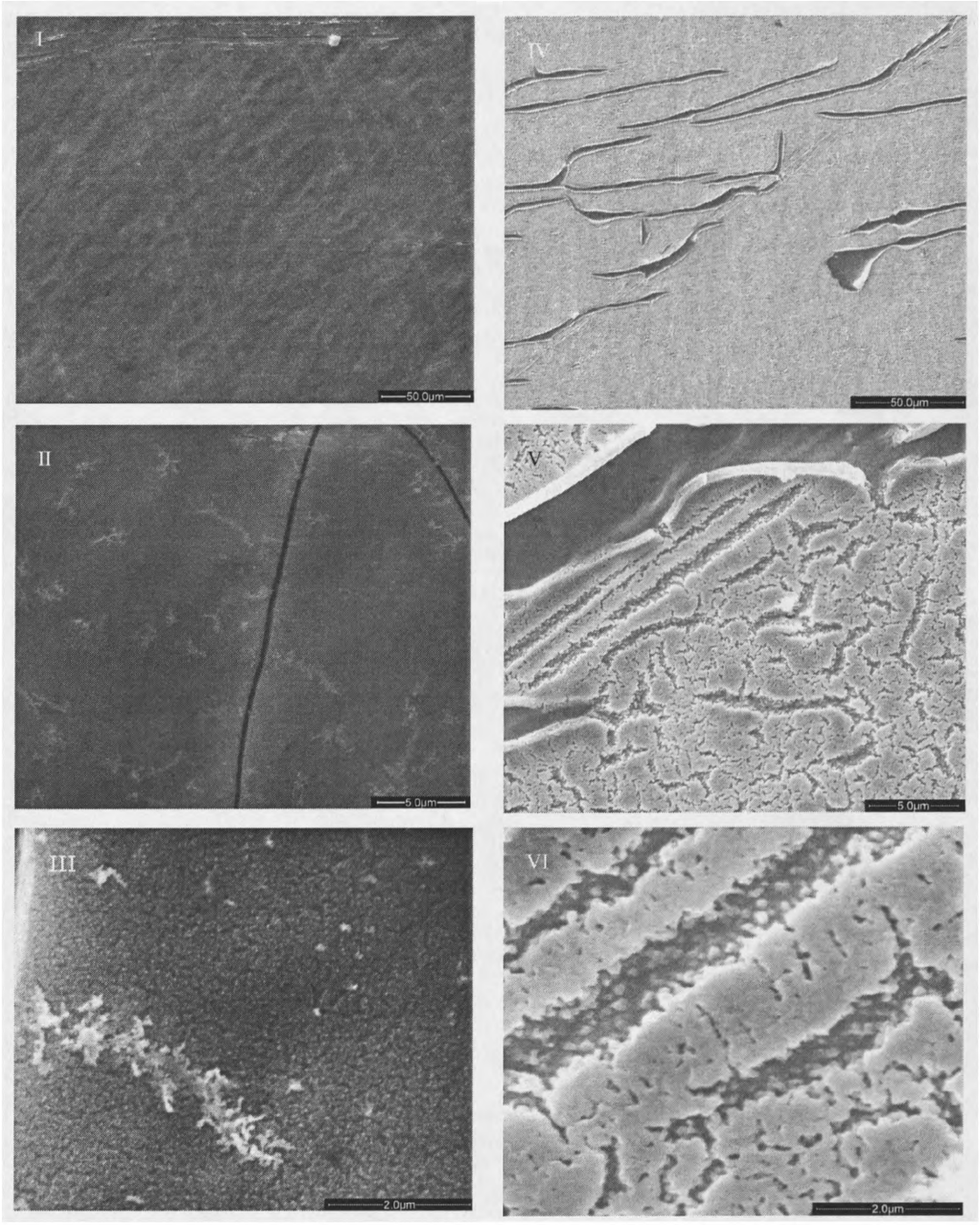

Fig. 4.2.11: SEM images of electrochemical oxidised gold foil. The untreated sample (left,

I-III) and after the temperature cycle in oxygen (right, IV-VI) (magnification: top 1000x, middle 10000x, bottom 40000x).

At a higher magnification, (image 4.2.10.VI) the differences between the treated and untreated samples become very clear. While the untreated sample still shows a rather smooth surface, the treated sample contains many small cracks and clefts. These smaller cracks do not penetrate down to the gold support – in contrast to the large cracks – and appear to be filled with small grains.

4.2.5 Discussion

4.2.5.1 CO interaction with anodic oxide layers

The C K-edge NEXAFS structure of the electrochemically oxidised gold foil before dosing CO is due to adsorption of hydrocarbons and other contamination on the sample during transfer from the preparation laboratory to the analysis chamber. This cannot be prevented, unless one would prepare directly under controlled conditions at the beamline. Cleaning of the surface by, e.g., ion bombardment is not possible either since it would not only remove the carbon but also reduce the oxidised gold. That the amount of initial carbon contamination on the sample is very small was indicated by two facts: Firstly, the C K-edge adsorption was very weak – almost within the noise level of the measurement. Secondly, the XANES changes dramatically after dosing CO and the structure of the initial carbon remains in the following spectra.

The chemical composition of the carbon overlayer after dosing CO into the chamber is of central interest for elucidating CO oxidation mechanisms over Au. The O K-edge could in principle provide insight into the chemical state of CO incorporated into the overlayer. Unfortunately it is not easy to interpret since the oxide layer sample contains oxygen itself in considerable concentration, so that the spectroscopic contrast of additionally formed oxygen species is insufficient. If the CO was incorporated as a different functional group (-COOH, -COH, $-CO_3$, etc) oxygen species with peaks in the region between 286 eV and 290 eV should appear [30, 31, 33, 36].
The carbon overlayer has some similarities with hydrocarbons, carbon nanotubes and graphite [30, 31, 33, 37]. The greatest similarities are with amorphous graphite as

prepared by Díaz *et al.* [30], but the spectra look different in the σ^* region (290-300 eV). Spectra of amorphous graphite reported in the literature show a wide "bump" in this region, but the spectra observed in this study are flat, likely due to the difference in normalization methods. The good agreement between these literature spectra and the C K-edge spectra of the overlayer on the oxidised gold foils indicate that the CO is incorporated only in its reduced state. This supports the estimation that no oxidised carbon is present on the sample suface, which was made for the building block theory to assign the different functional groups.

The reduction of the oxidised gold in CO atmosphere will most likely be by the following non-catalytic oxidation:

$$CO + AuO_x \rightarrow CO_2 + AuO_{x-1},$$

since it seems certain that the decomposition of oxidic gold species by CO is accompanied by the evolution of CO_2. This reaction has also been observed before in this laboratory [38] as well as in others [47]. Proof of this reaction would be the detection of the CO_2. Unfortunately, this was not possible - even though a mass spectrometer was employed to constantly monitor the gas composition in the experimental chamber. The CO_2 partial pressure appeared to remain constant over the scan time of the C K-edge XANES spectra (roughly 40 min). However, the apparent absence of any variation in gas composition may just reflect the fact that the volume of the sample chamber is so large that detection of the small amounts of formed CO_2 may well be below the sensitivity limit of the mass spectrometer.
That the oxidised gold species are reduced in vacuum is unlikely since Weiher [38] found that temperatures of about 550 K are required to do this without the aid of a reducing agent like CO.

The non-catalytic oxidation of carbon monoxide though, does not explain that the formation of a graphite like overlayer in the C K-edge XANES is observed. Also oxidised gold samples appear deep purple or black after being in a CO atmosphere, which suggest

the formation of an overlayer on these samples. A possible explaination is the deposition of carbon by a Boudouard like reaction:

$$2\ CO \rightarrow C + CO_2,\ \Delta H = -160.9\ \text{kJ/mol}\ [48].$$

The Boudouard reaction is known to be present on a variety of catalytic systems including iron oxide [49] and nickel containing catalysts [50, 51]. Because of the formation of carbon on these catalysts this process is also known as coking and the reverse reaction is also of interest [52], since the coking reduces or inhibits the catalytic activity.

For the reaction mechanism of the Boudouard reaction on metal oxides, it is assumed that only one carbon monoxide is adsorbed during the oxidation of the second carbon monoxide in the gas phase [53]. This can be followed from the facts that the CO bond is actually strengthend when adsorbed on e.g. FeO(100) and that the dissociation of two adsorbed CO molecules is energetically unfavourable. Therefore a reaction path such as presented in fig. 4.2.12, is assumed to be present.

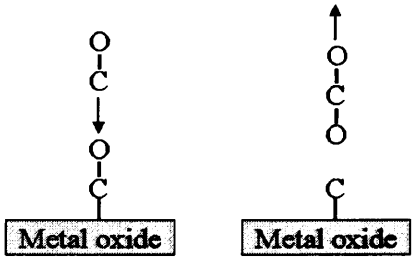

Fig. 4.2.12: Schematic reaction path for the Boudouard reaction over metal oxides.

It is also suggested that the Boudouard reaction takes place at defect sites in the metal oxide, since the calculated reaction path on a defect free metal oxide is very unfavourable for the Boudouard reaction [53]. Furthermore studies on TiO_2 showed that CO is only adsorbing on defect sites [54].

The non-catalytic oxidation of carbon monoxide and a Boudouard like reaction on the oxidised gold foil would lead to the general reaction schematic presented in fig. 4.2.13.

This could explain the finding of a graphite like overlayer in the C K-edge XANES spectra, the reduced amount of oxidised gold species found in XPS and the dark colour of the samples after CO treatment.

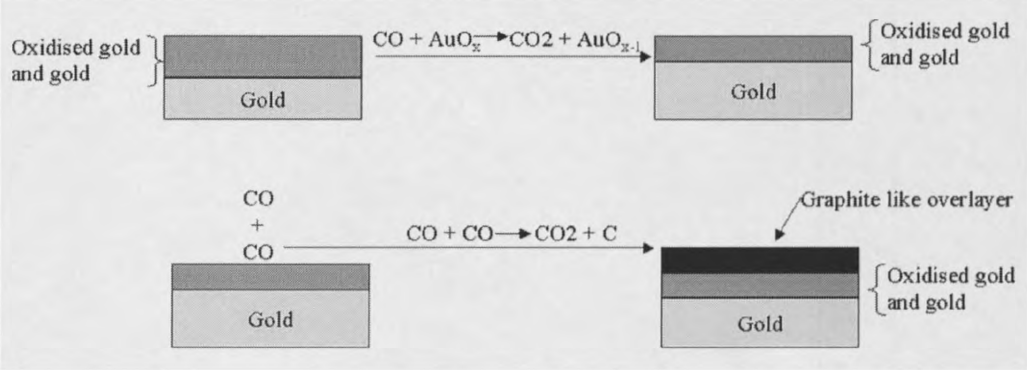

Fig. 4.2.13: Schematic drawing of the postulated reactions on going on an oxidised gold foil in CO atmosphere.

One point that has not been discussed so far is the effect of the X-ray beam on the results. The X-ray beam could affect the structure of the oxidised gold sample, but no indication for this was detected, e.g. development of a differently coloured spot on the sample where the X-ray had illuminated. Instead, the sample changed colour uniformly from yellow-brown to deep purple or black, indicating that the X-ray beam is not damaging the sample. A second effect would be the activation of the CO to adsorb or react on the surface. Again, if this was the case, a changing of the beam position on the sample should result in a different spectrum. This was not the case and thus it is assumed that the X-ray beam does not have a significant influence on the result.

4.2.5.2 Decomposition of oxidised gold spices

The XANES and XPS results show in fig. 4.2.5 and 4.2.6 that the electrochemical oxidation did not produce an about 1 μm to 2 μm thick oxide layer but a much thinner layer. The reason for this is most likely the use of a relative small electrochemical cell. Therefore the amount of electrolyte was too small to maintain a temperature close to

temperature. The temperature, although not measured, was elevated and seemed to be relative close to the boiling point of the electrolyte. This elevated temperature is the reason for the formation of only a small oxide layer, by suppressing the growth of a thicker oxide layer.

The thermal decomposition of oxidised gold has been studied several times before [38, 55, 56] but the data presented here is the first time oxidised gold was reduced in a pure O_2 atmosphere. The NEXAFS data show that the decomposition of the oxidised gold starts around 373 K and is completed for bulk gold at a temperature of 433 K. XPS data show that the topmost oxygen layer could not be fully reduced by O_2 even though the sample was heated to 573 K (cf. fig. 4.2.6). The thickness of this layer must be within the measurement depth of XPS (1 to 2 nm), as no indication for an oxide layer was given by the Au L_3-edge XANES.

When oxidised gold is decomposed thermally it usually requires temperatures of up to 573 K to fully decompose to gold metal [38, 55]. This temperature is slightly higher than the temperatures found for freshly prepared samples that are decomposed under helium. Weiher [38] found differences in the temperature for the decomposition of electrochemically prepared and commercially purchased samples, which can explain the difference of temperature required for the decomposition of bulk oxygen at lower temperature presented here.

The main difference between samples decomposed in helium and oxygen is the stability of the suface oxygen under oxygen conditions. The oxidised gold at the surface of the sample is not decomposed, even at temperatures up to at least 573 K. It seems plausible that the increased oxygen partial pressure over the sample surface under oxygen condition will prevent the surface gold oxygen species from decomposing. The surface oxygen will also not be produced by oxidation of the gold surface at the elevated temperature since gold is thermally oxidised at temperature above 600 K and presures above 3000 bar [57, 58].

For all XPS spectra it is remarkable that no O 1s peak around 533 eV can be found which would be assigned to aqueous/hydrous states [38, 56]. The explanation for this might be

rather simple and is due to the different time scales between preparation and XPS analysis. Whereas the samples of Weiher have been characterized roughly 1 h after the preparation, several days have passed between preparation and analysis in this case. This might lead to the decomposition of aqueous/hydrous states, which is also reported to be unstable under UHV conditions [38].
Furthermore, in the case of Weiher, the samples have been transferred between preparation and analysis without breaking vacuum. This was not possible in the present work and thus carbon depositions of the environment are always present on the samples presented here. This is the reason for the small near edge resonance of the sample in the Au L_{III}-edge spectra and the mixed Au^0 and Au^{+III} states in the XPS data.

4.2.6 Conclusion

Using Au L_{III}-edge XANES the reduction of laboratory environment prepared, and stored oxidised gold samples could be shown. The experiments showed that these samples are very sensitive to reduction prior to experimentation. To prevent the reduction before the experiment, the preparation in a chamber attached to the analysis chamber or the transfer of the sample under inert condition is necessary.
The reduction of oxidised gold in oxygen is completed at 430 K and is not reversible. A thin oxide layer remains near the surface on the sample, which is in contrast to samples reduced in helium.

The drastic changes in the soft X-ray C K-edge spectra after introducing CO into the measurement cell clearly indicate that CO is interacting with oxidised gold species. The adsorbed species are then transferred - possibly by the Boudouard reaction - into a graphite-like overlayer. Comparing the data with literature spectra suggests that the graphite is highly amorphous.

References

[1] Haruta, M; Kobayashi, T.; Sano, H.; Yamada, N.; Chemistry Letters, **1987**, *2*, 405-408.

[2] Boccuzzi, F.; Chiorino, A.; Manzoli, M.; Lu, P.; Akita, T.; Ichikawa, S.; Haruta, M.; Journal of Catalysis, **2001**, *202*, 256-267.

[3] Bond, G. C.; Thompson, D. T.; Catalysis Reviews - Science and Engineering, **1999**, *41*, 319-388.

[4] Guzman, J.; Gates, B. C.; Journal of the American Chemical Society, **2004**, *126*, 2672-2673.

[5] Haruta, M.; Catalysis Surveys from Japan, **1997**, *1*, 61-73.

[6] Haruta, M.; Cattech, **2002**, *6*, 102-115.

[7] Magkoev, T. T.; Rosenthal, D.; Schroder, S. L. M.; Christmann, K.; Technical Physics Letters (Translation of Pis'ma v Zhurnal Tekhnicheskoi Fiziki), **2000**, *26*, 894-896.

[8] Park, E. D.; Lee, J. S.; Journal of Catalysis, **1999**, *186*, 1-11.

[9] Sayo, K.; Deki, S.; Hayashi, S.; Journal of Colloid and Interface Science, **1999**, *212*, 597-599.

[10] Niemantsverdriet, J. W.; Engelen, A. F. P.; de Jong, A. M.; Wieldraaijer, W.; Kramer, G. J.; Applied Surface Science, **1999**, *144-145*, 366-374.

[11] van Hardeveld, R. M.; Gunter, P. L. J.; van IJzendoorn, L. J.; Wieldraaijer, W.; Kuipers, E. W.; Niemantsverdriet, J. W.; Applied Surface Science, **1995**, *84*, 339-346.

[12] Gottfried, J. M.; Schmidt, K. J.; Schroeder, S. L. M.; Christmann, K.; Surface Science, **2003**, *536*, 206-224.

[13] Gottfried, J. M.; Schmidt, K. J.; Schroeder, S. L. M.; Christmann, K.; Surface Science, **2003**, *525*, 197-206.

[14] Gottfried, J. M.; Schmidt, K. J.; Schroeder, S. L. M.; Christmann, K.; Surface Science, **2003**, *525*, 184-196.

[15] Gottfried, J. M.; Schmidt, K. J.; Schroeder, S. L. M.; Christmann, K.; Surface Science, **2002**, *511*, 65-82.

[16] Jugnet, Y.; Cadete Santos Aires, F. J.; Deranlot, C.; Piccolo, L.; Bertolini, J. C.; Surface Science, **2002**, *521*, L639-L644.

[17] Stiehl, J. D.; Kim, T. S.; McClure, S. M.; Mullins, C. B.; Journal of the American Chemical Society, **2004**, *126*, 1606-1607.

[18] Yang, Z.; Wu, R.; Goodman, D. W.; Physical Review B: Condensed Matter and Materials Physics, **2000**, *61*, 14066-14071.

[19] Santra, A. K.; Kolmakov, A.; Yang, F; Goodman, D. W.; Japanese Journal of Applied Physics, Part 1: Regular Papers, Short Notes & Review Papers, **2003**, *42*, 4795-4798.

[20] Lai, X.; St. Clair, T. P.; Valden, M.; Goodman, D. W.; Progress in Surface Science, **1998**, *59*, 25-52.

[21] Kolmakov, A.; Goodman, D. W.; Surface Science, **2001**, *490*, L597-L601.

[22] Chusuei, C. C.; Lai, X.; Luo, K.; Goodman, D. W.; Topics in Catalysis, **2001**, *14*, 71-83.

[23] Wahlström, E.; Lopez, N.; Schaub, R.; Thostrup, P.; Ronnau, A.; Africh, C.; Laegsgaard, E.; Norskov, J. K.; Besenbacher, F.; Physical Review Letters, **2003**, *90*, 026101/1-026101/4.

[24] Maeda, Y.; Okumura, M.; Tsubota, S.; Kohyama, M.; Haruta, M.; Applied Surface Science, **2004**, *222*, 409-414.

[25] Socaciu, L. D.; Hagen, J.; Bernhardt, T. M.; Woeste, L.; Heiz, U.; Haekkinen, H.; Landman, U.; Journal of the American Chemical Society, **2003**, *125*, 10437-10445.

[26] Wallace, W. T.; Whetten, R. L.; Journal of the American Chemical Society, **2002**, *124*, 7499-7505.

[27] Li, J.; Li, X.; Zhai, H.-J.; Wang, L.-S.; Science, **2003**, *299*, 864-867

[28] Kim, Y. D.; Fischer, M.; Gantefor, G.; Chemical Physics Letters, **2003**, *377*, 170-176.

[29] Schlögl, R.; Angewandte Chemie International Edition, **1993**, *32*, 381-383.

[30] Diaz, J.; Anders, S.; Zhou, X.; Moler, E. J.; Kellar, S. A.; Hussain, Z.; Physical Review B: Condensed Matter and Materials Physics, **2001**, *64*, 125204/1-125204/19.

[31] Hosokawa, S.; Sato, H.; Wang, Y.; Ohata, E.; Fukushima, A.; Journal of Electron Spectroscopy and Related Phenomena, **2004**, *137-140*, 235-237.

[32] Koprinarov, I.; Lippitz, A.; Friedrich, J. F.; Unger, W. E. S.; Woll, C.; Polymer, **1998**, *39*, 3001-3009.

[33] Muramatsu, Y.; Ueno, Y.; Hayashi, T.; Grush, M. M.; Gullikson, E. M.; Perera, R. C. C.; Journal of Electron Spectroscopy and Related Phenomena, **2000**, *107*, 177-184.

[34] Weiss, K.; Gebert, S.; Wuhn, M.; Wadepohl, H.; Woll, C.; Journal of Vacuum Science & Technology, A: Vacuum, Surfaces, and Films, **1998**, *16*, 1017-1022.

[35] Zwahlen, M.; Herrwerth, S.; Eck, W.; Grunze, M.; Haehner, G.; Langmuir, **2003**, *19*, 9305-9310.

[36] Stöhr, J.; *NEXAFS Spectroscopy*, Springer-Verlag, **1992**.

[37] Banerjee, S.; Hemraj-Benny, T.; Balasubramanian, M.; Fischer, D. A.; Misewich,

[38] Weiher, N.; *Combined in situ and ex situ Studies of an Electrochemical Interface – Investigation of Anodic Oxide Layers on Gold*, Dissertation, Freie Univerität Berlin, **2003**.

[39] Booth, A. M:.; Dissertation, University of Manchester, **to be submitted in 2007**.

[40] Booth, A. M.; Braun, S.; et al.; in preparation

[41] http://cars9.uchicago.edu/ifeffit/.

[42] Domke, M.; Xue, C.; Puschmann, A.; Mandel, T.; Hudson, E.; Shirley, D. A.; Kaindl, G.; Chemical Physics Letters, **1990**, *173*, 122-128.

[43] Domke, M.; Xue, C.; Puschmann, A.; Mandel, T.; Hudson, E.; Shirley, D. A.; Kaindl, G.; Chemical Physics Letters, **1990**, *174*, 668.

[44] Shimada, H.; Imamura, M.; Matsubayashi, N.; Saito, T.; Tanaka, T.; Hayakawa, T.; Kure, S.; Topics in Catalysis; **2000**, *10*, 265-271.

[45] Coffman, F. L.; Cao, R.; Pianetta, P. A.; Kapoor, S.; Kelly, M.; Terminello, L. J.; Applied Physics Letters; **1996**, *69*, 568-570.

[46] Aita, C. R.; Tran, N. C.; Journal of Vacuum Science & Technology, A: Vacuum, Surfaces, and Films, **1991**, *9*, 1498-1500.

[47] Soares, J. M. C.; Bowker, M.; Applied Catalysis, A: General, **2005**, *291*, 136-144.

[48] Safarova, M.; Kusy, J.; Andel, L.; Fuel, **2005**, *84*, 2280-2285.

[49] Mondal, K.; Lorethova, H.; Hippo, E.; Wiltowski, T.; Lalvani, S. B.; Fuel Processing Technology, **2004**, *86*, 33-47.

[50] Chun, D. H.; Xu, Y.; Demura, M.; Kishida, K.; Wee, D. M.; Hirano T.; Journal of Catalysis, **2006**, *243*, 99-107.

[51] Marta, G.; Arena, F.; Baricco, M.; Coluccia, S.; Marchese, L.; Parmaliana, A.; Catalysis Today, **1993**, *17*, 449-458.

[52] Minh, C. L.; Jones, R. A.; Craven, I. E.; Brown, T. C.; Energy & Fuels, **1997**, *11*, 463-469.

[53] Cheng, H.; Reiser, D. B.; Dean Jr., S.; Catalysis Today, **1999**, *50*, 579-588.

[54] Yates Jr.; J. T.; Surface Science, **1994**, *299*, 731.

[55] Peuckert, M.; Coenen, F. P.; Bonzel, H. P.; Surface Science, **1984**, *141*, 515-532.

[56] Juodkazis, K.; Juodkazyte, J.; Jasulaitiene, V.; Lukinakas, A.; Sebeka, B; Electrochemical Communications, **2000**, *2*, 503-507.

[57]: Jansen, M.; Mudring, A. V.; *The Chemistry of Gold Oxides,* John Wiley & Sons Ltd, **1999**.

[58]: Ashcroft, S. J.; Schwarzmann, E.; Journal of the Chemical Society Faraday Transactions I, **1972**, *68*, 1360.

4.3 Catalytic activity of gold powder of the CO oxidation

4.3.1 Abstract

The CO oxidation on pure metallic gold has been studied as function of temperature. Bulk gold becomes active at temperatures above 600 K. When heating the gold particles in a CO/O_2 mixture a conditioning of the catalyst at a temperature between 692 K and 713 K was observed. At temperatures below 692 K the rate of CO_2 production was increased in comparison to before the conditioning. Turnover Frequencies (TOF) of approximately 1 s^{-1} per surface gold atom at 692 K were observed. The activation energy was determined to be 53 kJ/mol. SEM and AFM images of the used powder revealed no change in size or shape of the gold particles as a result of the catalytic reaction. However, a mass transport on the particle surface, resulting in a reduced surface roughness after the reaction, is shown in the images. This change in the surface morphology might explain the conditioning effect. *Ex situ* XPS data showed only metallic Au^0 to be present at the surface of the gold particles before and after the CO oxidation.

4.3.2 Introduction

Gold nanoparticles are of great interest to catalytic science, as they posses high activity for various oxidation processes [1 - 3] even at very low temperatures. The mechanistic details of these reactions remain unclear [4 - 12]. The most controversial point is the activation of the oxygen-oxygen bond in the low temperature CO oxidation over supported nanoparticle gold catalysts. FTIR studies in the early 1990's showed the presence of carbonate species on the catalyst during the reaction [13]. But different groups have pointed out that these species are either only spectator states [14 - 16] or even inhibit the CO oxidation [17]. The presence of oxygen near or at the gold/support interface was found in FTIR studies as well [15, 18] characterised by a slight shift in the peak position of the oxygen-oxygen bond. It was proposed that defect sites in the support at these positions weaken the oxygen-oxygen bond. Either activated oxygen can directly

react with the CO [15, 18] or lattice oxygen of the support reacts with the carbon monoxide [19] and molecular oxygen only recompiles the created defect sites. Furthermore, the influence of water on the reaction is not clear, and it is argued whether water supports or inhibits the reaction, or if certain quantities are necessary [15, 20 - 22]. A positive influence of water could be the creation of hydroxy or superhydroxy species, which would lower the activation energy for breaking the oxygen-oxygen bond (for a more detailed discussion about the reaction mechanism see chapter 1).

In contrast to the high catalytic activity of gold nanoparticles, it is assumed that gold in its bulk state is catalytically inactive, and acts as the prototype inert material. Hence, it gives the opportunity to understand the changes in the behaviour of clusters compared to the bulk material. The major difference between a cluster and bulk material is the transition from a band structure of the energy levels in a bulk material to separated orbitals, as in molecules, for clusters [23]. Also d-band narrowing and shift of the Fermi energy relative to unoccupied states in the d-band of bulk materials occur [24]. Furthermore, the amount of defect states and low coordinated atoms is much higher in clusters than in bulk materials. Particularly for nm sized clusters the nearest-neighbour coordination number of all atoms can be low (about 4 to 7).

Gold nanoparticles can oxidize CO at temperatures well below room temperature, but "bulk gold" requires elevated temperatures of 550 K and more [25 - 27]. The temperature approximately correlates with the energy required to break the oxygen double bond. In a temperature range between 500 K and 550 K, dosed molecular oxygen recombines with pre-dosed atomic oxygen on Au(111). This correlates with the dissociation and adsorption of molecular oxygen [28] and indicates that a temperature of 550 K is required to create atomic oxygen on metallic, bulk gold.

Gold powders, sponges, wires and rods have been studied previously, which was reviewed by Bond and Thompson [29]. Previous studies include the oxidation of Ethylene and Propylene [30] and the CO oxidation of gold powder [25, 26] or woven gold mesh [27]. Attempts have been made to improve the activity of gold by oxidizing it [31, 32]. Bone and Andrew [27] conducted the first CO oxidation studies of unsupported gold in the 1920's. They showed, as well as Haruta *et al.* [26] (in the 1980's on colloidal

gold) that at a temperature of about 550 K the CO oxidation with molecular oxygen of unsupported bulk gold starts.

Soares *et al.* [32] showed that the temperature required for the CO oxidation can be drastically reduced when using macroscopic gold oxide and gold hydroxide physically mixed with TiO_2 powder. Only a temperature around room temperature is required to gain some CO oxidation activity. But this is a non-catalytic CO oxidation by oxygen of the gold oxide or hydroxide and not by molecular oxygen supplied by the gas feed. After reducing the Au(+III)-particles to metallic gold the temperature required for the CO oxidation is raised by about 100 K to 398 K. This temperature indicates the onset of the catalytic oxidation of the CO by molecular oxygen.

Zielasek *et al.* [33] and Xu *et al.* [34] prepared a high surface, sponge like, gold catalyst by leaching a gold/silver alloy. The advantage of a high surface area catalyst is the high amount of low coordinated surface atoms at step, kink and corner sites. These sites are also present in a high amount in clusters and on rough surfaces. Thus it was shown that roughened gold single crystal surfaces have a significant higher desorption temperature for CO and O_2 [35, 36], which supports the catalytic activity of these surfaces. The catalyst prepared by Zielasek *et al.* [33] shows catalytic activity already at 253 K and Xu *et al.* at 243 K [34], which is a significant improvement to other, unsupported gold catalysts. Due to the preparation technique, a high amount of silver remains, especially at the surface of this catalyst (4.4% by means of XPS analysis) [33], which leads to the unanswered question of whether the increased activity is due to the high surface area of the gold or, if the silver is the most important catalytic activity of this type of catalyst.

4.3.3 Experimental

4.3.3.1 Reaction kinetic studies

For the catalytic activity test of the gold particles (Aldrich, spherical, 1.5-3.0 µm, 99.9%) a modified tubular gas-flow reactor as presented by Willneff *et al.* [37] was used. The inner diameter of the quartz tube was 4 mm (see fig. 4.3.1). The gold particles were fixed in the tube using quartz wool plugs underneath. The reactor was mounted vertically into a

furnace, which allowed heating up to approximately 1000 K. The actual temperature in the reactor was monitored with a K-type inconel-shielded thermocouple that was introduced into the catalyst bed from the top.

The gases were mixed with mass flow controllers and the corresponding flows were calibrated with a flow meter attached to the outlet for the reactor effluent. Oxygen (BOC, N5.5) and Helium (BOC, 5.0) were used as supplied, whereas CO (BOC, AZ grade) was purified before use by passing it over a cool trap filled with an acetone/dry ice mixture. The usual flow settings for the gases were 24 ml/min CO, 18 ml/min O_2 and a total flow of 90 ml/min. The Helium flow was adjusted so that a flow of 90 ml/min was achieved. This gas stream was first purged through the by-pass for 30 min to stabilize the gas flow, and then switched to the reactor. The gas stream was monitored with a Stanford Research Systems (SRS) RGA 100. The gas phase was analyzed using the fragments listed in table 4.3.1.

Table 4.3.1: Fragments analysed with MS

Mass [atom units]	Fragment
2	H_2^+, He^{2+}
12	C^+
16	O^+
18	H_2O^+
28	CO^+, N_2^+
32	O_2^+
44	CO_2^+ ($C_3H_8^+$)
45	$C_2H_5O^+$

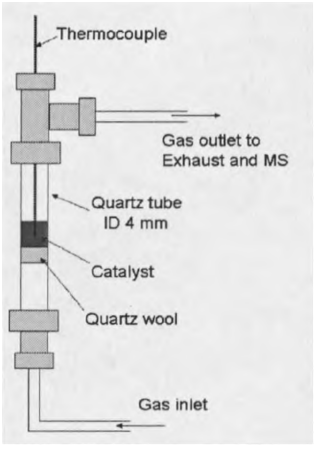

Fig. 4.3.1: Schematic drawing of the tubular flow reactor.

4.3.3.2 SEM

SEM images of gold powder were acquired with a FEI Quanta 200 ESEM. The acceleration voltage of the electron beam was usually 30 keV and the high vacuum mode (~ 1×10^{-4} torr) was used. The usual spot size of the electron beam was about 0.4 μm. Secondary electron images were acquired. For EDX measurements an EDAX Genesis analyser with an electron spot size of about 0.6 μm was used. An ultra-thin window was used to separate the EDX from the SEM chamber.

4.3.3.3 AFM

To collect AFM images, a Veeco™ Nanoscope III in tapping mode was used. The used tips were Al-coated single cantilever tapping mode tips (Budget Sensors, Resonant Frequent: 300 kHz, Force Constant 40 N/m). A typical scan was done with an initial gain of 0.2, a proportional gain of 2.0, 512 lines/sample and a scan speed between 0.5 Hz and 1 Hz. The scan range was varied between 10 μm and 250 nm. At scan ranges less than 1 μm special care had to be taken to achieve a noise-free image. The AFM was enclosed with a Plexiglas hood for the reduction of noise effects, and to have the option to keep the sample under controlled conditions (N_2 atmosphere, BOC 2.2). The gold particles were fixed with thermoplast (SPI supplies, Tempfix) on the specimen disk (Agar).

4.3.4 Results

The conversion of CO in a 4:3 ($CO:O_2$) mixture with O_2 over gold powder is shown in fig. 4.3.2, 4.3.3 and 4.3.4. After an initial phase of flushing the reactor with He for 35 minutes, the gases CO and O_2 were dosed *via* the by-pass directly into the mass spectrometer (MS). The conversion to CO_2 in this stage occurs entirely in the MS itself, on the walls with adsorbents but mostly on the filament where either CO and O_2 react with each other or the produced fragments.

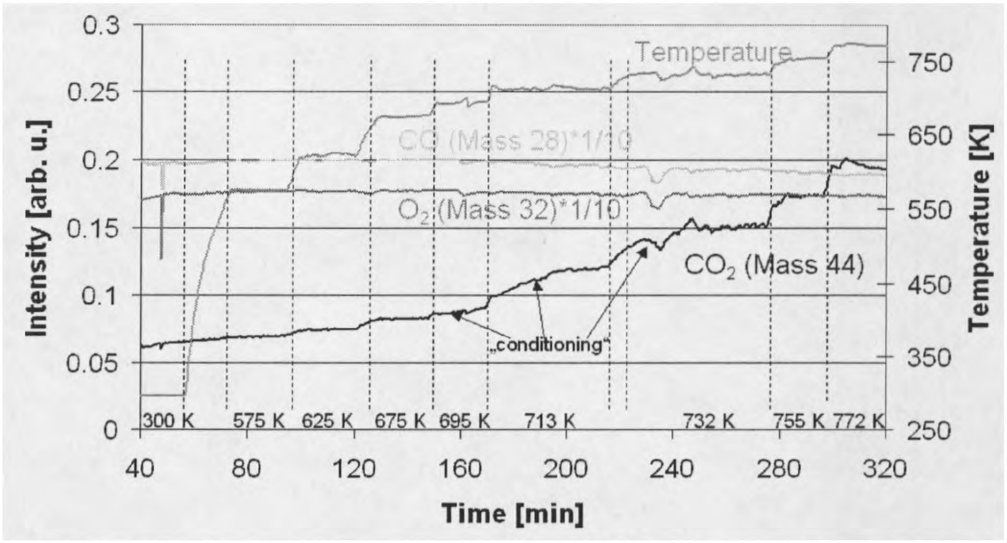

Fig. 4.3.2: Mass spectrometer traces of the conditioning of the gold powder in a 4:3 CO:O_2 mixture. The temperature as monitored by a thermocouple in the reactor bed is given in grey as well as indicated at the bottom of the graph. The MS traces of CO_2 (amu: 44) in black, O_2 (amu: 32) in dark grey and CO (amu: 28) in light grey.

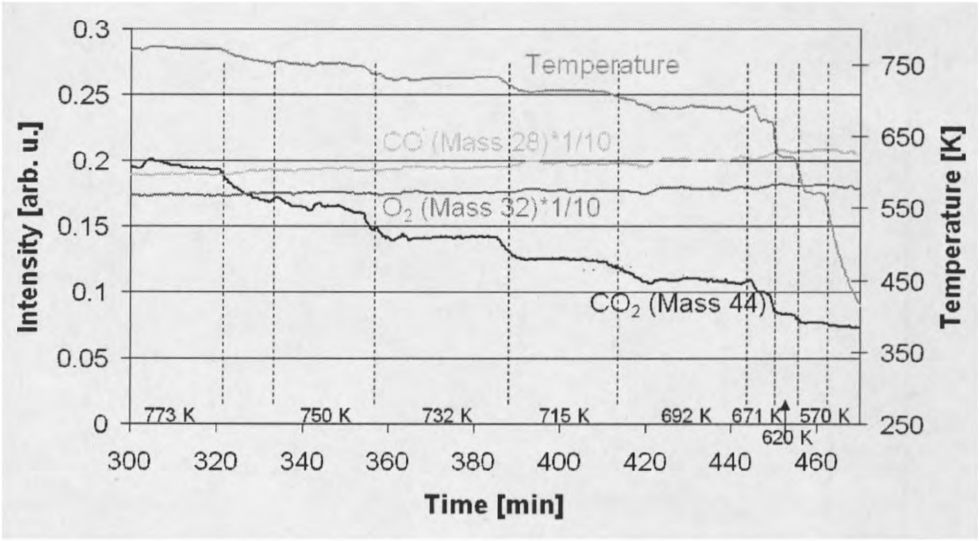

Fig. 4.3.3: Mass spectrometer traces of the catalytic activity of gold powder in the CO oxidation reaction. The temperature as monitored by a thermocouple in the reactor bed is given in grey as well as indicated at the bottom of the graph. The MS traces of CO_2 (amu: 44) in black, O_2 (amu: 32) in dark grey and CO (amu: 28) in light grey.

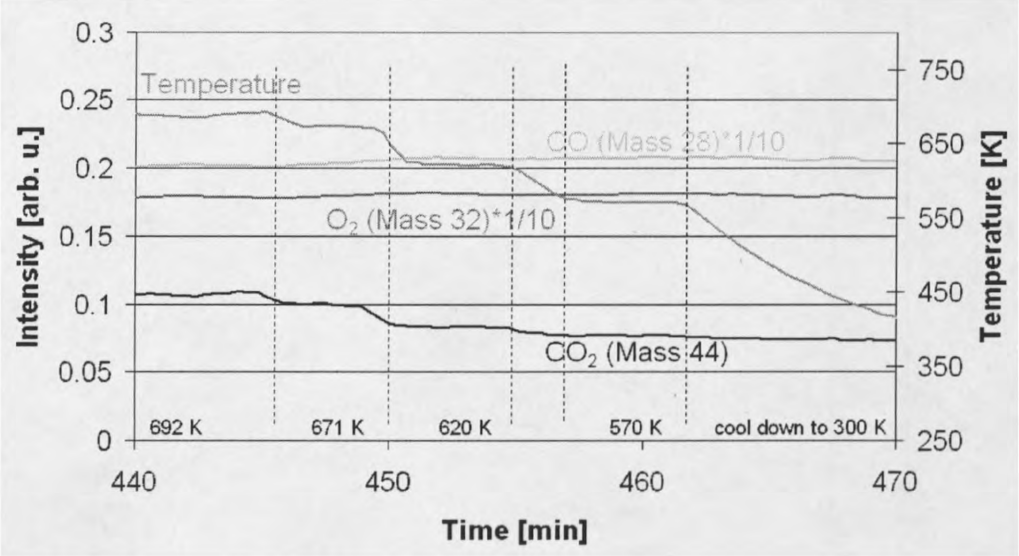

Fig. 4.3.4: Mass spectrometer traces of the CO oxidation over gold powder at low CO conversion. The temperature as monitored by a thermocouple in the reactor bed is given in grey as well as indicated at the bottom of the graph. The MS traces of CO_2 (amu: 44) in black, O_2 (amu: 32) in dark grey and CO (amu: 28) in light grey.

After 48 min the gas stream was changed from by-pass to flow in the reactor. As no significant increase in the CO_2 signal is observed, 1-2 μm gold particles are inactive at room temperature. After 57 min the temperature is increased from room temperature (295 K) to about 573 K. A small increase of CO_2 is observed over the temperature range but the gold is still inactive. Raising the temperature to about 623 K reveals the first small step in the CO_2 production. This suggests that the gold powder is catalytically active. Increasing the temperature to 673 K results in a slightly larger step in the CO_2 evolution. Raising the temperature to about 693 K not only results in a stepwise increase in the activity but also to an isothermal increase in CO_2 production over time. This effect is even more pronounced at a temperature of about 713 K. After reaching 713 K, the amount of CO_2 produced increases for nearly 30 minutes isothermally before the activity becomes stable again. This indicates that the catalyst undergoes a conditioning process at a temperature around 700 K.

Raising the temperature in a stepwise manner to about 773 K results in a consistently larger step in the CO_2 concentration, but no further conditioning at constant temperature is evident. However, a high sensitivity of the catalytic activity to small temperature changes (1-2 K) is noticeable.

Decreasing the temperature to 752 K and 732 K results in a slight decrease in CO_2 concentration in comparison to the temperature before the maximum temperature (cf. fig. 4.3.5). But at the "activation temperature" of 713 K and below, a higher catalytic activity is observed than before heating (see also fig. 4.3.5). At temperatures around 700 K the difference in CO_2 production is about 2 ml/min or an increase of about 111% for the catalyst after conditioning in comparison to the catalyst before conditioning. At lower temperatures, of about 625 K, the absolute effect decrease to 0.08 ml/min but the catalyst is roughly 200% more active at the end of the experiment.

At temperatures below 700 K a low conversion of 1% to 5% CO is present (cf. fig. 4.3.4). This is the most critical data for the determination of the activation energy, since no transport effects should be present in this conversion region. Consistent with this hypothesis is that the gas phase concentration, even at 770 K, is only a few % lower than at 300 K. This suggests that the reaction is not transport-limited under these conditions and that the activation energy is small for the conditioned catalyst.

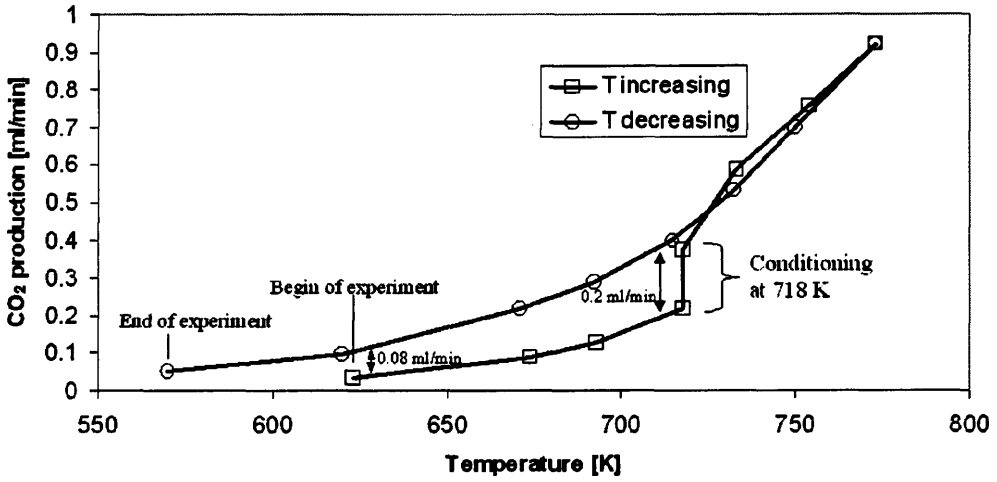

Fig. 4.3.5: Comparison of the rate of CO_2 production during the CO oxidation experiment. Values were determined from figures 4.3.2, 4.3.3 and 4.3.4.

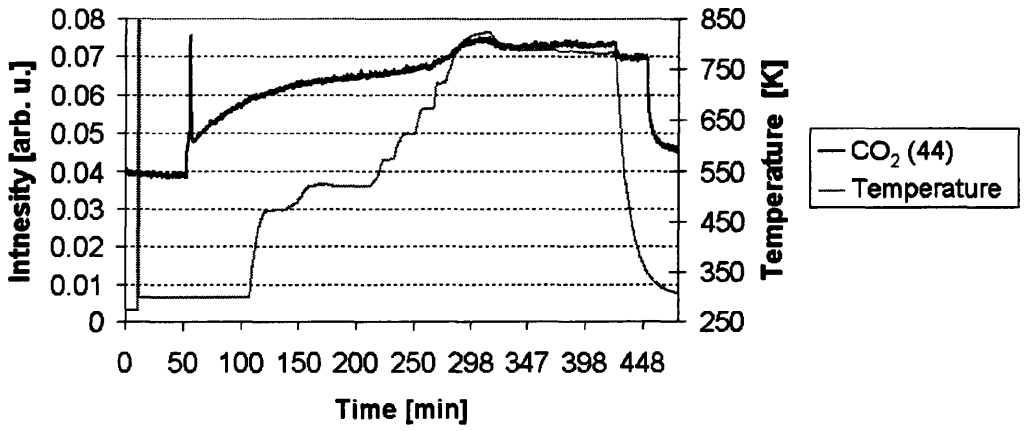

Fig. 4.3.6: Mass spectrometer traces of the control experiment for the activity of the reactor and cross contamination of the used glass wool in the CO oxidation shown in fig. 4.3.2 to 4.3.4.

To test whether the observed CO oxidation is catalysed by the gold powder itself, by any part of the reactor, or possible gold deposits on the used quartz wool, the reactor was loaded with the quartz wool used in the CO oxidation (cf. fig. 4.3.6). 56 minutes after introducing the reactants into the reactor a slight increase in activity over a time of 150 minutes can be seen, as in fig. 4.3.2. This is reactor determined, but minor in comparison to the catalytic activity measured and can be neglected.

At about 673 K an increase in CO_2 production is observed that is temperature induced, and increases by 0.01 units up to 823 K. This is still one order of magnitude smaller than the increase of CO_2 production that can be measured at 773 K with gold powder in comparison to room temperature (0.13 units). This means, that for the measured temperatures, increased CO_2 production is a catalytic effect of the gold powder. On the other hand it should be noted that at temperature above 700 K – 800 K the CO starts to be oxidized by either the reactor walls (silica glass) the supporting glass wool or impurities in either of them.

In the case of the gold catalysed CO_2 production, the amount of CO_2 and the turnover Frequency (TOF, per surface atom) of the reaction is calculated. In the experiment,

18 ml/min O_2 was dosed producing 0.96 ml/min CO_2 at 773 K. The number of surface atoms was calculated, assuming the gold particles have a spherical shape with a diameter of 1.5 µm (cf. table 4.3.2) as obtained from the SEM images. The small, disc like elevations will only minimally influence the surface area of the particles, since their heights is much smaller than their radius (r ~ 100 nm, h ~ 1 nm).

The active sites are thus hard to determine. If only the atoms at the grain boundary of the different discs would be active, about 2% of the surface atoms would be active (considering the ratio between the area and the extend of a circle: $\frac{\pi r^2}{2\pi r} = \frac{r}{2} = \frac{100}{2} = 50 \triangleq 2\%$). Therefore the TOF per active gold atom would increase by a factor of 50.

Table 4.3.2: TOF of the CO oxidation over gold powder.

Temperature [K]	773	750	732	715	692
Produced CO_2 (ml/min)	0.92	0.70	0.53	0.40	0.29
Reaction rate (µmol[CO_2]/s× g[gold])	0.14	0.11	0.082	0.062	0.044
TOF (1.5 µm diameter) [CO_2 molecules/surface gold atoms× s]	3.4	2.6	2.0	1.5	1.1
TOF ("active atoms") [CO_2 molecules/surface gold atoms× s]	170	130	100	75	55

Temperature [K]	671	620	570	273*
Produced CO_2 (ml/min)	0.22	0.099	0.050	2.1×10^{-7}
Reaction rate (µmol[CO_2]/s× g[gold])	0.034	0.015	0.0077	3.2×10^{-8}
TOF (1.5 µm diameter) [CO_2 molecules/surface gold atoms× s]	0.81	0.37	0.19	7.8×10^{-7}
TOF ("active atoms") [CO_2 molecules/surface gold atoms× s]	40.5	18.5	9.5	39×10^{-6}

* extrapolated from the given data at higher temperatures.

The activation energy of the reaction could be determined by the Arrhenius plot (cf. fig. 4.3.7). Assuming the reaction rate is equivalent to the rate of production of CO_2 per second, the activation energy is 53 kJ/mol.

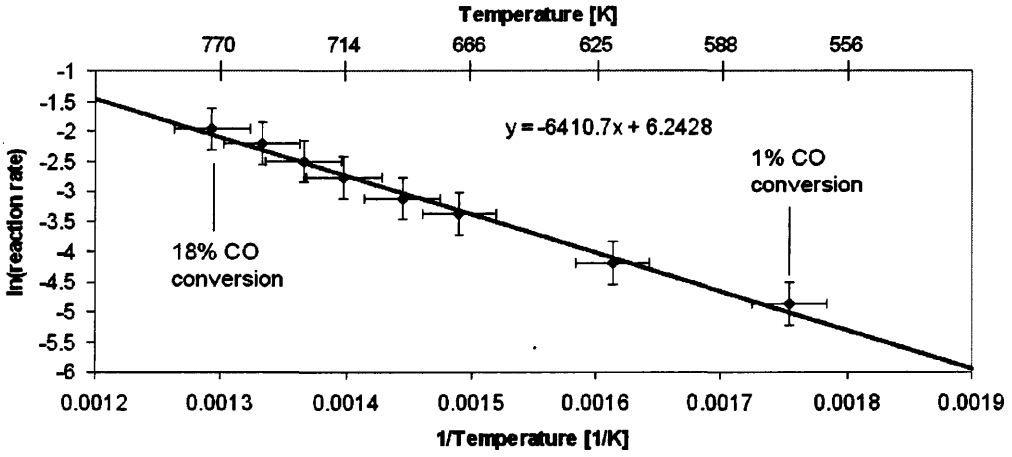

Fig. 4.3.7: Arrhenius plot for the catalytic activity of gold powder as seen in fig. 4.3.4 and 4.3.2. Indicated are the standard errors for the data points and the values for E_a/R = 6410.7 K and A = 6.2428.

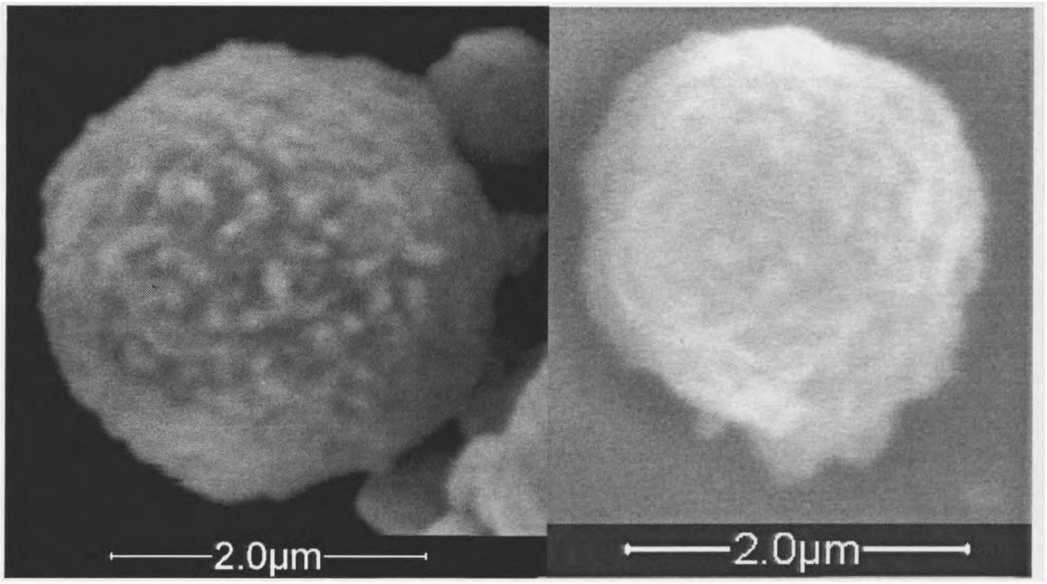

Fig. 4.3.8: SEM image of gold powder particle used in the CO oxidation (left image without CO oxidation, right image after CO oxidation).

An SEM image of the gold powder particles used in this work is shown in fig. 4.3.8. The particles have a size distribution between 0.5 µm and 3 µm. The particles tend to aggregate and form larger agglomerates. It was also found that the CO oxidation does not change the shape or size of the particles. This was also confirmed using AFM (cf fig. 4.3.9 and 4.3.10).

The SEM image in fig. 4.3.8 shows that the particles are mostly spherical. The surface is rough and contains many terraces. These defects are discs that build up the particle as revealed by AFM images. The discs have a diameter of about 50 to 200 nm and are polyhedral. Further, the discs are not flat but have a hemi-oblate shape with heights of, usually, not more than 1 nm. The surface "roughness" of the particles decreases after the CO oxidation and areas with large terraces are present. This indicates some mass transport of the gold on the surface during the CO oxidation.

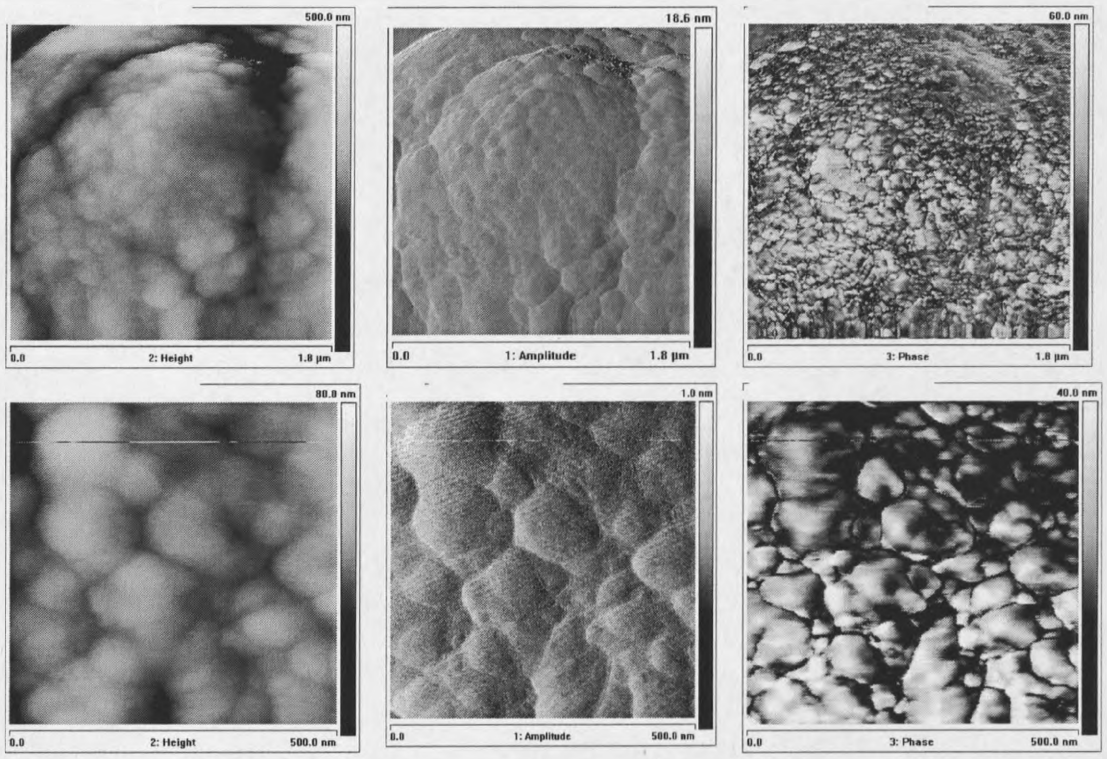

Fig. 4.3.9: AFM images of a gold powder particle as it was received from the manufacturer.

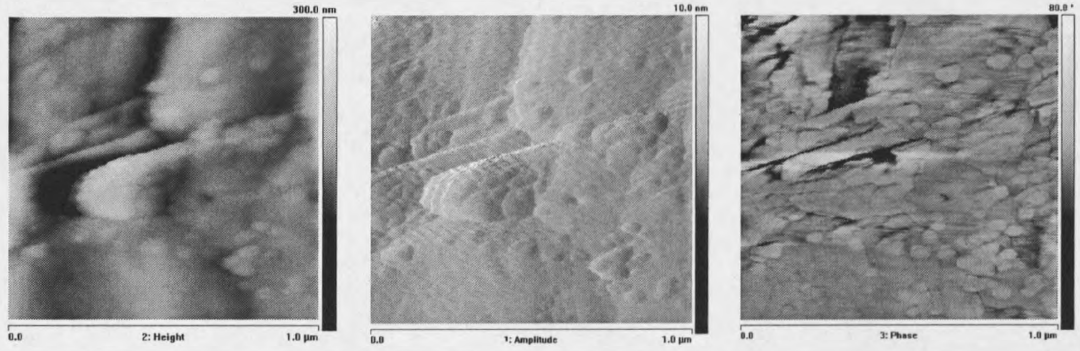

Fig. 4.3.10: AFM images of a gold powder particle after CO oxidation.

The surface analysis of the gold particles before and after the CO oxidation shows an elemental composition of Au, O and C (cf. fig. 4.3.11). The relative intensities do not vary significantly and the absence of Au(+III) should be noted (cf. fig. 4.3.12). The O 1s

peak will be from C-O bond containing dust, which forms an overlayer on the particle due to the storage of the gold powder in the laboratory environment.

The small Si 2p and Si 2s peaks in the spectrum after the CO oxidation are from Si^{4+} and will be from small amounts of quartz wool (SiO_2) that was used to hold the gold in the reactor. It was not possible to separate the gold and quartz wool after the reaction.

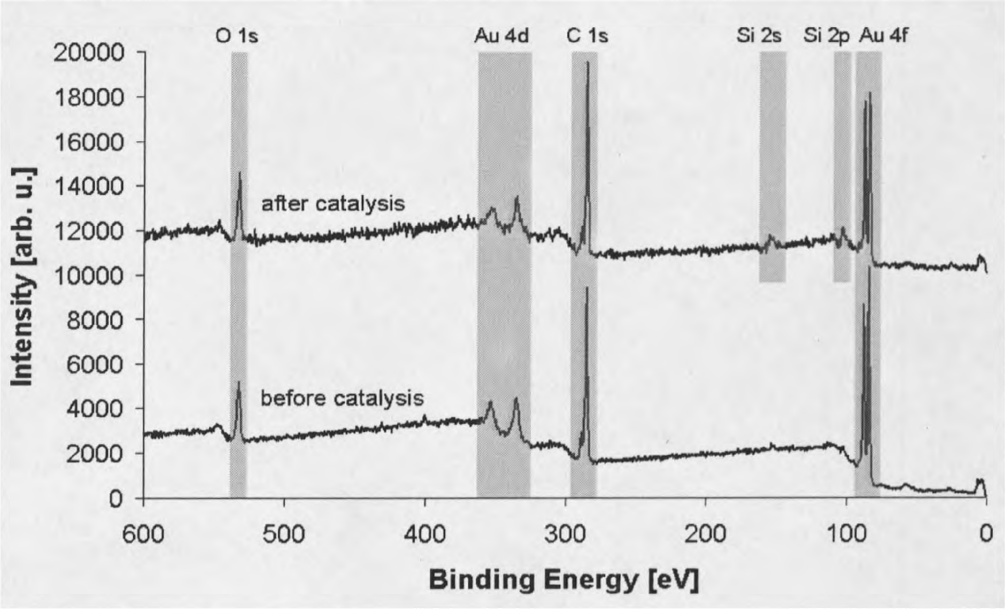

Fig. 4.3.11: XP spectra of gold powder used for the CO oxidation.

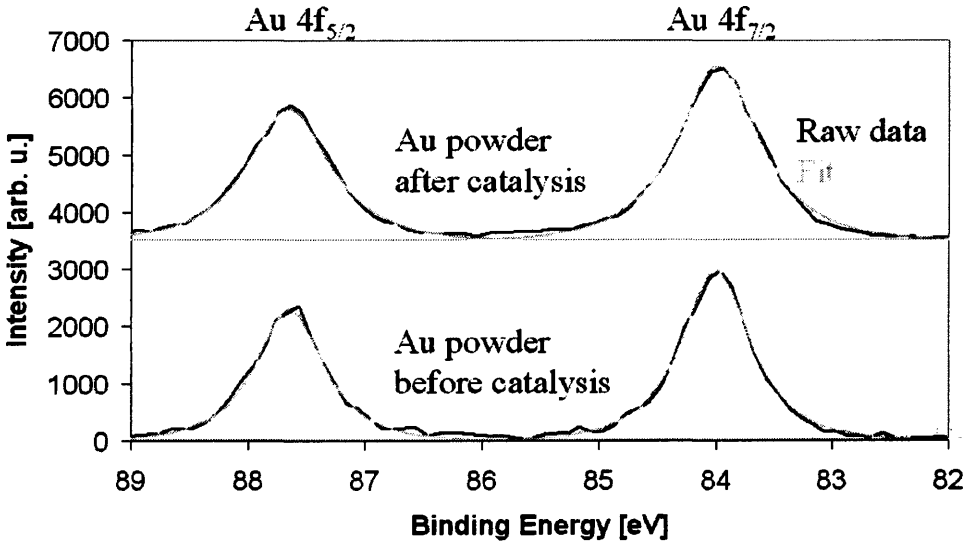

Fig. 4.3.12: Au 4f XP spectra of gold powder used for the CO oxidation.

4.3.5 Discussion

The analysis of the gold powder used in this study proves that pure, macroscopic gold is catalytically active. The effect of impurities on the surface of the catalyst can be ruled out, since no impurities have been found in the XPS studies. As the gold powder was not mixed with other materials, as e.g. TiO_2 as previously done [25, 38], support effects cannot occur as well. This means that bulk gold is catalytically active at temperature above 600 K. The site of reaction on the gold is not yet proven, but it seems plausible that low coordinated gold atoms on the surface are the preferential place for the reaction. This is supported by the conditioning effect found (see discussion below) and by TPD experiments, which show an increased ability to adsorb CO and O_2 when an ordered gold surface is roughened [35]. The increased ability to bind the reactants on the surface of low coordinated gold gives a greater probability that the reactants find each other and react.

The conditioning of the catalysts at temperature around 700 K can be explained by the creation of new active sites on the surface. This might happen by the migration of gold atoms on the particle, or by transportation of gold in the gas phase by carbonyl species as

reported by Willneff *et al.* [37]. A change in the surface morphology of the gold particles after the CO oxidation is present in the SEM and AFM images, supporting this theory. Bone and Andrew [33] also found a conditioning of their catalysts, but they performed their studies at around 600 K, where it took several hours to days for an increase in the catalytic activity. This effect was accelerated with the higher temperature, so that it was detected at temperatures around 700 K when keeping the temperature steady for 30 minutes.

The conditioning of the catalyst by the migration of gold atoms on the surface appears not to generate more active sites. It could also be possible that active sides are covered by e.g. carbon residuals that are left from storage of the gold powder. At the given temperature, these residuals might either react with the oxygen to from CO or CO_2, or just enter the gas phase and free these sites. By this, more active sites would be present at the catalyst. Since these effects will occur on an atomic scale, it is difficult to observe them on gold powder since they are not flat enough to be analysed with STM. AFM and SEM, however do not have the spatial resolution to indicate whether more of these low-coordinated atoms are created.

The conditioning of the catalysts might also be an effect of oxygen species on, or near, the surface [33]. It might be that oxygen is either incorporated into the gold lattice, or subsurface oxygen is formed [39]. This could lead to better adsorption, or easier dissociation of molecular oxygen on the gold surface. Atomic oxygen on the surface of gold single crystals is also known to increase the dissociation possibility of molecular oxygen [28]. This means that first atomic oxygen has to be formed on the surface, which can be expected to be a slow process. After the creation of the first atomic oxygen, the creation of more atomic oxygen out of the molecular oxygen is supported, such as in an autocatalytic process. This will give a slowly increasing amount of atomic oxygen on the surface, which would react quickly with CO to form carbon dioxide.

Another possibility is the formation of gold oxide, which is known to be more active for the CO oxidation than gold [32]. The formation of a gold oxide overlayer though seems to be unlikely. The XPS data presented here do not show any Au(+III) near the surface after the CO oxidation. However, gold oxide is a stable compound under ambient conditions and it would be expected that some gold oxide would be present at the end of

the experiment, since the conditioning effect was not lost. Therefore XPS should have detected some gold oxide if it was formed during the conditioning. It was also reported before that gold oxide is reduced under similar conditions [40].

The temperature required to induce CO oxidation over gold powder (623 K preconditioning, 570 K after conditioning) is comparable with the data found by Haruta on colloidal gold powder (~550 K) [26, 41] and by Bone and Andrew on gold mesh (~550 K) [33]. The temperature required for the CO oxidation over gold oxide can be even as low as 253 K [25, 33, 38]. This difference in temperature indicates that gold oxide is not formed when CO is catalytically oxidized by macroscopic gold.

The activation energy for the CO oxidation of gold powder has been found to be 53 kJ/mol. The Arrhenius plot shows no diversion for the data points at high CO conversion (18%) from the line of best fit for the data points at low conversion (1-5%). Hence the transport limit for the reaction is not reached at this point, and all data points can be used for the calculation of the activation energy.

Activation energies, reaction rates and TOF's of supported and unsupported gold catalysts show the wide range of results found (cf. table 4.3.3). The calculated activation energy for the used gold powder here is higher than found for gold particles mixed with TiO_2 powder (10-18 kJ/mol [38] and ~23 kJ/mol [25]). Several aspects have to be taken into account when comparing these samples: The particles used in [25, 38] are much small then present here and they seem to be supported by the TiO_2. It is also not clear which conversion has been used to create the Arrhenius plot, which might result in a transport limiting effect if the data is measured at too high a conversion.

The values measured for the activation energy of the CO oxidation of gold catalysts varies from 10 kJ/mol to 60 kJ/mol in the literature (cf. table 4.3.3). This indicates that on the gold particles, different active sites can be found, which most likely differ in the coordination number of the gold atoms. This is supported by the data gained on deposition precipitation and impregnation catalysts reported by Bamwenda [42]. The gold particles themselves should be similar, but a difference in activation energy of roughly 30 kJ/mol has been found. This suggests that most active sites are deactivated in the impregnated sample. The deactivation will be most like due to chlorine, which has been

found on similar samples and is known to inhibit the catalytic reaction [43]. The remaining active centre will be similar to the ones found in this study, which explains the good agreement in terms of activation energy.

Table 4.3.3: Kinetic data on supported and unsupported gold catalysts.

Catalyst	E_a (kJ(mol)	Reaction rate (mol/s·g_{cat})	TOF (s^{-1})	Ref.
Au/TiO_2	25	---	---	[44]
Au/TiO_2	---	$7 \cdot 10^{-6}$-1×10^{-5} (313 K)	---	[45]
Au/TiO_2-In_2O_3	---	$3 \cdot 10^{-6}$-5×10^{-6} (313 K)	---	[45]
Au powder – TiO_2	23.4	$13 \cdot 10^{-9}$ (313 K)	0.023 (313 K)	[25]
Au powder – TiO_2	10-18	5.9×10^{-10}-7.3×10^{-7} (213 K)	1.6×10^{-6}-4.6×10^{-2} (213 K)	[38]
Au/TiO_2(DP)	27	33×10^{-4}	1.3	[46]
Au/TiO_2(DP)	18-27	$0.4\text{-}20 \times 10^{-6}$ (300 K)	0.037-0.26 (300 K)	[42]
Au/TiO_2(FD)	56-57	$0.15\text{-}0.36 \times 10^{-9}$ (300 K)	$8\text{-}10 \times 10^{-6}$ (300 K)	[42]
Au/TiO_2(IMP)	58	17×10^{-9} (300 K)	---	[42]

DP: deposition precipitation, FD: photo deposition, IMP: impregnation, E_a: activation energy, TOF: Turn over frequency.

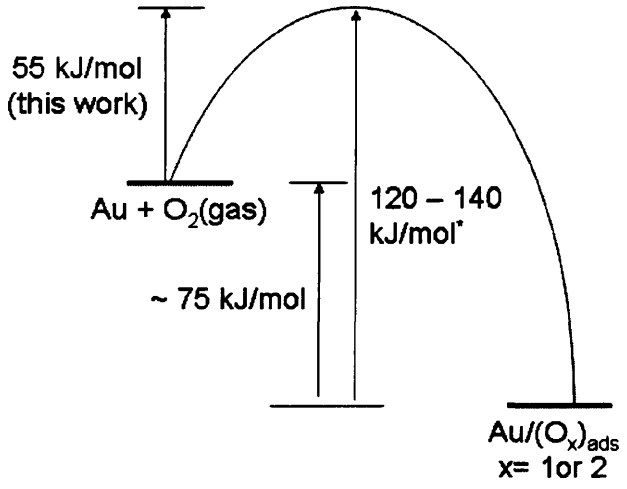

Fig. 4.3.13: Free energy diagram of the adsorption of oxygen on gold. * is taken from [47].

For the CO oxidation of the presented gold powder, it seems plausible that the adsorption and possible dissociation of the oxygen on the gold is the rate-determining step (cf. fig. 4.3.13). This means the measured activation energy of about 55 kJ/mol corresponds to the energy barrier between oxygen in the gas phase, and oxygen, atomically or molecularly, adsorbed on the gold particles. From single crystal studies the activation energy for the desorption of oxygen is known to be between 120 and 140 kJ/mol depending on the oxygen coverage [47]. From this, the energetic difference between the two states of gold and oxygen in the gas phase and oxygen adsorbed on the gold can be determined to be roughly 75 kJ/mol.

4.3.6 Conclusion

The reactivity and activation energy of an unsupported gold powder catalyst not mixed with a metal oxide was determined. The activation energy of 53 kJ/mol is at the higher end of the values reported for supported and unsupported gold catalysts. The temperature required for the CO oxidation over the gold powder is around 600 K, which corresponds with values found earlier for similar catalysts. A conditioning effect around 700 K increases the catalytic activity of the gold powder. An increased catalytic activity is also present when the catalyst is operated at temperature below 700 K after conditioning. AFM and SEM images reveal a mass transport on the gold particle surface, which might be the reason for the increased catalytic activity after the conditioning. The activation energy of the CO oxidation of unsupported gold particles was determined to be 53 kJ/mol.

This shows that macroscopic gold powder has catalytically active centres. It should also be noted that the reaction mechanism at elevated temperatures, as used in this work, would result in a different reaction mechanism than at, or close to, room temperature. But in comparison to nanoparticles prepared by deposition-precipitation, these active centres are much less active. In comparison to catalysts prepared by impregnation technique the

extrapolated activity at room temperature is similar. This indicates that the active centres present on catalysts prepared by impregnation are the same, or similar, to those present on the macroscopic gold powder. In the case of the catalysts prepared by impregnation, highly active centres, as present after preparation by deposition-precipitation, are most likely covered by chlorine atoms. In the case of the gold powder these active centres cannot be formed due to the low surface to bulk ratio. This all indicates that the most active centres on gold catalysts with high activity are low coordinated gold atoms.

References

[1] Sakurai, H.; Haruta, M.; Applied Catalysis, A; **1995**, *127*, 93-105.

[2] Hayashi, T.; Tanaka, K.; Haruta, M.; Journal of Catalysis; **1998**, *178*, 566-575.

[3] Carrettin, S.; McMorn, P.; Johnston, P.; Griffin, K.; Kiely, C. J.; Physical Chemistry Chemical Physics; **2003**, *5*, 1329-1336.

[4] Wallace, William T.; Whetten, Robert L.; Journal of the American Chemical Society; **2002**, *124*, 7499-7505.

[5] Olea, M.; Iwasawa, Y.; Applied Catalysis, A: General; **2004**, *275*, 35-42.

[6] Stiehl, J. D.; Kim, T. S.; McClure, S. M.; Mullins, C. B.; Journal of the American Chemical Society; **2004**, *126*, 13574-13575.

[7] Iizuka, Y.; Tode, T.; Takao, T.; Yatsu, K.; Takeuchi, T.; Tsubota, S.; Haruta, M.; Journal of Catalysis, **1999**, *187*, 50-58.

[8] Meyer, R.; Lemire, C.; Shaikhutdinov, S. K.; Freund, H. J.; Gold Bulletin, **2004**, *37*, 72-124.

[9] Costello, C. K.; Kung, M. C.; Oh, H. S.; Wang, Y.; Kung, H. H.; Applied Catalysis, A: General, **2002**, *232*, 159-168.

[10] Bondzie, V. A.; Parker, S. C.; Campbell, C. T.; Catalysis Letters, **1999**, *63*, 143-151.

[11] Haruta, M.; Catalysis Surveys from Japan, **1997**, *1*, 61-73.

[12] Daniells, S. T.; Overweg, A. R.; Makkee, M.; Moulijn, J. A.; Journal of Catalysis, **2005**, *230*, 52-65.

[13] Boccuzzi, F.; Chiorino, A.; Tsubota, S.; Haruta, M.; Journal of Physical Chemistry, **1996**, *100*, 3625-3631.

[14] Schumacher, B.; Denkwitz, Y.; Plzak, V.; Kinne, M. Behm, R. J.; Journal of Catalysis, **2004**, *224*, 449-462.

[15] Haruta, M.; Cattech, **2002**, *6*, 102-115.

[16] Schubert, M. M.; Hackenberg, S.; van Veen, A. C.; Muhler, M.; Plzak, V.; Behm, R. J.; Journal of Catalysis, **2001**, *197*, 113-122.

[17] Moreau, F; Bond, G. C.; Applied Catalysis, A: General, **2006**, *302*, 110-117.

[18] Boccuzzi, F.; Chiorino, A.; Manzoli, M.; Lu, P.; Akita, T.; Ichikawa, S.; Haruta, M.; Journal of Catalysis, **2001**, *202*, 256-267.

[19] Boccuzzi, F.; Chiorino, A.; Manzoli, M.; Lu, P.; Akita, T.; Ichikawa, S.; Haruta, M.; Journal of Catalysis, **2001**, *202*, 256-267.

[20] Haruta, M.; Cattech, **2002**, *6*, 102-115.

[21] Grunwaldt, J. D.; Kiener, C.; Wogerbauer, C.; Baiker, A.; Journal of Catalysis, **1999**, *181*, 223-232.

[22] Lian, H.; Jia, M.; Pan, W.; Li, Y.; Zhang, W.; Jiang, D.; Catalysis Communications, **2005**, *6*, 47-51.

[23] Freund, H.J.; Surface Science, **2002**, *500*, 271-299.

[24] Remediakis, I. N.; Lopez, N.; Norskov, J. K.; Applied Catalysis, A: General, **2005**, *291*, 13-20.

[25] Bollinger, M. A.; Vannice, M. A.; Applied Catalysis, B: Environmental, **1996**, *8*, 417-443.

[26] Haruta, M.; Kobayashi, T.; Sano, H.; Yamada, N.; Chemistry Letters; **1987**, 405-408.

[27] Bone, W. A.; Andrew G. W.; Proceedings of the Royal Society of London, A; **1925**, *109*, 459-476.

[28] Deng, X.; Min, B. K.; Guloy, A.; Friend, C. M.; Journal of the American Chemical Society, **2005**, *127*, 9267-9270.

[29] Bond, G. C.; Thompson, D. T.; Catalysis Reviews - Science and Engineering, **1999**, *41*, 319-388.

[30] Cant, N. W.; Hall, W. K.; Journal of Physical Chemistry, **1971**, *75*, 2914-2921.

[31] Cant, N. W.; Fredrickson, P. W.; Journal of Catalysis, **1975**, *37*, 531-539.

[32] Soares, J. M. C.; Bowker, M.; Applied Catalysis, A: General, **2005**, *291*, 136-144.

[33] Zielask, V; Jürgens, B.; Schulz, C.; Biener, J. Biener, M. M.; Hamza, A. V.; Bäumer, M.; Angewandte Chemie International Edition, **2006**, *45*, 8241-8244.
[34] Xu, C.; Su, J.; Xu, X.; Pengpeng, L.; Zhao, H.; Tian, F.; Ding, Y.; Journal of the American Chemical Society, **2007**, *129*, 42-43.
[35] Gottfried, J. M.; Schmidt, K. J.; Schroeder, S. L. M.; Christmann, K.; Surface Science, **2003**, *536*, 206-224.
[36] Yim, W., Nowitzki, T.; Necke, M.; Schnars, H.; Nickut, P.; Biener, J.; Biener, M. M.; Zielasek, V.; Al-Shamery, K.; Klüner, T.; Bäumer, M.; Journal of Physical Chemistry C, **2007**, *111*, 445-451.
[37] Willneff, E. A.; Klanner, C.; Schroeder, S. L. M.; Chemical Communications, **2003**, 258-259.
[38] Tsubota, S.; Nakamura, T.; Tanaka, K.; Haruta, M.; Catalysis Letters, **1998**, *56*, 131-135.
[39] Gottfried, J. M.; Elghobashi, N.; Schroeder, S. L. M.; Christmann, K.; Surface Science, **2003**, *523*, 89-102.
[40] Klanner, C.; *Diploma Thesis*, Freie Universität Berlin, **2000**.
[41] Haruta, M.; Yamada, N.; Kobayashi, T.; Iijima, S.; Journal of Catalysis, **1989**, *115*, 301-309.
[42] Bamwenda, G. R.; Tsubota, S.; Nakamura, T.; Haruta, M.; Catalysis Letters, **1997**, *44*, 83-87.
[43] Soares, J. M. C.; Hall, M.; Cristofolini, M.; Bowker, M.; Catalysis Letters, **2006**, *109*, 103-108.
[44] Konova, P.; Naydenov, A.; Venkov, C.; Mehandjiev, D.; Andreeva, D.; Tabakova, T.; Journal of Molecular Catalysis A: Chemical, **2004**, *213*, 235-240.
[45] Debeila, M. A.; Wells, R. P. K.; Anderson, J. A.; Journal of Catalysis, **2006**, *239*, 162-172.
[46] Haruta, M.; Catalysis Today, **1997**, *36*, 153-166.
[47] Gottfried, J. M.; Schmidt, K. J.; Schroeder, S. L. M.; Christmann, K.; Surface Science, **2003**, *525*, 184-196.

4.4 *In situ* XPS analysis of gold nanoparticles supported on TiO_2 powder

4.4.1 Abstract

In situ XPS data on gold nanoparticles supported by TiO_2 powder were taken under various atmospheric conditions at BESSY. The data show that gold particles with an average diameter of about 3 nm, as detected by TEM, exhibit a second component in the Au 4f spectra under pure oxygen and reactive (CO and O_2) atmospheres. The second component is not due to the partial oxidation of the gold particles but the interaction of gold particles with the dosed gases, presumably oxygen. This interaction can either lead directly to a changed screening possibility of the affected gold clusters, or by the change of the shape of the gold particles, which leads to more gold atoms with low coordination numbers that have slightly increased binding energies in comparison to metallic bulk gold.

4.4.2 Introduction

Gold powder catalysts, and other catalysts supported by porous materials, have been studied by a variety of *in situ* experiments in recent years, with Infrared [1, 2, 3] and XAS [2, 4] being the most common. The use of *in situ* experiments (meaning under or close to the conditions used during catalysis) is highly favoured since the catalyst often undergoes changes when under reaction conditions compared to being under vacuum or even ambient conditions.

X-ray photoelectron spectroscopy (XPS) is a very useful technique for surface scientists, since it is very surface sensitive and provides data on the chemical composition of that surface. Therefore it is a good tool for the study of catalysts, because the catalytic process occurs on the surface of the catalyst. The use of XPS under *in situ* conditions is not trivial, and only relatively recently have the first *in situ* XPS instruments been presented e.g. [5, 6]. The use of *in situ* XPS can provide chemical information on the catalyst, as well as information on possible adsorbates, and even structural changes in the catalytic active material, as proposed by Willneff *et al.* [7].

So far, only very few *in situ* XPS studies on gold catalysts have been performed [7, 8]. The author of this work was a part of one of these studies [7], which was performed on a gold catalyst with a much lower gold loading (0.5 wt%) and smaller particles (smaller than 1 nm) than given in this chapter. The research group of R. J. Behm, that conducted a recent second study, used a very similar catalyst to this study, and also supplied the catalyst for the data presented here. Common to both previous studies, is that changing the atmosphere or the temperature of the catalyst induces changes in the Au 4f spectra, and two separated gold states can be identified. The study presented by Denkwitz *et al.* [8] on the larger gold clusters show that under vacuum conditions, prior to dosing gases, one major peak at 84.0 eV is present that is assigned to metallic, bulk gold. The interpretation given for the shifting and splitting of the Au 4f peaks are thus different. Willneff *et al.* [7] concluded that the shifts are due to the adsorption of the reactants on the gold particles and/or a change in the gold particle shape (morphology change). Denkwitz *et al.* [8] on the other hand assigned these changes to different partial charging of the gold particles on the catalyst. But the sample charges reported by the authors do not exceed 10 V (resulting in a BE shift of 10 eV in the XP spectrum) for all spectra shown. This value does not, or only slightly exceeds the charges accumulated, even on charge neutralised samples, and would therefore mean that such shifts observed in all XP spectra might be due to differential charging of the sample. Evidence in this work suggests that this interpretation is implausible, as differential charging effects resulting from samples charged by 100 V to 200 V will be presented, which show different characteristics than the results presented by Denkwitz *et al.* Hence the analysis of the data will be given in this study analogous to the interpretation by Willneff *et al.* [7].

4.4.3 Experimental

4.4.3.1 *In situ* XPS

For determining the electronic structure of the Au nanoparticles as well as the support XP spectra were taken at the beamline UE56/2 of the BESSY synchrotron in Berlin.

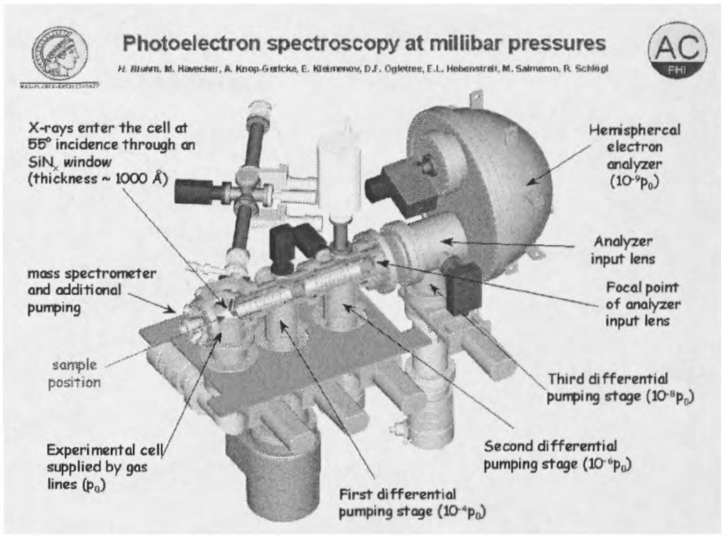

Fig. 4.4.1: *In situ* XPS apparatus of the FHI der MPG used at beamline UE56/2 of BESSY [5].

Due to the set up of the measurement chamber (cf. fig. 4.4.1 [5]) at the BESSY beamline, it allowed the use of different atmospheres while gathering the spectra. The analyser for the photoelectrons had a maximum sensitivity for electrons with a kinetic energy of about 200 eV.

The conditions used were high vacuum (HV) meaning the sample was held at the base pressure of the chamber (~10^{-6} mbar) without any gas added ("*ex situ*"). For *in situ* measurements the gases CO (0.1 mbar total pressure) and O_2 (0.1 mbar total pressure) were added. For "reaction conditions" a mixture of the gases (0.1 mbar each, total 0.2 mbar) was added.

The elements of interest were C, O, Ti and Au. To gain the maximum sensitivity for the electrons of a specific element, the excitation energy was varied (due to the fixed sensitivity of the detector). For the "normally" used excitation energies see table 4.4.1. For a region scan, a step width of 0.1 eV was used, and between 4 and 16 spectra were added. If the spectra were shifting due to sample charging *via* the measurements, multiple quick spectra were taken; then the energy shift due to charging was corrected in each individual spectrum and corrected spectra were then averaged.

Before a series of region scans at a specific energy, a "survey scan" (meaning the whole available spectral range at a step width of 1 eV) was taken.

Region	Excitation Energy [eV]
O 1s	820
Ti 2p	750
C 1s	580
Au 4f	380

Table 4.4.1: Used "normal" excitation energies for XPS measurements at the BESSY beamline UE56/2.

The actual energies used might differ from the values given, due to charging of the sample (see discussion 4.4.5) meaning the spectra had to be calibrated. Normally, the maximum of the Ti 2p in the survey scan was set to 37.5 eV. Afterwards the value for the corresponding O 1s, Ti 2p and C 1s were read and used to calibrate the region scans. In the case of the Au 4f, this method gave spectra that shift against each other. Hence the "Au $4f_{7/2}$ I" peak was set to 84.0 eV.

The sample used at BESSY was an Au/TiO_2 powder catalyst [9] supplied by a cooperation partner at the Universität Ulm in Germany. Briefly, the catalyst was prepared from a suspension of TiO_2 (Degussa P25) in 60°C warm water. An aqueous solution of $HAuCl_4 \cdot 4H_2O$ was added under stirring, and the pH was kept constant between 5.0 and 5.5 by adding a 0.16 M solution of Na_2CO_3. The solution was stirred for an additional 30 min. Subsequently, it was left to cool to room temperature, then filtered and washed. The filtrate was dried in vacuum overnight.

The determination of the Au content with inductively coupled plasma atom emission spectroscopy (ICP-AES) gave a loading of 3.4 wt%. The BET surface of the catalyst was 56 m^2.

states	ratio
$p_{1/2} : p_{3/2}$	1:2
$d_{3/2} : d_{5/2}$	2:3
$f_{5/2} : f_{7/2}$	3:4

Table 4.4.2: Intensity ratios for electron emitting orbitals.

For fitting the XP spectra, it was considered that the intensity ratios for p, d and f states are as estimated by the occupation of the electron emitting orbitals. That means $(2J_1+1)/(2J_2/1) = I_1/I_2$ [10]. For the actual ratios see table 4.4.2.

The components were fitted with a Gaussian/Lorentzian line shape containing 30% Gaussian and the Shirley function was used to fit the background. For corresponding

p, d and f peaks the full width at half distance (FWHM) values were set to equal each other.

4.4.3.2 Charging effects in XPS

Sample charging occurs due to the emission of electrons from the sample *via* the photoemission process. Almost always, a positive charge builds up on an electrically non-conducting sample. If the sample is electrically conductive and grounded then sample charges are neutralized.

If the sample is not electrically conductive (or only slightly, or semi-conducting) charge neutralisation cannot occur instantaneously. A minimum charge will be accumulated until the sample becomes sufficiently conductive (imperfection conductivity).

The positive charge on the sample decelerates electrons that are emitted. Such decelerated electrons have a lower kinetic energy, and thus appear in the XP spectrum at a "virtually" higher binding energy (BE). The BE scale in the spectra of samples that exhibit charging effects must be carefully calibrated, usually to a known emission line with known binding energy [11]. Often this is done *via* the C 1s peak of the ubiquitous graphitic or hydrocarbon contamination layers on the surface.

Small charging effects are normally homogenous across the whole sample, especially when the secondary electron emission characteristics (i.e. how many electrons are emitted from the sample by a single adsorbed photon) are homogeneous across the sample surface. However, when patches of strong secondary emitters are next to weak secondary electron emitters, then an effect known as 'differential charging' can occur.

4.4.4 Results

4.4.4.1 XPS

Figures 4.4.2 to 4.4.5 show the O 1s, Ti 2p, C 1s and Au 4f spectra, respectively. The spectra are stacked from bottom to top according to their temporal sequence. The conditions under which they were acquired were: a) immediately after transfer into the high vacuum measurement chamber (10^{-6} mbar), b) after leaving the sample for 16 h in high vacuum (without exposure to X-ray beam), c) after filling the chamber with

a 1:1 mixture of CO and O_2 (total pressure 0.2 mbar), d) the same conditions as under c), but heated from room temperature to 80°C, e) at 30°C and 0.1 mbar CO, f) at 30°C and 0.1 mbar O_2. The Ti 2p series only contains the first 4 steps.

Under O_2 exposure, an enormous sample charge was accumulated, corresponding to a binding energy (BE) shift of roughly 200 eV. Similarly, under reaction conditions at room temperature, a shift of 100 eV was observed. Under reaction conditions at 80°C, however, the BE shift was limited to 20 eV. Similarly, under high vacuum conditions and CO exposure, only a slight charge on the sample occurred, resulting in a BE shift of ~ 10 eV. The resulting shifts in the spectra were corrected by referencing to the Ti 3p peak (37.5 eV) for the O 1s, Ti 2p, C 1s and to the Au $4f_{7/2}$ (84.0 eV) for the Au 4f spectra, respectively. As shown below, the influence of the charges accumulated under some conditions makes the interpretation of the data difficult.

4.4.4.2 O 1s

The "TiO_2" component of the O 1s spectrum (fig. 4.4.2 and table 4.4.3) is the main component in the spectra 4.4.2.a, 4.4.2.b and 4.4.2.e (under high vacuum and CO conditions). The line width (FWHM 1.12 eV ± 0.01 eV) does not change and the intensity decreases slightly under CO conditions (60% instead of 75% and 76%). Only the position on the binding energy (BE) scale is shifted slightly, to 530.6 ± 0.2 eV.

Under reaction conditions, this component is also present (BE = 530.6 eV) but its width is larger (FWHM: 1.25 eV and 1.64 eV at room temperature and 80°C, respectively). The intensity is decreased (31% and 36%) because another component at lower BE appears (labelled as 'O 1s low energy'). This component has centroids at 529.6 eV and 530.0 eV at room temperature and 80°C, respectively. The width of this component is strongly increasing (1.42 eV at room temperature to 2.39 eV at 80°C). The relative intensity increases from 45% at room temperature to 50% at 80°C.

There is a common component to all spectra. The "O 1s C-O" component is centred on 532.2 eV under high vacuum (HV) and CO conditions. Its width decreases when stored for 16 h under HV (2.40 eV to 1.96 eV) but its intensity is nearly stable (25% to 24%). Under CO conditions this component becomes very broad 2.86 eV and intense (40%). Under reaction conditions its position varies from 531.9 eV at room

temperature to 532.4 eV at 80°C. The width and intensity decreases with increasing temperature (FWHM: 1.38 eV and 1.09 eV; Intensity: 8% and 5%).

A fourth component was inspected under reaction conditions. It is labelled "O 1s C-O sibling" and shows behaviour similar to the "O 1s C-O" component. Its BE increases from 532.7 eV to 533.1 eV when heated from room temperature to 80°C, while the width and the intensity decrease (FWHM: 2.70 eV to 1.88 eV; intensity: 16% to 9%).

Spectrum f (under O_2) shows a large offset in the BE (~ 4 eV) to these other spectra even after charge referencing. It is believed that the accumulated charge does not only lead to a simple slow-down of the emitted photoelectrons, but also to an additional, probably non-linear, distortion of the electric field conditions at the entrance of the electron analyser, resulting in an unreliable measurement. Hence it is not further described in the results section.

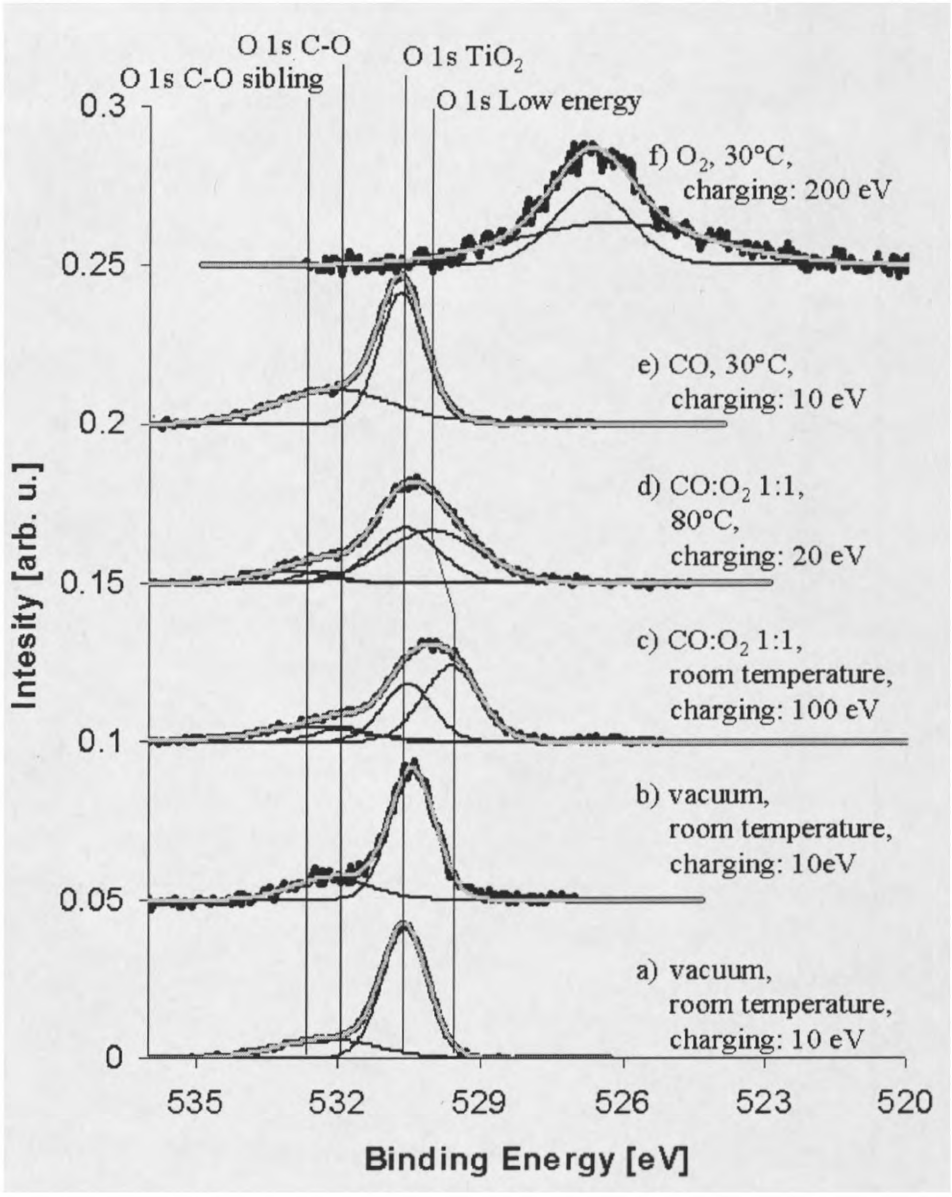

Fig. 4.4.2: O 1s of the Au/TiO_2 catalyst (background subtracted). a) under high vacuum conditions, b) after 16 h under high vacuum, c) under reaction conditions at room temperature d) at 80°C, e) under CO-atmosphere (30°C), f) under O_2-atmosphere (30°C). The raw data in thick black, the fitted peaks in thin black and the envelope of the fitted data in grey.

O 1s												
Spectrum	Component [eV, FWHM,%]											
	low energy			TiO_2			C-O			C-O "sibling"		
a) high vacuum				530.6	1.12	75	532.2	2.40	25			
b) high vacuum after 16 h				530.4	1.12	76	532.2	1.96	24			
c) reaction conditions room temperature	529.6	1.42	45	530.6	1.25	31	531.9	1.38	8	532.7	2.70	16
d) reaction conditions 80°C	530.0	2.39	50	530.6	1.64	36	532.4	1.09	5	533.1	1.88	9
e) CO conditions				530.7	1.11	60	532.2	2.86	40			
f) O_2 conditions	526.2	1.91	58	526.6	4.85	42						

Table 4.4.3: O 1s XP spectrum of an Au/TiO_2 powder catalyst. Values are calibrated to the Ti 3p peak at 37.5 eV in the survey spectrum.

Ti 2p									
Spectrum	Component [eV, FWHM,%]								
	Ti $2p_{3/2}$			Ti $2p_{1/2}$			Ti $2p_{3/2}$ 2nd satellite		
a) high vacuum	458.9	1.26	61	464.7	2.19	30	472.1	2.81	9
b) high vacuum after 16 h	459.2	0.99	61	464.9	2.03	30	472.5	2.71	9
c) reaction conditions room temperature	458.9	1.46	60	464.5	2.38	30	471.9	2.75	10
d) reaction conditions 80°C	458.4	1.84	61	464.0	2.77	31	471.7	2.73	8

Table 4.4.4: Ti 2p XP spectrum of an Au/TiO_2 powder catalyst. Values are calibrated to the Ti 3p peak at 37.5 eV in the survey spectrum.

C 1s																		
Spectrum	Component [eV, FWHM, %]																	
	C 1s Graphite			C 1s CH's			C 1s COH's			C 1s CHO's			C 1s COOH's			C 1s $(O-)_2C=O$'s		
a) high vacuum				285.0	1.63	82				286.7	1.49	8	289.2	1.65	10			
b) high vacuum after 16 h				285.0	1.41	72	285.8	2.42	21				289.3	1.84	7			
d) reaction conditions 80°C				285.1	2.69	82							288.9	2.34	18			
e) CO conditions	284.4	1.23	18	285.1	1.15	21	285.9	2.11	29				288.7	1.93	14	290.8	1.99	18
	artefacts			C 1s CH's									C 1s COOH's					
c) reaction conditions room temperature	276.1	6.64	--	285.3	2.25	74							288.8	1.84	26			
	281.0	11.6	--															
f) O_2 conditions	281.5	2.66	18	285.3	2.36	61							288.5	3.11	21			

Table 4.4.5: C 1s XP spectrum of an Au/TiO_2 powder catalyst. Values are calibrated to the Ti 3p peak at 37.5 eV in the survey spectrum.

Au 4f																				
Spectrum	Component [eV, FWHM, %]																			
	artefact			Au $4f_{7/2}$ I			Au $4f_{7/2}$ II			artifact			Au $4f_{5/2}$ I			Au $4f_{5/2}$ II			background		
a) high vacuum				84.0	0.73	43	84.3	2.14	14				87.7	0.75	32	87.8	2.27	11	89.6	2.00	--
b) high vacuum after 16 h				84.0	0.69	41	84.2	2.27	16				87.7	0.74	31	87.8	2.27	12			
c) reaction conditions room temperature	82.5	1.70	--	84.0	0.92	32	84.6	0.85	26	85.9	3.56	--	87.7	0.90	24	88.3	0.85	18			
d) reaction conditions 80°C				84.0	2.44	37	84.6	0.96	20				87.7	2.46	28	88.3	1.02	15			
e) CO conditions				84.0	0.72	45	84.5	2.53	12				87.7	0.76	34	88.1	2.53	9			
f) O_2 conditions				Au4 $f_{7/2}$ I secondary spectrum			Au $4f_{7/2}$ II secondary spectrum						Au $4f_{5/2}$ I secondary spectrum			Au $4f_{5/2}$ II secondary spectrum					
				81.4	0.71	4	82.5	1.05	5				85.0	0.93	3	86.5	1.39	3			
				Au4f 7/2 I			Au4f 7/2 II						Au4f 5/2 I			Au $4f_{5/2}$ II mirror					
				84.0	0.92	24	85.6	1.50	25				87.8	0.93	18	89.3	1.39	18			

Table 4.4.6: Au 4f XP spectrum of a Au/TiO_2 powder catalyst. Values are calibrated to the Au $4f_{7/2}$ peak at 84.0 eV.

4.4.4.3 Ti 2p

The Ti 2p XP spectra (see fig. 4.4.3 and table 4.4.4) contains 3 features (only the envelope of the three components is shown, since they are all separated from each other). These are the Ti $2p_{3/2}$ component at 459.0 ± 0.2 eV (in spectrum d at 458.4 eV), the Ti $2p_{1/2}$ at 464.7 ± 0.2 eV (in spectrum d at 464.0 eV) and the 2nd satellite of the Ti $2p_{3/2}$ component centred on 472.1 ± 0.4 eV (the 2nd satellite of the Ti $2p_{1/2}$ component is also observable at about 478 eV; for a discussion of the 1st satellite see 4.4.5.3).

Under reaction conditions at 80°C the "Ti $2p_{3/2}$" (1.84 eV) and "Ti $2p_{1/2}$" (2.77 eV) peaks are the widest, whereas after 16 h under high vacuum conditions they are the narrowest of all spectra (FWHM(Ti $2p_{3/2}$) = 0.99 eV, FWHM(Ti $2p_{1/2}$) = 2.03 eV). For the 2nd satellite of the Ti $2p_{3/2}$ the FWHM does not change much (± 0.05 eV). The intensities for all components are also nearly constant (± 1%).

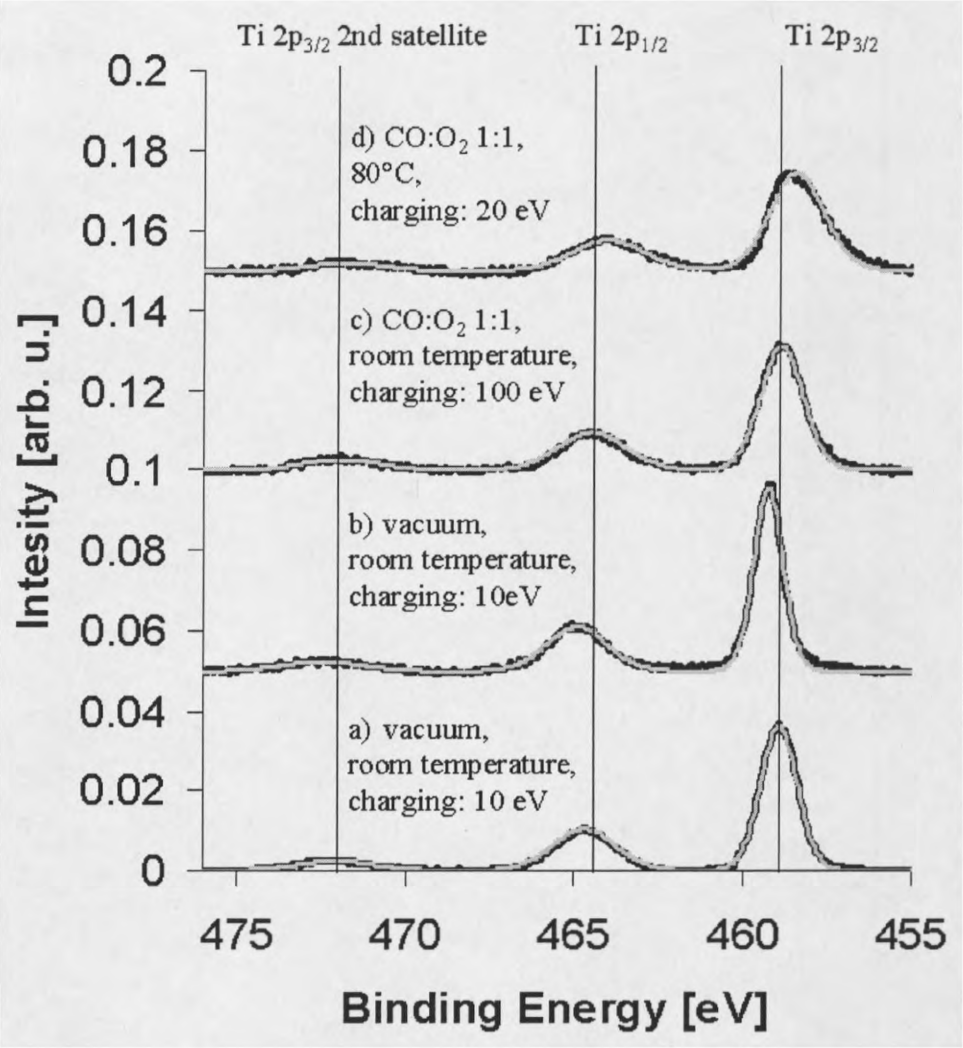

Fig. 4.4.3: Ti 2p of the Au/TiO_2 catalyst (background subtracted). a) under high vacuum conditions, b) after 16 h under high vacuum, c) under reaction conditions at room temperature d) at 80°C. The raw data are shown in thick black and the envelope of the fitted data in grey.

4.4.4.4 C 1s

In fig. 4.4.4 (see also table 4.4.5) the C 1s XP spectra are shown. In spectra 4.4.4.c two unusually broad components appear. Both are below 283 eV and are considered artefacts from the measurement. Therefore they are not further discussed.

Common to all spectra is one component centred on 285.1 ± 0.2 eV and labelled as "C 1s CH's". This component is, except in spectrum 4.4.4.e, the dominant peak (between 61% and 83% relative intensity). But the FWHM is varying from 1.41 eV to 2.69 eV. It is interesting to note the decrease of the intensity and width after 16 h in vacuum (82% to 72% and 1.63 eV to 1.41 eV, respectively). Under O_2 conditions the "C 1s CH's" component is quite weak (21%) but very sharp (FWHM = 1.15 eV).

Under high vacuum conditions, two more components are visible: First, a component centred at 289.3 ± 0.1 eV (C 1s COOH's) that is slightly decreasing in intensity. Second, a component in the first spectrum 4.4.4.a centred around 286.7 eV, which seems to be heavily shifted to lower BE in the second spectrum (285.8 eV). Further, the component is increasing in FWHM and gaining a lot of intensity. The component is assigned, because of this shift, as "C 1s CHO's" in spectrum 4.4.4.a but C 1s COH's in the spectrum 4.4.4.b.

Under reaction conditions (spectra 4.4.4.c and 4.4.4.d) two components can be seen. There is the ubiquitous "C 1s CH's" component, which slightly shifts to lower BE by 0.2 eV, and has increasing intensity and FWHM when the sample is heated to 80°C. The second component, labelled as "C 1s COOH's", is centred around 288.8 eV ± 0.1 eV, and also gains in width. However, it decreases in intensity at 80°C.

The most complex spectrum is spectrum 4.4.4.e measured under CO conditions. It contains five components, including the "C 1s CH's" component. Under this conditions the component is centred on 285.1 eV, has the smallest FHWM (1.15 eV) and a very small intensity in comparison to the other conditions.

The in energy lowest component is centred at 284.4 eV (C 1s Graphite) and is also quite narrow (FWHM: 1.23 eV). The intensity (18%) is similar to the "C 1s COOH's" (14%) and "C 1s $(O\text{-})_2C{=}O$'s" (18%) components of that spectrum. These "high" energy components are centred at 288.7 eV and 290.8 eV, respectively. The FWHM is similar with 1.93 eV and 1.99 eV for the "C 1s COOH's" and "C 1s $(O\text{-})_2C{=}O$'s".

The last component is the "C 1s COH's". This is centred at 285.9 eV and is the most intense component (29%). The FWHM is also not very wide (2.11eV).

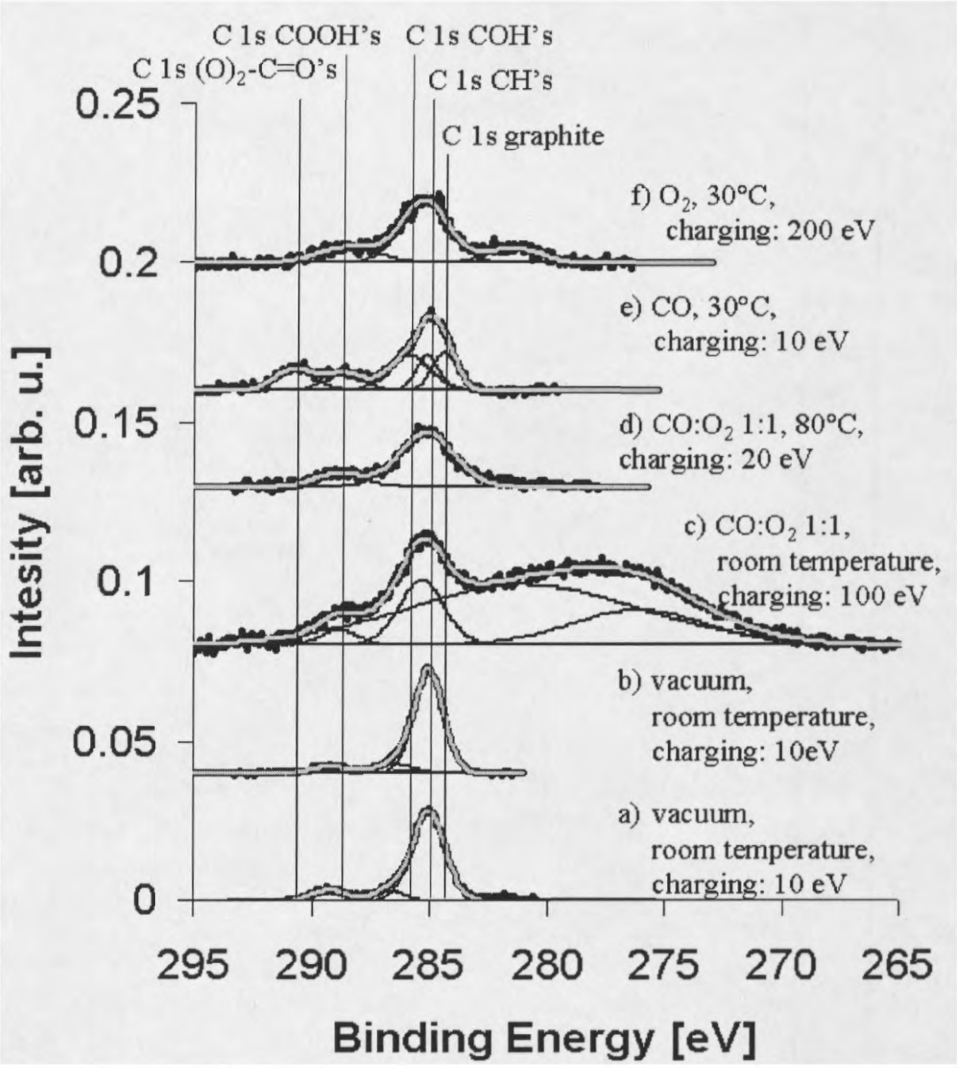

Fig. 4.4.4: C 1s of the Au/TiO_2 catalyst (background subtracted). a) under high vacuum conditions, b) after 16 h under high vacuum, c) under reaction conditions at room temperature d) at 80°C, e) under CO-atmosphere (30°C), f) under O_2-atmosphere (30°C). The raw data in thick black, the fitted peaks in thin black and the envelope of the fitted data in grey.

4.4.4.5 Au 4f

The Au $4f_{7/2}$ and $4f_{5/2}$ double peaks are shown in fig. 4.4.5 (for the specific values see table 4.4.6). The component centred on 84.0 eV (to which the spectrum is calibrated)

is labelled as "Au $4f_{7/2}$ I". Except for spectrum 4.4.5.d the FWHM is very narrow (0.9 eV to 0.7 eV) but the intensity is varying from 32% to 45% (excluding spectrum 4.4.5.f). This behaviour is reflected quite well in the Au $4f_{5/2}$ I component, which is centred around 87.7 eV ± 0.1 eV.

Under high vacuum conditions the "Au $4f_{7/2}$ II" components are centred very close to the "Au $4f_{7/2}$ I" components (84.3 eV ± 0.1 eV). Under CO conditions the peak is slightly shifted to higher BE (84.5 eV), but has a similar width (2.53 eV to 2.20 eV ± 0.07 eV) and intensity (12% to 14% and 16%) in comparison to the high vacuum conditions. Under reaction conditions, this component is further shifted to higher BE (84.6 eV) and becomes very narrow (0.90 eV ± 0.06 eV). The intensity varies between 26% at room temperature and 20% at 80°C. Finally, under O_2 conditions (spectrum 4.4.5.f) this component shifts to higher BE (85.6 eV) and gets wider than under reaction conditions (FWHM = 1.50 eV). Interestingly, under this condition the "II" component is more intense than the "I" component (25% : 24%). Also, the "Au $4f_{5/2}$ II" component (BE between 87.8 eV and 89.3 eV) shows a similar behaviour as the "Au $4f_{7/2}$ II" component.

In spectrum 4.4.5.f four further components appear. These components have a behaviour like they are images of the former discussed components but with an off-set in the BE and are labelled as "secondary spectrum".

In the spectra 4.4.5.a and 4.4.5.c novel components appear that are considered to be artefacts or background effects. Hence they have no chemical information pertaining to the sample and are not further discussed.

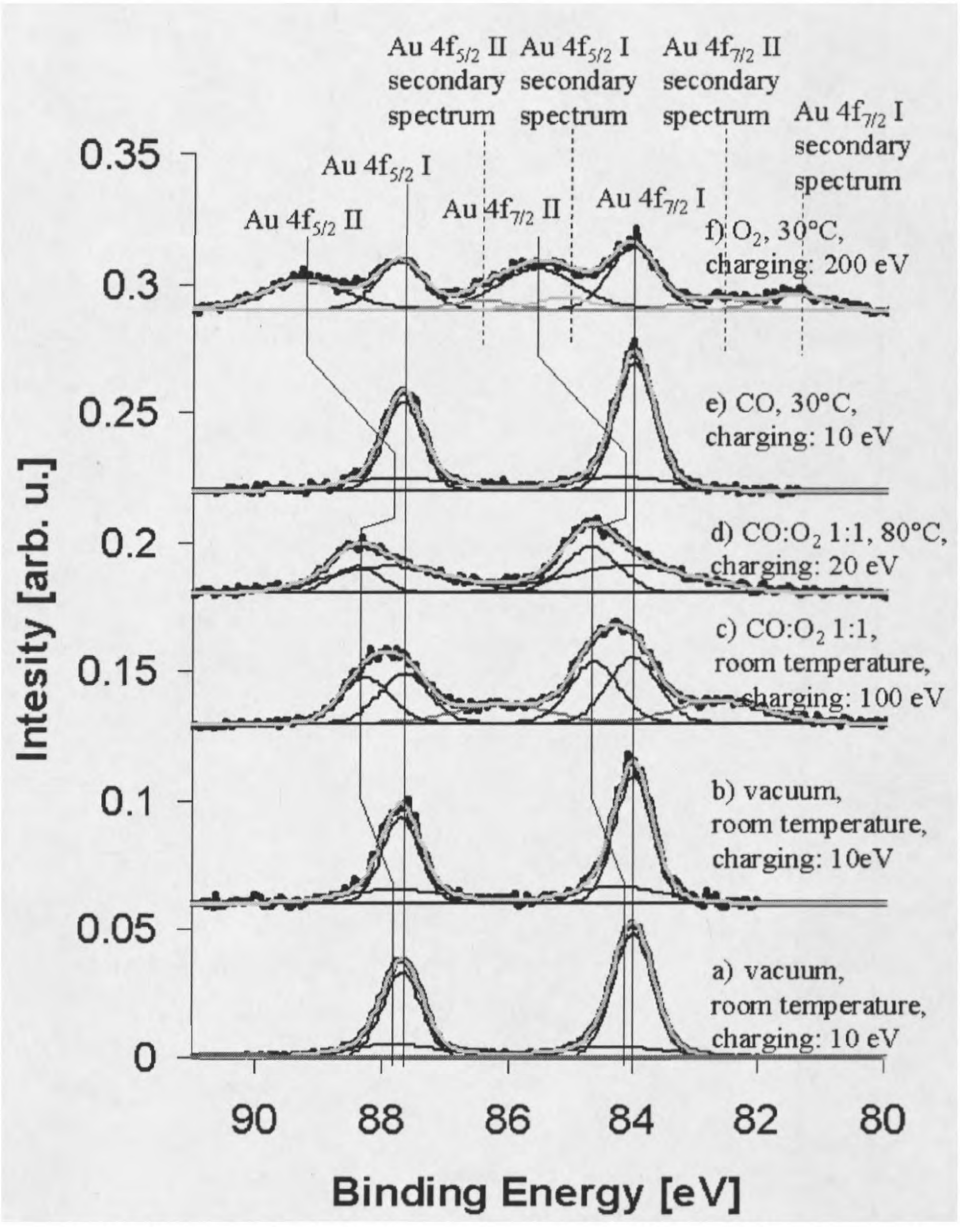

Fig. 4.4.5: Au 4f of the Au/TiO_2 catalyst (background subtracted). a) under high vacuum conditions, b) after 16 h under high vacuum, c) under reaction conditions at room temperature d) at 80°C, e) under CO-atmosphere (30°C), f) under O_2-atmosphere (30°C). The raw data in thick black, the fitted peaks in thin black, additional or artificial peaks in dark grey and the envelope of the fitted data in grey.

4.4.5 Discussion

4.4.5.1 XPS

Under O_2, and under reaction conditions at room temperature, high sample charging occurred (equal to a BE shift of about 200 eV and 100 eV, respectively). This effect seems to be related to the prolonged storage of the catalyst in vacuum (16 h) at the beamline before dosing gases, since either the low loaded (0.5 wt%) or the similar sample used in the studies presented before [7, 8] show such an effect. The storage in vacuum greatly decreases the amount of water adsorbed on the support. Therefore either the conductivity of TiO_2 powder or the contact between sample and sample holder is reduced, which leads to a bad charge neutralization. This effect seems to be further increased by oxygen adsorbed on the surface. The oxygen will increase the electric insulation of the sample from the sample holder, and therefore increase the sample charge. This is supported by the fact that sample charging is reduced when heating the sample under reaction conditions from room temperature to 80°C. Due to higher catalytic activity at 80°C, the amount of oxygen adsorbed will decrease, and therefore reduce the insulation of the catalyst.

Due to the high charging, the interpretation of the spectra taken under O_2 and under reaction conditions at room temperature is quite speculative. When the sample is highly charged it appears that the charge is no longer homogenously distributed across the surface, or that the response of the electron analyser becomes non-linear across the BE scale. This results in (i) artificial secondary spectra in the Au 4f spectrum under O_2 conditions, (ii) further artefacts under reaction conditions at room temperature, and (iii) the offset of the O 1s spectrum under O_2 conditions.

4.4.5.2 O 1s XPS

As mentioned in the Results section, the spectrum of the O 1s photoemission under oxygen conditions (spectrum 4.4.2.f) exhibits an offset. It appears that due to the sample charging the spectrum is shifted by about 4 eV to lower BE and a very broad component is included in the spectrum. It is not possible to determine whether this

broad component is a background or a real effect. Hence the spectrum will not be further discussed here.

The component centred at 530.5 eV ± 0.2 eV is due to lattice oxygen species in TiO_2 (and also labelled as "O 1s TiO_2"). The BE value reported in the literature [12] is 530.3 eV and fits the value of this work quite well (530.6 eV ± 0.2 eV). The second component common to all spectra is the "O 1s C-O" centred at 532.2 eV ± 0.3 eV. This component and the component labelled "O 1s C-O sibling" are due to carbon with at least one carbon-oxygen bond. The first peak is due to double bonded oxygen and the "sibling" due to weaker (single) bonded oxygen [13]. Therefore the "sibling" might be assigned to an activated intermediate carbon oxide, or to reaction spectators with C-O single bonds. A spectator is, for example, a carbonate like species, which might have been formed by oxidation of CO, but not yet desorbed as CO_2. Further reaction of this species could explain the strong carbonate signal in DRIFTS spectra of similarly prepared samples [14]. It is plausible that CO_2 could react with the TiO_2 support, especially surface hydroxyls, to create an adsorbed carbonate or acid species. The component labelled as "low energy" might be due to adsorbed O_2. Unfortunately, the spectrum acquired under O_2-conditions, which should in principle contain the information required to support this, is not interpretable and this assignment remains to be confirmed.

4.4.5.3 Ti 2p XPS

Oku *et al.* investigated an important point in the discussion of Ti 2p XP spectra [15]. For the first time they found further inelastic scattering satellite peaks, which are about 3 eV separated from the main peaks. It was further reported that these satellites could neither be interpreted, nor completely removed from the spectrum with a Shirley type background subtraction. Due to their small separation from the main peak, the 1st satellite of the Ti $2p_{3/2}$ peak is centred on the lower BE side of the Ti $2p_{1/2}$ peak. Therefore it is hard to observe bands in this region without fully resolving - or removal of - the 1st satellite resonance.

The best chance to resolve these satellites is to use combined XPS and EELS, however, this technique is not available for the present work. Thus it is not possible to resolve small extra components in the Ti $2p_{1/2}$ peak.

The value given for the Ti $2p_{3/2}$, which is assigned to TiO_2 (meaning Ti^{4+}), is 459.3 eV [12]. This value is in reasonable agreement with the value derived in this work (459.0 ± 0.4 eV). The relative shifts of the "Ti $2p_{1/2}$" and "Ti $2p_{3/2}$" 2^{nd} satellite are 6 eV and 13 eV, respectively [15]. This is in good agreement with the values obtained in this work: 5.7 eV ± 0.1 eV and 13.1 eV ± 0.1, respectively.

No band on the lower BE side of the Ti $2p_{3/2}$ peak can be seen in any spectrum. Hence, no evidence is given that large amounts of TiO_2 are reduced. It cannot be fully excluded that the surface contains no Ti^{3+} centres, because the sensitivity is, even with XPS in some cases, too small. The results are also in good agreement with the data from lower loaded catalysts [7]. Here, little or no, amounts of Ti^{3+} are found. The large shift of the main Ti $2p_{3/2}$ component (more than 1 eV under certain conditions) as reported in [8] cannot be supported. The Ti 2p spectra here are referenced to the Ti 3p peaks, and the good agreement of the C 1s values with literature data support this charge referencing (see point 4.4.5.4). Denkwitz *et al.* [8] unfortunately do not give any C 1s data; therefore it cannot be judged if this difference is due to a different referencing procedure or a difference in the sample.

4.4.5.4 C 1s XPS

Assignments of emission features in the C 1s data were interpreted by comparison with published assignments for organic functional groups, especially those in polymers [13]. The spectra from the catalyst are quite complex and it is not really possible to extract more than qualitative information from them, *i.e.*, whether there are carbon species with zero, a single (e.g., COH), two single, a double bond (CHO), or more bonds (COOH, $(O-)_2C=O$) to oxygen present.

The ubiquitous "CH" group is considered to be hydrocarbons, which are the commonly found contamination after samples were handled in a physical/chemical laboratorial atmosphere (without any clean air specification). Further sources of contamination are dust and aerosol particles from the ambient air, and other objects

the sample may have been in contact with. The hydrocarbon C 1s emission is usually considered a good "internal standard" and is therefore often used in XPS studies to calibrate the energy scale. This standard was not used here because the amount and oxidation state of the hydrocarbons might change during the oxidation reaction on the catalyst. Furthermore, complications arise because under the environmental conditions of the present *in situ* experiments, more carbon species are expected to be present on the sample. Hence complicating the determination of the position of the C 1s peak of the hydrocarbons. In any case, the C 1s emission was not available at all for referencing the Au 4f data, as the photon energy was too small to excite the C 1s electrons.

Comparing the spectra under high vacuum conditions, a clear shift of the "C 1s CHO" peak to lower binding energies can be seen. Hence in the second spectrum this species is labelled as "COH", because it is believed that higher carbon-oxygen species from surface contaminants are reduced. This reduction could, e.g., be from an ether to an alcohol, but this is not clearly determinable. Further the intensity of the "CH's" and the "COOH's" is slightly decreasing, but the intensity of the "CHO's/COH's" is increasing (8 % to 21 %). This may suggest that the "CHO's" (and some "COOH's") are reduced by the CH's under vacuum conditions.

Under reaction conditions neither "COH" nor "CHO" signatures can be detected. This means that these species have either been oxidised to a carboxylic acid (COOH) or reduced to a hydrocarbon. Hence all adsorbed species involved in CO oxidation appear to be in a "carboxylic acid" like oxidation state. This would include the reactant (CO), the product (CO_2) and the intermediates. Another hint for this interesting observation is the decreasing intensity when increasing the reaction temperature. This would be due to a faster reaction rate, which should lead to less "intermediates" on the surfaces in comparison to the stationary hydrocarbons.

In comparison to the spectra obtained under reaction conditions at 80°C, it is also interesting to have a look at the spectrum under O_2 conditions. The spectra look very similar (except the band at 281.5 eV, which is considered to be an artefact from the strong sample charging) in terms of the band position and the FWHM of the components. The reason could be that the reaction is running so slowly that an O_2 excess is present on the catalyst. Hence no intermediates or adsorb CO may be detected.

The most complex spectrum in the C1s series is spectrum 4.4.4.e (under CO conditions). Similar to the other spectra it contains the "CH" and the "COOH" component that shall not be discussed again. The highest BE component should be similar to a carbon with four bonds to oxygen. It might be that this is unreacted CO that is stored on the TiO_2, building a species similar to adsorbed carbonic acid, with four oxygen bonds.

Under CO conditions a component similar to spectrum 4.4.4.b (after 16 h in vacuum) appears at 285.9 eV. This is the most intense component. The intensity would imply that it is adsorbed CO, but this would mean that the C-O bond is weakened, or a final state effect not related to the chemical shift might be present (see techniques section). A new component can be seen in the spectrum taken under CO condition. This component is centred on 284.4 eV and is likely due to graphite. A Boudouard like reaction might produce the graphite. This was also suggested on results found in *in situ* XAS data on electrochemical oxidised gold foil.

4.4.5.5 Au 4f XPS

The spectra under high vacuum and CO conditions are practically equal, indicating that the gold particles investigated under high vacuum conditions are in the same chemical and structural state as in the presence of CO at elevated pressure. There is a major component (I) that corresponds to metallic bulk gold, as known from numerous previous studies of single crystals and polycrystalline foils of gold [16]. The peaks are narrow, as in bulk gold. An explanation may be that these particles have a sufficiently large diameter and narrow size distribution (the particle size distribution is centred between 2.5 nm and 3.0 nm [9]). It is known from cluster studies that particle sizes well below 2 nm are required to observe non-bulk behaviour. Hence CO adsorption would have a very small influence on the electronic state of these bulk-like particles. There is a second BE-shifted and a broad component (II) in the spectra of the particles. Their signature is in excellent agreement with that found in previous XPS studies [17] of very small (< 2 nm) metallic Au clusters, where the observed BE shift was unequivocally assigned to reduced final state screening in small clusters (see techniques section). It is therefore likely to be representative of the very small

metallic particles in the size distribution on the present catalyst (not observable with TEM).

Parallel work examined the properties of Au nanoparticles on a TiO_2 support under reaction conditions, and has led to the proposition of the tentative model described in fig. 4.4.6. This model was derived from *in situ* EXAFS and XPS data [18]. The catalyst used for these investigations had a loading of 0.5 wt% and less.
This catalyst showed low Au-Au coordination number (CN) of about 9-10, which is significantly smaller than in the bulk (CN: 12).

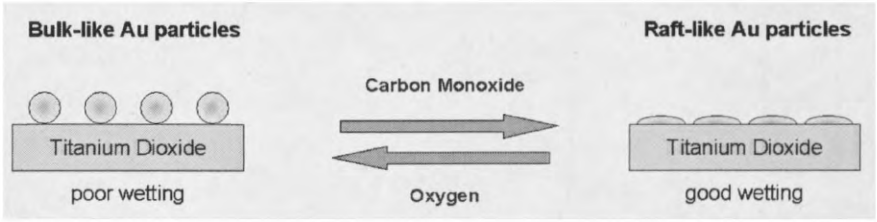

Fig. 4.4.6: Possible behaviour of gold nanoparticels on TiO_2 under different atmospheres.

To realise such a small CN the Au particles must be quite small, with particle sizes corresponding to only a few atom layers. This would be especially compatible with a high percentage of surface atoms, which have smaller CNs because they are missing one layer of coordinating atoms on the vacuum/gas side (cf. fig. 4.4.7).

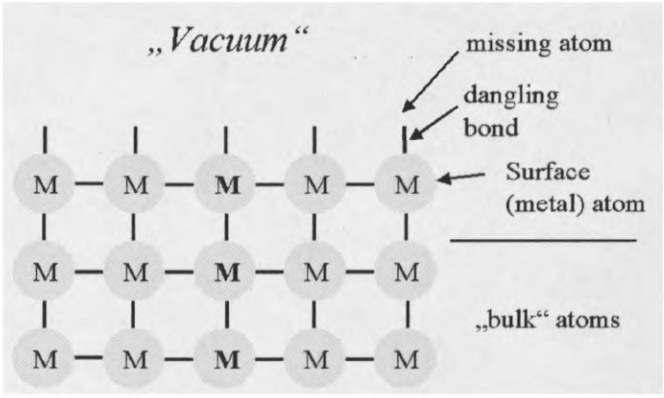

Fig. 4.4.7: Very simple model of the surface.

A second possibility to achieve more low coordinated atoms, besides making the clusters smaller, is to change their shape. The geometric body with the smallest surface to bulk ratio is the sphere. Changing this shape to any other increases the surface of the particle. This is done when a substance wets a surface. The better it wets the surface the more it flattens out until it forms a monolayer (or multilayer) film on the surface, which exhibits the ultimate, highest surfaces to bulk ratio. A few steps of how a particle can wet a particle surface is shown in fig. 4.4.8.

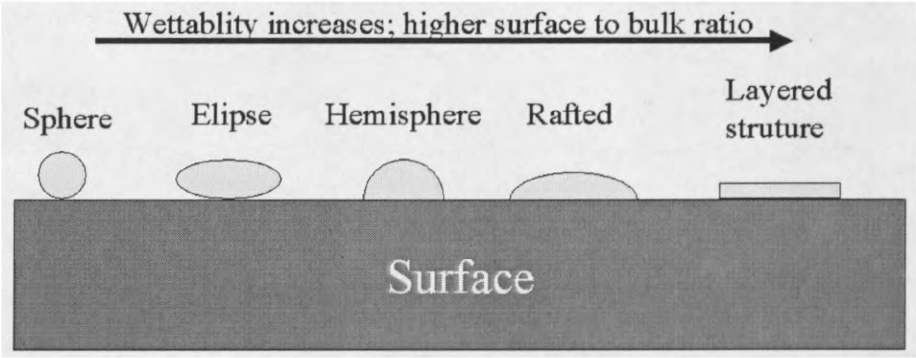

Fig. 4.4.8: Wettability of a particle on a surface and resulting shapes of the particle.

Different shapes of particles on flat surfaces are mostly determined by STM. The only problem that arises is the determination of the correct diameter of the particle. It has been shown that gold particles on certain substrates prefer to grow first laterally, and then with increasing thickness [19], in a modified Stranski-Krastanov growth mode.
Au 4f XPS results indicated, by a slight shift to higher BE, that small gold particles wet the substrate when the catalyst was exposed to carbon monoxide containing atmosphere [7, 8]. The metallic gold peak ($Au4f_{7/2}$: 84.0 eV) peak was attributed to bigger Au particles, which have a spherical shape. Besides the metallic peak, a broadened component with higher BE appeared, with an intensity that strongly increased under reaction ($CO + O_2$) conditions and in CO atmosphere. In this study, under CO this shift was not observed. This might be due to the previous CO oxidation, which might have led to an increase in size of the gold particles. Therefore no remaining small particles might have been present under CO conditions anymore.
An explanation for this effect would be to assume that the wettability of the Au changes under different atmospheres. Gold is expected to wet stoichiometric TiO_2 poorly, and exposure to practically non-adsorbing O_2 should not affect the interfacial structure. When the CO content is increased, defects in the TiO_2 (e.g. Ti^{3+}) surface are

expected to appear, which would create a more reactive surface that can be wetted by gold. Alternatively, it is known from single crystal studies that CO adsorbed much more strongly on gold than on TiO_2 and it was also possible to show this with *in situ* XAS in this study. Adsorption of CO would lower the surface tension of the Au particles, and may allow them to better wet the TiO_2 surface. A combination of these two CO-induced effects is also a possibility. This effect is more pronounced for the smaller gold particles, because the atoms can move more easily (lower melting temperature) [20].

The metallic peak in the XP spectra could then be interpreted as the signature of spherically shaped, big particles (< 2nm). The higher BE peak could be due to raft-like, smaller particles. With an increase in the reducing power (*i.e.*, by increasing the CO partial pressure) of the atmosphere, more and more of the smaller particles would change into a raft-like shape, whereas bigger, metallic particles remain spherical.

Increasing the temperature results in a broadening of the metallic component. This observation is unusual for Au metal, and could mean that Au atoms in the bigger particles are actually mobile and/or reactive enough to allow significant rearrangement or reaction. Higher temperatures might even result in more "non-metallic" gold clusters.

Finally, under oxygen conditions, component "I" is again very narrow, but component "II" is shifted to even higher BE than under reaction conditions in comparison. This might be taken as an indication that smaller Au clusters are present, but this seems unlikely in view of the fact that adsorption of molecular O_2 on these systems is known to be extremely weak. An alternative explanation might be that dissociation of O_2 by secondary electrons emitted from the sample, induced by the X-ray beam, takes place, which might lead to oxidation of the outer sphere of the small Au particles and/or deposition of an atomic oxygen layer on the larger particles. Secondary electron induced dissociation of O_2 has previously been used to deposit monolayers and oxide layers on single crystalline gold [21]. Alternatively, the shift might be related to the fact that the sample is highly charged (corresponding to a BE shift of 200 eV) – possibly differential charging of the two gold components occurs. If this effect were indeed present it would cast doubt on the validity of the previous interpretation of the Au 4f spectra acquired under reaction conditions at room temperature, where charging on the same order of magnitude was observed. To address this point it was attempted

to calibrate the Au4f spectra to the Ti 3p peak. This gave Au 4f spectra with quite different BE, where the lower BE component would be related to an "Au^-" species, which appears unreasonable. Instead, it appears to be that the two gold components in the spectra may have different electrically conducting contact with the support. This would explain why the calibration to the Ti 3p peak gives physically nonsensical shifts in the Au 4f spectra, as charging would lead to apparently different BE's.
Also the spectra taken by Denkwitz *et al.* [8] show the formation of a clearly separated second Au 4f component under oxygen conditions. Unfortunately, at these conditions only survey scans are present and no region scans, which makes a further comparison to the presented data impossible. But it indicates that only "secondary spectrum" marked peaks are due to charging effects.

4.4.6 Conclusion

Using *in situ* XPS it was found that changes in gold nanoparticles supported on TiO_2 powder could be monitored. The results indicate, as other publications show, that the gold nanoparticles can change their morphology under different atmospheric conditions, and that this is more prominent for particles with diameters smaller than 1 nm than for particles with diameters of about 3 nm. Under CO atmosphere the formation of graphite like species was observed, similar to the species observed by *in situ* XAS on oxidised gold foil treated as well as under CO conditions.

References

[1]: Henao, J. D.; Caputo, T.; Yang, J. H.; Kung, M. C.; Kung, H. H.; Journal of Physical Chemistry B, **2006**, *110*, 8689-8700.
[2]: Daniells, S. T.; Overweg, A. R.; Makkee, M.; Moulijn, J. A.; Journal of Catalysis, **2005**, *230*, 52-65.
[3]: Boccuzzi, F.; Chiorino, A.; Manzoli, M.; Lu, P.; Akita, T.; Ichikawa, S.; Haruta, M.; Journal of Catalysis, **2001**, *202*, 256-267.
[4]: Guzman, J.; Gates, B. C.; Journal of Physical Chemistry B, **2003**, *107*, 2242-2248.

[5]: Bluhm, H.; Hävecker, M; Knop-Gericke, A; Kleimenov, E; Ogletree, D. F.; Hebenstreit, E. L.; Salmeron, M; Schlögl, R.; *Fritz-Haber-Instiut der Max-Plank-Gesellschaft*, personal comunication.

[6]: Kleimenov, E.; Bluhm, H.; Hdvecker, M.; Knop-Gericke, A.; Pestryakov, A.; Teschner, D.; Lopez-Sanchez, J. A.; Bartley, J. K.; Hutchings, G. J.; Schlögl, R.; Surface Science, **2005**, *575*, 181-188.

[7]: Willneff, E. A.; Braun, S.; Rosenthal, D.; Bluhm, H.; Haevecker, M.; Kleimenov, E.; Knop-Gericke, A.; Schloegl, R.; Schroeder, S. L. M.; Journal of the American Chemical Society, **2006**, *128*, 12052-12053.

[8]: Denkwitz, Y.; Kieldbassa, S.; Schumacher, B.; Bansmann, J.; Behm, R. J; Schnörch, P.; Vass, E.; Hävecker, M.; Knop-Gericke, A.; Schlögl, R.; Catalysis Letters, **submitted**.

[9]: Schumacher, B.; Plzak, V.; Cai, J.; Behm, R. J.; Catalysis Letters, **2005**, *101*, 215-224.

[10]: Hüfner, S.; *Photoelectron Spectroscopy 2nd Edition*, Springer Verlag, **1995**.

[11]: Shukla, S.; Seal, S.; Nanostructured Materials, **2000**, *11*, 1181-1193.

[12]: Oku, M.; Wagatsuma, K.; Kohiki, S.; Physical Chemistry Chemical Physics; **1999**, *1*, 5327-5331.

[13]: Beamson, G.; Briggs, D.; *The XPS of Polymers Database*, Surface Spectra, **1992**.

[14]: Schumacher, B.; Denkwitz, Y.; Plzak, V.; Kinne, M.; Behm, R. J.; Journal of Catalysis, **2004**, *224*, 449-462.

[15]: Oku, M.; Matsuta, H.; Wagatsuma, K.; Waseda, Y.; Kohiki, S.; Journal of Electron Spectroscopy and Related Phenomena, **1999**, *105*, 211-218.

[16]: Aita, C. R.; Tran, N. C.; Journal of Vacuum Science & Technology, **1991**, *9*, 1498-1500.

[17]: DiCenzo, S. B.; Berry, S. D.; Hartford, E. H. Jr; Physical Review B, **1988**, *38*, 8465-8468.

[18]: Willneff, E. A.; *PhD Thesis*, University of Manchester, **2007**.

[19] Chusuei; C. C.; Lai, X.; Luo, K.; Goodman, D. W.; Topics in Catalysis, **2001**, *14*, 71-83.

[20]: Blackman, M.; Sambles, J. R.; Nature, **1970**, *226*, 938.

[21]: Gottfried, J. M.; Schmidt, K. J.; Schroeder, S. L. M.; Christmann, K.; Surface Science, **2002**, *511*, 65-82.

5 General Conclusions and further studies

Four different model catalysts for the low temperature CO oxidation promoted by supported gold nanoparticles were examined. To do so, equipment was designed and constructed to study the different catalysts with *in situ* spectroscopy. The studies show the general difficulty of preparing model catalysts that mimic the (potentially) industrially used catalysts. It is also difficult to use just one model catalyst, if all, or a wide range of classical surface science techniques should be used, and these techniques still need adoption to *in situ* experiments.
To continue this work I propose the following experiments for the different model catalysts:

Gold nanoparticles on high surface support: The most interesting question evolving from the *in situ* XPS results is, if the proposed morphologically changes of the gold particles can be detected with other methods. TEM would be an ideal candidate for this task, unfortunately it is very difficult to detect gold particles in the very low loaded catalysts, and the effects on the high loaded samples might be smaller, or only due to smaller particles possibly also present on these samples. There is also the problem that there are only very few *in situ* TEM machines. Therefore this is a very challenging task. Therefore studies on flat samples should be continued and with the use of an STM the proposed changes could be possibly studied.

Gold nanoparticles on flat support: A conducting or semi-conducting support would allow the use of scanning tunnelling microscopy (STM) to achieve an image of the gold nanoparticles. This would be possible by the use of either defective titanium oxides, or a support, like silicon. It should also be possible to prepare a thin TiO_2 layer (few atomic layers) on a substrate like silicon or tungsten. The thin overlayer of TiO_2 would not be totally insulating, and therefore a tunnelling current, as required for STM, could be achieved. This would presumably be the most realistic flat model catalyst for gold nanoparticles supported on TiO_2 powders like P25 from Degussa/Evonik, which can be studied by STM.
The reactivity of the gold nanoparticles on the flat support has to be determined as well. Therefore the leaking of reactants from the reaction chamber into the mass

spectrometer has to be stopped. This requires the installation of a leak valve that is able to sustain a pressure drop of roughly 1 bar to 10^{-8} mbar without leakage and the ability to be opened and closed regularly. In this work it was found to be hard to achieve this without the constant risk of the leak valve starting to leak after opening and closing it a few times. It might be helpful though to have an extra pumping system, which would be able to pump the connection between the reaction chamber and the mass spectrometer in case of small leaking. Hence, base pressure measurements of the mass spectrometer could be contained without the problem of gas leaking into the connection part between reaction chamber and mass spectrometer. The use of a combined gas chromatography and mass spectrometry analysis would lower the requirement for the pressure drop over the leak valve, but not more than a few µl of reaction gas per minute (in the best case) could be injected into the gas chromatometer.

Electrochemically oxidised gold foil: To remove the impurities of the electrochemically oxidised samples it would be useful to prepare the samples directly at the experiments without the need to transport them through the environmental atmosphere. Whereas this is relatively simple for experiments be sealed of from the vacuum, a special design is required if techniques like soft X-ray XAS or XPS should be used. In these cases the preparation needs to be sealed of from the vacuum part at all times to prevent the evaporation of the electrolyte and therefore damage or destruction of the vacuum experiment.
After the impurity problem is solved, interesting questions to address would be *e.g.* if the formation of a graphite overlayer can be also observed when CO and O_2 are dosed at the same time, and under which condition a graphite overlayer could be removed, e.g. with O_2 or O_2/H_2O. These experiments could also be coupled with *in situ* XPS studies that might give a deeper insight into the formation mechanism and the composition of the overlayer.

Gold powder: The activation of the gold particles under reaction conditions at temperatures around 700 K seems to be very interesting. It should be possible to test whether the catalyst loses its increased activity after heating to about 700 K in reaction conditions *e.g.* in ambient air, or more controlled, different atmospheric conditions like CO, O_2 or inert gas. It would also be interesting to discover whether

above room temperature but below 700 K. One can also study the activation of the catalyst under different atmospheric conditions like is done for most heterogeneous catalysts prior to the catalytic reaction (usually called "calcination").

To identify if the increase in activity is due to the formation of new active sites on the catalyst, temperature programmed desorption (TPD) could be used. Another option would be the use of AFM under reaction conditions. But there a special set up is required to protect the piezo-element from the heat that is required to achieve the conditioning. (see also fig. 5.1). The set up would require a specimen-disk to which a high current, as well as temperature insulating material is attached. This is required to shield the piezo-element from any heat or current that is produced or supplied to the heater. The heater itself is positioned on top of the insulating layer, and is either directly supporting the gold powder, or a second specimen-disk is induced between heater and gold powder.

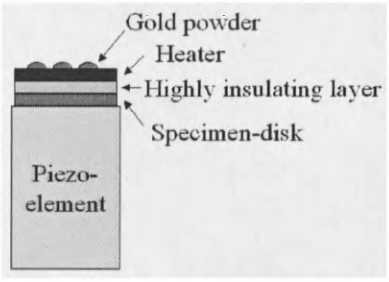

Fig. 5.1: Schematic drawing for the heating set up for AFM studies on gold powder under reaction conditions (temperatures required are close to 800 K). The insulating layer would need to insulate against heat and current, so that the gold powder would be at temperatures of about 800 K and the piezo-element very close to room temperature.